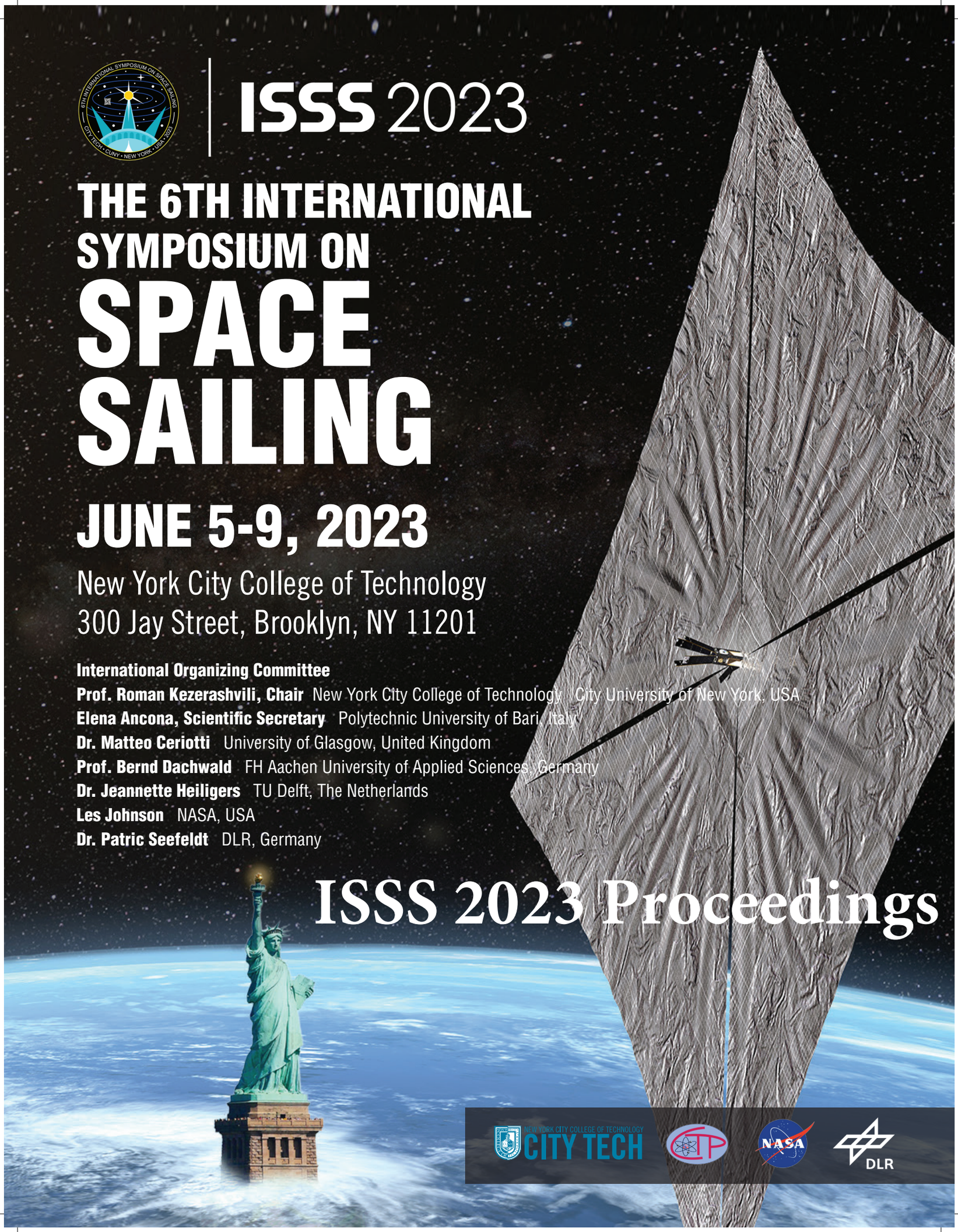

ISSS 2023

THE 6TH INTERNATIONAL SYMPOSIUM ON SPACE SAILING

JUNE 5-9, 2023

New York City College of Technology
300 Jay Street, Brooklyn, NY 11201

International Organizing Committee

Prof. Roman Kezerashvili, Chair New York City College of Technology, City University of New York, USA
Elena Ancona, Scientific Secretary Polytechnic University of Bari, Italy
Dr. Matteo Ceriotti University of Glasgow, United Kingdom
Prof. Bernd Dachwald FH Aachen University of Applied Sciences, Germany
Dr. Jeannette Heiligers TU Delft, The Netherlands
Les Johnson NASA, USA
Dr. Patric Seefeldt DLR, Germany

ISSS 2023 Proceedings

The submission of a paper was not mandatory to give a talk. The ISSS 2023 Proceeding includes submitted articles

Table of Contents

Research for and Early-Stage Development of the First Interstellar CubeSat Powered by Solar Sailing Technology

Piotr Fil[a,*], Gil Barbosa Ribeiro[a], Debdut Sengupta[a], Beatriz Soriano Tortosa[b]

[a]*Department of Aeronautics, Imperial College London, London, UK*
[b]*Department of Mechanical Engineering, Imperial College London, London, UK*

Abstract

Project Svarog is a student-led initiative aiming to reach the heliopause using a solar sail [1]. The sail is set to be passively stabilised and does not require gravity assists unlike previous interplanetary missions, thus making deep space exploration more feasible and flexible. Previous feasibility studies have been performed, demonstrating the potential of the mission and highlighting research focus. A high-fidelity orbital model has been developed for proving the feasibility of the trajectory and studying initial conditions. Currently, Scientific Machine Learning [2] is being implemented to study the optimal initial conditions, parameters, and the sensitivity of the trajectory with respect to those properties of the system. Initial studies show that the escape trajectory is feasible for a mass to area ratio of 12 g m^{-2}. Given the repeated close passes to the Sun, the long duration of the mission, and its sensitivity to solar events, understanding and modelling the space environment for the duration of the mission is paramount. So far, preliminary simulations of radiation dose received by the spacecraft using GRAS [3] coupled with data driven model of solar activity have been performed. Structural simulations from an in-house code which uses multi-particle model have been compared with commercial packages and paired with vacuum chamber testing for validation. Following the IKAROS team research and analysis [4], we have now developed non-dimensional analysis which will enable scaling of sail dynamics to reduce number of required simulations and enable conducting experimental validation of sail behaviour under influence of gravity. Mechanical and electronic design and prototyping have been undergoing in parallel with the research endeavours. These have made testing of deployment methods and communications architectures possible. A motor-controlled boom deployment is being studied in parallel with the flight proven spinning method [5]. Should these technologies be successful, the Svarog system could serve as a low-cost enabler for the testing of new technologies and research opportunities in deep space, piggybacking of the increasing number of interplanetary missions and fostering deep space exploration.

Keywords: Deep Space, CubeSat, Solar Sail, Orbital Mechanics, Structural Design

Nomenclature

B	bit rate
c	speed of light
E	energy
F, F_*	mass, characteristic scale
FEM	Finite Element Model
G	antenna gain
I	mean excitation potential
k, K	stiffness, characteristic scale
k_B	Boltzmann constant
l	length
L	Lagrangian
m, M	mass, characteristic scale
n	number of particles
N	noise
P	power
r	radius
t	time
T	characteristic timescale/temperature
x, y, z	position
X	characteristic lengthscale
z	charge of particle
α, δ	Euler angles
β	v/c
γ	Lorentz factor
λ	wavelength
Ω	spin rate

*Corresponding author, piotr.fil20@imperial.ac.uk

Superscripts

’	nondimensional time derivative

Subscripts

0	initial condition
i	i^{th} element
e	electron
k, p	energy type
n	noise
r	receiver
t	transmitter
x, y, z	spatial coordinate type

1. Introduction

High delta-V maneuvers are imperative for deep space exploration by the human race. They were usually conducted during missions based in the Outer Solar System, such as the Pioneer probes, both Voyagers and New Horizons. These missions provided vast amounts of data regarding the gas giants and Pluto, and currently, as they are escaping the Solar System, they will provide data on the properties of interstellar space. Similarly, considerable changes of momentum are required to go into orbits within the solar corona or out of the ecliptic plane. The former is of particular interest to the scientific community to properly build weather and climate models for the Sun. There has been no attempt at such orbits since the Ulysses mission, despite the need for data about the solar poles.

Such maneuvers were usually conducted using gravity assists from other celestial bodies encountered throughout the trajectory. While this approach achieves a high delta-V, it requires careful selection of the launch date and orbit to enable a sufficient change in velocity. As an alternative to the gravity assist approach, on multiple occasions solar sailing has been suggested. Project Svarog has been developed to take advantage of this technique in a novel approach, where a passively stabilized sail is accelerated purely by solar radiation and is capable of conducting maneuvers which go beyond the capabilities of both chemical and electric propulsion.

To achieve this goal, numerous aspects of the mission need to be matured and solutions to the various problems need to be suggested. The main difficulty associated with passively stabilized sails is the presence of disturbing torques due to the non-uniformity of the surface. This results in significant coupling between the structural dynamics and the orbital mechanics of the system. Beyond that, the dynamic deployment of the sail is a complex process to model, which in this paper is tackled both from a theoretical and an experimental point of view. Furthermore, to establish communication with the ground, a sufficient link budget must be provided in the design of the onboard transmitter. Finally, as the predicted duration of the mission is in the order of decades, sufficient consideration for environmental effects should drive the design process. The main focus of this paper is to present the approach taken by Project Svarog to design a mission within these constraints and provide solutions to challenges encountered in the process.

2. Mission Concept and previous work

Passively stabilised solar sails are a prominent area of research at Imperial College London. The initial trajectory analysis for such missions was conducted by Hotston-Moore and Knoll in 2019 [6]. Since the current development is being undertaken by a student society (Imperial College Space Society), great consideration is made for the affordability of the mission. Thus, the launch trajectory is designed to start as a piggyback mission to Mars or Venus. From the conducted simulations, it was determined that selecting a transfer trajectory to Venus results in a considerably lower time required to reach escape velocity from the Solar System. After deployment, the spacecraft is then spun for stability, in the orientation determined to be optimal for achieving a minimum time to heliopause under the given constraints. Preliminary trajectory design can be performed by considering the average perturbation along the orbit depending on the selected initial angle with respect to the Sun’s incoming radiation.

Initial work towards a systematic orbit investigation was done in 2020 by Filippos [7] using GMAT to propagate different mission profiles. This provided a deeper insight into the constraints related to the mission regarding its temperature requirements, ranging constraints and the validity of pre-existing models. From these studies, and a comparison against flight data from the IKAROS mission, it was determined that an investigation of the full six degree-of-freedom motion of the spacecraft is essential for the success of the mission, as solar radiation torques create a non-negligible perturbing effect on the sail’s rotation.

This aspect of the mission became the main focus of the design team over the span of 2021 and 2022, while the orbital mechanics team focused on developing methods for solving the coupled equations of motion for the spacecraft and quantifying the uncertainties of the orbit due to perturbations resulting from attitude changes. In parallel, the structural mechanics team focused on developing numerical models of the membrane as well as an experimental setup, which would be used for testing membrane dynamic behaviour under conditions of

Earth gravity and provide a means for validating the numerical models. Initial results of this investigation were published in the Journal of the British Interplanetary Society [1]. From that point onward, improvements were made both from theoretical and experimental perspectives. A brief overview of these areas will be presented in this paper.

In its current state, the mission is focused on developing a spacecraft capable of achieving an escape velocity and demonstrating this through received telemetry. The primary objective of the project is stated as *"Construct a spacecraft that will reach the Sun's escape velocity and the heliopause (assumed at 123 AU from the Sun) within 100 years from launch by using solar sail technology."* [1].

Secondary objectives, mainly dictated by the scientific requirements of the mission, are defined as: 1) *"Measure the trajectory of the craft up to 10 AU from the Sun and validate it against theoretical models"*, 2) *"Get a visual confirmation of deployment"*, and 3) *"Carry a payload representing human ingenuity on board"* [1].

3. Mission Development

3.1. Orbital Mechanics

The orbital feasibility of the trajectory has previously been studied by Fil et al., Hotston-Moore, and Geragidis [1, 6, 7] using MATLAB, Python and GMAT. For more detailed analysis of the coupling between the spacecraft's attitude and trajectory, a re-derivation of the six degree-of-freedom solar radiation pressure model introduced by Tsuda et al. [8] was implemented in quaternion notation with specifications given in Project Svarog's first paper [1]. The new derivation incorporated gravitational forces from nine bodies using general relativistic (GR) corrections, and currently, the effect of plasma drag is being studied using environmental simulations.

The first test to be carried out on this model was a feasibility study. After several manual trials it was noted that the heliopause could be reached within 100 years for a mass to area ratio of 12 gm^{-2}, which increases the previously known limit by 33%. The first 37 years of the trajectory and energy for such a mission is given in Fig. 1 and 2. The maximum mass to area ratio on the sail could however be increased by choosing suitable initial conditions, and for this, an optimisation code using Scientific Machine Learning [2] is currently being developed. The mission time span constraint as well as a temperature constraint needs to be applied, with the optimisation goal being set to maximise payload mass and the free parameters taken as the initial attitude.

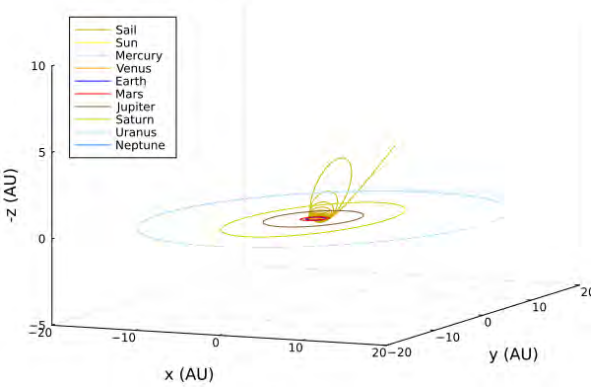

Figure 1: Potential trajectory of the sail in the first 37 years.

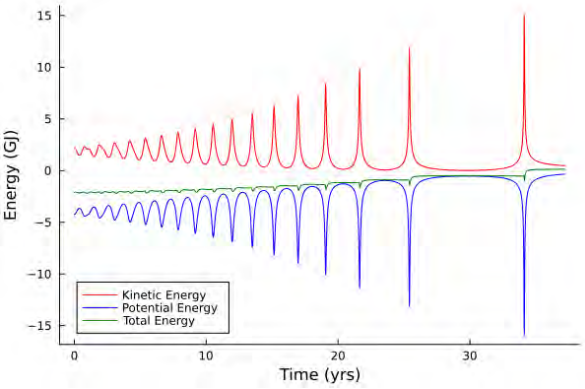

Figure 2: Plot of the energy of the sail in the first 37 years.

From the initial trajectory tests it was also noted that the system is highly non-linear, so an initial global sensitivity analysis using the Morris method [9] was conducted. The sensitivity of the trajectory with respect to the initial conditions was noted, and the mean sensitivities of the results are presented in Table 1. Firstly, it can be noted that the system is highly sensitive with respect to its initial conditions, which is to be expected given the non-linearity of the system. Moreover, the initial attitude of the sail has a particularly large impact on the trajectory. This has the advantage of allowing higher control over the trajectory by slightly altering the initial parameters, but also has the disadvantage of increasing the risk of mission failure if the initial attitude is perturbed due to deployment uncertainties. To estimate the likelihood of such risks, it would be useful to study the

timescale at which the system becomes chaotic. It must also be noted that the Morris method provides a simple measure of global sensitivity that is based on individual variations. But it does not take the coupling between variables and non-linearities into account, which in this case, play an important role. Thus, the results of this study should only be used to get a qualitative understanding of the sensitivity of the system with respect to its parameters, and does not necessarily provide any useful quantitative measure for the global sensitivity. This quantitative analysis is a point of further study, perhaps using methods such as the Sobol method [10].

Table 1: Sensitivity of the the final orbital radius with respect to initial conditions.

Independent variable	Mean sensitivity
x_0	0.069 AU/m
y_0	0.50 AU/m
z_0	-0.38 AU/m
$v_{x,0}$	-30 AU/(m/s)
$v_{y,0}$	-22 AU/(m/s)
$v_{z,0}$	-1.1 AU/(m/s)
α_0	-390 AU/rad
δ_0	38000 AU/rad
Ω_0	-490 AU/(rad/s)

Moreover, tests were also conducted to evaluate which terms in the acceleration of the sail had the lowest impact on its trajectory. The term which was most notably small was the GR correction since the relative differences of the state vector after 34 years were on the order of 1e-5 when comparing the case with and without general relativity. Nevertheless, due to the high sensitivity of the trajectory with respect to its states, neglecting this term could still impose highly inaccurate results. This could potentially be tested using a bifurcation analysis.

3.2. Structural Mechanics

In the case of this mission, the orbital mechanics of the spacecraft can not be solved without careful consideration of its structural behaviour. Due to interactions with the environment, the shape of the structure becomes deformed. Thus, torques due to the solar radiation pressure act as the main perturbation in attitude motion. The modelling of the structure, while can be simplified to an analytical case for circular sails, requires the use of numerical methods such as multi-particle models or shell dynamics solutions in FEM software such as ABAQUS [11]. Additionally, to conduct experimental testing, non-dimensional equations of motion need to be considered, so that it is possible to scale down the tested sail and use gravity to represent solar radiation pressure.

To turn the equations of motion into a non-dimensional form, an approach suggested by Suzuki [12] is used as a basis for the derivation. In this paper, a more systematic approach is used to determine the interactions between various elements of the spacecraft. Thus, further insight is gained into several aspects, such as attaching masses to better manage the deployment process and experimentally validating the requirements for a full scale attachment. To build the system of equations, the time and length scales first need to be normalized with respect to some characteristic parameter. For distance, the length of the sail in a flat configuration is taken and for time, the period of one rotation is taken. Then, the dimensional quantities can be expressed as Eq. (1) and Eq. (2).

$$t = T\bar{t} \tag{1}$$

$$x = X\bar{x} \tag{2}$$

Using the new non-dimensional coordinates, the dynamics can be determined by considering the Lagrangian of the system and solving the Euler-Lagrange equation with an external perturbation to model the forces acting on the sail. For the comfort of the reader, the sail will be considered as spring-mass system, which makes the formulation of the tension field easier to use. The derivation begins by scaling the forces with respect to the pressure multiplied by the area of the sail. Secondly, it follows the derivation of the equation of motion from the Lagrangian using Eq. (3) (4) (5) (6).

$$L = E_k - E_p \tag{3}$$

$$\frac{d}{dt}\frac{\partial L}{\partial \dot{x}_i} - \frac{\partial L}{\partial x_i} = F^* \bar{F}_i \tag{4}$$

$$E_k = \sum_{i=1}^{NODES} \left(\frac{1}{2} m_i \dot{x_i}^2 \right. \tag{5}$$

$$E_p = \sum_{i=1}^{EDGES} \left(\frac{1}{2} k_i (|x_{i1} - x_{i2}| - l_i)^2 \right. \tag{6}$$

Then, both mass and stiffness constants can be non-dimensionalised so that Eq. (7) (8) (9) (10) can be used

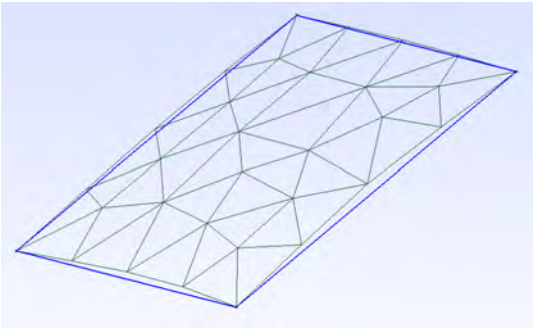

Figure 3: Visualization of sail modeled using the particle-spring system approximation.

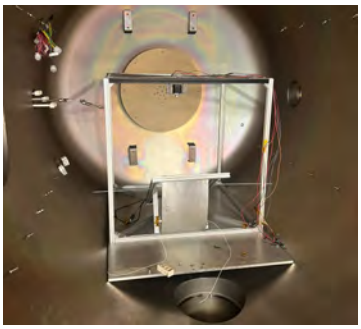

Figure 4: Photo of the experimental setup.

to find an equation of motion with the non-dimensional groups.

$$E_k = \frac{MX^2}{T^2} \sum_{i=1}^{NODES} \frac{1}{2} \bar{m}_i \bar{x}_i'^2 \tag{7}$$

$$E_p = KX^2 \sum_{i=1}^{EDGES} \left(\frac{1}{2} \bar{k}_i (|\bar{x}_{i1} - \bar{x}_{i2}| - \bar{l}_i)^2 \right. \tag{8}$$

$$\frac{d}{T d\bar{t}} \frac{\partial}{\frac{X}{T} \partial \bar{x}_i'} (E_k - E_p) - \frac{\partial}{X \partial \bar{x}_i} (E_k - E_p) = F^* \bar{F}_i \tag{9}$$

$$\frac{MX^2}{T^2} \bar{m}_i \bar{x}_i'' + KX^2 \sum_{j=1}^{NEIGH} \frac{\bar{x}_j - \bar{x}_i}{|\bar{x}_j - \bar{x}_i|} k_i (|\bar{x}_j - \bar{x}_i| - \bar{l}_i) = XF^* \bar{F}_i \tag{10}$$

In the final form of the equation, two dimensional groups can be identified, and experiments can now be designed by varying the mass, stiffness, size, spin rate and external forces.

From this derivation, it is evident that the non-dimensionalised dynamics at each node must be identical for all experimental cases. If only the membrane is considered, then scaling for the main features in a gravitational and pressure field is exactly defined, but for tip masses, it is considerably more complicated to properly match spin rate and gravity to model the actual physics. An initial simulation of the results for a validation case are presented in Fig. 3, where the model of the sail is attached at the corners.

This treatment can be easily expanded to membrane elements from ABAQUS and the current focus of the structural mechanics team is to generalize this approach to shells of finite thickness. While the ABAQUS solution offers higher quality results, for the purpose of keeping within the timeline of development it is more feasible to use a particle model to capture the dynamics of the membrane for shape estimation coupled with the solar radiation pressure effect in the orbital model.

3.3. The Vacuum Chamber Experiment

To validate the described numerical models, an experimental setup for spinning membranes in a vacuum was designed. The main aim of the experiment is to analyse the dynamics of spinning sails under gravity, in an arrangement based on non-dimensional analysis which should simulate solar radiation pressure acting on a full scale sailcraft. The test rig is composed of a hexagonal truss structure, with corners reinforced with metal plates to prevent damaging vibrations under the action of the electrical motor. Over the course of the experiments it was proven that, for extreme cases, the sail and frame might resonate, which could lead to damage of the equipment inside of the vacuum chamber. The size of the test rig is 0.67m in each direction and was dictated by the dimensions of the Boltzmann vacuum chamber at the Imperial Plasma Propulsion Laboratory, where the experiments were conducted.

To spin the sail, a BLDC motor was used, which has the advantage of being able to apply a rotation rate profile corresponding to a torque profile applied to the central hub of the spacecraft during the deployment process. This requires implementing a PID controller, which sets the torque by measuring currents and controlling the associated voltages. Due to the inductive term associated with the motor present in the system, there is a phase mismatch between the current output and voltage input, which might lead to instability in the control system. To account for this, the controller requires the implementation of a differential term, as the voltage generated by the inductor is proportional to derivative of current. In the hardware implementation,

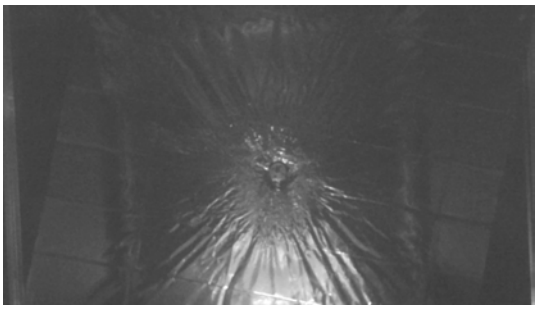

Figure 5: Buckled sail structure at spin rate of 400 RPM.

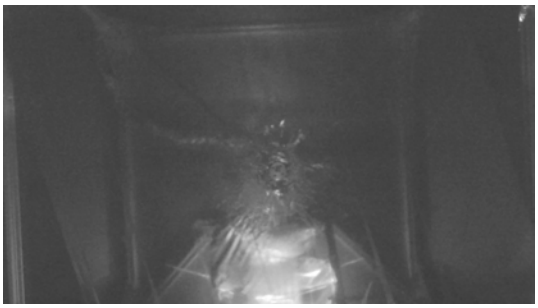

Figure 6: Stiffened sail structure at spin rate of 850 RPM.

a SimpleFOC running on B-G431B-ESC1 was used as the controller of the BLDC motor. Each motor requires careful tuning of control gains to match its characteristics, as depending on the manufacturer, different transient responses can be encountered.

The deflection of the sail was planned to be measured using a stereoscopic vision camera. For this purpose, a dual camera setup from Arducam, which used a common trigger, was designed to be used. Unfortunately, most likely due to the static discharge inside of the chamber, one of the cameras malfunctioned and due to tight time and budget constraints a backup camera was unavailable. Due to this fact, insight obtained from the experiments is more qualitative than quantitative.

During the experimental campaign, multiple sail arrangements were tested. During the analysis of the collected data it was determined that two prominent states of the structure can be observed depending on the spin rate of the structure. The first one, presented in Fig. 5, is a buckled structure, where radial wrinkles are visible on the surface of the sail. This deformation can be attributed to the structure reaching a minimum energy arrangement under the coupled stiffness, gravity and kinetic energy fields. Similar behaviour can be observed in a cloth supported at one point. With increasing spin rate, the minimum energy arrangement shifts towards a flattened plate, as can be observed in Fig. 6. Similar behaviour was also observed in other cases, but changing the boundary conditions leads to a change in the non-dimensional spin rates corresponding to stiffening. It warrants further investigation, which will be conducted in parallel to transient response testing.

Prototypes using booms for increased structural rigidity were also tested. The work of Soykasap [13] was used to size the booms to buckle in a static state, minimising mass. However, manufacturing constraints, mainly due to the low budget, rendered the analysis unfruitful since the expected behaviour was not observed.

3.4. Mechanical Prototyping

One of the major challenges faced by solar sailing missions is the sail deployment subsystem, primarily due to its various complex moving parts. In the case of Project Svarog, the team has begun early-stage mechanical prototyping to address this obstacle effectively. This will enable the identification of areas of difficulty before undertaking the preliminary design stage and gain valuable insight into the dynamic behaviour of the sail during deployment.

Solar sail deployment methods can be broadly divided into two main categories. The first, is the spin deployment method, which saw its first great success in 2010 during the IKAROS mission. This method makes use of the centrifugal force generated by the spacecraft's rotation to deploy and tension the sail. Since it has no rigid support structures, this method offers a lightweight and compact solution for the stowage and deployment of large solar sails. Second, is the boom deployment method which allows for a controlled expansion of the sail and has been successfully implemented in various missions such as LightSail 2. Although it is more mechanically complex, this method offers a high degree of control over the sail's deployment and is well suited to smaller sails.

A simple prototype mechanism has been developed to further understand the associated mechanical complexities of boom deployed systems. The blades of disassembled tape measures are being used to model the rigid, yet collapsible behaviour of the booms but in practice would be replaced by technology such as Triangular Rollable and Collapsible (TRAC) booms [14] or the newly developed Deployable Composite Booms (DCB) [15]. Similar to the early concepts of NASA's ACS3 system, this prototype makes use of four booms individually wrapped onto spools – Fig. 7, employing a simple geared mechanism that enables their simultaneous release while the strain energy stored in the spooled

booms acts to self-deploy them. A casing designed to closely outline the contours of the four spools allows the booms to exit the deployer at 90 degrees and applies a radial constraint.

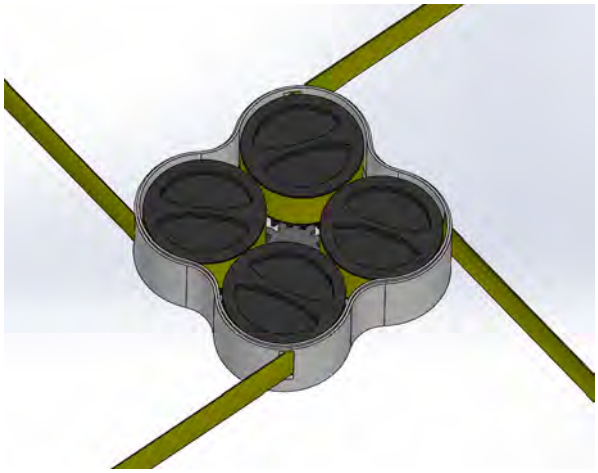

Figure 7: Four boom geared deployment prototype.

Testing of this prototype demonstrated that the overall mechanism satisfied its intended outcome and effectively highlighted areas with potential for improvement as outlined below:

1. The use of stored strain energy to self-deploy the booms led to a violent release that would pose a significant risk of tearing of the sail. In future prototypes, a stepper motor will be used to regain control over the deployment while still using the stored strain energy in the booms to minimise power consumption.
2. The packing efficiency of the deployment system can be improved significantly by wrapping all four booms around a single spool. This will also eliminate the need for the geared simultaneous release mechanism.
3. Despite the constraint applied by the casing, the system exhibited a reaction known as 'blooming' whereby the boom wraps expand radially inside of the case, leading to excessive friction and jams. 'Blooming' is a well-known issue in boom deployed mechanisms and extensive strategies such as those presented during development of the NEA Scout boom deployer [16] have been designed to mitigate it. These will be implemented and tested in future prototypes.

Subsequent work in the mechanical prototyping team at Project Svarog will focus on applying these insights into new prototypes that will be iteratively designed, built, and tested upon. The development of a reliable deployment mechanism will also allow for experimentation with various sail folding patterns and stowage arrangements.

3.5. Tracking and Communication

To validate the dynamics of the probe it is essential to track the satellite up to the point when the orbit becomes hyperbolic and the spacecraft enters an escape trajectory. Within the initial scope of the mission this was considered to be a sufficient condition to prove that the spacecraft escapes the Solar System. For more sophisticated communication, a phased array is suggested as a possible improvement to the communications system.

Regardless of the applied method of communication, Eq. (11) can be applied to investigate the signal to noise ratio.

$$P_r/N = \frac{P_t G_t G_r \lambda^2}{4\pi R^2 k_B T_n B} \tag{11}$$

Using this formula, the signal to noise ratio for detection using a single radio telescope can be evaluated. This mission aims to avoid active communication systems, so the only feasible approach for determining velocity and position is Doppler effect measurements. These will recover the spacecraft's velocity using the telescope's orientation and Very Long Baseline Interferometry (VLBI) to determine the position of the spacecraft. To conduct a more detailed trade-off, a preliminary transmitter design was conducted and the signal received on Earth at 10 AU was modeled. The time variation of the signal is presented as a moving spectra averaged with a period of 1.5 seconds. This is presented in Fig. 8 and the phase shift required for further analysis is given in Fig. 9.

Despite the evidently high quality of the signal during the short frame presented, for the entire period of the mission, the Brownian drift in frequency of the onboard oscillator becomes non-negligible. To mitigate this, a high precision cesium reference could be used. This would significantly increase the complexity of the solution, as components on the market use customer electronics, which are not space grade and cannot withstand Deep Space conditions.

In this case, only VLBI remains as a feasible method of tracking, which can be applied to this mission concept. This method is based on the detection of the probe using multiple radiotelescopes scattered across the globe and correlating their signal to act as a single huge interferometer. This method has been applied

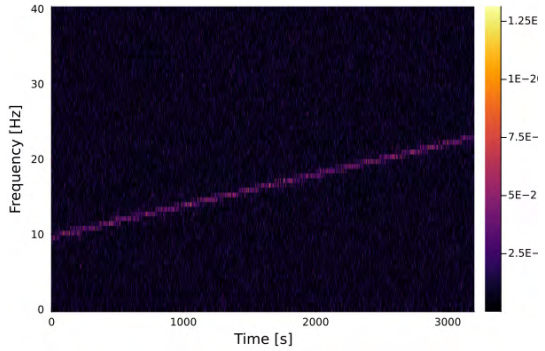

Figure 8: Time variation of averaged spectra received on the ground.

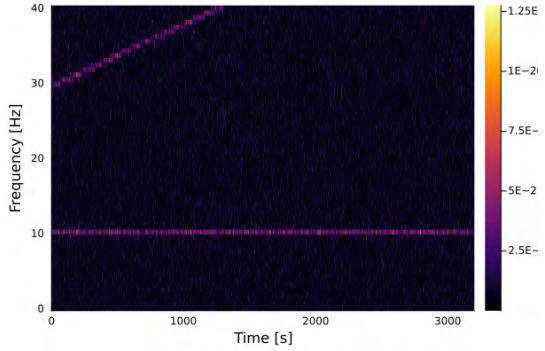

Figure 9: Phase corrected spectra of spacecraft signal.

in multiple previous missions and enables high precision measurements of distances in the Solar System. The processing pipeline for VLBI follows an algorithm developed for tracking the Huygens probe and is used by various other spacecrafts. Currently, the focus of work in this area is related to creating a fully simulated pipeline for generating a simulated signal received on each station, cross-correlating the given signals, and determining the position of the spacecraft [17].

3.6. Plasma environment

During the mission, the spacecraft will be subject to considerable variations in environmental conditions. During close passes to the Sun, both solar, wind and radiation flux increase considerably and so these parameters need to be considered in the design process. All environmental models considered in the design adhere to the ECSS standard, which describes how various aspects should be designed and which environmental properties should be modelled.

The standard radiation flux model in ECSS is CREME96. This model provides a standard for cosmic background coupled with solar particle flux and depends on solar activity. The spectrum from the model can then be used as an input to a code for analysing the impact of the radiation on the electronics. At this stage, two approaches with different levels of feasibility are being assessed.

The first order approximation in the model would be to model the particle propagation in the structure using the Bethe-Bloch equation for the propagation of ionized particles with higher order corrections for interactions with electron shells. This formulation is given by Eq. (12).

$$\frac{dE}{dx} = 2\pi r_e^2 m_e c^2 n_{el} \frac{z^2}{\beta^2} \times \times \left[\left(\mathrm{n} \quad \frac{2m_e c^2 \beta^2 \gamma^2 T_{up}}{I^2} \right) - 2\beta^2 - \delta \right] \left(\tag{12}$$

It can be seen that there is a prominent Bragg peak as the energy of the particle decreases. It is particularly important to consider this behaviour in order to minimize placement of the peaks in the volume of the electronics. This approach, while providing an initial solution, does not account for secondary emission in the material and needs to be validated against high fidelity Monte-Carlo simulations.

For conducting high fidelity numerical simulations, ESA guidelines suggest using GEANT4, a software for modelling particle physics problems developed at CERN. There is a GRAS toolbox developed as the extension of this library, which is aimed at providing a module for reading arbitrary spacecraft geometries, and conducting inverse ray tracing to estimate the total energy deposited in the electronics, without the need to model flux throughout the entire spacecraft. Due to the highly eccentric orbit used in this mission and the variable incidence with respect to the Sun, the simulation environment needs to be extended to consider a non-isotropic source of radiation. This is given as a modification of the ray tracing weight implementation in GEANT, done by implementing a classifier function to assess which diversions from the initial direction are physically plausible. With this modification, the flux on the surface of the electronics can be matched with any directional source and thus, it can be applied to the analysis of missions where the spacecraft is in a Sun-pointing attitude. An initial test of the solver for the inverse ray-tracing of particles propagating through a lead block to an ion source is presented in Fig. 10.

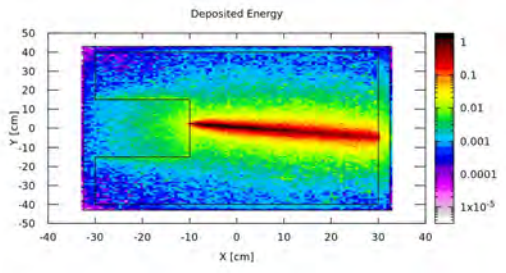

Figure 10: Backpropagation of proton radiation.

4. Further Steps

Currently, most of the efforts are directed towards creating an accurate mission definition. Due to the high complexity of the system, this is a crucial stage, providing an opportunity to minimize the chance of experiencing unexpected risks, and to understand the couplings between various design variables.

The main further area of development at the current stage is to polish the software system required for the development and validation of the mission requirements. This includes an in-house orbital propagator, a structural dynamics solver, a communications simulator, and environmental models. Beyond that, based on the findings from initial testing in the vacuum chamber, transient deployment experiments with 3D vision setup are planned to be conducted in the coming months and will be used as a means of validation of the structural models, providing data for future development designs.

The ultimate aim of said activities is to develop sufficient understanding of the mission to create a preliminary design review and then conduct the interstellar mission in early 2030s, when an appropriate launch window is available.

5. Conclusions

In conclusion, the conducted research indicates that the proposed mission is feasible within the requirements stated in the initial section. However, there are still unresolved challenges associated with the structural behaviour of the sail and manufacturing of the satellite. With further development and creating a broad network of partnerships with providers of subsystems, all of the issues will be mitigated and the mission will become the first civilian mission to enter an escape trajectory from the Solar System.

Acknowledgements

The team would like to deeply thank Dr Aaron Knoll, the group's academic supervisor, for his advice and vision.

Moreover, the following members, despite not having been involved in this paper, have provided invaluable contributions to the team's design effort during the past year (in alphabetical order): Harry Allen, Botond Branyicskai-Nagy, Ziming Huang, Sihun Hwang, Aleks Kent, Chang Liu, Carla Miquel-Davidson, Kai Mulcock, Lucas Newman, Killai Parameswaran, Anlan Qiu, Ivan Revenga Riesco, Golf Rojnuckarin, Junglin Sung and Mathias Volkai.

References

[1] P. Fil, F. Szczebak, D. Sengupta, I.R. Riesco, B.S. Tortosa, B. Krawczyk, and et al. Mission concept and development of the first interstellar cubesat powered by solar sailing technology. *Journal of the British Interplanetary Society*, 2023.

[2] Christopher Rackauckas, Yingbo Ma, Julius Martensen, Collin Warner, Kirill Zubov, Rohit Supekar, Dominic Skinner, and Ali Jasim Ramadhan. Universal differential equations for scientific machine learning. *CoRR*, abs/2001.04385, 2020. URL `https://arxiv.org/abs/2001.04385`.

[3] G. Santin, V. Ivanchenko, H. Evans, P. Nieminen, and E. Daly. GRAS: a general-purpose 3-d modular simulation tool for space environment effects analysis. *IEEE Transactions on Nuclear Science*, 52(6):2294–2299, 2005. doi: 10.1109/{TNS}.2005.860749.

[4] Yoji Shirasawa, Osamu Mori, Yasuyuki Miyazaki, Hiraku Sakamoto, Mitsue Hasome, Nobukatsu Okuizumi, Hirotaka Sawada, Hiroshi Furuya, Saburo Matsunaga, Michihiro Natori, and Jun'ichiro Kawaguchi. Analysis of membrane dynamics using multi-particle model for solar sail demonstrator "IKAROS". 04 2011. ISBN 978-1-60086-951-8. doi: 10.2514/6.2011-1890.

[5] Hirotaka Sawada, Yoji Shirasawa, Osamu Mori, Nobukatsu Okuizumi, Yasuyuki Miyazaki, Saburo Matunaga, Hiroshi Furuya, Hiraku Sakamoto, M. C. Natori, and Yuichi Tsuda. On-orbit result and analysis of sail deployment of world's first solar power sail IKAROS. *The Journal of Space Technology and Science*, 27:54–68, 2013.

[6] Esme Hotston-Moore. Feasibility analysis of a solar sail propelled spacecraft for extrasolar trajectories. *Department of Aeronautics South Kensington Campus Imperial College London*.

[7] Filippos Vasileios Geragidis. Preliminary design of a solar sail propelled spacecraft for extrasolar trajectories. *Department of Aeronautics South Kensington Campus Imperial College London*.

[8] Yuichi Tsuda, Takanao Saiki, Ryu Funase, and Yuya Mimasu. Generalized attitude model for spinning solar sail spacecraft. *Journal of Guidance Control and Dynamics*, 36:967–974, 2013.

[9] Vaibhav Kumar Dixit and Christopher Rackauckas. Globalsensitivity. jl: Performant and parallel global sensitivity analysis with julia. *Journal of Open Source Software*, 7(76):4561, 2022.

[10] I.M. Sobol', S. Tarantola, D. Gatelli, S.S. Kucherenko, and W. Mauntz. Estimating the approximation error when fixing unessential factors in global sensitivity analysis. *Reliability Engineering System Safety*, 92(7):957–960, 2007. ISSN 0951-8320. doi: https://doi.org/10.1016/j.ress.2006.07.

001. URL https://www.sciencedirect.com/science/article/pii/S0951832006001499.

[11] Abaqus finite element analysis for mechanical engineering and civil engineering. https://www.3ds.com/products-services/simulia/products/abaqus/. Accessed: 2023-05-05.

[12] Shuto Suzuki. Construction of similarity rule of spin deployment membrane. *Department of Aeronautics, College of Science and Technology, Nihon University*.

[13] Ömer Soykasap. Analysis of tape spring hinges. *International Journal of Mechanical Sciences*, 49(7):853–860, 2007. ISSN 0020-7403. doi: https://doi.org/10.1016/j.ijmecsci.2006.11.013. URL https://www.sciencedirect.com/science/article/pii/S0020740306002852.

[14] Jeremy A. Banik and Thomas W. Murphey. Performance validation of the triangular rollable and collapsible mast. Utah, USA, August 2010. AIAA/USU Small Satelite Conference.

[15] William K. Wilkie. Overview of the NASA advanced composite solar sail system (ACS3) technology demonstration project. AIAA Scitech Forum, January 2021.

[16] Alexander R. Sobey and Tiffany Russell Lockett. Design and development of NEA Scout solar sail deployer mechanism. California, USA, May 2016. Aerospace Mechanisms Symposium.

[17] Duev, D. A., Molera Calvés, G., Pogrebenko, S. V., Gurvits, L. I., Cimó, G., and Bocanegra Bahamon, T. Spacecraft VLBI and Doppler tracking: algorithms and implementation. *A&A*, 541: A43, 2012. doi: 10.1051/0004-6361/201218885. URL https://doi.org/10.1051/0004-6361/201218885.

Test of a Full-Scale Quadrant for the 1,653m^2 Solar Cruiser Sail

Zachary McConnel [a]*, Brian Sanders [a], Anan Takroori [a], Craig Hazelton [a], Jim Pearson [b], Carlos Diaz [c], Ashley Benson [c]

[a] *Redwire Space Systems, Longmont, Colorado, USA*
[b] *NeXolve, Huntsville, Alabama, USA*
[c] *NASA Marshall Space Flight Center, Huntsville, Alabama, USA*
* Corresponding Author email: zachary.mcconnel@redwirespace.com

NASA Marshall Space Flight Center (MSFC), in collaboration with Redwire and NeXolve, is advancing the design of a 1653 m^2 Solar Sail System (SSS) for the Solar Cruiser mission; a technology demonstration mission to enable missions to high solar inclination orbits, sub-L1 halo orbits, non-Keplerian solar and other planetary orbits. Since 2019, the program has been developing key components, including: the Sail Deployment Mechanism (SDM), high strain composite Triangular Rollable and Collapsible (TRAC) booms, and the ~ 413 m^2 thin film sail quadrants. This effort has culminated in the successful ground deployment demonstration of a flight-scale prototype quadrant in late 2022. This paper provides an overview of the results from this test. This paper also outlines critical lessons learned that will inform ongoing efforts to further develop the technology towards flight.

Keywords: Solar Cruiser, Redwire, NeXolve, MSFC, Solar Sail

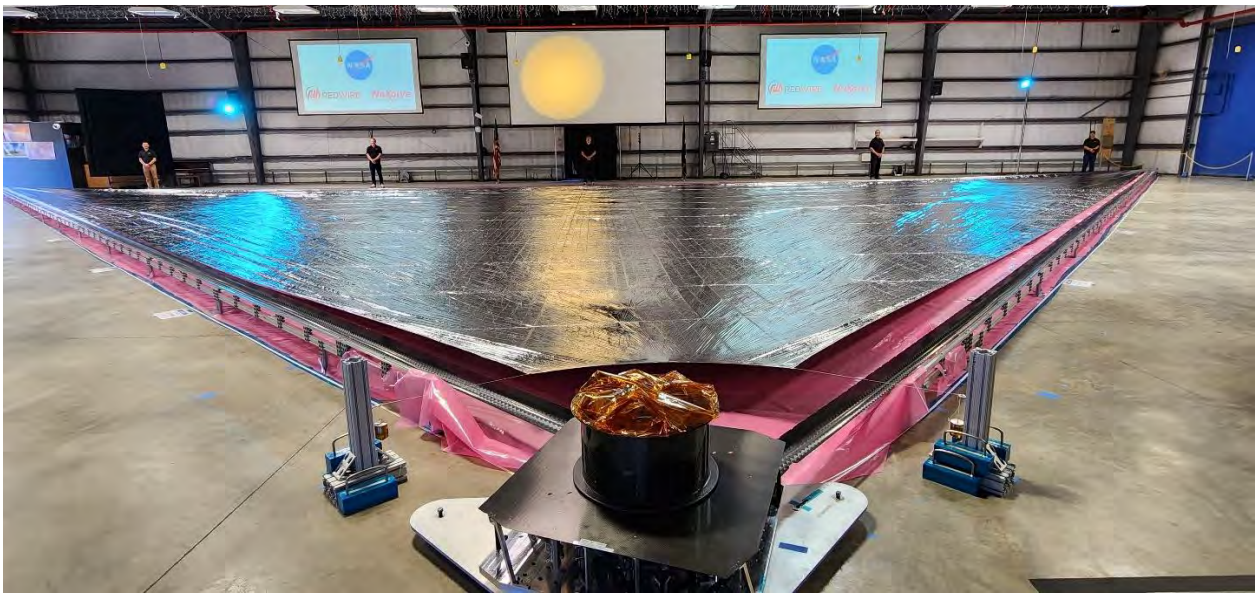

Fig. 1. Fully Deployed Single Quadrant Prototype Sail, TRAC-Booms and Deployer

1. Introduction

This paper summarizes a test program to deploy a single full-scale quadrant of the sail designed for NASA's Solar Cruiser Mission [1]. This test consisted of fully deploying two booms perpendicular to one another with a 413m^2 (4435ft^2) sail quadrant tensioned in between (Fig. **1**). The primary objectives of this test were to demonstrate the operation of key features of the Sail Deployment Mechanism (SDM) and evaluate design concepts for critical ground support equipment (GSE) and procedures for full-scale sail testing, hence pushing the limits of solar sail technology forward for 2,000 m^2 class sails. This demonstration included many stage gates through which associated risks were mitigated. The team built on the preliminary sub-scale tests to verify hardware and procedures for the full-size deployment test. Ultimately, the test campaign confirmed that the designed hardware is mature, while identifying several design features that can be improved in the next hardware maturation cycle towards flight.

2. Test Unit

Fig. **2** illustrates the test unit in its stowed configuration. The test unit consists of the Sail

Deployment Mechanism (SDM) and two TRAC booms [2] manufactured by Redwire and a 2.5 micron thick Colorless Polyimide -1 / Vapor Deposited Aluminium (CP-1/VDA) sail quadrant manufactured by NeXolve. To achieve the single quadrant deployment, the assembly contains two nearly 30m TRAC booms and one full-scale sail quadrant. When stowed the system occupies roughly 1/3m^3, after deployment the full sail spans 1,653m^2, with a single quadrant measuring 413m^2 in area.

The sail quadrant was spooled onto a flight-like sail spool designed to accommodate four sail quadrants. To adjust for a single quadrant deployment test, an Adjoining Sail Simulator was constructed to simulate the packaged volume of the three remaining sail quadrants. Similarly, a Sail Ramp was constructed to ease the transition of the sail from the upper deck to the ground deployment area, preventing the sail quadrant from folding onto itself. The sail hub spins freely on a set of trundle bearings, only moving once the booms pull on the sail through distal end connections.

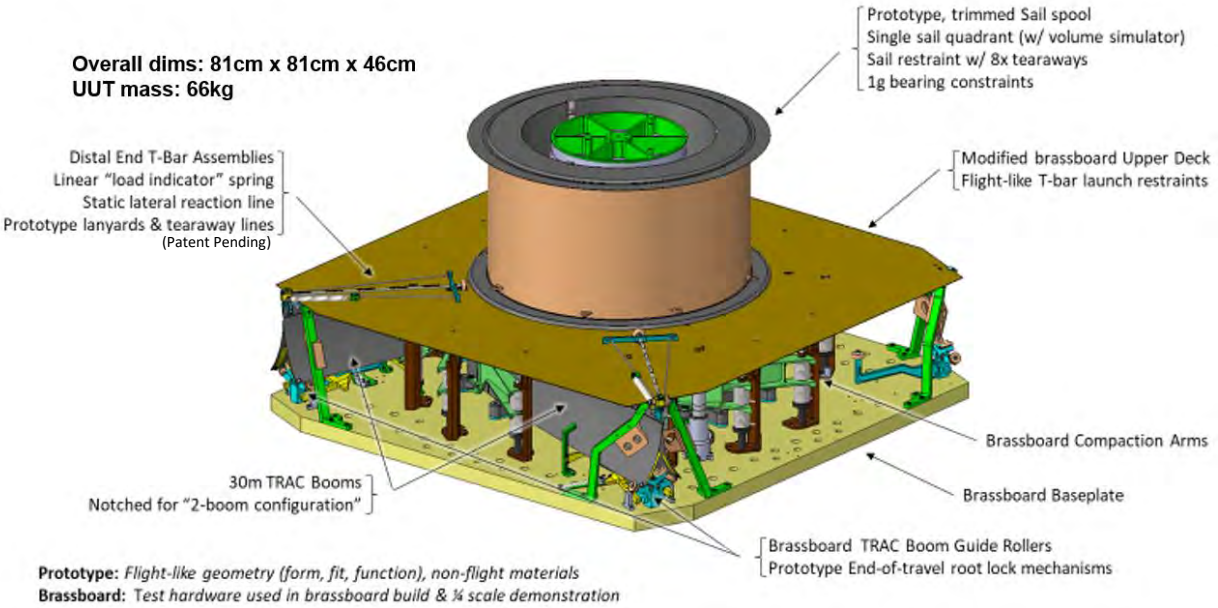

Fig. 2. Test unit components.

Fig. 3. Panoramic view and floor layout of test facility (MSFC B4316).

The key structural elements of the flight sail system are four 30m-long, high-aspect ratio TRAC booms [3] that serve as the sail's skeletal system and are designed to *deploy* the packaged reflective sail membrane as well as *provide* operational sail tension loads for flight. The full-scale quadrant test unit incorporated two full-scale TRAC booms manufactured to meet the flight system structural, thermal, and packaging requirements.

3. Description of Facility and Test Setup

The full-scale quadrant deployment test took place in Building 4316 at NASA's Marshall Space Flight Center (MSFC, Fig. 3). The open layout of B4316 provided sufficient floor space for the full quadrant test as shown in the floor layout sketch in Fig. 3.

Prior to the test, the facility was cleaned, and ground support equipment was put in place. This includes the SDM base, the boom support sections and the ground cover material. The ground cover material, ULINE Anti-Static Poly Sheeting, was determined to be the best option due to its low coefficient of friction, its ability to dissipate static charges which could provide additional drag on the sail and relatively low cost for area needed. Other design options were traded for the sail deployment surface, such as an air hockey table-like structure that would provide a cushion of air beneath the sail, however this method would have been prohibitively expensive. Small scale tests were used to determine the lowest friction against other materials. The material was also used in all preliminary deployments on smaller scale tests. The material would serve the critical role of a uniform surface for the sail to slide across throughout deployment.

The TRAC booms were offloaded with support tracks with the TRAC boom flanges gliding along a series of rollers. A horizontal rail and trolley assembly was installed on the outer edges of these support sections (opposite side of the sail, between boom support sections) along the length of the booms. This rail assembly balanced the lateral loads the sail put on the distal ends of the booms. This is necessary when testing a single quadrant, as there are no other sail quadrants to balance this adjoining sail lateral load.

The test unit (Fig. **2**) was positioned on top of a turntable that allowed for its rotational alignment to the rest of the GSE during the test to be adjusted. As the booms deploy, the tangent angle between the boom and the hub changes, as the boom's spooled diameter decreases. This change in boom angle was accommodated by manually rotating the test unit periodically during the test.

4. Preliminary Deployment Tests

Leading up to the full-scale deployment test, a series of five preliminary tests were conducted to validate the ground support equipment and expose test process risks. Three quarter-scale sail deployment tests were conducted at Redwire's facilities in Longmont, Colorado on a complete sail with four quarter-length booms and four quarter-scale sail quadrants (Fig. **4**) to facilitate development of the ground support equipment. Once the ground support equipment was finalized and installed at MSFC B4316 a full-length boom deployment test was conducted without the sail, and an additional quarter-scale mylar sail quadrant deployment test was done to ensure the alterations to ground support equipment were effective in reducing deployment risks.

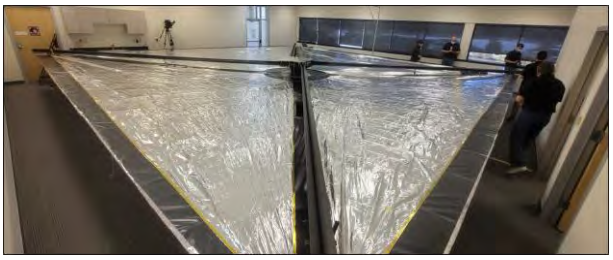

Fig. 4. Quarter-scale sail deployment test.

The quarter scale sail deployments were done with mylar sails roughly eight meters on each side (being referred to quarter scale by deployment length). These tests provided critical understanding of the deployment dynamics of the sail in a 1g environment. The mylar material is stronger than the CP-1/VDA material being used on the full-scale deployment but showed the unfolding movements that could be expected. Any snagging risks observed in these preliminary deployments, due to test conditions, were recorded and mitigated with additional MGSE for the last quarter scale deployment and the full sail deployment. These test conditions are due to deploying in a 1g and with only a single quadrant.

The TRAC booms themselves were also load tested prior to the deployment testing to ensure they wouldn't buckle under the testing conditions in gravity. The booms proved to be extremely robust, only buckling at loads 19x nominal operating load in flight. These results validated analysis models which predicted very similar performance and buckling dynamics.

The lessons learned from these preliminary deployment tests, both at Redwire's facility and the deployments prior to the CP-1/VDA sail, informed refinements to the GSE and procedures for the full-scale test that minimized snagging and damage to the ultra-thin CP-1/VDA quadrant.

5. Full-Scale Quadrant Deployment Test

The full-scale single quadrant prototype sail deployment test began on October 12th 2022 and was completed on October 14th 2022. While the deployment time alone is less than an hour at full speed, the close monitoring, 1g environment and testing procedures

increased the time necessary to complete the program. The following sections describe the deployment test steps.

5.1 Test Day One. As per the test plan, the team started with a review of the test plans for the day to ensure the test team was well coordinated. NASA, NeXolve and Redwire were present. Test personnel were in place and first motion was commanded to the SDM to deploy the booms. The booms moved approximately 2cm and the boom distal end features disengaged from the SDM's launch stowing location. This then caused successful release of the sail restraint (Fig. **5**).

After successful release of the booms and sail quadrant from their retention devices, deployment continued with a goal to extend the system initially to 5m (roughly 1/6 of the full deployment distance). During this phase, the unfurling sail quadrant was observed to migrate between the upper deck of the SDM (Fig. **5**) and the Adjoining Sail Simulator. The sail migrated between the Adjoining Sail Simulator and the test article due to gravity and raised a concern that pinching of the quadrant could cause the sail to rip. The situation was monitored until the test was stopped to assess changes to the ground support equipment and test procedures to mitigate the issue.

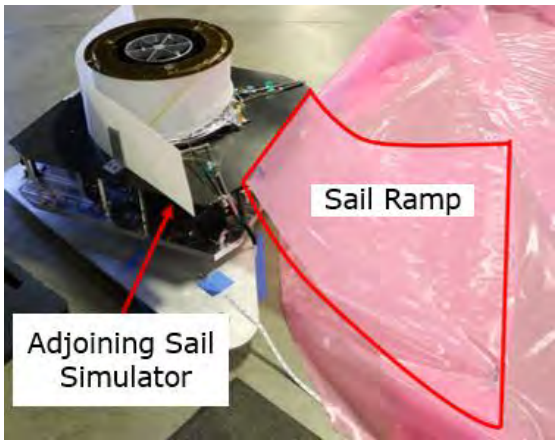

Fig. 5. Sail test unit after first motion.

The root cause of the sail migration problem was ultimately attributed to the design of the Adjoining Sail Simulator (i.e., the material designed to fill the volume of the three adjoining sail quadrants left out of the present tests). In space, and with the adjoining sails present, the Adjoining Sail Simulator would not be necessary. So the issue was purely a result of the single-quadrant test configuration. To complete the test, an additional ground support equipment feature, referred to as the Adjoining Sail Simulator Extension, was installed to prevent the sail test quadrant from getting pinched.

The test resumed with the boom deployment to 3m. Deployment then continued without significant issues to 27m. The local time was 4:00pm and test was halted for the day. Data and pictures were saved, and the hardware was safed with the sail quadrant tensioned.

5.2 Test Day Two. The team reconvened at the test site and the daily planning meeting was held. Hardware was inspected, all appeared normal, and in the state it was left in the previous evening. The test resumed at 9:11am on October 13th, 2022. The first motion resulted in disconnection of one of the TRAC boom distal end fittings and the sail. The test was halted, and the situation was assessed. Upon inspection it was discovered that a solder bead in the sail clevis had separated from the stainless-steel cable. This was likely due to the connection only being proof tested in short term loading conditions, unlike the overnight loading that took place between test days. The design deficiency was noted, and a field repair was affected involving the use of a compression sleeve in place of the failed solder bead. Then the repaired connection was proof tested using spare materials to ensure the fix would hold for the duration of the test under expected loads.

With the distal cable fitting anomaly repaired the final deployment and sail tensioning proceeded nominally. The team slowly tensioned the sail at slow deployment rates and continually monitored the booms and sail tension. This was a key factor to monitor throughout deployment was the load imparted on the sail from the distal end hardware of the booms. In flight this load would be negligible, but in gravity the force of friction between the sail and deployment area put tension in the corners of the sail attached to the booms. The sail corner fittings are designed to withstand 22 newtons (5lbs) of load from the distal end chords. Indicator springs were integrated into the boom's distal end hardware to monitor this load and partial results are presented in Fig. **6**. Test team members followed the ends of the booms and called stop to deployment when the tension hit 18 newtons (4lbs). On these occasions, sail luffing methods were used to break the sail free from the deployment surface and reduce static cling that had built up to that point in the test. A few luffing methods were tried, but the most successful was directing an ionizing fan beneath the edge of the sail near the connection to the boom.

The tension at each boom was near zero for the first quarter of deployment but the tension loads increased as more of the sail's mass left the spool and was resting on the ground. The tension spiked at 27.7m of deployment, and the luffing method was used to prevent damage to the sail. Once the tension was reduced and the sail settled back to the ground, the deployment continued. The two corners experienced different tensions throughout, but both steadily increased throughout the test. The distribution of the folding pattern on the deployment surface likely explains why the two booms experienced different loads.

Fig. 6. Loads on sail ends during the final few meters of deployment, with some key events labelled in red.

Deployment to a full length of 28.9m was achieved with the final lock out of the booms in the Sail Deployment Mechanism observed by the test team at 5:34pm. End of deployment was determined by observing the boom lockout with the full engagement of the root support mechanism. The fully deployed quadrant is shown in Fig. **7** prior to tensioning of the sail, which involved the use of additional ground support equipment.

5.3 Test Day Three. The team reconvened at the test site and the daily planning meeting was held. Hardware was inspected and all appeared normal and in the same state it was left in the previous evening. The test resumed at 6am on October 14th, 2022. The primary objective of the third day of testing was to fully tension the quadrant with the additional ground support equipment that simulate the root connections of the sail quadrant to adjacent sail quadrants (Fig. **8**).

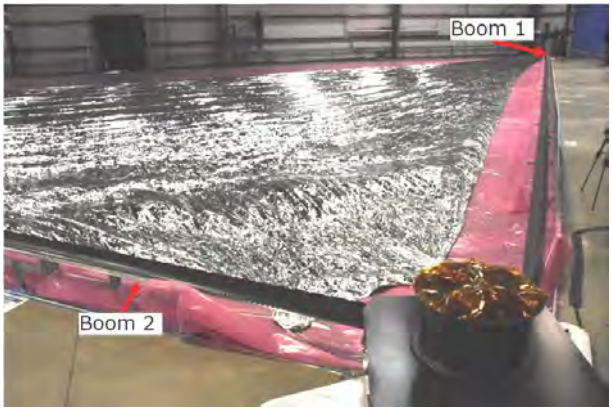

Fig. 7. Sail after full deployment, before manual tensioning (end of test day two), with booms labelled.

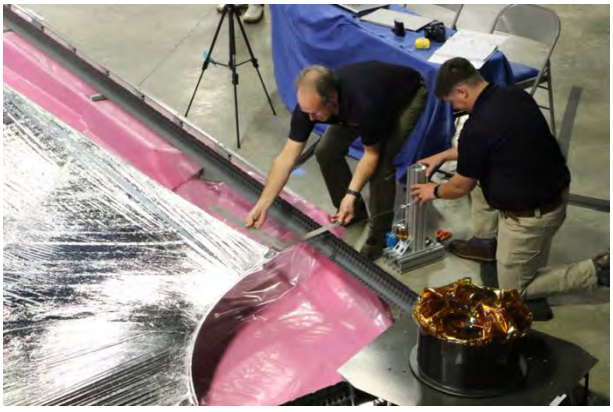

Fig. 8. Sail root cross-tie simulators being installed to tension the sail quadrant**.**

The final steps of the test included measuring electrical resistance across key reference points of the system to establish the performance of static grounding treatments applied to the hardware. The sail was found to exhibit several open circuits associated with minor damage to the hardware primarily from interactions with the ground support equipment. Importantly, the electrical resistance from the SDM to the distal end of the TRAC booms was found to satisfy the grounding requirement. Fig. **9** presents a sequence of images captured throughout the full-scale quadrant deployment test.

5.4 Follow on Activities. After the test had commenced the sail remained in its tensioned state to present to interested parties.

A final set of measurements were taken to validate the size of the sail as manufactured. Each section of the sail was folded as it was adhered together, so the first opportunity to measure its full area was after the deployment. The sail was detached from the distal ends of the booms and the cross-tie simulators, then laid flat on the ground. The NeXolve team members took extensive measurements, by use of a laser tracker, at key points along the edges of the sail to compare with the designed specifications.

6. Key Takeaways

Throughout this deployment test the team encountered and overcame many challenges, developing lessons learned which can be applied to Solar Cruiser testing and other space sail technology. Redwire is currently developing a TRL 6 (Technology Readiness Level 6) prototype for ground qualification testing of flight loads and environments.

The boom offloading system was extensive and not without its flaws. The team improvised solutions during assembly to ensure few to none snags could occur between the hardware and GSE. These included shingling the low friction film across the TRAC boom offloading structure, over metallic elements that could potentially damage the booms, minimizing friction on all sliding surfaces that the booms or sail may encounter.

Deploying a single sail quadrant out of four, a testing condition that would seem to simplify the procedure, presented a need for more GSE to simulate the effects the adjacent sails would have on the existing quadrant. These structures include the aforementioned Adjoining Sail Simulator, the cross-tie tensioning system as well as the trollies on the TRAC boom offloading system. These trollies road along a rail during deployment, reacting the loads put on the distal end of the boom by the sail. An action which in flight would be done by the adjoining booms and sail quadrants.

The team's diligence in recording data during the test, which was predominantly a technology demonstration, helped to inform analysis models that are currently in development to understand the dynamics of sail flatness on orbit, and the resultant design modifications to ensure flatness. This data includes the final measurements of the sail quadrant dimensions and the loads imparted on the distal end of the boom from the sail (despite those loads being mostly a result of gravity).

Qualitative observations of the system led to innovative design changes for future prototypes.

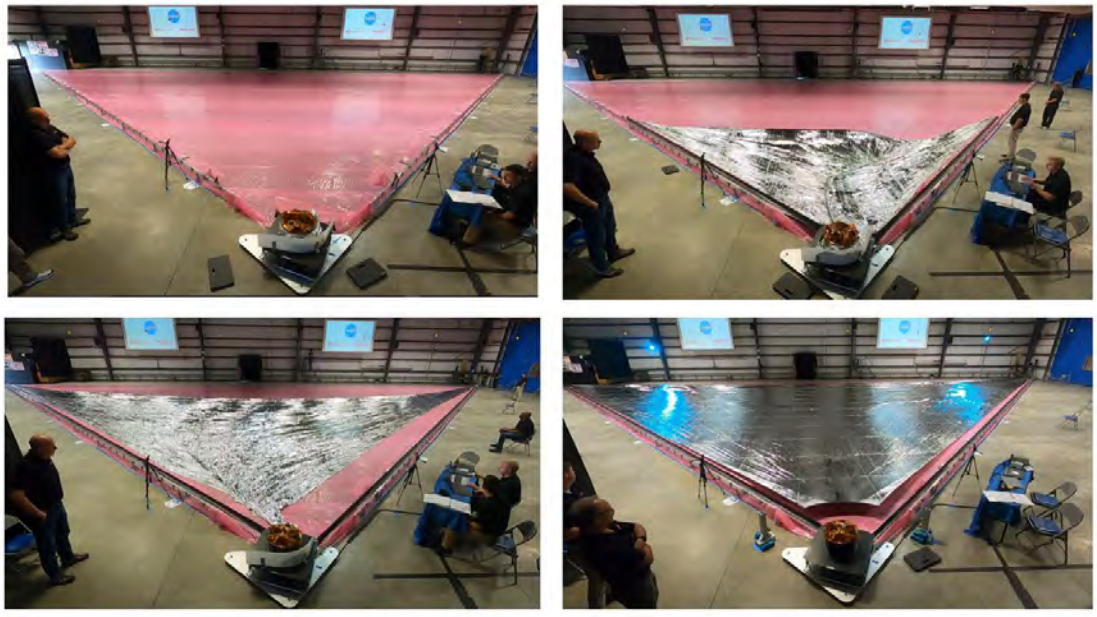

Fig. 9. Full-scale sail quadrant deployment images captured throughout deployment.

The nature of the sail quadrant's wrinkles concluded a greater nominal tension would be required to optimize deployed sail flatness. Additionally, as a result of the testing, the TRAC boom root lockout system was modified for reliability in the TRL 6 prototype.

Also significant was the confidence and cohesiveness this test instilled in the team members who developed the technology and ran the deployment. A technology demonstration of this magnitude not only proves it is possible, it established the foundation for future prototype testing, in both technology and team dynamics.

7. Conclusion

The deployment of the prototype full-scale sail quadrant was successful, with the sail deployment mechanism (SDM) and TRAC booms performing as designed and sail quadrant movement and management working mostly as planned with minor issues encountered related to the interactions of the sail quadrant with ground support equipment. The 1g environment created many challenges to demonstrating this technology, however the ground support equipment performed sufficiently to validate all critical elements of the system design towards flight.

At present, the nearly 1,700m^2 sail system is undergoing continued development through TRL 6 ground qualification to flight loads and environments. The design has been updated for functional reliability and mass efficiency, with intention to repeat the single quadrant deployment test in a similar fashion. This next iteration will have four booms installed instead of the two, requiring additional GSE to be developed in parallel. The manufacturing of the TRAC booms has also been refined for consistency and are currently being manufactured for the TRL 6 prototype.

Redwire, NASA and NeXolve are collaboration to developing analytical models to predict the behavior of Solar Cruiser in flight. This is critical to provide feedback on the latest design which will enable a future Solar Cruiser flight opportunity.

Acknowledgements

The work herein was funded by NASA under Marshall Spaceflight Center contract 80MSFC21CA008. Thank you to team members from NASA, Redwire and NeXolve who made this test possible. Go Cruiser.

References

[1] Johnson, L., Curran, F., Dissly, R., Heaton, A., Turse, D., The Solar Cruiser Mission: Demonstrating Large Solar Sails for Deep Space Missions, December 2020, https://www.researchgate.net/publication/347079622 (accessed 03.02.23)

[2] Murphey, T. W. and Banik, J., "Triangular rollable and collapsible boom". US Patent No. 7,895,795, March 1, 2011 (licensed exclusively by Redwire 08.12.16)

[3] Nguyen, L., McConnel, Z., Medina, K., and Lake, M., Solar Cruiser TRAC Boom Development, Presented at AIAA SciTech 2023, AIAA Paper No. 2023-1507.

Development of a Flight-Like Solar Sail Quadrant for NASA's Solar Cruiser

Kirk Maddox[a]*, James C. Pearson, Jr.[a], Les Johnson[b], Leslie McNutt[b]

[a] *NeXolve, Huntsville, Alabama, USA*
[b] *NASA Marshall Space Flight Center, Huntsville, Alabama, USA*
* *Corresponding Author email: kirk.maddox@nexolve.com*

Abstract

In 2021 and 2022, NeXolve successfully collaborated with their NASA Solar Cruiser (SC) partners, NASA Marshal Space Flight Center (MSFC) and Redwire Space, to design, develop, fabricate, package, and test a flight-like Prototype Sail Quadrant (SQ) designed for NASA's Solar Cruiser solar sail mission. The SC solar sail system includes 4 right triangular quadrants, deployed radially from a central spool by 4 equally spaced deployable booms. The total SC sail area is 1653 m^2, with each quadrant having a design area of 413.25 m^2. NeXolve was responsible for the Prototype SQ design, development, manufacturing, and packaging as well as supporting a deployment test of the Prototype SQ at NASA MSFC. NeXolve developed all manufacturing process and mechanisms to support the Prototype SQ manufacturing flow [1] which enables NeXolve to design and build solar sails with a larger footprint than the facility in which they are manufactured. This is successfully accomplished by a delicate balance of sail fabrication and sail folding, simultaneously. The sail is made from NeXolve's 2.5-micron thick CP1 [2] polyimide film with a 1000Å aluminum coating. The Prototype SQ has surface features including edge and corner reinforcements for structural loading, electrical jumpers for continuity, ripstops for tear-propagation, and seams that join the 60-inch-wide rolls of material together. These features are installed by a resin bonding process developed by and propriety to NeXolve. Following sail manufacturing, the Prototype SQ was spooled and packaged at NeXolve and delivered to Redwire Space.

Keywords: NeXolve, Solar Cruiser, Solar Sail, CP1, Large Deployable Thin Film Structures

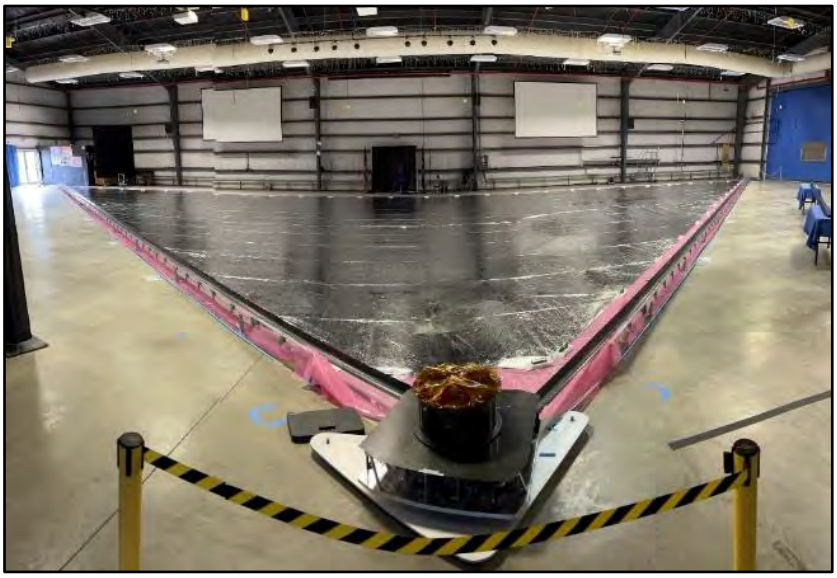

Figure 1. SQ deployed at NASA MSFC building 4316 (non-tensioned)

1. Introduction

This paper outlines the successful development of the Prototype Sail Quadrant (SQ) for NASA's Solar Cruiser mission. The Prototype SQ matches the design accepted by NASA at the Sail Quadrant Membrane Assembly Critical Design Review (SQ MA CDR) in October of 2021. The full design is a 4-quadrant architecture consisting of 4 identical right-triangular quadrants. Each quadrant is approximately 413 m^2 made from NeXolve's 2.5-micron thick Colorless Polyimide 1 (CP1) film with a 1000Å Vapor Deposited Aluminum (VDA) coating, with the full size 4-quadrant structure totalling 1653 m^2. Included in the quadrant design are corner reinforcements, edge reinforcements, ripstops, seams, and electrical seam jumpers. NeXolve, in partnership with MSFC and Redwire Space, led the efforts for the design, development, manufacturing, and packaging of the SQ as well as the 4-quadrant solar sail architecture. This design and development effort included SQ requirements development, sail membrane thermal and structural analysis, key enabling infrastructure and GSE development, manufacturing process development and documentation, key techniques and procedures that are essential for the quality and accuracy of the SQ fabrication, as well as final verification, testing, and shape measurements.

2. Development of the Prototype SQ Requirements

NeXolve provided significant support and key inputs to the development of Solar Cruiser SQ requirements, SQ design, and analysis of Solar Cruiser Sail Quadrants (SQ)s. Typically, requirements would have "flowed down" to NeXolve but, based on the uniqueness of this development, NeXolve worked with Redwire and NASA to define the set of flight SQ requirements and verification plans, and presented them at SQ Membrane Assembly (MA) Critical Design Review (CDR) in October of 2021. Following SQ MA CDR and the closure of several related Request for Action (RFA), Redwire provided NeXolve with the Authority to Proceed (ATP) into flight SQ manufacturing, following the completion of the Prototype SQ [3]. However, the flight program for Solar Cruiser was not confirmed at a key decision point due to programmatic constraints. The SQ Requirements including system performance, interfaces, environments, and key constraints were presented at the SQ MA CDR and are summarized in Figure 2.

SQ Requirements (Assumed)

Architecture
- 4 right triangular sail quadrants (SQ) oriented symmetrically about a centrally located sail spool
- 1-m diameter center hole
- SQ diagonal edge spacing equal to ¼ sail spool circumference
- Outer corners of sail (2) are connected to distal end of respective TRACBooms
- Inner corners of sail (2) are connected to adjacent inner corners via a "cross tie"
- Sail area: 1653m2.

Sail features / materials
- Sail: <3 micron CP1 with ~1000Å VDA on 1 side
- Seams: resin bonds
- Rip-stop: TCP1, 60 inch spacing
- Edge reinforcements (4): 1-mil 0.5" wide Kapton tape, ¾" wide TCP1 covers resin bonded to sail
- Corner reinforcements (4): 2-mil Kapton film with PSA, ¾" wide TCP1 covers resin bonded to sail, aluminum grommets
- Jumpers: sail film + ¾" wide TCP1 covers, resin bonded to sail
- Catenaries (if included):
  - 1-mil 0.5" wide Kapton tape, ¾" wide TCP1 covers resin bonded to sail, circular profile with 3% depth
  - Outer edge (1)
  - Diagonal edge (2)
  - No catenary on inner edge
- Cross tie: length is ¼ sail spool circumference, material is tbd
- RCD Deployment Mechanism: 10 per corner, <22cm x 22cm (there are more RCD requirements)
- LISA Photovoltaic cell: 19.5cm x 31cm CIGS, 1 per corner (there are more LISA PV requirements)

Figure 2. Initial SQ requirements

3. Analysis Completed for the Development of the Prototype SQ

The main objective of our analysis was to support the decision for not using catenaries. It became apparent that catenaries would not be beneficial for this sail because of the corner tensions and stresses. We also used analysis to ensure we meet our strength and stress requirements for the non-catenary model we're moving forward with.

Initially we thought we would use catenaries to tension the membrane, however our analysis showed the loads for catenary tensioning at this size become prohibitive. After we decided to go with the non-catenary model, we focused our analysis on the four-corner tensioning approach along with the reinforcements and features required to react the loads in the corners. For NEASCOUT, the sail was monolithic, but because of the requirement for a hole to be cut into the center of the sail for Solar Cruiser, and the need to fabricate this in a quadrant architecture due to its size, we developed a unique design feature to enable it to behave like a monolithic sail [3]. These features are called cross ties and they aren't connected to the space craft but to each adjacent sail instead.

As our level of analysis began to mature, we added solar sail features to our model. This includes 1-mil thick, 0.5"-wide Kapton tape acting as an edge reinforcement along with a specifically designed corner reinforcement (Shown in Figure 3) including a stainless-steel stiffener, VDA-coated Kapton for loading, electrical jumpers for surface conductivity, and a grommet for a connection point to connected to either a crosstie or a distal end spring to be attached to the booms. This corner reinforcement was loaded with a distributed load from the location of the grommet the sail will be pulled from to simulate on-orbit film stress fields across the quadrant. The loading value input is based on the axial capability of the TRAC-boom

provided by Redwire Space which was determined to be approximately 3 Newton's for on-orbit conditions.

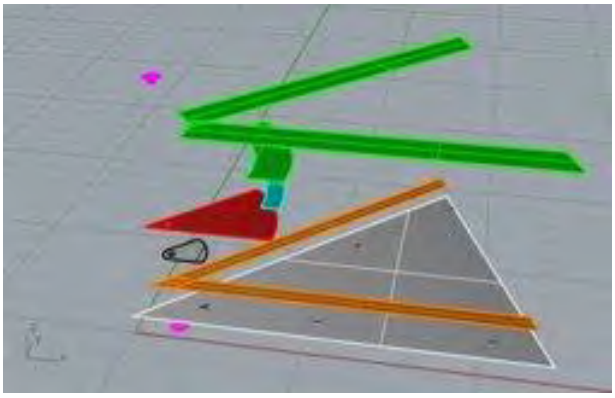

Figure 3. Sail corner features stack-up (side view)

4. NeXolve's Manufacturing Facility

The flight scale footprint of the NeXolve solar sail fab and fold mechanism was established along with the placement of all Ground Support Equipment (GSE) elements including the Fab and Fold table, the corner Sub-assembly tables, a sail spooler, and the marking gantry. Figure 4 is a photo of NeXolve's solar sail manufacturing facility located at 355 Quality Circle in Huntsville, AL. This facility is a 12,000 sq. ft. cleanroom compliant with ISO Class 7/10K class cleanroom standards and requirements. The photo also shows the Z-folded Prototype SQ on the edge of the fab and fold table. Although tweaks to the fab and fold table continued throughout Prototype SQ fabrication, as part of the vetting process, the mechanisms were used effectively to support prototype SQ fabrication.

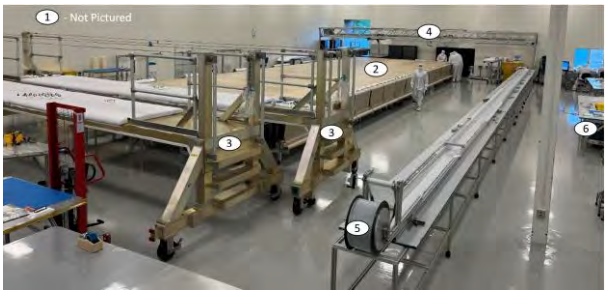

Figure 4. NeXolve's cleanroom manufacturing facility and key enabling GSE

5. Key Enabling Ground Support Equipment (GSE) for SQ Manufacturing

1. The Eastman Cutting Table (#1 in Figure 4 not pictured) is a CNC machine with cutting, punching, and marking capabilities. NeXolve has used the Eastman Cutting Table (ECT) for many different applications as it is a very versatile piece of equipment. For Solar Cruiser, the sail film panels that form the corner subassemblies (SA1 and SA14 pictured in Figure 5) are produced.
2. The Fabrication and Folding (F&F) Table (#2 in Figure 4) is arguably the most important piece of GSE for sail manufacturing. This table contains the rolls of sail material, the work surface where the SQ midspan (SA2 thru SA13 in Figure 5) is formed and features are installed, the backer removal system, the transport system, where the corner subassemblies are integrated to the SQ midspan, as well as the SQ folding area.
3. The working gantries (#3 in Figure 4) are the GSE that enable the manufacturing staff to reach the work surface and execute the tasks to build the SQ.
4. The Marking Gantry (#4 in Figure 4) is a large bridge-like structure that spans over the F&F Table and houses an automated arm that is equipped with a sail marking pen that marks sail feature locations.
5. The Spooling Mechanism (#5 in Figure 4) allows the SQ folded stack to maintain the right amount of compression while being wrapped onto the spool with extreme accuracy.
6. The corner subassembly fabrication tables (#6 in Figure 4) allow for the corner subassemblies to be built in parallel to the SQ midspan. This was necessary in order to install Reflectivity Control Devices (RCDs) and Lightweight Integrated Solar Array (LISA) panels on each of the (8) corner subassemblies of the full sail. The RCDs and LISAs were descoped from the program in April of 2022 due to programmatic cost restraints and risk mitigation.

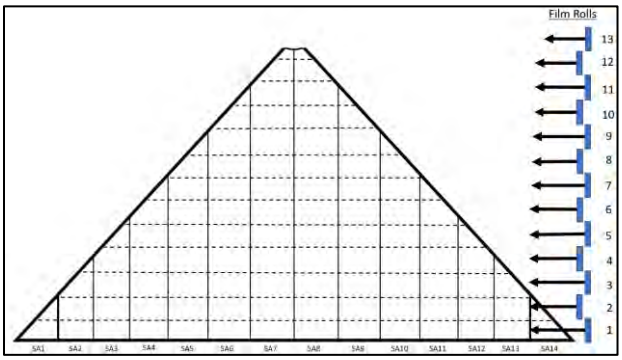

Figure 5. Sail quadrant sub-assembly layout.

6. SQ Manufacturing Flow and Manufacturing Processes

The SQ is broken up into 14 subassemblies (SAs) numbered 1 through 14 from left to right, shown in Figure 5. Each subassembly is approximately 10 feet wide so that it can fit on the 15 feet wide work surface of the F&F Table. The corner subassemblies are SA1 and SA14, and the SQ midspan is made up of SA2

through SA13. The SQ contains corner reinforcements at each of the 4 corners (2 inner corners, 1 on SA1, and 1 on SA14), edge reinforcements with covers along the perimeter of the SQ, seams joining the 60”-wide rolls of sail film together (the dotted lines shown in Figure 5), ripstops that are also placed 60” apart from each other but perpendicular to the seams, and electrical seam jumpers for surface continuity and electro-static discharge (ESD) bleed off. The base material sail film is NeXolve’s VDA-coated CP1 polyimide film which is produced on a backer. This backer allows the manufacturing staff to be able to handle such thin film with precision, and it allows the resin bonding process to be possible. The edge reinforcements are made of 0.5” wide Kapton tape to act as a reinforcement but also a load bearing path around the perimeter of the SQ. The edge reinforcements are also covered with a polyimide film to encapsulate any potential adhesive leach out over time or in the harsh environments of space, as any uncovered adhesives have proven to be extremely damaging to these films. The seams, ripstops, and edge reinforcement covers are made from NeXolve’s Toughened CP1 film (TCP1) which is the base uncoated CP1 material infused with PTFE for tear resistance and durability.

The SQ corner subassemblies (SA1 and SA14) are manufactured in parallel to the midspan on the corner subassembly fabrication tables. This was originally planned to accommodate the installation of RCDs and LISAs in each of the (8) corner subassemblies of the full sail. When the RCDs and LISAs were descoped from the program, NeXolve elected to continue to fabricate the corner subassemblies in parallel due to consistency and that it had no negative effect on production schedule. The corner subassemblies are made up of (2) panels produced on the ECT and transported to the fabrication table. These panels are then seamed together with CP1 resin produced by NeXolve by utilizing a NeXolve proprietary process of an adhesiveless bonding technique. This bonding technique can also be thought of as a resin weld or polymerization process. This same process is also used to install the ripstops, to prevent tear propagation, which are perpendicular to the already-installed seams and are also spaced 60” apart. The corner subassemblies also contain corner and edge reinforcements. The corner reinforcement construction is shown in Figure 3 utilizing a stainless-steel plate (grey part in Figure 3) and VDA-coated Kapton doubler (red part in Figure 3). These reinforcements provide the additional support needed for the added loads introduced by the radially deployed TRAC booms that are connected through a grommet embedded in the corner construction.

The SQ midspan is fabricated completely on the F&F Table from the time the material comes off the film rolls until the sail gets z-folded for spooling. The process begins on the “feed out” side of the table shown in Figure 6 where the sail film is introduced to the F&F table (Figure 7) as it comes off the material rolls shown. The film is then brought out onto the table surface by hand and laser aligned to be parallel to one another. When the material is aligned and on the work surface, the rolls are then seamed together using TCP1. After the seams have been installed, the sail is then marked by the marking gantry. The marking gantry is first aligned to the roll 1 portion the subassembly (the bottom edge of the SQ triangle) and will mark edge lines, fold lines, and ripstop locations. The marking gantry will then be positioned on the roll 2 portion of the sub assembly by using fiducial marks made in the previous step so that it can “lock” into the correct position. This process is repeated until the whole sub assembly has been marked. The edge reinforcements, edge reinforcement covers, ripstops, and seam jumpers are then installed, also by using CP1 resin and NeXolve’s adhesiveless bonding technique, based on the markings to complete the build of the subassembly. All features installed to the midspan are the same as the features installed to the corner subassemblies. All bonding steps and feature installation occurs while the film is still on the backer.

Figure 6. The “feed out” side of the F&F table

Figure 7. The F&F table

Once the subassembly construction is complete and all features have been installed, the subassembly is then transported and folded. The transport system is a key inhibitor of the F&F Table as it transports the sail across the table so that the already-completed subassembly can be moved through what is called the backer removal station. The system works such that the Armalon (the brown material) in Figure 8 is strung through a series of rollers and pulleys in a certain fashion that allows a "clamping bar" to clamp the material in the region where the slacked Armalon is on the left side of Figure 8. Once the clamping bar is clamped onto the material, a series of actuators move the bar downward in unison so that it pulls the Armalon across the whole F&F Table as the Armalon is also fed onto the table on the "feed out" side in sequence with the sail film. A certain load of weight must be sitting on each panel of the sail (seen in Figure 8) so that there is minimal if any slippage between the Armalon and sail. Approximately 5 feet from the clamping bar side of the F&F Table is what is called the "separator board" which separates the film from the backer. At the beginning, and as a new roll of material is added to the SQ, the backer is slightly peeled off by hand and fed underneath the separator board so that throughout the rest of that roll of material for that SQ the backer will continue to be peeled off at the separator board. This process is repeated throughout the duration of the SQ until completion.

Since the corner subassemblies are built in parallel to the SQ midspan, they must be integrated at a certain point in the flow of production. SA1 is completed first or in parallel with SA2 such that they are both completed at the same time. SA1 is attached with a vertical seam joining the two along with connecting edge reinforcements and covers, and seam jumpers. These two, now-joining, subassemblies will be transported and folded as one. A similar process is used to integrate SA14. Once SA13 is finished and ready to begin transport, it will be transported just enough that SA14 can fit on the F&F Table work surface and then joined to SA13 with the same steps as SA1 was joined to SA2. Once this is complete, final integration will be complete with only the final transporting and folding left to finish.

Throughout the duration of the SQ build, it is also folded. The design of the SQ is to be z-folded such that once it is deployed it will unfold and open out to full deployment in a controlled and orderly manner. NeXolve has developed a proprietary process that is semi-automated, semi-manual for folding a sail this large. This process enables NeXolve to successfully build solar sails and solar sail quadrants larger than the facility they are manufactured in. The Prototype SQ for example, if fully deployed would not fit in NeXolve's manufacturing facility. The fold pitch or fold width for the Solar Cruiser Prototype SQ is 22 cm, or ~8.66 inches. The z-folded stack and fold width is shown in Figure 8. This entire process would repeat 4 times for a 4-quadrant full size sail for the Solar Cruiser mission as all 4 quadrants are identical.

Figure 8. The transport system on the F&F table

7. Prototype SQ Spooling and Final Packaging

Once all fabrication is complete, the sail quadrant(s) are then spooled onto a carbon fiber spool, provided by Redwire Space, and packaged with a sail restraint attached. The spooling mechanism is shown as GSE #5 in Figure 4. The spooling mechanism is a piece of GSE hardware that is built and designed by NeXolve through previous solar sail programs such as NEAScout. This mechanism is wrapped with a thin mostly static-free material called Syntrex and designed such that a series of cranks, turns, and bars being leveraged against one another wraps the z-folded stack of the SQ around the

spool as well as collects the Syntrex material away from the sail at the same time. The Syntrex material is extremely important as it is wound through the spooling system in such a way that is maintains the correct amount of pressure on the SQ so that it doesn't blossom or balloon with air pockets throughout the entire process. When spooling 4 SQs onto a single spool for a flight size sail, the 4 z-folded SQs are laid on top of each other in a staggered fashion spaced out by ¼th the circumference of the spool and then spooled in the same way. Once the SQ or SQs have been spooled the inner crossties are attached joining adjacent SQs. For the Prototype SQ and the upcoming Ground Test Quadrant to be deployed in January of 2024, a crosstie simulator will be installed given that there is only one SQ being spooled and will not have any adjacent sails.

After the SQ has been spooled, the sail restraint is installed. This restraint is produced from uncoated 2-mil Kapton for its mechanical properties. The restraint is designed such that it is attached to the top of the spool with pressure sensitive adhesive (PSA) and wrapped around the circumference of the sail with a slight gap at the bottom of the sail for venting. For visual purposes, the restraint performs similar to how a cupcake wrapper works. The function of the restraint is so that throughout the lifetime of the spooled sail, the sail does not blossom, entrap any unwanted air, nor become slack and release from the spool at an undesired time. Figure 9 below shows a sequential picture collage of the Prototype SQ build, spool, and package. The far bottom right image in Figure 9 shows the restraint installed to the spooled Prototype SQ.

Figure 9. Collage of prototype SQ manufacturing and packaging

8. Verification Testing

Over the life of the Prototype SQ after manufacturing, folding, and packaging, the NASA, Redwire, and NeXolve teams conducted multiple verification tests involving SQs including [3]:

- 4-SQ architecture BrassBoard (1/16th scale) deployment test at Redwire Space led by NeXolve
- (1) spooled Prototype SQ with 3SQ volume simulator Ascent Vent Test led by NeXolve
- 4-SQ architecture BrassBoard deployment test at NASA MSFC led by Redwire Space
- (1) Prototype SQ ground deployment test at NASA MSFC led by Redwire Space

9. Post-Deployment SQ Shape Measurement Process

Prior to measuring the quadrant, the long edge was aligned with a tensioned string that spanned from grommet to grommet on the long edge. A weight was placed near each ripstop/edge intersection on the long edge to reduce wrinkles introduced in the deployment process and to keep the sail from moving during the measuring. After securing the long edge, the short edges of the quadrant were flattened and weights were added. No string was used on the short edges [3].

The four grommet locations were measured with the laser tracker by placing a 0.5" Spherically Mounted Retroreflector (SMR) seated in the center of each grommet. A best fit algorithm located the CAD model relative to the physical sail quadrant. Measurements around the perimeter were made by mounting the 0.5" SMR into a clear acryllic tool which enabled positioning the SMR above the points of interest [3].

7. July-August 2022 - Ascent Vent Testing of the Spooled Prototype SQ at NASA MSFC
8. September 2022: BrassBoard SQ Deployment at Redwire and NASA MSFC to verify the prototype deployment configuration
9. September / October 2022 – Prototype SQ Deployment Demonstration at NASA MSFC

10. Conclusion

NeXolve has successfully developed the capability of manufacturing large solar sails, such as Solar Cruiser, as well as many other large deployable thin film structures. NeXolve's current manufacturing facility setup and operating GSE is expandable and scalable to support the production of a 4-quadrant solar sail up to 5000 m^2. Architectures other than a 4-quadrant structure are supported as well. In partnership with MSFC and Redwire Space, NeXolve led the efforts for the design, development, manufacturing, and packaging of the SQ as well as the 4-quadrant solar sail architecture. The Solar Cruiser design 4-quadrant architecture totals 1653 m2 and has a total sail mass of 6.91 kilograms The single Prototype SQ came to a total ~1730 grams. The Prototype SQ took approximately 7 months to complete. After incorporating lessons learned and completing some observed areas for improvement, the Ground Test Quadrant is on track to be completed in approximately 6 months and NeXolve believes that we can achieve a full future SQ build in 5.5 months. The Prototype SQ

successfully completed an Ascent Vent test, led by NeXolve, and conducted at NASA MSFC facilities as well as a ground-based deployment test in November of 2022, led by Redwire Space and conducted at NASA MSFC. The Ground Test Quadrant is currently underway as its purpose is for technology advancement of the entire Solar Sail System (SSS) to achieve TRL6. This system includes the Sail Deployment Mechanism, Active Mass Translator, and TRAC booms provided by Redwire Space along with the Sail Quadrant provided by NeXolve. The Ground Test Quadrant will be integrated with the rest of the SSS to undergo a full testing campaign of Thermal Vacuum, Vibration, and Deployment Testing. The deployment test for the Ground Test Quadrant is planned for January of 2024 at NASA MSFC.

Acknowledgments

The completed and ongoing work described in this paper was funded by NASA's Marshall Space Flight Center, where NeXolve supported Redwire Space as a subcontractor under Redwire Subcontractor Agreement RCSC717-10066-2. Thank you to all team members involved from NASA, Redwire Space, and NeXolve.

References

[1] "Packaging and Manufacturing Processes to Enable Production of Very Large Solar Sails for Next Generation Missions", final report, NASA contract #: 80NSSC19C0200, 8/13/19- 9/27/22

[2] https://nexolve.com/wp-content/uploads/2021/10/TDS_CP1_Clear.pdf

[3] Pearson, J. Prototype Solar Cruiser Sail Quadrant Development and Testing. TR22-1058.

Momentum Management Strategies for Solar Cruiser and Beyond (ISSS 2023)

John INNESS[1*], Daniel TYLER[1], Benjamin DIEDRICH[2], Saba RAMAZANI[1], Juan ORPHEE[1]
[1] *Marshall Space Flight Center, Huntsville, Alabama, USA*
[2] *NASA MSFC/ESSCA/Axient Corporation, Huntsville, AL, USA*

Abstract

Solar Cruiser is a small (ESPA-class) satellite Technology Demonstration Mission (TDM) to mature solar sail propulsion technology using a solar sail larger than 1600 square meters, demonstrating performance both as a propulsion system and a stable pointing platform for science observations in an artificial halo orbit sunward of the Sun-Earth Lagrange Point 1 (sub-L1). To ensure attitude control throughout the mission, momentum accumulated on the reaction wheels (RWs) used for attitude control must be managed such that the sailcraft does not lose control due to RW momentum saturation. Momentum builds up on the wheels from environmental disturbance torques caused by solar radiation pressure combined with a center of mass (CM)/center of pressure (CP) offset, deformed sail shape, and an off-sun pointing angle, plus other factors. Solar Cruiser mitigates this momentum build up by utilizing an Active Mass Translator (AMT) that maintains pitch and yaw momentum by trimming the CM/CP offsets, and thrusters to maintain roll momentum. A survey was conducted by the Solar Cruiser team to assess the feasibility and tradeoffs of novel momentum management concepts such as Reflectivity Control Devices (RCD's), different thruster configurations, and control vanes and other articulated control surfaces. In addition, techniques to reduce disturbance torque buildup, such as reducing boom tip deflections and clock angle control, were assessed. Similar sailcraft momentum management strategies can be used for future missions such as space weather monitoring and Earth magnetotail science missions.

Keywords: Solar Cruiser, Momentum Management, GNC, ADCS

Nomenclature

ACC	Active Clock Control
AMT	Active Mass Translator
ADCS	Attitude Determination and Control System
GNC	Guidance, Navigation, and Controls
L1	Sun-Earth Lagrange Point 1
RCD	Reflectivity Control Device
RCS	Reaction Control System
RCD	Reflectivity Control Device
SIA	Sun Incidence Angle

1. Introduction

The need for momentum management system integrated with the ADCS is crucial for the success of solar sail missions as once the control actuators become saturated, the sailcraft loses control. NASA's Solar Cruiser utilizes four reaction wheels as the primary control actuators for controlling roll, pitch, and yaw attitudes. Disturbance torques build up because of different environmental factors and sail shape. For pitch and yaw momentum management, Solar Cruiser utilizes an AMT to trim the CM/CP alignment and create a restoring moment to desaturate the wheels. For roll momentum management, the baseline Solar Cruiser design features RCDs and RCS thrusters which create an opposing moment to desaturate the reaction wheels. An additional study after Solar Cruiser PDR was completed investigated alternative roll momentum management techniques such as control vanes.

The ADCS configuration of Solar Cruiser is seen in Figure 1. The RCDs are laid upon as part of the sail membrane and are deployed as part of the sail deployment sequence. The AMT is part of the Solar Cruiser satellite bus along with the RCS thrusters denoted on the figure as IFMs.

*Corresponding author, john.p.inness@nasa.gov

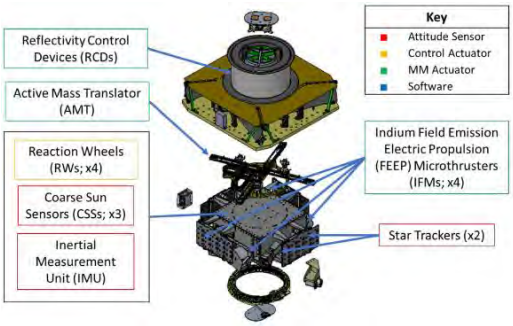

Fig. 1. ADCS Configuration of Solar Cruiser [1]

Solar Cruiser's overall mission is to serve as demonstration mission for solar sailing technology in a sub L1 halo orbit, then demonstrate a plane change maneuver to raise the orbit above the Earth's orbital plane after completion of the primary mission phase. Solar Cruiser features Heliophysics scientific instruments and will also serve as demonstration mission for technologies key for larger future solar sail missions such as the RCDs and AMT.

2. Disturbance Torques

The primary design driver for MM systems, especially the sizing of MM actuators, is the disturbance torques experienced by the sailcraft, dominated by those originating from the solar radiation pressure (SRP) on the sail. Given the amount of uncertainty inherent in these SRP-derived disturbances, detailed and conservative modeling of this effect was implemented on Solar Cruiser, as is advisable for other solar sail missions [1].

The SRP-induced disturbance torque is the sum of the CM/CP offset torque and the net applied torque due mainly to a deformed (i.e., non-flat) and asymmetric sail shape. For given sail size, optical properties, and distance from the sun, these torques are only a function of sun-incidence angle (SIA) and clock angle (assuming an anisotropic shape, such as a square sail). SIA and clock angle are the second and third Euler rotations, respectively, in a Z→Y→Z rotation sequence, where Z is normal to the sail plane facing toward the sun. Effectively, SIA is the half-cone angle of the sun with respect to the sail normal and the clock angle orients the SIA axis of rotation relative to the sail body.

The CM/CP offset torque can be broken into two components: a specular effect caused by the normal component (specular reflection) of the net force to the sail applied at a moment arm in the sail plane and a diffuse effect caused by the tangential component (diffusive reflection) of the net force. The specular effect can be a considerable contribution to pitch/yaw disturbance torques (i.e., those applied about the in-plane axes, X and Y, of the sail) and has been traditionally used to size actuators [2]. The diffuse effect is a result of light scattering upon reflecting at a non-zero angle of incidence on a realistic sail with some degree of diffusivity. According to the McInnes solar sail force equations, the specular effect monotonically decreases in magnitude with the cosine squared of SIA, whereas the diffuse effect varies with the product of the cosine and sine, peaking at 45 degrees, and can result in both pitch/yaw and roll (about sail normal) disturbance torques [3]. Therefore, for realistic sails without perfect specular reflection, even perfectly flat sails, care must be taken to ensure adequate 3 axis control for mission attitude profiles that require considerably large SIAs nearing 45 degrees.

$$\vec{\tau}_{\frac{CM}{CP}} = \vec{r}_{\frac{CM}{CP,in-plane}} \times \vec{F}_{specular} cos^2(SIA) + \vec{r}_{CM/CP} \times \vec{F}_{diffuse} \cos(SIA) \sin(SIA) \quad (1)$$

In addition, the shape of the sail can cause applied torques at the CP, independent of CM location. The net applied torque is a result of the imbalance in local torques applied across the sail due to varying local SIAs. This effect can be modeled using a mesh model and calculating and summing the forces and torques applied at each element, as if the sail consists of many smaller sails with slightly different SIAs, or by using a reduced-order model, such as the Rios-Reyes generalized sail tensor model, to represent the problem in a more computationally efficient manner, as is done on Solar Cruiser [4]. The sail shape-induced disturbance torques can be relatively large in all axes, generally dominating the disturbance torques about the roll axis, and highly variable with SIA and clock angle, given some anisotropy in the shape (square sail and asymmetric shape deformations). Figures 2 and 3 shows a graphical representation of the summation of disturbance torques.

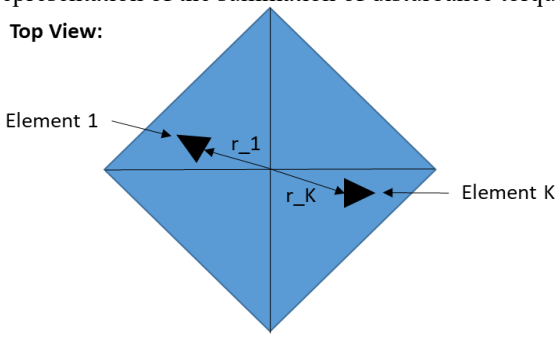

Fig. 2. Elements of a sail membrane

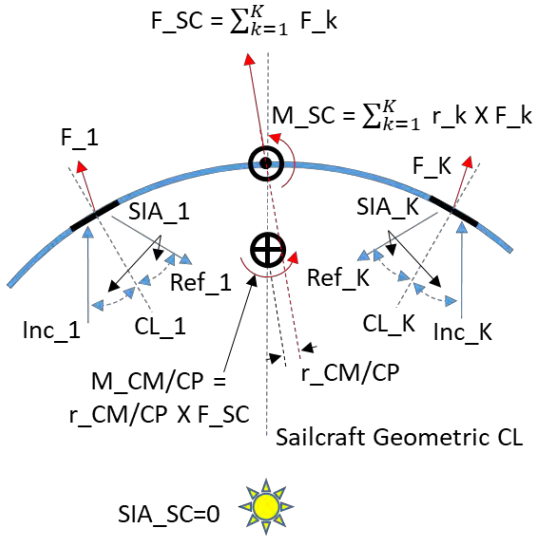

Fig. 3. Disturbance torque analytical model

Combining all these effects together leads to a complex disturbance torque "profile" as a function of several mission and system design parameters. Figure X illustrates the effect various sources of disturbance torques has on the overall profile. The different features of this profile have different impacts on the selection, sizing, and design of MM systems. E.g., a large CM/CP offset torque, especially a large specular component, may make use of a CM/CP control actuator, such as an AMT, favorable. Or large asymmetric shape deformations that make disturbance torque highly variable with clock angle may drive the use of constraints on, or control of, clock angle for the purpose of minimizing torques. The logic and considerations for these kinds of design decisions is further discussed in following sections. Graphs of the largest disturbance torque models for Solar Cruiser are shown in Figures 4 and 5.

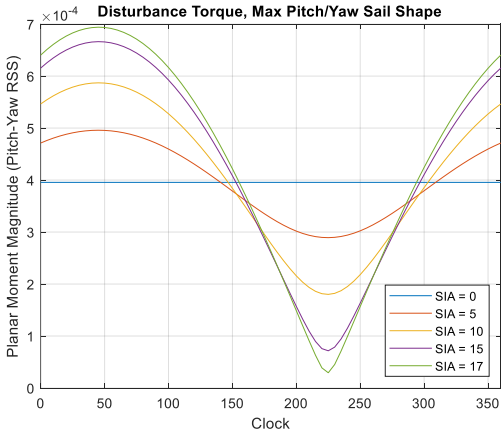

Fig 4: Max Pitch/Yaw Disturbance Torques

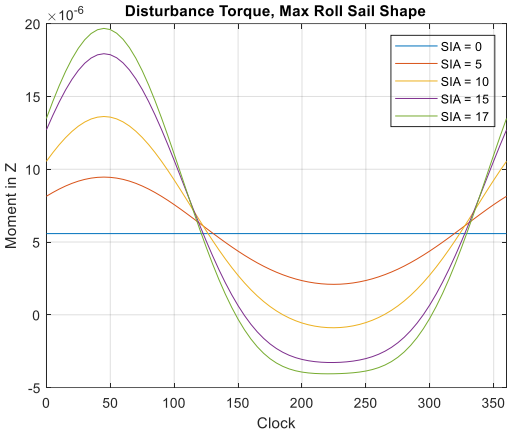

Fig 5. Maximum Roll Disturbance Torque

3. Pitch and Yaw Momentum Management

Torque on a solar sail consists of two components, one from the 3-dimensional shape of the sail and the other from the sailcraft CM crossed with the sail force. For pitch and yaw control, the displacement of the CM in the plane of the sail directly results in torques in those axes that can be used for momentum management about those axes.

Solar Cruiser, like the Near Earth Asteroid (NEA) Scout solar sail mission before it, was developed to use an Active Mass Translator (AMT) to change the CM/CP offset of the sail for pitch/yaw momentum management of the RWs. The effectiveness of this technique depends on the sailcraft having large bus mass relative to the sail (>= ~1:1 ratio) and range of motion from the mass translation actuators, which the Solar Cruiser design is well suited to.

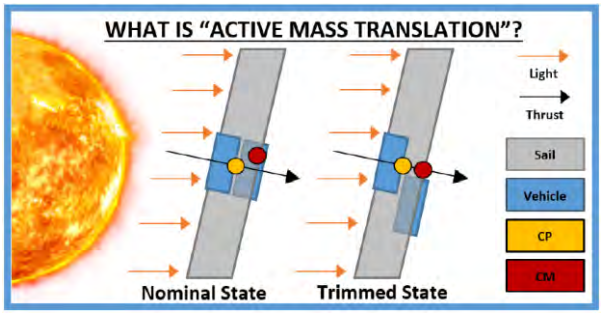

Fig 6: AMT Trimming the Sailcraft (5)

The displacement of the CM in the trimmed satellite can be seen in Figures 6. The differences in CM and CP create a restoring moment on the torque axis to desaturate the reaction wheels and can also be used to find a neutral state to prevent buildup of momentum in the sailcraft. Figure 7 shows the control method for the AMT.

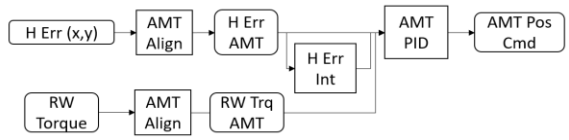

Fig 7: AMT Control System (1)

The controller is designed to help move the AMT to desired position where it will actively desaturate the wheels. A demonstration of the AMT control in the Solar Cruiser GNC simulation is shown below:

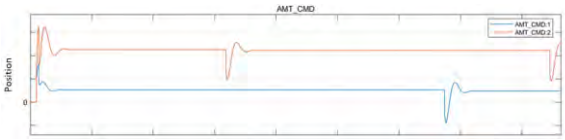

(a) AMT Position Command

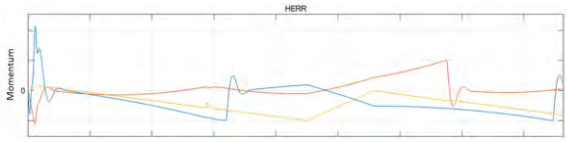

(b) Pitch/Yaw Momentum Error

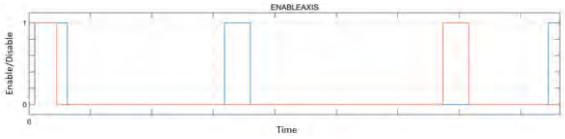

(c) AMT Axes On/Off States

Fig 8: AMT Simulated Example

As the AMT moves, it changes the center mass which can be seen as the AMT is commanded to different positions and lead to decreasing in overall momentum error per axis. The red color refers to the pitch axis, blue color represents the yaw axis, and yellow represents the roll axis. Each movement of the AMT can betide to a decrease in momentum in each given axis.

However, sail designs with a small bus mass or difficult moving the CM would require other methods like vanes, shape deformation, or optical property control at the edges or corners of the sail to change the pitch/yaw torque.

4. Survey of Roll Momentum Management

As part of the development for Solar Cruiser, a survey of different actuators for roll momentum management was conducted. These methods include utilizing RCS thrusters, a novel RCD, control vanes, and active roll management control of the system. Each of these design trades focused on trade space of the effectiveness of the design, technical maturity, and integrated system analysis.

The baseline design of Solar Cruiser features RCDs as the primary roll momentum desaturation actuator and IFM RCS thrusters as a backup option with active clock control to minimize disturbance torque buildup during long periods of attitude hold.

4.1 RCD

RCDs are innovative devices that are selected as baseline to perform roll momentum management for solar cruiser. The IFM thrusters are back-up actuators in case of RCDs underperformance. The functionality of RCDs have been made possible by a new generation of electroactive polymer-dispersed liquid crystal (PDLC) material. When a voltage is applied to the RCD panel, the PDLC material changes reflectivity. The molecules in the PDLC material are randomly oriented and the RCDs are reflective when no voltage is applied. However, with applied voltage, the PDLC molecules are reoriented, and the RCDs becomes transmissive and active. Multiple RCD coupons are mounted as a panel with a tent angle near the sail boom tips. When two opposing RCDs are in opposite states, one “off” and one “on” a differential force that acts tangent to the sail plane at a large moment arm near the boom tips produces a roll torque. To determine whether Counterclockwise (CCW) or Clockwise (CW) moment must be applied, a controller logic is designed for RCDs (Figure 9).

Reaction wheels are Solar Cruiser’s main control actuators for all phases of the mission. As momentum accumulates on the wheels and there is a need for desaturation, ADCS algorithms will perform MM using the available MM actuators on the sail. Once the sail is deployed, RCDs are the main roll MM actuators. At a very high level, to perform moment management, RCD controllers deactivate when the momentum, H Err, drops below a set deactivation threshold, and reactivate when momentum increases above an activation threshold. Figure 10 shows RCDs are triggered when the roll momentum accumulation on reaction wheels increases above the activation threshold. RCDs apply moment in the CW or CCW direction to decrease the momentum until it is lower than deactivation threshold.

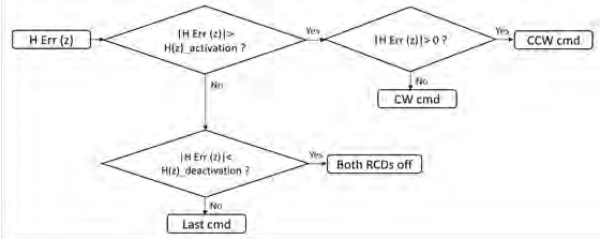

Fig 9. RCDs Roll Momentum Controller (1)

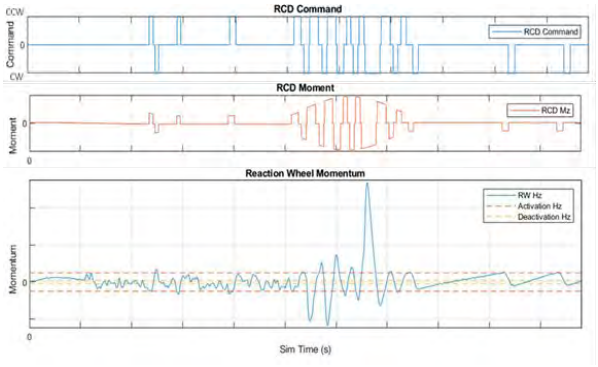

Fig 10. RCDs roll momentum controller performance

4.2 RCS

The IFM RCS thrusters as part of Solar Cruiser design for as backup in case the RCDs do not perform as desired. The design space is similar to RCDs with the SSADCS having activation and deactivation thresholds to keep the roll momentum within desired thresholds. An example of the IFM thrusters being used for momentum management can be seen in Fig 11.

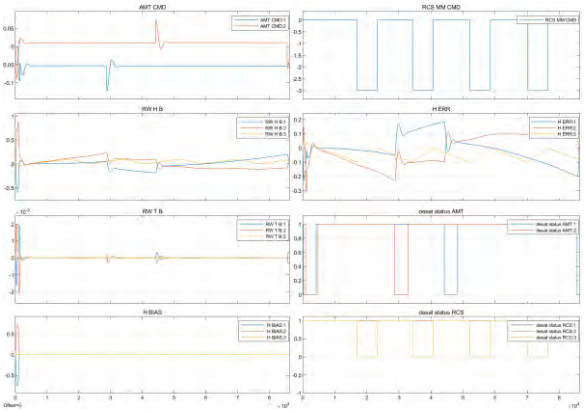

Fig 11. IFM RCS Roll Momentum System in Action

In Fig 11, it's possible to activation points for the IFM RCS thrusters. The design of the RCS control system is like the RCDs where a desired activation and deactivation threshold are defined, and it induces an opposing moment to decrease the momentum build up on the reaction wheels.

With RCS thrusters, there are some system wide challenges introduced as part of it. These include sizing the propellent tank to account for all the momentum dumping burns, and power and thermal constraints for firing the thrusters at different intervals and how long for the thrusters to fire. These efforts must be coordinated with other subsystems

4.3 ACC

Another option that can be used in conjunction with other design actuators is implementing an ACC as part of the ADCS algorithms. This implementation controls the clock angle of the sailcraft to minimize roll momentum buildup. Additionally, this method can be used in conjunction with the pitch/yaw channels to minimize momentum build up. This method has the advantage of being able to use existing control actuators to implement this momentum management strategies and supplement other methods.

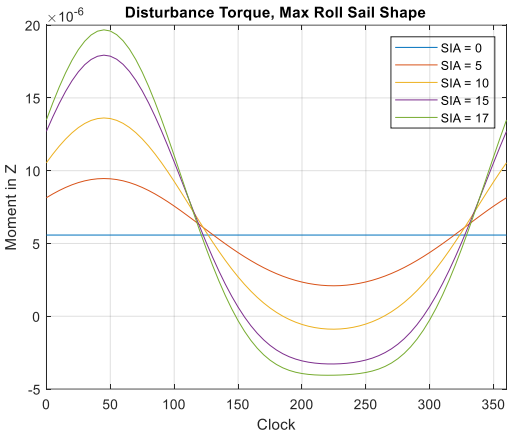

Fig 12. Maximum Roll Disturbance Torque

These figures 12 was generated to represent the worst-case disturbance torques would look with different SIA angles and sail shapes contributing to differences in magnitude of disturbance torques. If a zero crossing exists at the sailcraft SIA's as shown in Fig 12, it enables the active roll controller to utilize that zero crossing to have a set angle offset to desaturate the reaction wheels during periods of attitude hold.

The ACC works by observing the torque build up on the reaction wheels and takes a pre-designated step in the direction to offload the momentum build up. These steps take effect over extended periods of time as the roll momentum buildup is a slow process and if the ACC acts too quickly, it might interfere with flex modes of the spacecraft. A flow diagram of this control process is seen in Fig. 13.

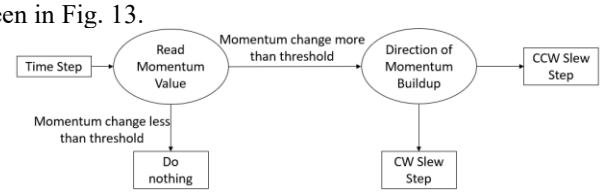

Fig 12. ACC Algorithm Flow Chart

However, if the roll disturbance torques do not have a zero crossing, the active roll controller focuses on minimizing the disturbance torque build up on the sailcraft as indicated by the local minimums. To best

manage roll momentum levels utilizing ACC, other momentum management actuators for the roll channel must be used due to the lack of guarantee for a zero-crossing.

4.4 Control Vanes

Attitude control using solar radiation pressure was first proposed by Sohn in 1959 [6]; and since then, the use of solar radiation pressure to perform attitude control has been studied extensively in references 7-12, not an exhaustive list. The use of solar pressure for attitude control was implemented on geostationary satellites as well as interplanetary, including OTS, TELECOM 1, IMMARSAT, INSAT and GOES satellites [12].

The principle of a control vane is fundamentally the same as the solar sail, that reflecting photons that generate an equal and opposite momentum. Satellites have used solar pressure to control attitude by gimbaling solar panels or reflective trim tabs, as control vanes, to generate solar torques needed to control attitude dynamics. Control vanes at the tip booms would scale with sail size by taking advantage of increased moment arm for an increased solar sail size. Figure 13 shows boom tip mounted control vanes proposed by NASA JPL as early as 1977. Also, boom tip control vanes had been proposed for the NASA Sunjammer mission concept in 2014, later canceled, including development of the control architecture and simulated performance [13].

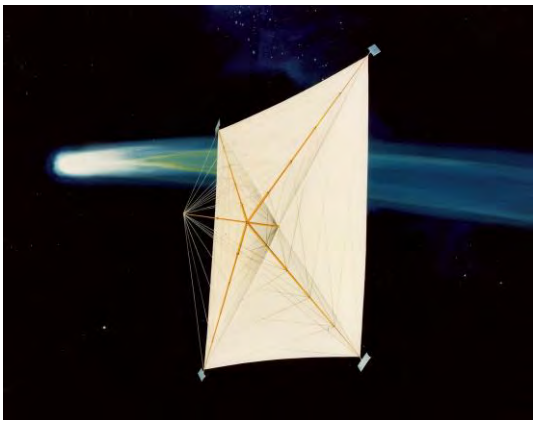

Figure 14: An 800x800-m solar sail proposed by JPL in 1977 for a rendezvous mission with the Halley's comet for the 1986 passage.

However, the challenge with boom tip mounted control vanes for solar sails is not in its fundamental working principles, which are well understood and proven, but on its practical implementation. Storing and deployment of solar sails and booms require the sail and boom structure to be highly flexible to fit the deployer and be capable of recovering its shape after deployment. Therefore, a boom tip vane control mechanism that can be steerable while also flexible to be stored and deployed poses structural design challenges.

Furthermore, a control vane would need a gimbal system and a motor driver. The Motor driver would need power and control commands from the flight computer. The power and command would need to run along boom cables to the spacecraft bus.

Alternatively, power could be generated locally, and control commands may be sent wirelessly from the bus to a local control vane board system. Finally, having control vanes implies having a moving mechanism, which adds a layer of complexity and therefore additional failure modes. Failures could include, inadequate deployment of the control vane, or failure of gimbal and motors mechanisms, which may cause a control vane to remain stuck in an undesirable attitude. Therefore, the challenge of control vanes is not on its fundamental acting principle but on the complexity of its implementation, adding potential failure modes.

5. Comparison of Roll Momentum Management Methods

Each of these different momentum management strategies have different advantages and disadvantages relative to the other systems. These differences can be seen in the table below.

Table 1. Comparison of Roll Momentum Management Methods

Roll Momentum Management Actuator	Advantages	Disadvantages
RCS	Commercial offerings readily available for mission use	Requires mass of the propellent to be carried as well as possible thermal and power constrains from thruster firings, limited fuel which constrains firing time
RCD	Low mass, volume, and power requirements	Low TRL system, Potential RCD degradation over time, Requires wiring and control at RCD location which ideally is near the sail edge

Control Vanes	Proven fundamental principle, high Technology Readiness Level. Scalable with sail size when used at boom tips.	Storage and deployment for tip vanes may be challenging. Additional moving mechanisms including motor and gimbals, which add risk for additional failures modes. Require power and control commanding at boom tips.
ACC	Can be directly implemented into the ADCS design in conjunction with other methods	Potential for no zero-crossing due to sail shape and SIA induced moments

Each solution has unique advantages and disadvantages as individual systems. For example, the control vanes are a high TRL technology on their own and have been proven to be successfully utilized in mission but have challenges with integrating with the sailcraft. RCS thrusters are available commercially-off-the-shelf (COTS) which provide a seemingly simple solution by firing thrusters in the opposite direction to create an opposing moment. Although RCS provides a stable COTS solution, there are some system level challenges faced with RCS such as thermal and power constraints from when firing the RCS as well as sizing a propellent tank to ensure RCS can serve the duration of the mission. RCDs function similarly to RCS thrusters in terms of control systems design where RCDs can contribute opposing moments and similar challenges to control vanes with integrating to the deployed sail surface. However, RCDs offer the advantages of both where RCDs don't require propellent and could be easier to integrate with a sailcraft versus control vanes. ACC requires no additional hardware as part of the sailcraft and just integration within the GNC design of the sailcraft. However, ACC runs into areas where there isn't a zero-crossing allowing the ACC to unload the roll momentum.

Understanding each option for roll control is key as one single option for roll momentum management is not sufficient to completely manage the roll axis. The baseline design for Solar Cruiser features RCDs to desaturate the reaction wheels as the primary method, ACC to minimize roll disturbance build up, and RCS as a backup in case RCD performance is not to the level as predicted or any degradation in RCD performance.

6. Conclusions

Momentum management is a critical part to ensure mission success for large sailcraft. Momentum will build up throughout a mission as when a sailcraft slews to desired attitudes to fulfil its mission or holds an attitude. Solar Cruiser utilizes an AMT for the pitch/yaw momentum management and a combination of ACC, RCDs, and RCS for roll momentum management. These systems can be utilized for future similar sized solar sails as well as further investigation into other roll momentum management actuators such as control vanes.

Acknowledgments

The authors would like to thank the Solar Cruiser Project for the opportunity to conduct this innovative work as well as provided the funding which it was completed, and this paper was written. Thanks to partners of Solar Cruiser, Redwire Corp. ATA Engineering, NeXolve Holding Company, LLC, and Blue Canyon Technologies for helping provide different inputs for the SSADCS team to design the momentum management system. Finally, thanks to all former SSACDS team members, including interns and detailees, who worked on aspects of the momentum management system.

References

[1] D. Tyler, B. Diedrich et al. Attitude Control Approach for Solar Cruiser, A Large, Deep Space Solar Sail. AAS-23-117 AAS Guidance, Navigation and Control Conference. Breckenridge, Colorado, 2015, 3 – 8 February.

[2] B. Wie. Solar Sail Attitude Control and Dynamics, Part 1. Journal of Guidance, Control, and Dynamics (Vol. 27, No. 4, 2004) 526-535.

[3] C.R. McInnes. *Solar Sailing. Technology, Dynamics and Mission Applications*. Springer-Praxis Series in Space Science and Technology. Springer-Praxis, 1999.

[4] L. Rios-Reyes, D. J. Scheeres. Generalized Model for Solar Sails. *Journal of Spacecraft and Rockets* Vol. 42, No. 1. doi: 10.2514/1.9054

[5] J. Orphee, A. Heaton. Solar Torque Management for the Near Earth Asteroid Scot CubeSat Using Center of Mass Position Control. AIAA SciTech 2018.

[6] Sohn, R. L "Attitude Stabilization by Means of Solar Radiation Pressure," ARS Journal, Vol. 29, May 1959, pp. 371-373.

[7] Acord, J. D., and Nicklas, J. C., "Theoretical and Practical Aspects of Solar Pressure Attitude Control for Interplanetary Spacecraft," Guidance and Control II, Progress in Astronautics and Aeronautics, Vol. 13., Academic Press, New York, 1964, pp. 73-101.

[8] Modi, V. J., and Kumar, K., "Attitude Control of Satellites Using the Solar Radiation Pressure," Journal of Spacecraft and Rockets, Vol 9, No 9, 1972, pp. 711-713.

[9] Joshi, V. K., and Kumar, K., "New Solar Attitude Control Approach for Satellites in Elliptic Orbits," Journal of Guidance and Control, Vol 3, No 1, 1980, pp. 42-47.

[10] Stuck, B. W., “Solar Pressure Three-Axis Attitude Control,” Journal of Guidance and Control, Vol. 3< No 2, 1980, pp. 132-139.
[11] Angrilli, F., and Bortolami, S., “Attitude and Orbital Modeling of Solar-Sail Spacecraft,” European Space Agency Journal, Vol. 14, No. 4, 1990, pp. 431-446.
[12] Wie, B. 2015 “Space Vehicle Guidance, Control, and Astrodynamics”
[13] Eldad, O. Lightsey G. “Attitude Control of the Sunjummer Solar Sail Mission,” Small Satellite Conference, 2014.

Photon-Sail Trajectories Towards Exoplanet Proxima b

Tim J. Rotmans[a,*], Jeannette Heiligers[a]

[a]*Department of Astrodynamics and Space Missions, Faculty of Aerospace Engineering, Delft University of Technology, Delft, The Netherlands*

Abstract

This paper investigates trajectories within the Alpha Centauri system to reach planet Proxima b. These trajectories come in the form of connections between the classical Lagrange points of Alpha-Centauri's binary system (composed of the stars Alpha Centauri A and B, AC-A and AC-B) and the classical Lagrange points of the Alpha Centauri C (AC-C)/Proxima b system. These so-called heteroclinic connections are sought using a patched restricted three-body problem method. A genetic algorithm is applied to optimize the linkage conditions between the two three-body systems, focusing on minimizing the position, velocity, and time error at linkage. Four different futuristic, graphene-based sail configurations are used for the analyses: two sails with a reflective coating on only one side of the sail with lightness numbers equal to $\beta = 100$ and $\beta = 1779$, and two sails with a reflective coating on both sides (again, considering $\beta = 100$ and $\beta = 1779$). Results from the genetic algorithm show that, for example, a transfer from the L_2-point in the AC-A/AC-B system to the L_1-point in the AC-C/Proxima b system can be accomplished with a transfer time of 235 years for the one-sided graphene-based sail with $\beta = 1779$.

1. Introduction

While tracking a comet with his telescope in 1689, astronomer Jean Richaud came across the Centaurus constellation. For the first time, he noticed that the star known back then as Alpha Centauri was, in fact, a binary star system [1]. Another 80 years later, in 1915, astronomer Robert T. A. Innes discovered Alpha Centauri C (also referred to as Proxima Centauri) [2], located at 4.25 lightyears from the Solar system, therefore taking on the title of being our closest neighbor. As of today, there is strong evidence that Proxima Centauri is in bound orbit about the binary system [3]. At least two planets are confirmed to be in orbit about Proxima Centauri: Proxima b and Proxima c [4, 5]. One of these two, Proxima b, is a rocky planet in the habitable zone of Proxima Centauri, potentially bearing life. In-situ measurements of Proxima b would provide valuable information in the discussion about life formation on Proxima b and would help our understanding of life formation on rocky exoplanets. A mission to this system is thus endorsed by a strong scientific interest.

The Breakthrough Initiatives have proposed a mission to the Alpha Centauri system using photon sails: Breakthrough Starshot.[1] The aim of this project is to send a swarm of ultra-lightweight sails with gram-sized payloads to Alpha Centauri to perform a flyby of the binary system. Using a 100 GW Earth-based laser array, the sails are propelled to 20% of the speed of light, reaching the system in a little over twenty years. In References [6, 7, 8], several alternative mission scenarios are investigated. Using a futuristic graphene-based sail, the authors studied the possibility of getting captured in the binary system, to then continue towards Proxima Centauri using gravity assists. To get captured in bound orbit about Proxima Centauri, they calculated a maximum arrival speed in the Alpha Centauri A/B system of 5.7% of the speed of light. This results in a 75 years journey from Earth and an additional 46 years towards Proxima Centauri. In Reference [9], comparable results are presented for capture in the Alpha Centauri A-B system using the same sail configuration.

The research presented in this paper focuses on finding photon-sail trajectories starting from the classical colinear Lagrange points in the binary system to the classical colinear and triangular Lagrange points in the AC-C/Proxima b system. As described in previous research [10], the classical triangular Lagrange points are not suited as departure locations in the binary system, because to maintain at the classical Lagrange points, the sail should not create any acceleration. This requires an edge-on position with respect to the incoming sunlight

*Corresponding author, timrotmans@gmail.com

[1] breakthroughinitiatives.org/initiative/3, access date: 18/10/2022

Table 1: Parameters for the three stars within the Alpha Centauri system. The mass, luminosity and radius are expressed in Solar units: $m_\odot = 1.989110 * 10^{30}$ kg, $R_\odot = 6.9598 * 10^5$ km and $L_\odot = 3.854 * 10^{26}$ W [15, 16, 17].

		AC-A	AC-B	AC-C	Sun	Unit
Mass	m	1.100	0.9070	0.1230	1	$m_\odot$
Luminosity	L	1.519	0.5002	0.0015	1	$L_\odot$
Radius	R	1.230	0.8570	0.1450	1	$R_\odot$
Avg. Temperature	T	5790	5260	3040	5770	K

which is not achievable due to the binary star nature of the AC-A/AC-B system. Due to the significant eccentricity of both the AC-A/AC-B system (referred to as the departure system) and the AC-C/Proxima b system (referred to as the arrival system), the elliptic restricted three-body problem (ERTBP) is adopted as dynamical framework. Adequate connections between the two systems are sought by using a patched restricted three-body problem approximation method [11, 12, 13]. In this method, the two systems are "patched" together on a suitable Poincaré section to find a transfer.

The aim is to connect the unstable manifolds of the Lagrange points of the departure system, with the stable manifolds of the Lagrange points in the arrival system. This approach has already proved to be successful for finding transfers between Lagrange points in other photon-sail dynamical systems [13, 14]. To find a proper link between the two systems, the error between the departure and arrival segments of the trajectory at the Poincaré section is evaluated. A numerical optimization problem unfolds in which the error in position, velocity and time is minimized. Similar as in Reference [13], this work uses two techniques to solve this numerical problem. Initial knowledge of the problem is gathered by means of a design space exploration, after which a genetic algorithm is applied to further optimize the link between the systems.

2. Alpha Centauri System

As briefly mentioned in Section 1, Alpha Centauri is a triple star system located at 4.37 light-years from the Sun [15]. In Table 1, some relevant parameters of the stars in the system are given. Figure 1 gives an overview of the orbits of the different bodies in the system. Note that the orbits and the binary system and Proxima b are enlarged to clearly visualize the system. In the center of the system, stars AC-A and AC-B form a binary star system, mutually rotating around the barycenter with a period of approximately 80 years [18]. In reference [19], it is demonstrated with a high degree of confidence that the third star AC-C is in a bound orbit about the binary system. Improved orbital parameters of AC-C's orbit can be found in Reference [20]. The used data is given in the departure observer frame O_d, which is further explained in Section 3.1. AC-C orbits the binary system at approximately 13,000 AU. It is a red-dwarf star with a significantly smaller luminosity and mass than AC-A and AC-B.

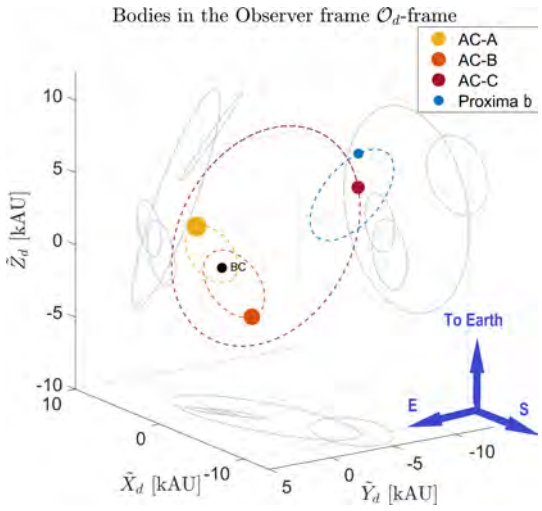

Figure 1: An overview of the positions and orbits of the three stars, including the assumed orbit of Proxima b, at reference epoch J2000. The orbit of AC-C is to scale. The orbits of AC-A and AC-B are enlarged by a factor 200. Proxima b's orbit is enlarged by a factor of 80,000.

Table 2: Orbital elements of Proxima b, AC-A and AC-B [4, 9, 21, 22, 23]. The elements for Proxima b and AC-A/AC-B are given in the observer frame O_a and O_d, respectively.

		Proxima b	AC-A	AC-B	Unit
Semi-major axis	s	0.05	10.79	12.73	AU
Eccentricity	e	0.105	0.52	0.52	-
Inclination	i	Unknown	79.32	79.32	deg
Longitude of the ascending node	Ω	Unknown	205.06	205.06	deg
Argument of periastron	Ψ	310.0	52.0	232.0	deg
Ref. time of periastron	T_0	August 2035	August 2035	August 2035	-

In present, it has been confirmed that two planets are in orbit about AC-C: Proxima b and Proxima c [21, 24]. Only the parameters of Proxima b are presented in Table 2, given in the arrival observer frame O_a, see Section 3.1, since its location and characteristics make it the most interesting of the two. Proxima b is an Earth-like, rocky planet located in the habitable zone. From the data in Table 2 it is clear that there are two unknown orbital elements: the inclination i and right ascension

of the ascending node Ω. However, it is known that Proxima b does not transit AC-C [25], therefore an inclination of close to 90 deg with the plane tangential to the line-of-sight is impossible. Thus, in this work an inclination of $i = 45$ deg is assumed. Based on values presented in [4, 21, 23], the mass of Proxima b, m_{proxb}, is assumed to be 1.3 times that of Earth's mass ($m_\oplus = 5.972 * 10^{24}$ kg).

The reference epoch t_0 used in this paper is August 2035, when AC-A and AC-B are at periastron. Since the true anomaly of Proxima b is unknown, its periastron is set to be at the reference epoch t_0. Note that the period of Proxima b is short (11.186 days), whereas transfer times of hundreds of years are considered reasonable. The assumption on the exact periastron of the arrival system is thus of minor influence on the results. The relationship between the independent variable θ_i and dimensional time t_i, is indirectly given by Kepler's equation [26].

3. Dynamical model

This section provides the dynamical model used and reference frames employed in this work.

3.1. Reference Frames

The following reference frames are used in this research (the corresponding frame transformations can be found in Reference [10]):

1. Inertial frames $\mathcal{I}_d(\mathbf{X}_d,\mathbf{Y}_d,\mathbf{Z}_d)$ (origin in the barycenter of stars AC-A and AC-B) and $\mathcal{I}_a(\mathbf{X}_a,\mathbf{Y}_a,\mathbf{Z}_a)$ (origin in the barycenter of star AC-C and planet Proxima b)
   - $\mathbf{X}_d$, $\mathbf{X}_a$ Aligned with the major axis of the elliptic orbits of the bodies concerned, positive in the direction of AC-B/Proxima b's periastron
   - $\mathbf{Z}_d$, $\mathbf{Z}_a$ Aligned with the angular velocity vector of the system, denoted as $\boldsymbol{\omega}_d$ and $\boldsymbol{\omega}_a$, respectively
   - $\mathbf{Y}_d$, $\mathbf{Y}_a$ Complete the right-handed frames
2. Observer frames $\mathcal{O}_d(\tilde{\mathbf{X}}_d, \tilde{\mathbf{Y}}_d, \tilde{\mathbf{Z}}_d)$ (origin in the barycenter of stars AC-A and AC-B) and $\mathcal{O}_a(\tilde{\mathbf{X}}_a, \tilde{\mathbf{Y}}_a, \tilde{\mathbf{Z}}_a)$ (origin in the barycenter of star AC-C and planet Proxima b)
   - $\tilde{\mathbf{X}}_d$,$\tilde{\mathbf{X}}_a$ Directed towards the intersection between a plane perpendicular to $\tilde{\mathbf{Z}}_d$ or $\tilde{\mathbf{Z}}_a$ and a line through the Celestial Poles.
   - $\tilde{\mathbf{Z}}_d$,$\tilde{\mathbf{Z}}_a$ Aligned with the vector pointing towards the Solar system barycenter
   - $\tilde{\mathbf{Y}}_d$,$\tilde{\mathbf{Y}}_a$ Complete the right-handed frames
3. Rotating pulsating barycentric frames $\mathcal{P}_d(\mathbf{x}_d,\mathbf{y}_d,\mathbf{z}_d)$ (origin in the barycenter of stars AC-A and AC-B) and $\mathcal{P}_a(\mathbf{x}_a,\mathbf{y}_a,\mathbf{z}_a)$ (origin in the barycenter of star AC-C and Proxima b)
   - $\mathbf{x}_d$,$\mathbf{x}_a$ Aligned with the line connecting the two primaries, positive in the direction of AC-B/Proxima b
   - $\mathbf{z}_d$,$\mathbf{z}_a$ Aligned with the angular velocity vector of the system, denoted as $\boldsymbol{\omega}_d$ and $\boldsymbol{\omega}_a$, respectively
   - $\mathbf{y}_d$,$\mathbf{y}_a$ Complete the right-handed frames
4. Sail-centered frames $\mathcal{S}_d(\hat{\mathbf{r}}_A,\hat{\boldsymbol{\theta}}_A,\hat{\boldsymbol{\eta}}_A)$ and $\mathcal{S}_a(\hat{\mathbf{r}}_C,\hat{\boldsymbol{\theta}}_C,\hat{\boldsymbol{\eta}}_C)$ - both with origin in the geometric center of the sail
   - $\hat{\mathbf{r}}_A$,$\hat{\mathbf{r}}_C$ Unit vector from the star (either AC-A or AC-C) to the sail
   - $\hat{\boldsymbol{\theta}}_A = \frac{\mathbf{Z}_d \times \hat{\mathbf{r}}_A}{\|\mathbf{Z}_d \times \hat{\mathbf{r}}_A\|}$, $\hat{\boldsymbol{\theta}}_C = \frac{\mathbf{Z}_a \times \hat{\mathbf{r}}_C}{\|\mathbf{Z}_a \times \hat{\mathbf{r}}_C\|}$
   - $\hat{\boldsymbol{\eta}}_A = \frac{\hat{\mathbf{r}}_A \times \hat{\boldsymbol{\theta}}_A}{\|\hat{\mathbf{r}}_A \times \hat{\boldsymbol{\theta}}_A\|}$, $\hat{\boldsymbol{\eta}}_C = \frac{\hat{\mathbf{r}}_C \times \hat{\boldsymbol{\theta}}_C}{\|\hat{\mathbf{r}}_C \times \hat{\boldsymbol{\theta}}_C\|}$
5. Galactic frames $\mathcal{G}_d(\tilde{\mathbf{x}}_d,\tilde{\mathbf{y}}_d,\tilde{\mathbf{z}}_d)$ (origin in the barycenter of stars AC-A and AC-B) and $\mathcal{G}_a(\tilde{\mathbf{x}}_a,\tilde{\mathbf{y}}_a,\tilde{\mathbf{z}}_a)$ (origin in the center of star AC-C)
   - $\tilde{\mathbf{x}}_d$,$\tilde{\mathbf{x}}_a$ Aligned with a line connecting the Sun with the center of the Milky Way
   - $\tilde{\mathbf{z}}_d$,$\tilde{\mathbf{z}}_a$ Aligned with a vector pointing towards the North Galactic Pole
   - $\tilde{\mathbf{y}}_d$,$\tilde{\mathbf{y}}_a$ Complete the right-handed frame
6. ICRS-frames $\mathcal{E}_d(\mathbf{j}_{d,1}, \mathbf{j}_{d,2}, \mathbf{j}_{d,3})$ (origin in the barycenter of stars AC-A and AC-B) and $\mathcal{E}_a(\mathbf{j}_{a,1}, \mathbf{j}_{a,2}, \mathbf{j}_{a,3})$ (origin in the center of star AC-C). Axes of these frames are defined relative to extragalactic radio sources, see Reference [27].

3.2. Photon-Sail Augmented Elliptic Restricted Three-Body Problem

Due to the large eccentricity of both the departure and arrival systems, the photon-sail augmented elliptic restricted three-body problem is employed. For the equations of motion, the models provided in References [14, 28] are followed. The independent variable is the true anomaly θ_i, where $i = a, d$, referring to variables in the arrival and departure, respectively.. The equations of motion are expressed in the pulsating rotating barycentric frame $\mathcal{P}_i$. The equations of motion are written in

dimensionless form using normalized units: the sum of the two masses as the unit of mass, the distance between the masses as the unit of length, and the inverse of the system's angular velocity $1/\omega_i$ as the unit of time. The mass parameter is introduced, $\mu_i = \frac{m_{2,i}}{(m_{1,i}+m_{2,i})}$, in which $m_{1,i}$ corresponds to the primary with the larger mass, see Table 1. In dimensionless form, the masses become $m_{1,i} = 1 - \mu_i$ and $m_{2,i} = \mu_i$ and these masses are located along the x_i-axis at a distance $-\mu_i$ and $1 - \mu_i$ from the origin, respectively. The period of both systems now becomes 2π.

To model the acceleration from the Solar radiation pressure, an ideal-sail model is used. The ideal-sail model assumes a perfectly flat, specular reflecting sail surface. This means that absorption, re-rediation, and wrinkles in the sail are neglected [29]. This assumption results in a radiation pressure force that is perpendicular to the sail surface, in the direction of the normal vector $\hat{\mathbf{n}}$. The performance of a photon sail can be expressed using its lightness number β [29]. The lightness number is a performance ratio that describes the radiation pressure acceleration relative to the gravitational acceleration of the star that emits the radiation. The relation between the Solar lightness number $\beta_\odot$ and the lightness number relative to another star depends on the mass and luminosity of the respective star [28]. This relation can be expressed as $\beta_k = \epsilon_k \beta_\odot$, with the ratio ϵ_k defined as $\epsilon_k = \frac{L_k m_\odot}{L_\odot m_k}$, see Table 1. The subscript k is used to distinguish between the three stars AC-A, AC-B and AC-C ($k = A, B, C$) The photon-pressure acceleration acting on a sail in a binary-star system is different from that in a single-star system, because in a binary system, the sail will receive radiation emitted by two stars. When considering the binary star system, Eq. 7 given in Reference [28] is used; when the sail is in the AC-C/Proxima b system, the sail acceleration is defined by Eq. 2 in Reference [14]. To potentially increase the capabilities of the sail in the binary system, both a one-sided reflective and a double-sided reflective sail acceleration model are used, as described in Reference [28]. To describe the orientation of the sail with respect to the incoming light, a normal vector $\hat{\mathbf{n}}_k$ is introduced ($k = A, B, C$). The normal vector's direction is expressed by using the cone and clock angles α_k and δ_k. The cone angle is the angle between the normal vector $\hat{\mathbf{n}}_k$ and the local $\hat{\mathbf{r}}_k$-axis. The clock angle is the angle between the $\hat{\boldsymbol{\eta}}_k$-axis and the projection of the normal vector on the plane perpendicular to vector $\hat{\mathbf{r}}_k$ (the $\hat{\boldsymbol{\theta}}_k, \hat{\boldsymbol{\eta}}_k$-plane). The cone and clock angles in the departure system are measured with respect to star AC-A and in the arrival system with respect to star AC-C.

4. Methodology

To design a photon-sail transfer trajectory between AC-A/AC-B and AC-C/Proxima b, a method based on the patched restricted three-body problem approximation [12, 13] is utilized. This section describes this method, as well as an extrapolation method to reduce the computational load associated with the trajectory propagation in the arrival phase, and a brief overview of the optimization problem. The sail configurations analyzed in this study are based on previous research [10]. Four sail configurations (indicated with number 1 to 4) are evaluated: a single-sided and double-sided sail with two different lightness numbers. The lightness numbers for configurations 1 and 2 represent a lower limit that appeared to ensure sufficient acceleration and deceleration during the departure/arrival phases ($\beta = 100$). The lightness numbers for sail configurations 3 and 4 are based on sail configurations previously studied for photon sailing in Alpha Centauri [6] ($\beta = 1779$).

4.1. Patched restricted three-body problem approximation method

The patched restricted three-body problem approximation method used in this work is based on previous studies to find photon-sail transfers between different restricted three-body problems [12, 13]. The unstable manifolds from the colinear Lagrange points in the departure system are used to initiate motion away from the AC-A/AC-B system. In the arrival system, the stable manifolds are exploited to obtain motion towards the Lagrange points. However, the L_4 and L_5-points in the arrival system are stable and do not exhibit manifolds. But, manifolds can be artificially created by exploiting the photon-sail acceleration when the sail is positioned in a non-edge one attitude, which then disrupts the stable motion around the equilibrium. Note that the location of the classical Largange points in the departure and arrival systems are given in Table 5 of Reference [10].

To add flexibility in the design of the transfers, a range of cone and clock angles is considered to create photon-sail assisted unstable and stable manifolds. A constant sail attitude is assumed along these photon-sail assisted manifolds to limit the search space (note that, from here on the addition "photon-sail assisted" is omitted for brevity). Additionally, the non-autonomous nature of the ERTBP adds another dimension to the search space through the time-dependent true anomaly θ_i, at which a trajectory departs or arrives. The resulting manifolds form tube-like structures called photon-sail dedicated sets [12].

The manifolds must then be connected in phase space and time to find a transfer trajectory. A detailed overview of the steps taken to find such transfers, using combinations of sail attitude and departure/arrival time, is given in Reference [10]. In order to evaluate the connection between the photon-sail dedicated sets in phase space, the state of the sail is propagated to a Poincaré section (surface Q). Surface Q is defined in the departure observer frame O_d. It is a section perpendicular to the line connecting the barycenter of the departure system and the barycenter of the arrival system, located exactly halfway along this line. On this surface, the state error, in terms of position, velocity, and time, is evaluated. To reach this surface, the unstable manifolds of the Lagrange points in the departure system are propagated forward in time up to surface Q. In the arrival system, the stable manifolds of the Lagrange points are propagated backwards up to surface Q. These propagations are executed with the ode45 function in Matlab® using relative and absolute tolerances of 10^{-11} and 10^{-11}, respectively The error at surface Q is calculated by comparing the state $\mathbf{x}_{f,d}$ and time $t_{f,d}$ at the end of the unstable manifold with the state $\mathbf{x}_{f,a}$ and time $t_{f,a}$ at the end of the stable manifolds. The magnitude of this error is an indication of the feasibility of the transfer trajectory between the departure and arrival systems. The aim then becomes to find a set of initial/target conditions for the sail that will result in a minimum error (i.e., successful) transfer trajectory. It must be noted that not all initial/target conditions result in a trajectory crossing surface Q. In such a case, the final state of that trajectory will automatically produce a large error, so that the corresponding initial/target conditions are not further considered.

4.2. Arrival system cut-off

A challenge lies in the computation cost associated with the propagation of the stable manifolds in the arrival phase. This computational cost arises from the short period of the arrival system (11.186 days) relative to the total transfer time, which results in the need to propagate the state of the sail over numerous system revolutions, which can be up to thousands. Contrary, the departure system, with a period of approximately 80 years, requires less computational effort. Therefore, based on the research in Reference [10], a linear state extrapolation method is used (also called "cut-off" method) to approximate the state and time of the sail at surface Q without having to propagate the entire (artificial) stable manifold. The method analytically computes the state and time at which the sail reaches surface Q based on the state and time at a predefined cut-off point.

4.3. Optimization problem

The objective of the optimization problem is to minimize the error at linkage as described in Section 4.2. The following sections will further explain the objective function, constraints, and decision variables of this optimization problem.

4.3.1. Objectives

To find a feasible transfer trajectory, three objectives (J_1, J_2 and J_3) are introduced that must be minimized. These objectives are the different errors on the surface Q: position error Δr, velocity error Δv, and time error Δt. The position and velocity errors are calculated using the Euclidean norm difference of the departure and arrival states on surface Q. The time error is calculated in days by subtracting the Julian Date at which the departure phase passes surface Q from the Julian Date at which the arrival phase passes surface Q. It is important to note that the error in sail attitude at surface Q is not considered in the optimization. This means that at surface Q, a sudden, rapid change in sail attitude is allowed. For a real-life mission scenario, the attitude rate of change might be limited and a sudden change not possible. To solve this, a transition phase could be added in between the departure and arrival phase, in which the sail is allowed to slowly change its attitude. To limit the complexity of the computation in this research, such an approach is not used. The impact of this design choice on the final trajectory and results is not expected to be significant.

4.3.2. Constraints

A first set of constraints is defined to prevent that the non-reflective side of the sail faces one of the stars. For all sail configurations these constraints are given as: $\hat{\mathbf{r}}_C \cdot \hat{\mathbf{n}}_C \geq 0$, $\hat{\mathbf{r}}_A \cdot \hat{\mathbf{n}}_A \geq 0$, and $\hat{\mathbf{r}}_B \cdot \hat{\mathbf{n}}_B \geq 0$. To simplify the problem, these constraints are only enforced while the sail remains in the respective systems (departure or arrival) until surface Q is passed. This means, for example, that while the sail trajectory is propagated in the departure system, the back of the sail is allowed to face AC-C. Similarly, in the arrival phase the back of the sail is allowed to face AC-A and AC-B.

Another set of constraints must be enforced to prevent the sail from passing one of the stars too closely. Although a significant sail acceleration can be obtained with close stellar flybys [30], the temperature of the sail can also increase to harmful levels. Therefore, a minimal distance is set to prevent the sail from heating up

too much. Based on values obtained from literature [7], a minimum safe distance of five stellar radii is used in this research: $\mathbf{r}_A > 5 \times R_A$, $\mathbf{r}_B > 5 \times R_B$, and $\mathbf{r}_C > 5 \times R_C$ (where R_k represents the radius of the respective star).

4.3.3. Decision variables

Six variables are defined to tune the trajectories and find a smooth link on surface Q. These six variables (**DV**) are the cone and clock angles during each phase (α_A,δ_A,α_C,δ_C) and the arrival/departure times (t_d and t_a):

$$\mathbf{DV} = \begin{bmatrix} \alpha_A & \alpha_C & \delta_A & \delta_C & t_d & t_a \end{bmatrix} \tag{1}$$

The bounds on the cone and clock angles during both phases are: $-90^\circ \leq \alpha_A, \alpha_C \leq 90^\circ$ and $0^\circ \leq \delta_A, \delta_C \leq 180^\circ$. As described in the introduction, this work is inspired by the Breakthrough Starshot project, which would, in a best-case scenario, launch its sails in 2036, resulting in an arrival at the Alpha Centauri system around 2056. However, it was already shown [3, 9] that to get captured in bound orbit about AC-A or AC-B, which is a necessity when starting from one of the Lagrange points, longer travel times should be expected (up to 80 years). Therefore, it is more reasonable to postpone the time of departure of the mission investigated here to a window in a more distant future. So, the bounds on the departure time from the Lagrange points are set to $01/01/2095 \leq t_d \leq 01/01/2195$. The bounds on the arrival time depend on the sail configuration since a larger lightness number will result in shorter transfer times, and thus, a different arrival window is used for each lightness number ($\beta = 100$ and $\beta = 1779$). For sail configurations 1 and 2 ($\beta = 100$), the arrival time is set to $01/01/3042 \leq t_a \leq 01/01/3122$. For sail configurations 3 and 4 ($\beta = 1779$), the arrival window is bounded as: $01/01/2330 \leq t_a \leq 01/01/2420$. Note that the search space for the departure and arrival time is slightly larger than one period of the departure system. This is intentionally chosen to investigate the impact of the true anomaly at departure, θ_d, on the transfer.

4.4. Optimization methods

In previous work [10], a design space exploration was executed, so that it is possible to limit the design space significantly and obtain initial results for a transfer between the two systems. The conclusions from that design space exploration are briefly summarized here. For sail configurations 1 and 2, using $\beta = 100$, the L_2-point appeared to be the most suitable departure location, and the L_1-point as the most suitable arrival location. For sail configurations 3 and 4, i.e., for $\beta = 1779$, the most optimal departure and arrival locations were L_2 and L_3,

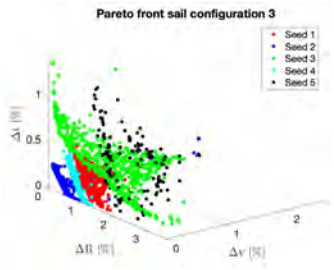

Figure 2: Results from the genetic algorithm for sail configuration 3, where the displays the Pareto front with three objectives using the relative errors.

respectively. In addition, in the current set-up, using a constant sail attitude along the manifolds, the double-sided sail proved to not add any value to solving the problem.

To solve the optimization problem defined in Section 4.3, a genetic algortihm is employed. In particular, Matlab®'s implementation of a multi-objective genetic algorithm *gamultiobj.m* is employed. Three genetic algorithm parameters are tuned to optimize the performance of the algortihm. These parameters are the population size, the number of generations, and the crossover rate. The tuning of these parameters resulted in a population size of 2000, a number of generations of 120, and a crossover fraction of 0.8. To account for the statistical nature of the algortihm, the algorithm is run for five different seeds[2] (with the Mersenne Twister random number generator in Matlab®[3],) to initialize the population. For the sake of simplicity, the seeds in this paper are referred to as seed one to five, while their true values are given in the footnote.

5. Results

This section presents the results of the optimization problem and its implementation described in Section 4. The Pareto fronts for the five different seeds for sail configuration 3 are given in Fig. 2, using relative errors. The relative errors are obtained by dividing the position error Δr by the total distance traveled, the velocity error Δv by the velocity of the sail at surface Q, and the time error Δt by the total travel time of the transfer. The results show that the genetic algorithm is able to converge to solutions that minimize all three objectives effectively. Many solutions fall within a 1-5% error

[2]Seed nrs. (conf. 1): seed 1,2,3,4,5 = [4,12,43,58,12345]. Seed nrs. (conf. 3): seed 1,2,3,4,5 = [4,14,27,55,67]

[3]https://nl.mathworks.com/help/matlab/ref/rng.html, access date 15-02-2023

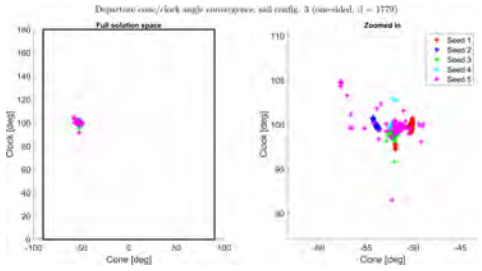

Figure 3: Departure phase: decision variable values (cone and clock angles) of the Pareto front solutions for sail configuration 3.

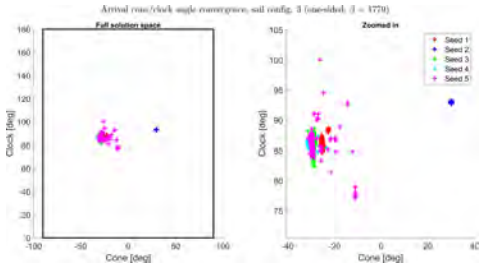

Figure 4: Arrival phase: decision variable values (cone and clock angles) of the Pareto front solutions for sail configuration 3.

margin on all three objectives, and some solutions score even below 1% on all three objectives. This means that the genetic algorithm is able to find a link on surface Q between the departure and arrival phases within reasonable error margins. However, from the Pareto fronts, it can be seen that the quality of the results varies among different seeds. For example, there is a substantial gap in the quality of the results obtained with seed 2 (best Pareto front) and seed 5 (worst Pareto front). This indicates the dependency of the genetic algorithm on the initial population and the algorithm parameter settings, which might be further improved in future research.

In Figs. 3-5, the values of the decision variables corresponding to the Pareto solutions is shown. It is important to note that, although these decision-variable values are plotted separately for the departure and arrival phases (see Figs. 3 and 4), the plots are coupled. The departure phase shows clear convergence to an optimal solution for the cone and clock angles for each seed. All five seeds show convergence to a specific area in the solution space: $-45\,\text{deg} \leq \alpha_d \leq -65\,\text{deg}$, $90\,\text{deg} \leq \delta_d \leq 110\,\text{deg}$. However, the arrival phase shows a less clear area of convergence; from Fig. 5, it can be observed that the algorithm converged to two different regions in the solution space. Only with seed 2 did the algorithm converge to the area with cone angles slightly larger than zero, whereas using the other seeds it converged to cone angles slightly smaller than

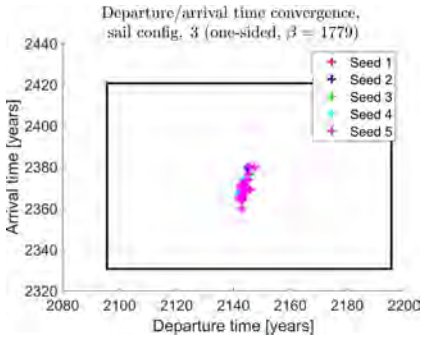

Figure 5: Decision variable values (departure/arrival times) of the Pareto front solutions for sail configuration 3.

zero. Figure 3 already showed that the Pareto front for seed 2 contains much better solutions than for the other seeds. Thus, four out of five seeds got trapped in a local minimum, and, even for seed 2, it is difficult to conclude whether it has converged to a globally optimal solution. Figure 5 shows the final values for the departure and arrival times. Most solutions are in good agreement; the five seeds converged to the same, narrow area: $2140 \leq t_d \leq 2150$, $2360 \leq t_a \leq 2380$. Since the multi-objective optimization results in a 3D Pareto front, no absolute best solution can be selected. However, since the objective is to minimize all three of them, it makes sense to look for a solution in the Pareto front closest to the origin, i.e., the solution (Δr, Δv, Δt) = (0,0,0). Subsequently, the arrival phase is fully propagated to surface Q without employing the "cut-off method" described in Section 4.2, using the initial conditions and sail attitudes corresponding to the optimal solution. This yields the true arrival conditions on the Poincaré surface Q. The resulting trajectories can be found in Reference [10], but the corresponding decision variable values and remaining errors are given in Table 3.

The transfer time found in this research for the solution with the smallest link error (i.e., 235 years for configuration 3, see Table 3) is much longer than results in the literature [7] for a similar sail configuration. In reference [7], a transfer time of 46 years from AC-A/AC-B to AC-C was found. The reason for this shorter transfer time is that, in the cited work, the departure towards AC-C is initiated with a much larger initial velocity. This larger initial velocity results from an interstellar journey at a speed equal to several percentages of the speed of light. However, for the work presented in this paper, the initial inertial velocity depends the on much smaller rotational velocity of the Lagrange points, resulting in much longer transfer times. When adding the

Table 3: Best results from the genetic algorithm for sail configurations 1 and 3. The results give the six decision variables for each phase, as well as the times at linkage $t_{Q,d}$ and $t_{Q,a}$, and link errors.

	Departure loc., arrival loc.	α_d, α_a [deg]	δ_d, δ_a [deg]	t_d, t_a [$yyyy-mm-dd$]	$t_{Q,d}$, $t_{Q,a}$ [$yyyy-mm-dd$]	Transfer time [yrs]	Δr [AU]	Δv [km/s]	Δt [$days$]
Sail conf. 1	L_2,L_1	-56.40, 5.11	98.65, 106.35	2143-02-27, 3168-09-02	2666-11-25, 2667-09-03	1025	70.32	0.236	281.52
Sail conf. 3	L_2,L_3	-53.66, 30.07	99.53, 92.93	2144-11-03, 2379-03-18	2269-03-13, 2268-10-02	235	9.13	0.761	161.08

75-80 years needed to reach AC-A/AC-B from Earth [7] to the 235 year travel time for sail configuration 3 (β = 1779, one-sided), a total mission time of approximately 320 years results. This total mission time includes some margin to maneuver to the L_2 point of the AC-A/AC-B system after the sail's interstellar journey.

6. Conclusion

In this paper, a methodology to compute transfer trajectories from the colinear Lagrange points in the Alpha Centauri A/B (AC-A/AC-B) system to all five Lagrange points of the Alpha Centauri C (AC-C)/Proxima b system has been presented. The photon-sail assisted manifolds originating from the departure Lagrange points and those arriving at the arrival Lagrange points are forwards and backwards propagated up to a suitable Poincaré section where the link errors between the manifolds in terms of position, Δr, velocity, Δv and time, Δt, are evaluated. Results were provided for two particular transfers depending on the lightness number, β, used: 1) For β = 100 from AC-A/AC-B L_2 to AC-C/Proxima b L_1; 2) For β = 1779 from AC-A/AC-B L_2 to AC/Proxima b L_3. The best result for β = 100 showed remaining link errors of: Δr = 70.32 AU, Δv = 0.236 km/s, and Δt = 281.52 days, with a total transfer time of 1025 years, departing in the year 2143 and arriving in 3168. The best result for β = 1779 showed remaining link errors of: Δr = 9.13 AU, Δv = 0.761 km/s, and Δt = 161.08 days, with a total transfer time of 235 years, starting in the year 2144 and arriving in 2379. These errors are small considering the total distance travelled and time passed until reaching the Poincaré section as well as the velocity at the Poincaré section. These results demonstrate that it is most likely possible to find transfers between the Lagrange points of the AC-A/AC-B and AC-C/Proxima b systems with the purpose of, for example, visiting Proxima b. However, starting these transfers to Proxima b from the Lagrange points in the AC-A/AC-B comes at the cost of a much longer travel time than those previously found in literature [7] where the large velocity of the sailcraft after its interstellar journey was exploited to reach Proxima b from AC-A/AC-B in only 46 years.

References

[1] N. Kameswara-Rao et al. Father j. richaud and early telescope observations in india. *Bulletin of the Astronomical Society of India*, 12:81, 1984.

[2] I. S. Glass. The discovery of the nearest star. *African Sky*, 11: 39, 2007.

[3] P. Kervella, F. Thévenin, and C. Lovis. Proxima's orbit around α Centauri. *Astronomy and Astrophysics*, 598, 2017. ISSN 14320746. doi: 10.1051/0004-6361/201629930.

[4] A. Bixel and D. Apai. Probabilistic constraints on the mass and composition of proxima b. 836(2):31, 2017. URL `https://doi.org/10.3847/2041-8213/aa5f51`.

[5] G.F. Benedict and B.E. McArthur. A moving target—revising the mass of proxima centauri c. 4(6):86, jun 2020. URL `https://doi.org/10.3847/2515-5172/ab9ca9`.

[6] R. Heller and M. Hippke. Deceleration of high-velocity interstellar photon sails into bound orbits at Alpha Centauri. *The American Astronomical Society*, 835(2), 1 2017. URL `http://dx.doi.org/10.3847/2041-8213/835/2/L32`.

[7] R. Heller, M. Hippke, and P. Kervella. Optimized Trajectories to the Nearest Stars Using Lightweight High-velocity Photon Sails. *The Astronomical Journal*, 154(3):115, 2017. ISSN 1538-3881. URL `http://dx.doi.org/10.3847/1538-3881/aa813f`.

[8] D.H. Forgan, R. Heller, and M. Hippke. Photogravimagnetic assists of light sails: A mixed blessing for Breakthrough Starshot? *Monthly Notices of the Royal Astronomical Society*, 474(3): 3212–3220, 2018. ISSN 13652966. doi: 10.1093/mnras/stx2834.

[9] F. Schoutetens. Photon-sail trajectory optimization in alpha centauri using evolutionary neurocontrol. Master's thesis, 2019. URL `http://repository.tudelft.nl/`.

[10] T. J. Rotmans. Photon-sail trajectories towards exoplanet proxima b. Master's thesis, Delft University of Technology, Delft, The Netherlands, 2023. URL `http://repository.tudelft.nl/`.

[11] H. Peng et al. Libration transfer design using patched elliptic three-body models and graphics processing units. *Journal of Guidance, Control, and Dynamics*, 40:1–12, 08 2017. doi: 10.2514/1.G002692.

[12] G. Mingotti, J. Heiligers, and C.R. McInnes. First-guess generation of solar sail interplanetary heteroclinic connections. *Advances in the Astronautical Sciences*, 153:1633–1651, 2015. ISSN 00653438.

[13] M. Vergaaij and J. Heiligers. Time-optimal solar sail heteroclinic-like connections for an earth-mars cycler. *Acta Astronautica*, 152, 08 2018. doi: 10.1016/j.actaastro.2018.08.008.

[14] J. Heiligers, G. Mingotti, and C.R. McInnes. Optimal solar sail transfers between halo orbits of different sun-planet systems. *Advances in Space Research*, 55(5):1405–1421, 2015. ISSN 18791948. doi: 10.1016/j.asr.2014.11.033.

[15] P. Kervella et al. A family portrait of the alpha centauri system, 2003. URL `https://www.eso.org/public/news/eso0307/#1`.

[16] F. Thévenin et al. Asteroseismology and calibration of alpha cen

binary system. *Astronomy and Astrophysics*, 392, 2002. doi: 10.1051/0004-6361:20021074.

[17] I.J. Sackmann, A.I. Boothroyd, and K.E. Kraemer. Our sun. iii. present and future. *The Astrophysical Journal*, 418:457–468, 1993.

[18] K. W. Kamper and A.J Wesselink. Alpha and proxima centauri. *The Astronomical Journal*, 83(12):1653–1659, 1978.

[19] P. Kervella et al. Close stellar conjunctions of tauri a and b until 2050 - an mk = 7.8 star may enter the einstein ring of en a in 2028. *Astrodynamics & Astrophysics*, 594:A107, 2016. URL `https://doi.org/10.1051/0004-6361/201629201`.

[20] R. Akeson et al. Precision millimeter astrometry of the centauri ab system. *The Astronomical Journal*, 162, 2021. URL `https://doi.org/10.3847/1538-3881/abfaff`.

[21] A. Suarez Mascareno et al. Revisiting proxima with espresso. *Astronomy Astrophysics*, 639, 2020. URL `https://doi.org/10.1051/0004-6361/202037745`.

[22] G. Anglada-Escudé et al. A terrestrial planet candidate in a temperate orbit around proxima centauri. *Nature*, 536 (7617):437–440, Aug 2016. ISSN 1476-4687. doi: 10.1038/nature19106.

[23] S.R. Kane, D.M. Gelino, and M.C. Turnbull. On the orbital inclination of proxima centauri b. 153(2):52, jan 2017. URL `https://doi.org/10.3847/1538-3881/153/2/52`.

[24] G. Fritz Benedict and Barbara E. McArthur. A preliminary mass for proxima centauri c. 4(4):46, apr 2020. URL `https://doi.org/10.3847/2515-5172/ab84f3`.

[25] E. Gilbert et al. No transits of proxima centauri planets in high-cadence tess data. *Frontiers in Astronomy and Space Sciences*, 8, 2021. doi: 10.3389/fspas.2021.769371.

[26] M. Capderou. *Satellites: Orbits and Missions*. 2005.

[27] G. Kaplan. The iau resolutions on astronomical reference systems, time scales, and earth rotation models. 2006.

[28] J. Heiligers, F. Schoutetens, and B. Dachwald. Photon-sail equilibria in the alpha centauri system. *Journal of Guidance, Control, and Dynamics*, 44(5):1053–1061, 5 2021. ISSN 1533-3884. doi: 10.2514/1.g005446.

[29] C.R. McInnes. *Solar Sailing: Technology, Dynamics, and Mission Applications*. 2 edition, 1999. ISBN 978-1-4471-3992-8. doi: 10.1007/978-1-4471-3992-8.

[30] B. Dachwald. Optimal solar-sail trajectories for missions to the outer solar system. *Journal of Guidance, Control, and Dynamics*, 28(6):1053–1061, 11 2005. doi: 10.2514/1.13301.

Long-term mission of the spacecraft with a degrading solar sail into the asteroid belt

Bakhyt N. ALIPOVA[a,**], Olga L. STARINOVA[b], Miroslav A. Rozhkov[b]

[a] *Department of Aerospace and Mechanical Engineering, University of Kentucky, Lexington KY, USA, International Information Technology University, Almaty, Kazakhstan*
[b] *Flight Dynamics and Control Theory Department, Samara national Research University, Samara, Russia*

Abstract

The Mars-Jupiter asteroid belt remains one of the least explored regions of the solar system. The use of the Solar Sail Spacecraft (SSSC) will enable a long-term mission into the asteroid belt. We propose the following ballistic scheme for the mission: (1) at the first stage, the upper stage of the launch vehicle takes the SSSC out of the Earth's action sphere and imparts to it the necessary hyperbolic excess velocity; (2) the SSSC makes an Earth-Earth flight, ending with a gravitational manoeuvre in the Earth's action sphere and entering a trajectory with an aphelion of 3.6 AU and zero inclination; then due to the use of light pressure, a circular orbit is formed with a semi-major axis of 2.9 AU; (3) at the last long stage of research, the SSSC is oriented perpendicular to the direction of the light flux and moves along a twisting spiral. At the same time, the spacecraft will fly over and study many objects of the asteroid belt. In this paper, a complete ballistic calculation of this mission is carried out for a degrading solar sail with a non-ideally reflective surface [1]. In addition, during the mission, mathematical models of the SSSC movement and degradation of its surface will be refined.

Keywords: Solar Sail Spacecraft (SSSC), asteroid belt, gravitational manoeuvre, Earth, degrading solar sail

1. Description of the ballistic scheme of the mission and the design parameters of the spacecraft

1.1. Ballistic scheme of the mission

We propose to carry out a long-functioning spacecraft mission with a solar sail to the main asteroid belt according to the following ballistic scheme. A spacecraft with a folded sail is brought out of the Earth's sphere of action onto a heliocentric flight trajectory that provides the specified parameters of a gravitational manoeuvre near the Earth due to the propulsion system of the upper stage. A year later, after performing a gravitational manoeuvre in the Earth's gravity field, the spacecraft fairing is reset and the solar sail opens. Further heliocentric movement is carried out due to light pressure and the spacecraft enters orbit, most of the time lying in the asteroid belt. The solar sail assumes a position perpendicular to the light stream, and further trajectory changes occur only due to the degradation of the sail surface, long-term studies of the asteroid belt are carried out.

1.2. Prototype spacecraft and sails

As a prototype, the solar sail of the SPACECRAFT project is used to deliver soil samples from the surface of Mercury to Earth [2]. The main design parameters of the spacecraft under consideration are given in Table 1, and its mass characteristics in Table 2. According to the calculations of the authors [2], a frame-type solar sail delivered by a Japanese H-2A launch vehicle with an excess of speed to reach a heliocentric trajectory will be able to give a payload weighing 1905 kg an acceleration of 0.25 * 10-3 m/s^2. Fig. 1 shows the placement of this spacecraft under the fairing of the H-IIA launch vehicle.

Table 1. Design parameters of the spacecraft [4]

Weight of the device, kg	Payload weight, kg	The mass of the solar sail, kg	Sail shape, m	Acceleration, m/s^2	Sail thickness,mkm	
					Polyimide CP1	Aluminum
2353	1905	448	275x275	$0.25 \cdot 10^{-3}$	2	0.1

* Corresponding author, alipova.bakhyt@gmail.com

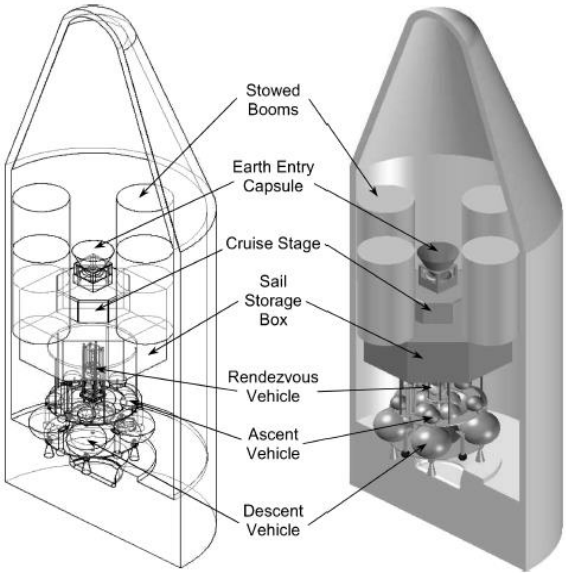

Fig. 1. Placement of a spacecraft with a solar sail delivering soil from the surface of Mercury under the fairing of the H-IIA launch vehicle [2].

Table 2. Mass characteristics of the solar sail for the delivery of Mercury soil

Element Description	Weight, kg
Payload weight of the sail	1905
The bearing film of the CP1 sail is 2 mkm	216
Aluminum reflective coating with a thickness of 0.1 mkm	41
Binding coating	26
Frame beams sails	54
Mechanical deployment and management systems	111
Total mass of solar sail assembly	448
Initial mass of the spacecraft	2353

The dimensions of the solar sail of such a space transport system is 275 by 275 m, which forms a sail area of 75625 m^2 and provides a characteristic acceleration of 0.25 mm/s^2during the flight from Earth to Mercury and 0.78 mm/s^2 on the way back, since the descent compartment and docking mechanisms are discarded at Mercury. The energy characteristics of the Japanese H-IIA 202-4S launch vehicle, with the reference of which the device was designed, make it possible to put up to 2,600 kg of payload into a parabolic orbit out of the Earth's sphere of action (11.2 km/s). This project demonstrates the possibilities of creating space transport systems with a solar sail capable of transporting a payload of about 2 tons between planets.

We chose a lighter spacecraft weighing 500 kg for our calculations, since it is intended for research, not for payload delivery. In this case, the sail area can also be reduced to 16070 m^2. The remaining parameters of the spacecraft under consideration are presented in Table 3.

Table 3. Parameters of the selected spacecraft

Design parameters of the device		Meaning
Initial mass of the spacecraft, kg		500
Sail area, m2		16070
Reflection Coefficient (Al)		0,777
Specular Reflection Factor (Al)		0,900
Secondary radiation coefficient	Al	0,540
	Cr	0,540
Non-Lambert coefficient	Al	0,790
	Cr	0,550

2. The mathematical model used for the motion of a spacecraft with a solar sail

2.1. Mathematical model of motion

The following assumptions are used to describe the motion of the spacecraft:

- the motion of the spacecraft in the plane of the ecliptic is considered, the orbits of the planets are considered circular;

gravitational or other disturbances from any celestial objects are not taken into account;

- the intensity of the Sun's radiation varies inversely proportional to the square of the distance and does not change with time (does not depend on solar activity).

The system of differential equations of motion is described in a flat polar coordinate system in a dimensionless form:

$$\frac{dr}{dt} = V_r, \qquad \frac{dV_r}{dt} = a_r(r, \lambda_1, t) - \frac{1}{r^2} + \frac{V_u^2}{r},$$
$$\frac{du}{dt} = \frac{V_u}{r}, \qquad \frac{dV_u}{dt} = a_u(r, \lambda_1, t) - \frac{V_r V_u}{r} \tag{1}$$

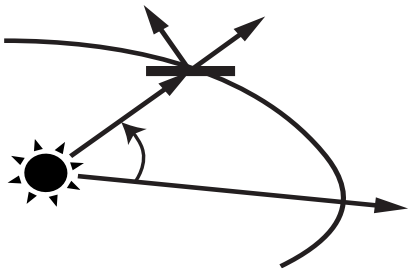

Fig. 2. Polar plane heliocentric coordinate system

Here r, u are the coordinates of the apparatus (radius vector and latitude argument), V_r, V_u are the radial and transversal components of the velocity vector, a_r, a_u are the projections of acceleration generated by the solar sail, the magnitude of which depends on the distance to the Sun r and the angle of the sail λ_1. The coordinates and directions of the vectors are shown in Fig. 2.

In the system of Eq. 1, the phase coordinates of the spacecraft are related to the average radius of the Earth's orbit around the Sun, the average circular velocity and the centripetal acceleration of the Earth. The latitude argument is counted counterclockwise from the axis of the polar coordinate system, which begins at the center of mass of the Sun and is directed towards the point of the vernal equinox.

The boundary conditions correspond to the achievement of the spacecraft target orbit and have the form

$$t = T, \qquad r = r_t, \quad V_r = V_{r_t}, \qquad V_u = V_{u_t}, \tag{2}$$

where T is the duration of the flight, r_t, V_{r_t}, V_{u_t} are the heliocentric radius and velocity components in the target orbit, which depend on the angle of the true anomaly at the final moment of time.

2.2. *Acceleration from an imperfectly reflective degrading solar sail*

The acceleration of a spacecraft with a flat imperfectly reflecting sail from the light pressure is the sum of two components: directed along the normal to the surface of the sail ($a_\perp$) and parallel to the surface of the sail in a plane passing through the radius vector ($a_{||}$) [3].

$$a_\perp = \frac{S_r}{cm} S \cdot cos\,\theta \cdot (a_1 \cos\theta + a_2) \tag{3}$$

$$a_{||} = \frac{S_r}{cm} S \cdot cos\,\theta \cdot a_3 \sin\theta \tag{4}$$

$$a_1 = 1 + \varsigma\rho,$$

$$a_2 = B_f(1-\varsigma)\rho + (1-\rho)\frac{\varepsilon_f B_f - \varepsilon_b B_b}{\varepsilon_f + \varepsilon_b},$$

$$a_3 = 1 - \varsigma\rho, \tag{5}$$

where S_r - is the power of the solar electromagnetic wave incident on a unit surface of a sail located at a heliocentric distance r; c - the speed of light; m - the mass of the spacecraft; S - surface area of the sail; θ - the angle between the direction to the Sun and the normal to the surface of the sail (installation angle); ρ - reflection coefficient; ς - the mirror reflection factor of the sail surface; ε_f, ε_b - the radiation coefficients of the front and rear surfaces of the sail; B_f, B_b - are non-Lambert coefficients of the front and rear surfaces of the sail, which describe the angular distribution of emitted and diffusely reflected photons. For the front, reflective surface of a solar sail, well-reflecting aluminium or beryllium are usually chosen. For the rear surface, on the contrary, a well-radiating chrome is chosen (to maintain a moderate sail temperature). The power of the solar electromagnetic wave varies inversely-proportional to the square of the heliocentric distance:

$$S_r = S_0 \left(\frac{r_0}{r}\right)^2, \tag{6}$$

where $S_0 = 1{,}36 \cdot 10^3$ Вт/м^2 – solar constant (the intensity of the Sun's radiation in the Earth's orbit): $r_0 = 1$ a.e.$= 1{,}496 \cdot 10^8$ km - is the average distance from the Earth to the Sun.

An imperfect reflection from the surface of the sail leads to several negative effects.

Firstly, it is a decrease in the magnitude of acceleration from the forces of light pressure

$$a = \frac{S_r}{cm} S \cos\theta \sqrt{1 + 2\varsigma\rho\cos 2\theta + (\varsigma\rho)^2 + 2a_2(1+\varsigma\rho)\cos\theta + {a_2}^2} \tag{7}$$

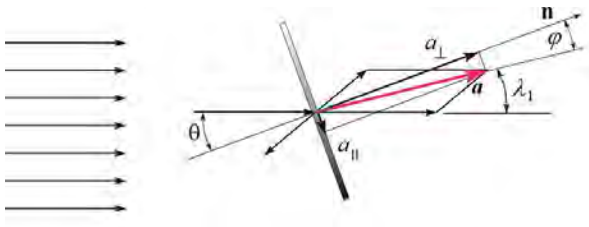

Fig. 3. Magnitude and direction of acceleration

and the deviation of the thrust created by the sail from the direction of the normal to the surface of the sail by an angle φ at Fig. 3.

$$tg\varphi = \frac{a_{||}}{a_\perp} = \frac{a_3 \sin\theta}{a_1 \cos\theta + a_2} = \frac{(1-\varsigma\rho)\sin\theta}{(1+\varsigma\rho)\cos\theta + a_2} \tag{8}$$

If we do not take into account the processes of secondary radiation and diffuse reflection from the surface of the sail, then the formulas at Eq. 3, Eq. 4, Eq. 7, Eq. 8 for the thrust from the forces of light pressure and the deviation of the thrust direction from the normal to the surface can be simplified and presented in the following form:

$$a = \frac{S_r}{cm} S(\theta)\sqrt{1 + \rho^2 - 2\rho\cos(\pi - 2\theta)} = \frac{S_r}{cm} S\cos\theta\sqrt{1 + \rho^2 + 2\rho\cos 2\theta}, \tag{9}$$

$$\sin\varphi = \frac{(1-\rho)\sin\theta}{\sqrt{1+\rho^2+2\rho\cos 2\theta}}. \tag{10}$$

Other negative impacts include a narrowing of the range of available acceleration angles relative to the

direction of the luminous flux and an increase in the share of absorbed energy of the luminous flux, which leads to an increase in surface temperature and acceleration of degradation processes of the sail surface.

2.3. *Degradation of optical parameters of the sail surface*

The surface of the sail degrades due to the impact of various factors of outer space. In particular, the reflection coefficient decreases, and the proportion of absorbed radiation increases accordingly. If only solar radiation is taken into account, then the change in optical characteristics can be calculated by the parametric dependencies proposed in [4]:

$$\frac{p(t)}{p_0} = \begin{cases} \frac{1+de^{-\lambda\Sigma(t)}}{1+d} & for\ p \in \{\rho, \varsigma\}, \\ 1 + d\left(1 - e^{-\lambda\Sigma(t)}\right) & for\ p = \varepsilon_f, \\ 1 & for\ p \in \{\varepsilon_b, B_f, B_b\}, \end{cases} \quad (11)$$

where $\Sigma(t)$ – the dimensionless total dose of solar radiation received during the flight; λ - degradation coefficient; d - degradation factor. The dimensionless total dose of solar radiation is calculated as the ratio of the total radiation power received by the sail during the flight to the solar radiation power received by a platform of 1 m^2 at a distance of 1 AU in one year $\tilde{\Sigma}_0 = 15{,}768 \cdot 10^{12}$ J/m^2.

$$\Sigma(t) = \frac{\tilde{\Sigma}(t)}{\tilde{\Sigma}_0} = \frac{r_0^2}{T_0}\int_{t_0}^{t} \frac{\cos\theta(t)}{r(t)^2}\,dt \quad (12)$$

where $T_0 = 365 \cdot 24 \cdot 3600$ s – corresponds to one year in seconds.

The degradation coefficient λ is determined based on half the lifetime of the sail under the influence of solar radiation:

$$\lambda = \frac{ln\,2}{\hat{\Sigma}}. \quad (13)$$

where $\hat{\Sigma}$ - the dose of solar radiation, which leads to a half deterioration of optical characteristics, that is, corresponds to the value of the optical characteristic

$$\hat{p} = \frac{p_0 + p_\infty}{2}.$$

The degradation factor d determines the value of the optical characteristic p_∞, at which the sail should stop functioning. At the same time

$$\rho_\infty = \frac{\rho_0}{1+d}, \qquad \varsigma_\infty = \frac{\varsigma_0}{1+d}, \qquad \varepsilon_{f\infty} = \varepsilon_{f0}(1+d) \quad (14)$$

Even a preliminary analysis of formulas at Eq.11. – 14. shows that the acceleration from the solar sail, and, consequently, the laws of sail control and the corresponding trajectories of motion depend on the optical characteristics of the surface, and the optical characteristics, in turn, depend on the laws of control and flight path. Therefore, a comprehensive analysis of possible interplanetary missions of spacecraft with a solar sail requires taking into account all these interrelated parameters.

3. Solar sail control on the flight sections

3.1. *Earth-to-Earth flight and gravity manoeuvre*

As we have already mentioned, the entire mission is calculated on the assumption that the trajectory of the spacecraft lies in the plane of the ecliptic and the Earth's orbit is circular. If we consider the passive motion of the spacecraft after leaving the Earth's sphere of action in an orbit with a large semi-axis of 1 AU, then the next meeting of the spacecraft and the Earth will occur in a year. In this case, the variable parameters are the eccentricity of the Earth-to-Earth flight orbit and the radius of the pericentre of the geocentric hyperbola along which the spacecraft will move when performing a gravitational manoeuvre.

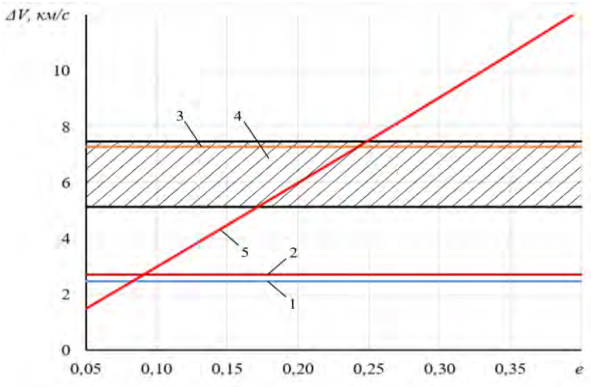

Fig. 4. Graph of the dependence of the required velocity on the eccentricity of the transition orbit. 1 – Venus, 2 – Mars, 3 – Mercury, 4 – Asteroid belt, 5 –the cost of speed to create an Earth-Earth orbit with a given eccentricity

Let's consider the effectiveness of using a gravitational manoeuvre for flights to various objects of the Solar System as in Fig. 4. To do this, compare the costs of the characteristic velocity to reach objects of the Solar System (horizontal lines) and to create a transition orbit with a given eccentricity (inclined line). For example, for a flight to Venus, only with values of eccentricities less than 0.08 – 0.09 we can expend less energy than with a single-pulse manoeuvre. For the flight we are considering to the asteroid belt, the eccentricity of the transition orbit should not be greater

than 0.264. Otherwise, it is easier to launch the spacecraft directly into the asteroid belt without using gravitational manoeuvres and a solar sail.

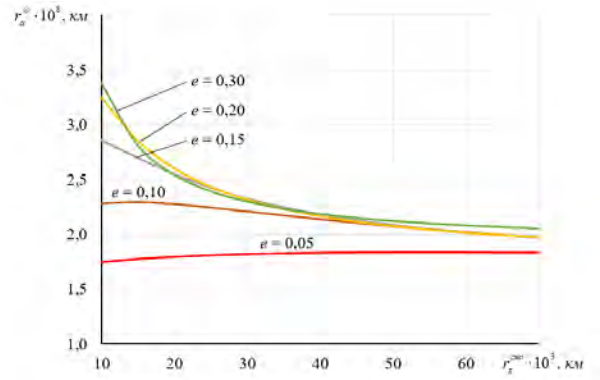

Fig. 5. Graph of the dependence of the aphelion of the resulting orbit on the geocentric perigee and the eccentricity of the transition

Fig.5 shows the aphelion radii of the spacecraft's passive orbits achievable after performing a gravitational manoeuvre. For eccentricities of transition orbits greater than 0.15, the highest aphelion value is achieved at the smallest radii of the pericenter of geocentric orbits. We will use in further calculations a safe distance from the center of the Earth of 10 thousand km and we will get that with the selected eccentricity of the orbit, the maximum value of aphelion 2.27 AU is achieved with the eccentricity of the heliocentric orbit after performing a gravitational manoeuvre 0.41506 and a large semi-axis 1.70958 AU.

During the calculations, we considered the duration of the movement of the section of the geocentric trajectory to change the position and speed of the Earth at the time of completion of the manoeuvre.

3.2. Heliocentric motion control after performing a gravity manoeuvre

In the system of equations of motion Eq. (1), the acceleration from the solar sail $\boldsymbol{a}$ has two projections, radial a_r and transversal a_u, the direction of which is shown in Fig. 5, and their scalar value can be determined using the acceleration projections calculated by Eq. 3, Eq. 4:

$$a_r = a_\perp \cos\theta + a_{||}|\sin\theta| = a_\perp \cos(\lambda_1 + \varphi) + a_{||}|\sin(\lambda_1 + \varphi)|, \quad (15)$$

$$a_u = a_\perp \sin\theta - a_{||}\cos\theta \cdot sign(\theta) = a_\perp \sin(\lambda_1 + \varphi) - a_{||}\cos(\lambda_1 + \varphi) \cdot sign(\lambda_1 + \varphi) \quad (16)$$

We will look for the law of changing the angle of the sail $\lambda_1 \in \left[-\frac{\pi}{2}; \frac{\pi}{2}\right]$, such that it reaches the required orbit as soon as possible, that is, the boundary conditions in Eq. 2 are met and the minimum functionality is provided by

$$T = \int_0^T dt \to \min. \quad (17)$$

To solve this problem, we write down the Hamiltonian:

$$H = P_r \cdot V_r + P_u \cdot \frac{V_u}{r} + P_{V_r}\left(\frac{V_u^2}{r} - \frac{1}{r^2} + \frac{a_c}{r^2}cos^3\,\lambda_1\right) + P_{V_u}\left(-\frac{V_u V_r}{r} + \frac{a_c}{r^2}cos^2\,\lambda_1\,sin\,\lambda_1\right)$$

$$\mathrm{H} = V_r\psi_r + \frac{V_u}{r}\psi_u + \left(a_c\frac{cos^3\,\theta}{r^2} - - \frac{1}{r^2} + \frac{V_u^2}{r}\right)\psi_{Vr} + \left(a_c\frac{cos^2\,\theta\,sin\,\theta}{r^2} - - \frac{V_u V_r}{r}\right)\psi_{Vu}, \quad (18)$$

where P_r, P_u, P_{V_r}, P_{V_u} – conjugate variables, a_c – nominal maximum acceleration acting on the sail at a distance of 1 AU.

According to the Pontryagin maximum principle, the control law and the corresponding trajectory of the device will be optimal if the value of the Hamiltonian is maximal. The control providing the maximum of the Hamiltonian is known [5]:

$$\lambda_1 = \frac{1}{2}\left(\eta - arcsin\frac{P_{V_u}}{\sqrt[3]{{P_{V_r}}^2 + {P_{V_u}}^2}}\right), \quad (19)$$

where $\eta = arccos\frac{P_{V_r}}{\sqrt{{P_{V_r}}^2 + {P_{V_u}}^2}}$.

The next step to determine optimal control is to solve a two-point boundary value problem. The system of equations in Eq. 1 is supplemented by differential equations describing the change of conjugate variables:

$$\frac{dP_r}{dt} = P_{V_r}\left(\frac{{V_u}^2}{r^2} - \frac{2}{r^3}\right) - P_{V_u}\frac{V_r V_u}{r^2} + \frac{2a_c}{r^3}cos^3\,\lambda_1,$$

$$\frac{dP_u}{dt} = 0 \Rightarrow \quad P_u \equiv const,$$

$$\frac{dP_{V_r}}{dt} = -P_r + P_{V_u}\frac{V_u}{r},$$

$$\frac{dP_{V_u}}{dt} = \frac{P_{V_u}V_r - 2P_{V_r}V_u}{r}. \quad (20)$$

If the angular range of the flight is not fixed, then the problem of finding optimal control is reduced to a three-parameter boundary value problem in which it is necessary to find such initial values of conjugate

variables that would ensure the fulfillment of boundary conditions in Eq. 2.

3 The results obtained during the simulation

The energy capabilities of the launch vehicle make it possible to launch the spacecraft on a departure trajectory with an eccentricity of the transition orbit of 0.264. The parameters of the passive motion of the spacecraft from the moment of leaving the Earth's sphere of action before performing a gravitational manoeuvre and after it are presented in Table 4.

Table 4 – Parameters of the heliocentric orbit of the spacecraft before the deployment of the solar sail

	Intermediate Earth-Earth orbit	Orbit after gravitational manoeuvre
Big half-axis, million km	149.6	255.75273
Eccentricity	0.264	0.41506
The angle of the true anomaly, deg	105.308	37.233
Radial component of the spacecraft velocity, km/s	7.863	4.802
Transversal component of the spacecraft velocity, km/s	28.728	34.631

After performing the gravitational manoeuvre, the solar sail unfolds, and further movement is carried out with the optimal angle of the sail installation. Fig. 6 - 7 show the optimal change in the angle of installation of the solar sail and the change in the parameters of the flight path after the gravitational manoeuvre.

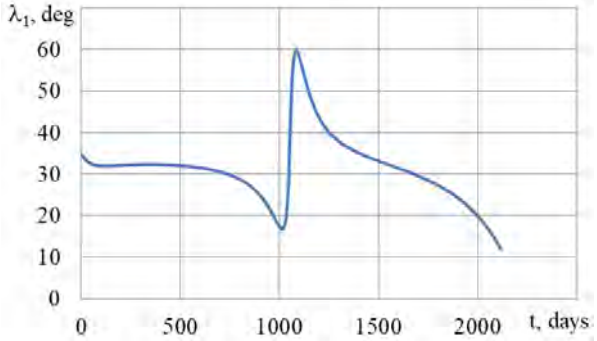

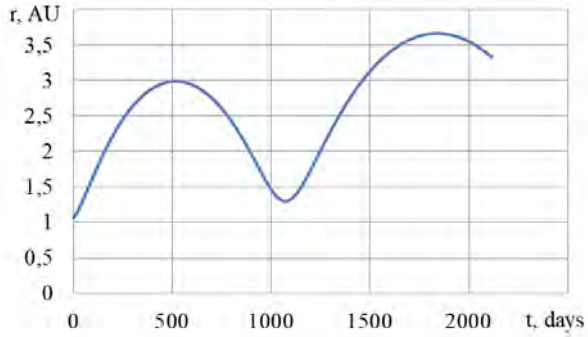

Fig. 6. Changing the angle of the sail and the radius vector of the spacecraft

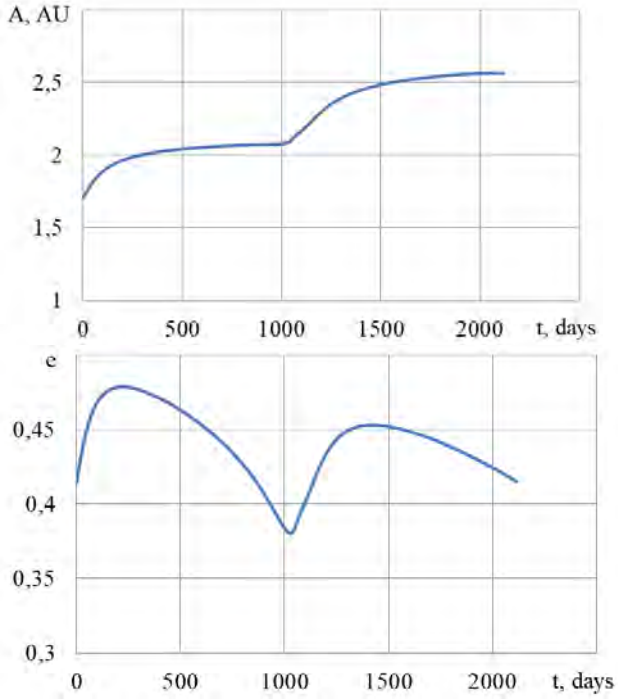

Fig. 7. Change in the semimajor axis and eccentricity of the spacecraft orbit

The duration of the spacecraft's movement to the asteroid belt is 2116.08 days. or about 5.8 years. Considering the passive motion of the spacecraft before the gravitational manoeuvre, the total duration of launching the spacecraft into a working orbit is 6.8 years. Further operation is limited by the service life of scientific devices and power plants.

Fig. 8. shows the full ballistic scheme of the mission, calculated taking into account the degradation of the surface for a sail with an imperfectly reflective surface.

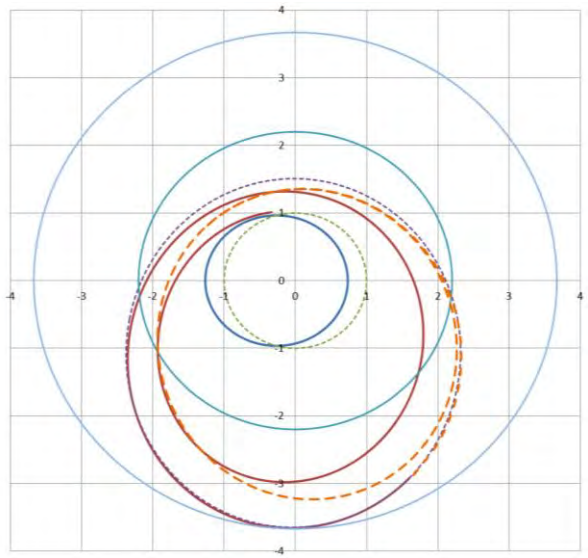

Fig. 8. Full ballistic scheme of spacecraft movement

Fig. 8. shows the trajectory of a spacecraft with a folded sail along an intermediate heliocentric trajectory that provides the specified parameters of a gravitational manoeuvre near the Earth. A year later, after performing a gravitational manoeuvre in the Earth's gravity field, the spacecraft fairing is reset and the solar sail opens. Further heliocentric movement is carried out due to light pressure (dark red fat shedding in Fig. 8). The spacecraft makes a transition to an orbit with an apocenter of 3.6 AU and a pericentre of 1.5 AU, that is, it enters an orbit most of the time lying in the asteroid belt (shown by the purple dotted line). Further changes in the trajectory due to the degradation of the sail are shown by an orange dotted line.

References

[1] Rozhkov, Miroslav A., Olga L. Starinova, and Irina V. Chernyakina, Influence of optical parameters on a solar sail motion, Advances in Space Research 67.9, 2757-2766, 2021

[2] Hughes G.W., Macdonald M., McInnes C.R., и др. Sample return from mercury and other terrestrial planets using solar sail propulsion. Journal of Spacecraft and Rockets. 2006. Т. 43, № 4. С. 828–835.

[3] Forward R.L. Grey solar sails. Journal of the Astronautical Sciences. 1989. Т. 38, № 2. С. 161–185.

[4] Dachwald B., Macdonald M., McInnes C.R., and others. Impact of optical degradation on solar sail mission performance. Journal of Spacecraft and Rockets. 2007. Т. 44, № 4. С. 740–749.

[5] Zhukov A.N., Lebedev V.N. Variational problem of a flight between heliocentric circular orbits using a solar sail. Space Research. 1964, vol. 2, no. 1, pp. 46–50.

Blended Locally-Optimal Control Laws for Space Debris Removal in LEO Using a Solar Sail

Christian Bianchi[a,b,*], Lorenzo Niccolai[b], Giovanni Mengali[b], Matteo Ceriotti[a]

[a] *James Watt School of Engineering, University of Glasgow, Glasgow, United Kingdom*
[b] *Department of Civil and Industrial Engineering, University of Pisa, Pisa, Italy*

Abstract

This paper proposes a preliminary design for a space debris removal mission in low Earth orbit that makes use of a solar sail as a chaser satellite to reach, capture and de-orbit a debris object. The sail employs solar radiation pressure as the main source of thrust, and it is also subjected to the effects of the aerodynamic forces, the oblateness of the Earth, as well as the occurrence of eclipses. Locally-optimal laws are used to control the transfer with the aim of maximizing (or minimizing) the rate of change of a specific orbital element or a suitable linear combination of them, depending on the phase of the transfer. When blended control laws are used to target the debris, optimal weighing factors are derived through a genetic algorithm to assess the relative importance of each orbital element. Numerical simulations show the effectiveness of locally-optimal laws in driving the sail towards the target even in the presence of the aforementioned orbital perturbations. In a test-case scenario, the sail, departing from 600 km of altitude, is able to reach the debris' orbit at 1200 km of height in less than 200 days with good accuracy for a preliminary study.

Keywords: Solar sail, Space debris, Locally-optimal control laws

1. Introduction

The increasing number of space debris objects in low Earth orbit poses a threat to operative satellites and might soon lead to the overcrowding of this orbital slot that would result in a much higher risk of collisions [1]. Several strategies to remove these objects have been proposed and investigated in the literature, such as passive de-orbiting that exploits natural perturbations (e.g., aerodynamic forces, solar radiation pressure) and drag-augmentation devices [2, 3, 4, 5, 6, 7, 8].

On the other hand, active removal strategies usually involve the use of a chaser satellite that can capture the debris and de-orbit it. These techniques are needed for larger objects, for which a controlled re-entry might be necessary, or objects located at higher altitudes where natural perturbations have little or no effect [9, 10].

Active strategies might also be employed for multiple debris removal missions, where a single spacecraft can dispose of more debris objects, thus drastically reducing the cost of the mission [11, 12, 13].

Most of these proposed strategies make use of conventional propulsion systems such as chemical or electric thrusters, that would constrain the mission duration to the limited amount of propellant that can be carried on board. Besides, chemical propellants also represent a very high percentage of the spacecraft mass, which results in a much higher cost of the launch.

The use of propellantless propulsion systems, such as solar sails, might represent a viable option for space debris removal missions around the Earth. Kelly and Bevilacqua [14, 15] analyzed minimum-time solar sail transfers to remove debris in geostationary orbit where the effect of the aerodynamic forces is negligible.

The aim of this paper is to investigate a single debris removal strategy in LEO that makes use of a solar sail to reach the debris' orbit, capture the object, and bring it down to a lower altitude where it can re-enter and burn into the atmosphere thanks to the aerodynamic forces. The advantage of using a solar sail lies in the fact that no propellant must be carried on board, which drastically reduces the spacecraft mass and the cost of launch.

In addition to the effect of the solar radiation pressure as the main source of thrust, the dynamical model used in this work considers also the natural perturbations present in low Earth orbits, such as the aerodynamic forces and the gravitational perturbation caused by the oblateness of the Earth. The presence of eclipses

*Corresponding author, christian.bianchi@phd.unipi.it

is also considered assuming that the Earth casts a cylindrical shadow.

The manuscript is organized as follows. Section 2 describes in detail the dynamical model used in this study, the equations of motion to propagate the sail trajectory, and all the perturbing accelerations acting on the spacecraft. In Section 3, the transfer model is introduced, and each phase is thoroughly described, together with the locally-optimal control laws used to optimize the trajectory. The results of the numerical simulations are shown and analyzed in Section 4 for each phase of the transfer. Finally, Section 5 draws the conclusions of this work and lays the foundations for further developments.

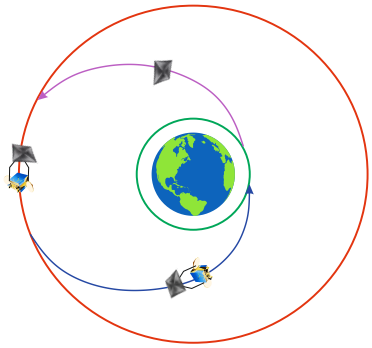

Figure 1: Simple scheme of the mission scenario. The sail departs from a circular parking orbit (green) to reach the target's orbit (red). After phasing, rendezvous and capture of the debris, the sail brings it down to a lower altitude.

2. Dynamical model

The dynamical model used in this work takes into account the presence of orbital perturbations such as the oblateness of the Earth through the J_2 coefficient, the atmospheric drag and lift acting upon the sail, as well as the solar radiation pressure (SRP) as the main source of thrust. To avoid singularities in presence of circular orbits, the spacecraft dynamics is described by means of a set of modified equinoctial orbital elements (MEOEs) [16, 17]

$$\begin{aligned} p &= a\,(1-e^2) \\ f &= e\,\cos(\Omega+\omega)\,, \quad g = e\,\sin(\Omega+\omega) \\ h &= \tan(i/2)\,\cos(\Omega)\,, \quad k = \tan(i/2)\,\sin(\Omega) \\ L &= \Omega+\omega+\nu \end{aligned} \tag{1}$$

The equations of motion in terms of MEOEs can be written in vector form as [18]

$$\dot{\boldsymbol{x}} = \mathbb{A}(\boldsymbol{x})\,\boldsymbol{a} + \boldsymbol{b}(\boldsymbol{x}) \tag{2}$$

where $\boldsymbol{x} = [p,\ f,\ g,\ h,\ k,\ L]^{\mathrm{T}}$ is the spacecraft state vector.

The coefficients of the matrix $\mathbb{A} \in \mathbb{R}^{6\times 6}$ are

$$\begin{aligned} A_{1,2} &= \frac{2p}{q}\sqrt{\frac{p}{\mu}}\,, \quad A_{2,1} = \sqrt{\frac{p}{\mu}}\sin L \\ A_{2,2} &= \sqrt{\frac{p}{\mu}}\frac{1}{q}\{(q+1)\cos L + f\} \\ A_{2,3} &= -\sqrt{\frac{p}{\mu}}\frac{g}{q}\{h\sin L - k\cos L\} \\ A_{3,1} &= -\sqrt{\frac{p}{\mu}}\cos L \\ A_{3,2} &= \sqrt{\frac{p}{\mu}}\frac{1}{q}\{(q+1)\sin L + g\} \\ A_{3,3} &= \sqrt{\frac{p}{\mu}}\frac{f}{q}\{h\sin L - k\cos L\} \\ A_{4,3} &= \sqrt{\frac{p}{\mu}}\frac{s^2\cos L}{2q}\,, \quad A_{5,3} = \sqrt{\frac{p}{\mu}}\frac{s^2\sin L}{2q} \\ A_{6,3} &= \sqrt{\frac{p}{\mu}}\frac{1}{q}\{h\sin L - k\cos L\} \end{aligned} \tag{3}$$

while the remaining ones are all zero.

The vector $\boldsymbol{b}$ is simply

$$\boldsymbol{b} = \left[0 \quad 0 \quad 0 \quad 0 \quad 0 \quad \sqrt{\mu p}\,\left(\frac{q}{p}\right)^2\right]^{\mathrm{T}} \tag{4}$$

where $q = 1 + f\cos L + g\sin L$ and $s^2 = 1 + h^2 + k^2$.

The term $\boldsymbol{a}$ is the vector of perturbing accelerations expressed in the Radial-Transversal-Normal (RTN) reference frame $\mathcal{T}_{\mathrm{RTN}}$, whose different contributions are explained in detail in the following subsections.

2.1. Solar radiation pressure

In this study, an ideal force model is used to express the thrust generated by the solar sail [19], which is therefore assumed to be a flat and perfectly reflecting surface, able to generate a propulsive acceleration given by

$$\boldsymbol{a}_{\mathrm{SRP}} = \eta\, a_c\, \cos^2\alpha\, \hat{\boldsymbol{n}} \tag{5}$$

where $\eta = \{0, 1\}$ is the shadow factor that models the occurrence of eclipses, a_c is the sail characteristic acceleration, $\hat{\boldsymbol{n}}$ is the unit vector perpendicular to the sail plane, and $\alpha \in [0,\ \pi/2]$ is the sail cone angle between $\hat{\boldsymbol{n}}$ and the Sun-sail direction. In this work, the dependence of the SRP on the distance from the Sun is neglected due to the small eccentricity of Earth's orbit. In accordance with Carzana et al. [20], introduce a sail-centered Sun-light reference frame $\mathcal{T}_S$, whose $\hat{\boldsymbol{x}}_S$ axis coincides with

the instantaneous Sun-sail vector, $\hat{\boldsymbol{y}}_{\mathrm{S}} = \hat{\boldsymbol{z}}_{\mathrm{I}} \times \hat{\boldsymbol{x}}_{\mathrm{S}}$ (where $\hat{\boldsymbol{z}}_{\mathrm{I}}$ is the third axis of a Geocentric-Equatorial reference frame) and $\hat{\boldsymbol{z}}_{\mathrm{S}}$ completes the right-handed frame (see Fig. 2). The unit vector $\hat{\boldsymbol{n}}$ expressed in the Sunlight reference frame $\mathcal{T}_S$ is

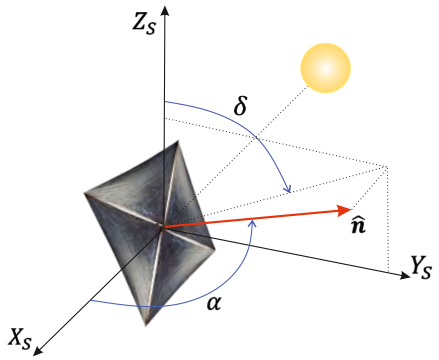

Figure 2: Cone ($\alpha \in [0, \pi/2]$) and clock ($\delta \in [0, 2\pi]$) angles that define the orientation of the sail normal unit vector $\hat{\boldsymbol{n}}$ with respect to the Sunlight reference frame $\mathcal{T}_S$.

$$[\hat{\boldsymbol{n}}]_{\mathrm{S}} = [\cos\alpha \quad \sin\alpha\,\sin\delta \quad \sin\alpha\,\cos\delta]^{\mathrm{T}} \tag{6}$$

which must be transformed into the RTN reference frame $\mathcal{T}_{\mathrm{RTN}}$ by means of the transformation matrix $\mathbb{R}_{\mathrm{S}\to\mathrm{RTN}}$ which depends on the sail state and the Sun's position.

2.2. Atmospheric drag and lift

When the sail orbits through the Earth's atmosphere, it experiences aerodynamics forces (drag and lift) that can be modelled assuming the sail to be a flat plate. Moreover, in agreement with Refs. [20, 21], a hyperthermal free-molecular flow is considered, which means that the spacecraft velocity is much larger than the thermal velocity of the atmospheric particles [22].

Under these assumptions, the drag and lift accelerations can be expressed as

$$\boldsymbol{a}_{\mathrm{D}} = -\frac{1}{2}\frac{\rho v^2}{\sigma} C_D\, \hat{\boldsymbol{v}} \tag{7}$$

$$\boldsymbol{a}_{\mathrm{L}} = \frac{1}{2}\frac{\rho v^2}{\sigma} C_L\, \hat{\boldsymbol{L}} \tag{8}$$

where ρ is the atmospheric density provided by the MATLAB built-in function *atmosnrlmsise00* based on the NRLMSISE-00 model [23], v and $\hat{\boldsymbol{v}}$ are the sail velocity magnitude and direction, respectively, and σ is the sail loading, defined as the ratio of the total mass to the sail area. The unit vector $\hat{\boldsymbol{L}}$, which identifies the lift orientation, can be computed as [24]

$$\hat{\boldsymbol{L}} = \mathrm{sign}\left(\hat{\boldsymbol{v}} \cdot \hat{\boldsymbol{n}}\right)\left(\frac{\hat{\boldsymbol{v}} \times (\hat{\boldsymbol{v}} \times \hat{\boldsymbol{n}})}{\|\hat{\boldsymbol{v}} \times \hat{\boldsymbol{n}}\|}\right) \tag{9}$$

The drag and lift coefficients C_D and C_L are defined as

$$C_D = 2\left[\sigma_T + \sigma_N V_R\,|\cos\zeta| + (2 - \sigma_N - \sigma_t)\cos^2\zeta\right]\left(|\cos\zeta| \right. \tag{10}$$

$$C_L = 2\left[\sigma_N V_R + (2 - \sigma_N - \sigma_T)\cos^2\zeta\right]\left(|\cos\zeta|\,\sin\zeta \right. \tag{11}$$

where $\zeta \in [0, \pi]$ is the angle between the sail normal vector $\hat{\boldsymbol{n}}$ and the spacecraft velocity $\hat{\boldsymbol{v}}$, σ_N and σ_T are the normal and tangential accommodation coefficients, and V_R is the ratio of the average particle thermal speed to the spacecraft velocity. Typical values for these coefficient can be found in the literature [20, 21] to be $\sigma_N = \sigma_T = 0.8$, $V_R = 0.05$.

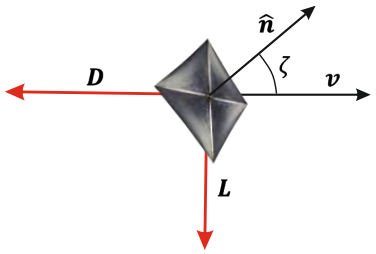

Figure 3: Orientation of drag $\boldsymbol{D}$ and lift $\boldsymbol{L}$ vectors. Also shown is the angle ζ between the velocity vector $\boldsymbol{v}$ and the sail unit vector $\hat{\boldsymbol{n}}$.

2.3. Earth's oblateness

The non-spherical gravitational field of the Earth is modelled by means of the J_2 harmonic coefficient, and the perturbing acceleration in the RTN reference frame can be expressed in terms of MEOEs as

$$[\boldsymbol{a}_{J_2}]_{\mathrm{R}} = -\frac{3\mu J_2 R_\oplus^2}{2r^4}\left[\left(1 - \frac{12\,(h\sin L - k\cos L)^2}{(1 + h^2 + k^2)^2}\right)\right.$$

$$[\boldsymbol{a}_{J_2}]_{\mathrm{T}} = -\frac{12\mu J_2 R_\oplus^2}{r^4}\left[\left(\frac{(h\sin L - k\cos L)\,(h\cos L + k\sin L)}{(1 + h^2 + k^2)^2}\right)\right.$$

$$[\boldsymbol{a}_{J_2}]_{\mathrm{N}} = -\frac{6\mu J_2 R_\oplus^2}{r^4}\left[\left(\frac{(1 - h^2 - k^2)\,(h\sin L - k\cos L)}{(1 + h^2 + k^2)^2}\right)\right. \tag{12}$$

where $R_\oplus = 6378.14\,\mathrm{km}$ is the mean equatorial radius of the Earth and $J_2 = 1.082\,626\,925\,639 \times 10^{-3}$ is the Earth's second harmonic coefficient.

2.4. Eclipses

The occurrence of eclipses is taken into account in this paper by means of a cylindrical model (see Fig. 4), which only distinguishes between sunlit phases (shadow factor $\eta = 1$) and shadow ($\eta = 0$). At the beginning of each propagation arc, the sail and Sun positions with respect to the Earth are used to verify whether the sail is in eclipse or not by means of the geometrical approach described in Ref. [25].

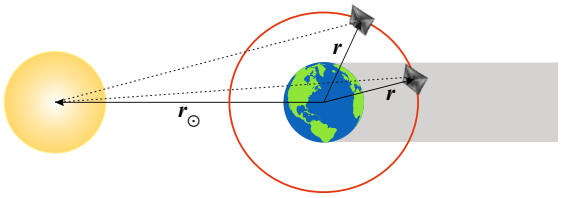

Figure 4: Cylindrical model used for eclipses.

3. Transfer Strategy

This section describes the transfer strategy to reach the debris' orbit starting from a lower altitude parking orbit which is assumed to be circular and at the same inclination as the one of the target debris. This assumption is consistent with a population of debris objects spread on circular orbits at a different right ascensions at the same inclination.

Due to the complex dynamics in a highly-perturbed environment, locally-optimal control laws have been employed to optimize the sail trajectory [26, 27]. The aim of these laws is to maximize (or minimize) the rate of change of an osculating orbital element as given by Gauss' form of the Lagrange planetary equations [25]. When the perturbing accelerations are small enough, these laws have been proven to be a good approximation to minimum-time transfers, especially in a preliminary mission design. Besides, several works have shown the possibility of blending these laws in order to control more orbital elements at the same time [26, 28].

The first part of the mission consists in reaching the debris' orbit starting from a lower altitude parking orbit, and it has been divided into two phases as shown in Fig. 5. In the 1st leg, the sail is controlled in such a way to increase its semimajor axis as quickly as possible to get away from the densest layers of the atmosphere. This phase ends as soon as the sail's osculating orbit reaches a perigee altitude $h_P = 1000$ km. This threshold has been chosen *a priori* as a height where the atmospheric density becomes almost negligible, but it might be possible to optimize it in a future work.

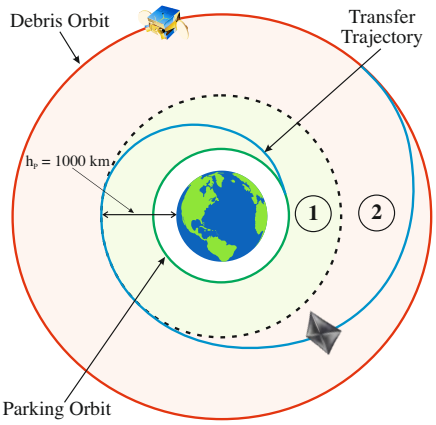

Figure 5: Transfer strategy to reach the debris' orbit (red) starting from a circular parking orbit at a lower altitude (green). The ascending part is divided into two phases, which are thoroughly described in Subsections 3.1-3.2.

During the 1st phase, only the semimajor axis is actively controlled, while the other orbital parameters are free, meaning that a 2nd phase is needed in order to drive all the four orbital elements of interest (i.e., a, e, i, Ω) to match those of the target at the end of the transfer. It must be observed that, as we are dealing with transfers between circular orbits, the argument of perigee ω is meaningless.

Once the sail has reached the debris' orbit, it will perform phasing maneuvers, rendezvous and capture, before starting the descent phase at the end of which the debris is brought down to a lower altitude and released to re-enter into the atmosphere.

3.1. 1st Phase: semimajor axis increase

As previously stated, the aim of the 1st phase is to increase the semimajor axis of the sail's orbit as quickly as possible. This can be achieved by looking for the sail attitude that maximizes the time derivative of the semimajor axis at each time instant, that is

$$\max_{\{\alpha,\delta\}} \frac{da}{dt} \tag{13}$$

where da/dt is given by the corresponding Lagrange's planetary equation

$$\frac{da}{dt} = 2\sqrt{\frac{a^3}{\mu\,(1-e^2)}}\left[e\,\sin\nu\,a_R + (1+e\,\cos\nu)\,a_T\right] \tag{14}$$

This amounts to maximizing the component of the thrust along the velocity vector [21].

The transfer has been divided into short-duration arcs of a few minutes each. At the beginning of each arc, the

Sun and sail positions are computed, as well as the local atmospheric density. The optimal sail attitude is then derived and maintained constant during the propagation along that arc. The simulation is stopped as soon as the osculating perigee altitude reaches 1000 km.

3.2. 2nd Phase: debris targeting

In this phase, it is necessary to control more orbital elements at the same time in order to reach the target's orbit at the end of the transfer. As already mentioned, the actual phasing between the sail and the debris is neglected in this work, and thus the true anomaly ν is not actively controlled. Besides, as the transfer takes place between circular orbits, also the argument of perigee ω is meaningless. Of the four remaining parameters, it must be observed that three of them (i.e., a, e, i) undergo only zero-averaged fluctuations due to the J_2 effect. On the other hand, the right ascension of the ascending node Ω has a well-known secular drift (negative for prograde orbits) of up to a few degrees per day, depending on the characteristics of the orbit. As the SRP thrust is extremely small, its effect on Ω is negligible if compared to the aforementioned secular drift. For this reason, the right ascension is not included in the solar sail's control law, but the need of phasing it with the target sets the duration of the transfer.

To this aim, a simple approach has been used to estimate the flight time of the 2nd phase, based on the constraint that, at the end of the transfer, the right ascension of the sail Ω must match the one of the target (indicated as Ω_t from now on). Starting from the sail state at the beginning of the 2nd leg $\{a_0, e_0, i_0, \Omega_0\}$ (which coincides with the state at the end of the 1st phase) and knowing the characteristics of the target's orbit $\{a_t, e_t, i_t\}$, an averaged linear drift is assumed for the sail's right ascension, that is

$$\dot{\Omega}_{\text{avg}} = -\frac{3}{2} \frac{J_2 \sqrt{\mu} R_\oplus^2}{a_{\text{avg}}^{7/2} (1 - e_{\text{avg}}^2)^2} \cos i_{\text{avg}} \tag{15}$$

where

$$a_{\text{avg}} = \frac{a_0 + a_t}{2}, \quad e_{\text{avg}} = \frac{e_0 + e_t}{2}, \quad i_{\text{avg}} = \frac{i_0 + i_t}{2} \tag{16}$$

Given this assumption, the RAAN of the sail and of the debris both decrease linearly according to

$$\Omega(t) = \Omega_0 + \dot{\Omega}_{\text{avg}}\, t \tag{17}$$

$$\Omega_t(t) = \Omega_{t,0} + \dot{\Omega}_t\, t \tag{18}$$

The flight time Δt is therefore given by the condition $\Omega(\Delta t) = \Omega_t(\Delta t)$ (see Fig. 6).

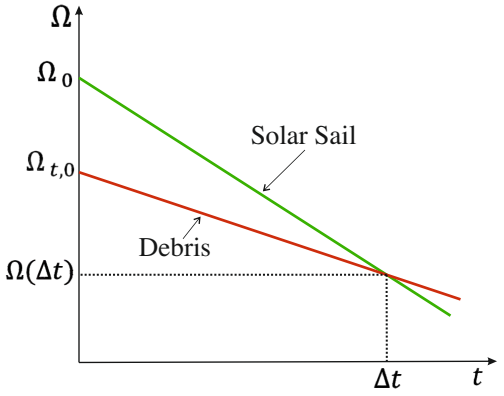

Figure 6: Flight time Δt of the 2nd phase derived from the RAAN matching condition.

The remaining three orbital elements (i.e., a, e, i) are actively controlled by a suitable blending of the corresponding time derivatives which are

$$\frac{de}{dt} = \sqrt{\frac{a\,(1 - e^2)}{\mu}} \left[\sin\nu\, a_R + \left(\cos\nu + \frac{e + \cos\nu}{1 + e\cos\nu} \right) a_T \right] \tag{19}$$

$$\frac{di}{dt} = \sqrt{\frac{a\,(1 - e^2)}{\mu}} \frac{\cos(\omega + \nu)}{1 + e\cos\nu}\, a_N \tag{20}$$

together with Eq. (14). The objective function J to locally-optimize has been written as a linear combination of these time derivatives, such as

$$J = W_a R_a \frac{d(a/a_0)}{dt} + W_e R_e \frac{de}{dt} + W_i R_i \frac{di}{dt} \tag{21}$$

where $\{W_a, W_e, W_i\}$ are constant weights that express the relative importance of each orbital element, and $\{R_a, R_e, R_i\}$ are variable weights that depend on the "distance" from the target's orbit [29], that is

$$R_a = \frac{a - a_t}{|a_0 - a_t|}, \quad R_e = \frac{e - e_t}{|e_0 - e_t|}, \quad R_i = \frac{i - i_t}{|i_0 - i_t|} \tag{22}$$

The optimal sail attitude $\{\alpha_{\text{opt}}, \delta_{\text{opt}}\}$ is computed as the one that minimizes the objective function J at each time. The role of these weights is to adjust the relative importance of each orbital element as the sail approaches the target and prioritize the one that is furthest from the target. As a matter of fact, these weights tend to zero as the corresponding element tends to the target value. Moreover, the numerators provide the sign of the weight, which indicates whether the corresponding time derivative has to be maximized or minimized.

The constant weights can be chosen in the range [0, 1] without loss of generality, and must be selected in such

a way that the sail reaches the target after a flight time set by the RAAN matching condition. To do so, a genetic algorithm has been set up with the objective of minimizing the function

$$F = \left(\frac{a_{\text{fin}} - a_t}{a_0} \right)^2 + (e_{\text{fin}} - e_t)^2 + (i_{\text{fin}} - i_t)^2 + (\Omega_{\text{fin}} - \Omega_{t,\text{fin}})^2 \tag{23}$$

As the time to simulate a single transfer was long and computationally expensive, an approximate model has to be employed to run the genetic algorithm. As shown in Fig. 7, the first step in the approximate model consists in computing the keplerian orbital period T_1 at the current semimajor axis a_1 according to Kepler's third law. The local optimization and propagation is then carried out for a time equal to the orbital period and the difference Δoe_1 between the final and the initial orbital elements is evaluated. At this point, the model assumes a linear evolution of all the orbital elements for a time interval equal to N times the orbital period T_1. After the time NT_1, the value of each orbital element is simply computed as $oe(NT_1) = oe(0) + N\,\Delta oe_1$. The same procedure is repeated M times, where M is given by the total flight time derived by the RAAN matching condition described in Subsec. 3.2. On the other hand, the value of N is a trade-off choice between a more accurate approximation (smaller N) and a shorter computational time (greater N). In the numerical simulations described in Subsec. 4.2, a value $N = 30$ is used.

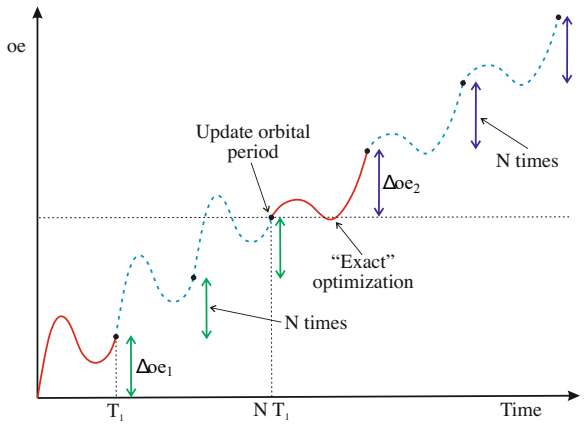

Figure 7: Approximate model for the 2nd phase transfer used to reduce the computational time of the genetic algorithm.

3.3. Descent Phase

After capturing the debris, the sail has to bring it down to a lower altitude and release it. In this descent phase, the sail departs from the debris' orbit and targets the initial circular parking orbit at a lower altitude, but at the same inclination. Obviously, no RAAN matching is needed in this phase and the flight time is left free. The only parameters of interest to be actively controlled are the semimajor axis a, the eccentricity e and the inclination i. It must be pointed out that the additional mass of the captured debris has to be considered, resulting in a higher sail loading $\sigma_{\text{desc}} > \sigma$ and a lower characteristic acceleration $a_{c,\text{desc}} < a_c$.

A blended control law similar to the one in Eq. (21) has been used, that is

$$J = R_a \frac{d(a/a_0)}{dt} + R_e \frac{de}{dt} + R_i \frac{di}{dt} \tag{24}$$

where the variable weights are now defined as

$$R_a = \frac{a - a_t}{|a_0 - a_t|}, \quad R_e = e - e_t, \quad R_i = i - i_t \tag{25}$$

since the initial and final orbits have now the same eccentricity and inclination, and therefore some denominators in Eq. (22) would be equal to zero. As the flight time is not constrained, there is no need to include and optimize the constant weights, but the trajectory is propagated until the sail reaches the disposal orbit within a certain tolerance.

4. Numerical Simulations

In this Section, the transfer strategy described in Sec. 3 is applied to a test-case scenario using a solar sail with characteristic acceleration $a_c = 0.1\,\text{mm/s}^2$, that departs from a circular parking orbit at an altitude $h_0 = 600\,\text{km}$ above the Earth and initial right ascension $\Omega_0 = 0\,\text{deg}$. The departure date is the 1st January 2030, when the solar activity is close to a minimum.

4.1. 1st Phase: numerical results

The results obtained for the 1st phase of the transfer are shown in Fig. 8. In this case, the sail has reached the threshold perigee altitude $h_P = 1000\,\text{km}$ after about 92 days, showing an increase in the semimajor axis of roughly 450 km, which is compatible with similar analyses carried out in the literature [20]. The three orbital elements $\{a, e, i\}$ clearly show the fluctuations due to the J2 effect, which is also responsible for the evident secular drift in the right ascension Ω.

4.2. 2nd Phase: numerical results

The 2nd phase of the transfer consists in targeting the debris' orbit using the blended control law defined in Eq. (21). As explained in Subsec. 3.2, the flight time

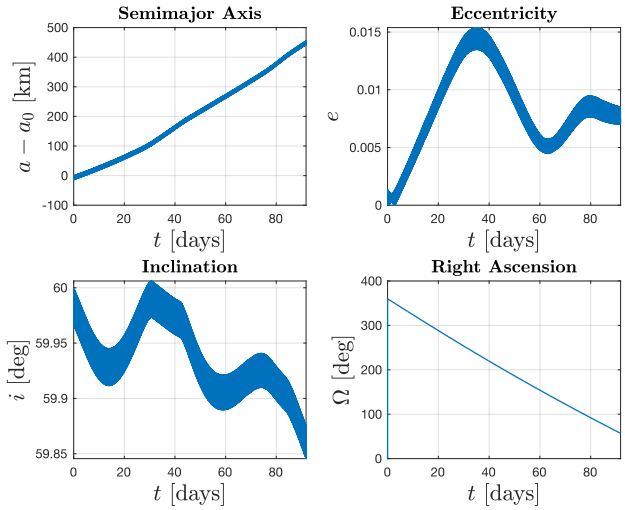

Figure 8: Evolution of the four orbital elements of interest $\{a, e, i, \Omega\}$ during the 1st phase of the transfer for a solar sail with characteristic acceleration $a_c = 0.1\,\mathrm{mm/s^2}$.

is fixed and provided by the RAAN matching condition. As a test-case scenario, an initial RAAN difference $\Delta\Omega_0 = 10\,\mathrm{deg}$ between the sail and the debris has been assumed, which lead to a flight time of approximately 101.9 days. It is worth pointing out that, if the initial RAAN difference is too small, the flight time would be shorter as well, and it might be impossible to drive some orbital elements towards the target in such a short time. On the other hand, longer flight times drastically increase the computational time for the genetic algorithm.

Given the flight time, a genetic algorithm is run with the approximate model to find the optimal values of the constant weights $\{W_a, W_e, W_i\}$. These values have been then used to propagate the trajectory both with the approximate and with the "exact" model.

The settings of the genetic algorithm and the optimal weights are shown in Tab. 1. Despite the low number of generations used in this simulation, the results plotted in Fig. 9 show that all the orbital elements are effectively driven towards their target values.

Table 2 shows the final values of the sail orbital elements obtained with both the approximate and the "exact" model. The final error in the semimajor axis obtained with the more accurate propagation is less than 4 km, the final eccentricity is about 1.7×10^{-3}, and the inclination seems to match very well the target value. These results are considered to be acceptable in a preliminary study, and are expected to improve if the genetic algorithm has time to better explore the solution space.

A comment is needed on the final right ascension, which, despite being very close to the target according to the approximate model, it actually shows a 2.84 deg discrepancy when the "exact" model is used. This error is due to the fact that it is sometimes difficult to precisely match the desired flight time with the approximate model, as the shortest time interval is made of $N = 30$ cycles which correspond to more than 2 days. This time step is then multiplied for an integer number M, which might lead to a little discrepancy between the flight time imposed by the RAAN matching condition (and used to propagate the exact model) and the one used in the approximate model. Despite this difference being relatively small, the right ascension has a drift of about 3 deg per day on that orbit, thus leading to the observed error in the final value. A possible solution to this issue might be to reduce the number of cycles N, but this would also lead to a much longer computational time.

Table 1: Genetic algorithm settings, flight time and optimal weights for the 2nd phase of the transfer.

Population Size	50
Elite Count	2
Generations	10
Function Tol	1×10^{-6}
Flight Time Δt	101.9 days
W_a	0.27849822
W_e	0.83082863
W_i	0.76324954

Table 2: Numerical results of the 2nd phase. Both the approximate and the "exact" models are propagated using the weights obtained from the genetic algorithm.

Orbit	a [km]	e	i [deg]	Ω [deg]
Sail initial	7433.5	0.0074	59.87	56.98
Debris initial	7578.1	0	60	46.98
Debris final				130.07
Sail (approx.)	7588.7	0.0009	59.99	130.05
Sail ("exact")	7574.4	0.0017	60	127.23

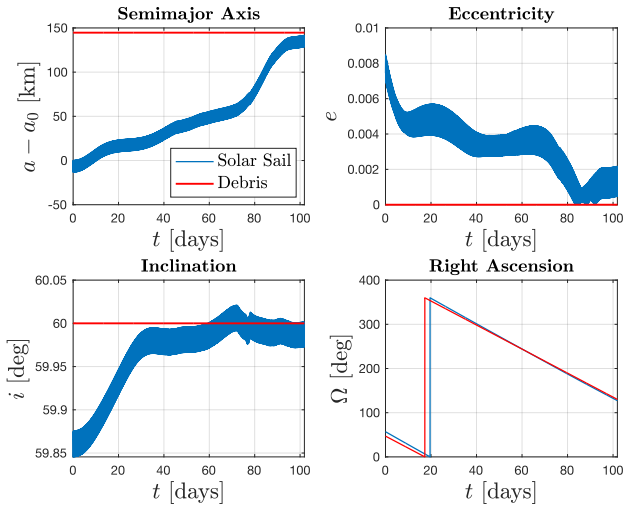

Figure 9: Evolution of the orbital elements in the 2nd phase of the transfer.

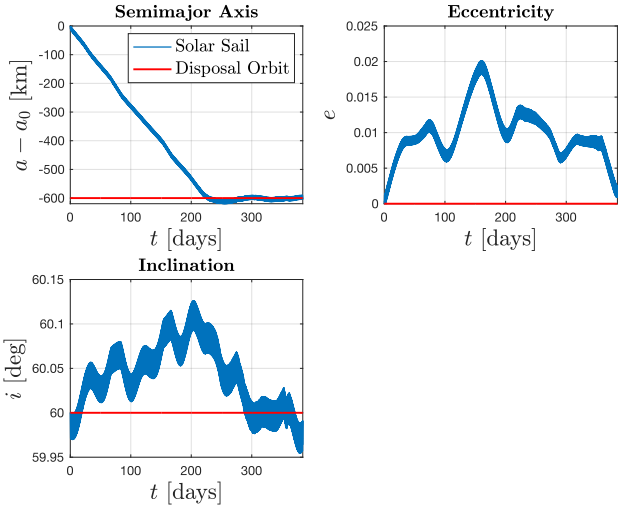

Figure 10: Evolution of the three orbital elements $\{a, e, i\}$ (blue) during the descent phase after capturing the debris. The red lines indicate the orbital elements of the target orbit, which coincides with the initial parking orbit.

4.3. Descent: numerical results

The last phase of the mission is the descent to bring the debris down to the initial sail parking orbit and release it where the aerodynamic forces can lead to its atmospheric re-entry. The additional mass of the debris is taken into account by doubling the sail loading $\sigma_{\text{desc}} = 2\sigma$, which means that the new characteristic acceleration of the sail is $a_{c,\text{desc}} = a_c/2 = 0.05\,\text{mm/s}^2$. The simulation is started roughly 45 days after the end of the 2nd phase, to allow for phasing maneuvers, rendezvous and capture. The simulation has been propagated for 400 days, and the minimum value of the function $D = ((a-a_t)/a_0)^2 + (e-e_t)^2 + (i-i_t)^2$ has been used as a stopping criterion to generate the plots in Fig. 10. With this approach, the descent phase lasts about 384 days, but it must be observed that both the semimajor axis and the inclination have reached the target values after around 300 days. The residual small eccentricity after that time might be negligible if no particularly accurate orbit is required for the debris disposal.

A possible improvement to this approach would be to include some constant weights in the blended control law in Eq. (24), and look for the values of these factors that drive the sail towards the disposal orbit in the minimum time.

5. Conclusion

This work has investigated a space debris removal strategy that uses a solar sail to actively dispose of a debris object in low Earth orbit. Locally-optimal control laws have been employed to optimize the sail trajectory, and have proved to be particularly suited and effective in driving the spacecraft towards its target in a highly-perturbed environment where global-optimization techniques would have been challenging to implement.

A blending strategy has been used to control a set of orbital elements at the same time in order to reach the debris' orbit. Despite the fact that the search for optimal weighing factors has required a considerable amount of time, even a low number of generations in the genetic algorithm has provided good solutions for a preliminary design. Besides, the proposed approximate model has not only reduced the computational time, but also provided a good approximation to the more accurate approach.

A future work could include the switching point between 1st and 2nd phases into the optimization process in order to derive the best possible sequence depending on the characteristics of the debris' orbit.

An interesting application of this method could be a multiple debris removal mission, where a single sail can sequentially capture and de-orbit many objects, thus making the use of this propulsion system even more attractive.

References

[1] D. J. Kessler and B. G. Cour-Palais. Collision frequency of artificial satellites: The creation of a debris belt. *J Geophys Res*, 83 (A6):2637–2646, 1978.

[2] C. Lücking, C. Colombo, and C. R. McInnes. A passive satellite deorbiting strategy for medium earth orbit using solar radiation pressure and the j2 effect. *Acta Astronautica*, 77:197–206, 8 2012. ISSN 00945765. doi: 10.1016/j.actaastro.2012.03.026.

[3] J. P. Carvalho et al. Analysis of the orbital evolution of space debris using a solar sail and natural forces. *Advances in Space Research*, 70:125–143, 7 2022. ISSN 18791948. doi: 10.1016/j.asr.2022.04.014.

[4] C. Colombo et al. Effects of passive de-orbiting through drag and solar sails and electrodynamic tethers on the space debris environment. In *Proceedings of the 69th International Astronautical Congress (IAC)*, 2018.

[5] V. Schaus et al. On the practical exploitation of perturbative effects in low earth orbit for space debris mitigation. *Advances in Space Research*, 63:1979–1991, 4 2019. ISSN 18791948. doi: 10.1016/j.asr.2019.01.020.

[6] G. Schettino, E. M. Alessi, A. Rossi, and G. B. Valsecchi. Exploiting dynamical perturbations for the end-of-life disposal of spacecraft in leo. *Astronomy and Computing*, 27:1–10, 4 2019. ISSN 22131337. doi: 10.1016/j.ascom.2019.02.001.

[7] I. Iakubivskyi et al. Coulomb drag propulsion experiments of estcube-2 and foresail-1. *Acta Astronautica*, 177:771–783, 12 2020. ISSN 00945765. doi: 10.1016/j.actaastro.2019.11.030.

[8] M. M. Pellegrino and D. J. Scheeres. Optimal deployment of solar radiation pressure enhancement devices for space debris mitigation. American Institute of Aeronautics and Astronautics Inc, AIAA, 2018. ISBN 9781624105333. doi: 10.2514/6.2018-2229.

[9] J.C. Liou. A parametric study on using active debris removal for leo environment remediation. *NASA Johnson Space Center*, 4, 2010.

[10] C. Bonnal, J.M. Ruault, and M.C. Desjean. Active debris removal: Recent progress and current trends. *Acta Astronautica*, 85:51–60, 2013. ISSN 0094-5765. doi: https://doi.org/10.1016/j.actaastro.2012.11.009.

[11] N. Bérend and X. Olive. Bi-objective optimization of a multiple-target active debris removal mission. *Acta Astronautica*, 122: 324–335, 2016. ISSN 0094-5765. doi: https://doi.org/10.1016/j.actaastro.2016.02.005.

[12] V. Braun et al. Active debris removal of multiple priority targets. *Advances in Space Research*, 51(9):1638–1648, 2013. ISSN 0273-1177. doi: https://doi.org/10.1016/j.asr.2012.12.003.

[13] G. Viavattene et al. Design of multiple space debris removal missions using machine learning. *Acta Astronautica*, 193:277–286, 4 2022. ISSN 00945765. doi: 10.1016/j.actaastro.2021.12.051.

[14] P. Kelly and R. Bevilacqua. An optimized analytical solution for geostationary debris removal using solar sails. *Acta Astronautica*, 162:72–86, 9 2019. ISSN 00945765. doi: 10.1016/j.actaastro.2019.05.055.

[15] P. Kelly and R. Bevilacqua. Geostationary debris mitigation using minimum time solar sail trajectories with eclipse constraints. *Optimal Control Applications and Methods*, 42:279–304, 1 2021. ISSN 10991514. doi: 10.1002/oca.2676.

[16] M. J. H. Walker, B. Ireland, and J. Owens. A set modified equinoctial orbit elements. *Celestial Mechanics*, 36:409–419, 8 1985. doi: 10.1007/BF01227493.

[17] M. J. H. Walker. A set of modified equinoctial orbit elements. *Celestial Mechanics*, 38:391–392, 1986. doi: 10.1007/BF01238929.

[18] J. T. Betts. *Practical Methods for Optimal Control and Estimation using Nonlinear Programming*. 2010.

[19] C. R. McInnes. Solar sailing technology, dynamics and mission applications, 1999.

[20] L. Carzana, P. Visser, and J. Heiligers. Locally optimal control laws for earth-bound solar sailing with atmospheric drag. *Aerospace Science and Technology*, 127, 8 2022. ISSN 12709638. doi: 10.1016/j.ast.2022.107666.

[21] G. Mengali and A. A. Quarta. Near-optimal solar-sail orbit-raising from low earth orbit. *Journal of Spacecraft and Rockets*, 42:954–958, 2005. ISSN 15336794. doi: 10.2514/1.14184.

[22] J. A. Storch. Aerodynamic disturbances on spacecraft in free-molecular flow. *The Aerospace Corporation*, 2002.

[23] J. Picone, A.E. Hedin, D. Drob, and A. Aikin. Nrlmsise-00 empirical model of the atmosphere: Statistical comparison and scientific issues. *Journal of Geophysical Research*, 107, 12 2002. doi: 10.1029/2002JA009430.

[24] V. Stolbunov, M. Ceriotti, C. Colombo, and C. R. McInnes. Optimal law for inclination change in an atmosphere through solar sailing. *Journal of Guidance, Control, and Dynamics*, 36:1310–1323, 2013. doi: 10.2514/1.59931.

[25] H. D. Curtis. *Orbital Mechanics for Engineering Students*. Elsevier, 2020. doi: 10.1016/b978-0-08-102133-0.09982-7.

[26] M. Macdonald and C. R. McInnes. Analytical control laws for planet-centered solar sailing. *Journal of Guidance, Control, and Dynamics*, 28:1038–1048, 2005. ISSN 15333884. doi: 10.2514/1.11400.

[27] M. Macdonald, C. R. McInnes, and B. Dachwald. Heliocentric solar sail orbit transfers with locally optimal control laws. *Journal of Spacecraft and Rockets*, 44:273–276, 2007. ISSN 15336794. doi: 10.2514/1.17297.

[28] M. Bassetto, A. A. Quarta, and G. Mengali. Locally-optimal electric sail transfer. *Proceedings of the Institution of Mechanical Engineers, Part G: Journal of Aerospace Engineering*, 233:166–179, 1 2019. ISSN 20413025. doi: 10.1177/0954410017728975.

[29] H. J. Holt. *Trajectory Design using Lyapunov Control Laws and Reinforcement Learning*. PhD thesis, University of Surrey, 2023.

Solar-sail Steering Laws to Calibrate the Accelerations from Solar Radiation Pressure, Planetary Radiation Pressure, and Aerodynamic Drag

Livio CARZANA[a,*], W. Keats WILKIE[b], Andrew HEATON[c], Ben DIEDRICH[c], Jeannette HEILIGERS[a]

[a] *Faculty of Aerospace Engineering, Delft University of Technology, Kluyverweg 1, 2629 HS Delft, The Netherlands*
[b] *Langley Research Center, National Aeronautics and Space Administration, Hampton, Virginia, 23681-2199, USA*
[c] *Marshall Space Flight Center, National Aeronautics and Space Administration, Huntsville, Alabama, 35808, USA*

Abstract

Solar sailing is a propulsion method which takes advantage of solar radiation pressure (SRP) as main source of thrust. However, around Earth, other sources also affect the solar-sail dynamics, including planetary radiation pressure (PRP) and atmospheric drag. In literature, the accelerations from SRP, PRP, and atmospheric drag are modeled using different theoretical and idealistic models, which make use of simplifying assumptions to describe the near-Earth dynamical environment, the sail's geometry, and optical properties. Consequently, sailcraft in orbit experience accelerations different from the theoretically predicted ones. In order to quantify these discrepancies between the real and modeled solar-sail dynamics, a first definition and preliminary assessment of a set of calibration steering laws is provided in this paper. These steering laws allow to characterize the solar-sail acceleration at every sail orientation and to identify the contributions due to solar radiation pressure, planetary radiation pressure, and aerodynamic drag. The analyses presented make use of NASA's upcoming ACS3 mission as baseline scenario and account for different possible orientations of its orbit. The results highlight the benefits and implementation challenges of each steering law and the impact that they have on the orbital elements, with particular focus on the orbital altitude.

Keywords: solar sail, calibration, steering laws, operational constraints, Earth-bound, ACS3 mission

1. Introduction

Solar sailing is a propulsion method using solar radiation pressure (SRP) as primary source of thrust [1]. Over the last years, solar sailing has drawn increasing attention in the scientific community particularly because of its propellantless nature and potential for a variety of mission applications, both in the near-Earth and interplanetary environments [2, 3]. In light of this, several solar sails have been launched in the recent past to increase the solar-sail technology readiness level and assess its potential for real-life mission applications. Most of these sailcraft have flown in close proximity of the Earth and, similarly, even more Earth-bound missions are planned for the near future. Among these are, for example, the recently launched Alpha sailcraft by Gama and the upcoming NASA's Advanced Composite Solar Sail System (ACS3) and Gama's Beta missions [4]. Orbiting about the Earth, the dynamics of these solar sails are, apart from SRP, also affected by other sources of acceleration. The main non-gravitational ones include the Earth's planetary radiation pressure (PRP) and atmospheric drag. Because the PRP and aerodynamic accelerations depend on the sail attitude and can perturb sailcraft orbits to a significant extent [5, 6], accurately predicting their magnitudes is crucial for the design of Earth-bound solar-sail missions. In literature, the accelerations from SRP, PRP, and atmospheric drag are modeled using different theoretical and idealistic models, most of which assume the sail to be a thin, flat surface with known optical properties [1, 7, 8]. These models therefore do not account for secondary effects, like the sail billowing, presence of wrinkles, degradation, and uncertainties in the sail's optical properties. Furthermore, these models make use of simplifying assumptions to describe the near-Earth dynamical environment, particularly with respect to the atmospheric density [5, 9, 10] and the intensity of the solar and planetary radiation [6, 11, 12]. Because of these assumptions, real-life sailcraft generally experience accelerations that differ from the predicted ones. In order to quantify these

* Corresponding author, L.Carzana@tudelft.nl

differences, the calibration of the actual SRP, PRP, and aerodynamic accelerations experienced by sailcraft in orbit can be performed. In this way, these accelerations can be measured and compared to the predicted ones, therefore providing insights into, and an opportunity to improve, the accuracy and fidelity of the solar-sail dynamical models. Calibration of the SRP, PRP, and aerodynamic accelerations requires the definition of steering laws designed ad hoc for this purpose. In addition, the implementation of these control strategies in real life can prove challenging for different reasons, including the presence of operational constraints and deorbiting effect on the sailcraft orbit. In light of the above and the fact that studies on the design of such steering laws have never been conducted, this paper presents a set of calibration steering laws (CSLs) specific for Earth-bound solar sails and provides a first-order assessment of their calibration capacity and implementation challenges.

2. Dynamics

In this paper, the equations of motion describing the solar-sail dynamics are expressed in an inertial Earth-centered reference frame, $\mathcal{I}(x, y, z)$, with the x-axis pointing towards the vernal equinox, the z-axis perpendicular to the equatorial plane and pointing towards the north pole, and the y-axis completing the right-handed frame. Within this frame, the equations of motion of a solar sail subject to the SRP, PRP, aerodynamic, and J_2 gravitational accelerations can be expressed in vectorial form as:

$$\ddot{\boldsymbol{r}} + \frac{\mu}{r^3}\boldsymbol{r} = \boldsymbol{a}_{SRP} + \boldsymbol{a}_{PRP} + \boldsymbol{a}_{Aero} + \boldsymbol{a}_{J2} \tag{1}$$

where μ = 398600.4415 km^{3}s^{-2} is the Earth's gravitational parameter [13], $\boldsymbol{r} = [x, y, z]^{\mathrm{T}}$ is the sailcraft position vector, $r = \|\boldsymbol{r}\|$, and $\boldsymbol{a}_{SRP}$, $\boldsymbol{a}_{PRP}$, $\boldsymbol{a}_{aero}$, and $\boldsymbol{a}_{J2}$ are the SRP, PRP, aerodynamic, and Earth's J_2 gravitational accelerations, respectively. The full definition of these accelerations is provided in the following sections.

2.1. Solar Radiation Pressure Acceleration

The SRP acceleration is computed considering an ideal sail model, that is, the sail is assumed to be flat and perfectly reflecting on both sides. Under this assumption, the SRP acceleration is given as [1]:

$$\boldsymbol{a}_{SRP} = \nu a_c \cos^2(\alpha)\, \kappa \hat{\boldsymbol{n}} \tag{2}$$

In Eq. (2), ν represents the shadow factor, computed using a conservative conical shadow model [5]. This model assumes $\nu = 0$ when the sailcraft is in umbra or penumbra and $\nu = 1$ when the sailcraft is completely illuminated. The characteristic acceleration, a_c, represents the maximum achievable SRP acceleration at a distance of 1 AU from the Sun and is defined as [1]:

$$a_c = \frac{2\mathbb{S}_\oplus}{c\sigma} \tag{3}$$

where $\mathbb{S}_\oplus = 1367$ W/m^2 is the solar flux at Earth [13], $c = 299792.458$ km/s is the speed of light in vacuum [14], and σ represents the sailcraft loading parameter, i.e., its mass-to-sail area ratio. Finally, $\alpha \in [0, \pi]$ is the solar-sail pitch angle measured between the direction of sunlight, $\hat{\boldsymbol{s}}$, and the normal direction of the sail back side, $\hat{\boldsymbol{n}}$, see Fig. 1a, while κ is a sign function indicating whether the sail front side is illuminated ($\kappa = 1$) or the sail back side is illuminated ($\kappa = -1$).

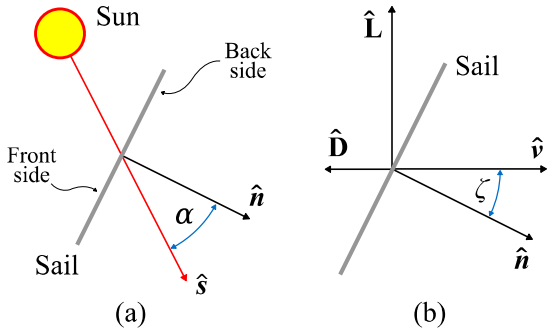

Fig. 1. Relevant solar-sail attitude angles and directions used to determine the SRP and aerodynamic accelerations.

2.2. Aerodynamic Acceleration

The aerodynamic acceleration is computed assuming the sail to behave as a perfectly flat plate in hyperthermal free-molecular flow conditions, that is, the sailcraft is assumed to orbit with a velocity much larger than the thermal velocity of the atmospheric particles [15]. Under these conditions, the aerodynamic acceleration is found as [5, 9]:

$$\boldsymbol{a}_{aero} = \frac{\rho v^2}{2\sigma}(C_D\hat{\mathbf{D}} + C_L\hat{\mathbf{L}}) \tag{4}$$

In Eq. (4), v is the magnitude of the sailcraft inertial velocity and ρ is the atmospheric density, which is modeled using an averaging technique based on the NRLMSISE-00 atmospheric model, see Ref. [5]. $\hat{\mathbf{D}}$ and $\hat{\mathbf{L}}$ represent the drag and lift directions pointing opposite and perpendicular to the inertial velocity direction, $\hat{\boldsymbol{v}}$, respectively, see Fig. 1b. C_D and C_L are the drag and lift coefficients, respectively, given by [5, 9]:

$$C_D = 2\left[\sigma_T + \sigma_N V_R |\cos\zeta| + (2 - \sigma_N - \sigma_T)\cos^2\zeta\right]|\cos\zeta| \tag{5}$$

$$C_L = 2\left[\sigma_N V_R + (2 - \sigma_N - \sigma_T)|\cos\zeta|\right]|\cos\zeta|\sin\zeta \tag{6}$$

where V_R is the ratio of the atmospheric particle thermal velocity to the sailcraft velocity, σ_N and σ_T are the normal and tangential momentum accommodation coefficients, respectively, and ζ represents the complementary angle to the angle of attack, see again Fig. 1b. Based on Ref. [16], in this paper $\sigma_N = \sigma_T = 0.8$ and $V_R = 0.05$.

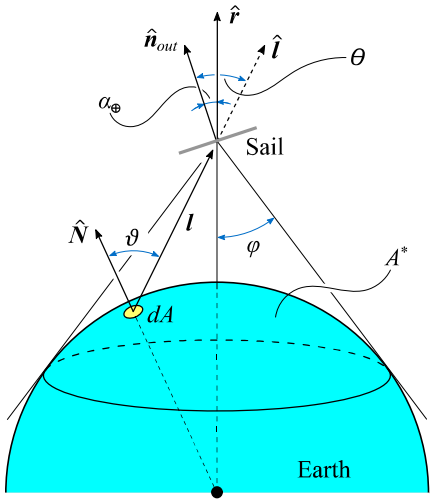

Fig. 2. Geometry of the problem to determine the PRP acceleration exerted on a solar sail.

2.3. *Planetary Radiation Pressure Acceleration*

To compute the PRP acceleration, the so-called spherical uniform model presented in Refs. [6, 17] is employed. This model is valid for flat, perfectly reflecting solar sails and assumes the Earth to be a spherical radiation source emitting radiation isotropically, i.e., with a constant radiation flux. When this model is employed, the PRP acceleration is found through the following integral equation [6, 17]:

$$\boldsymbol{a}_{PRP} = \frac{2\overline{S}}{\pi c \sigma}\left(\int_{A^*} \frac{\cos(\vartheta)\cos^2(\theta)}{l^2} dA\right)\hat{\boldsymbol{n}}_{out} \qquad (7)$$

As depicted in Fig. 2, dA represents an elementary piece of Earth's surface irradiating, ϑ is the angle between the zenith direction at dA, $\hat{\boldsymbol{N}}$, and the vector pointing from dA to the sailcraft, $\boldsymbol{l}$, θ is the angle between $\boldsymbol{l}$ and the sail normal direction pointing away from the Earth, $\hat{\boldsymbol{n}}_{out}$, and $l = \|\boldsymbol{l}\|$. Finally, $\overline{S}$ represents the Earth's planetary flux, which is found through a surface averaging process and is assumed constant over the entire visible surface of the Earth as seen from the sailcraft, A^*. Its value depends on the Earth's blackbody radiation flux and albedo coefficient which, based on Ref. [6], have been set to 234.732 W/m^2 and 0.3259, respectively. For the full analytical expressions of $\overline{S}$ and the solution to the acceleration integral of Eq. (7), the reader is referred to Refs. [6, 17].

2.4. *J_2 Gravitational Acceleration*

The Earth's J_2 gravitational acceleration is defined in frame $\mathcal{G}(x, y, z)$ as follows [18]:

$$\boldsymbol{a}_{J2} = -\frac{3}{2}\frac{R^2}{r^5}\mu J_2\left[(x\hat{\boldsymbol{x}} + y\hat{\boldsymbol{y}})\left(1 - 5\frac{z^2}{r^2}\right) + z\left(3 - 5\frac{z^2}{r^2}\right)\hat{\boldsymbol{z}}\right] \qquad (8)$$

where $\hat{\boldsymbol{x}}$, $\hat{\boldsymbol{y}}$, and $\hat{\boldsymbol{z}}$ are the unit vectors along the $\mathcal{G}(x, y, z)$ frame's axes, $R = 6378.1363$ km is the Earth radius [13], and $J_2 = 1.082626925639 \cdot 10^{-3}$ is the Earth's J_2 gravitational field constant of the JGM-2 geopotential model [13, 19].

3. Calibration Steering Laws

In this section, the definition of a set of steering laws designed to calibrate the SRP, PRP, and aerodynamic accelerations of solar sails in Earth-bound, circular orbits is discussed. To this aim, it is crucial to firstly define the concept of the acceleration envelope (AE) curve: this is a curve representing the set of all possible accelerations achievable by a sailcraft when changing its attitude. Because the SRP, PRP, and aerodynamic accelerations change their magnitudes and directions with the sail attitude, an AE curve can be defined for each of them. When the acceleration models presented in Section 2 are considered, these curves assume the shapes depicted in Fig. 3. As can be seen, all AE curves are symmetric with respect to a different reference direction; these are the sunlight direction, $\hat{\boldsymbol{s}}$, radial direction, $\hat{\boldsymbol{r}}$, and velocity direction, $\hat{\boldsymbol{v}}$, for the SRP, PRP, and aerodynamic AE curves, respectively. The reference directions provide information on which attitudes maximize or minimize a particular acceleration. Indeed, if the sail normal direction, $\hat{\boldsymbol{n}}$, is directed along a reference direction or perpendicular to it, the corresponding acceleration is maximized or minimized, respectively. On the other hand, for arbitrary orientations of $\hat{\boldsymbol{n}}$, intermediate accelerations are obtained whose magnitude and direction are described by the AE curves, see Fig. 3.

Given the notion of AE curve, the CSLs can be regarded as control strategies that solar sails can adopt to reconstruct the AE curves based on the in-orbit accelerations experienced. The difficulty in designing CSLs for the SRP, PRP, and aerodynamic accelerations is the fact that all these accelerations depend on the sail attitude and are therefore coupled. Consequently, in most cases it is not possible to calibrate a single acceleration independently without experiencing a perturbing effect from the others. In addition, it is worth noting that the design

of the CSLs also depends on the relative orientation of the orbit with respect to sunlight, as the presence of eclipses hinders the calibration of the SRP acceleration.

Hereinafter seven CSLs with different degrees of complexity are presented. In Section 3.1, steering laws to calibrate the maximum SRP, PRP, and aerodynamic accelerations are discussed. Afterwards, Section 3.2 presents another three CSLs to calibrate the entire SRP, PRP, and aerodynamic AE curves. Finally, in Section 3.3 a steering law designed to calibrate the residual accelerations acting on solar sails in the absence of SRP, PRP, and aerodynamic accelerations is discussed.

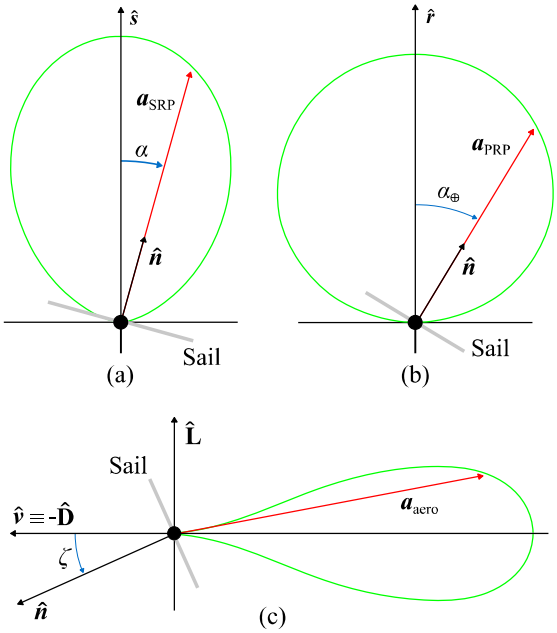

Fig. 3. Acceleration envelope curves of the SRP acceleration (a), PRP acceleration (b), and aerodynamic acceleration (c).

3.1. *Calibration of the Maximum Accelerations*

The steering laws discussed in this section aim to calibrate the maximum magnitudes of the SRP, PRP, and aerodynamic accelerations, therefore allowing to determine the characteristic dimensions of their AE curves. To achieve this, for each of these acceleration a steering law can be designed in which the sail is constantly oriented with its normal parallel to the acceleration's reference direction, that is, $\hat{\boldsymbol{n}}$ points along $\hat{\boldsymbol{s}}$, $\hat{\boldsymbol{r}}$, and $\hat{\boldsymbol{v}}$ when calibrating the maximum SRP, PRP, and aerodynamic accelerations, respectively. This approach can be used to calibrate the maximum PRP and aerodynamic accelerations at any point along the orbit and the maximum SRP acceleration only when the sailcraft is illuminated. Indeed, when the sailcraft is in eclipse conditions ($\nu = 0$), sunlight cannot reach the sailcraft and, therefore, the SRP acceleration cannot be measured. In this case, an alternative control strategy can be adopted: the sail is oriented edgewise with respect to the velocity direction, $\hat{\boldsymbol{v}}$, and with its normal pointing along the radial direction, $\hat{\boldsymbol{r}}$. This configuration minimizes drag, therefore preventing the sail from deorbiting. On the other hand, the PRP acceleration is maximized, hence potentially enabling its calibration. It should be noted that this variant of the CSL is only implemented when eclipses longer than a specified threshold duration, Δt_{Ecl}, take place. The reason for this is that switching to this alternative control strategy requires a sudden re-orientation of the sailcraft, which can prove demanding for real-life attitude control systems. As a consequence, it may be preferable not to implement this variant of the CSL when short eclipses are experienced, despite the perturbations PRP acceleration and drag may yield. In this paper, a value of Δt_{Ecl} equal to 1/5 of the orbital period is considered for all CSLs where applicable.

3.2. *Calibration of the Acceleration Envelope Curves*

This section presents three CSLs that aim to calibrate the entire AE curves of the SRP, PRP, and aerodynamic accelerations.

3.2.1. *Solar Radiation Pressure Acceleration*

In order to calibrate the SRP AE curve, the sailcraft shall to change its attitude gradually, so as to cover all pitch angles in the range 0-90 deg. Depending on whether eclipses occur, two possible control strategies are adopted.

If the sailcraft is continuously illuminated along the entire orbit, the sail's normal direction, $\hat{\boldsymbol{n}}$, points along the sunlight direction, $\hat{\boldsymbol{s}}$, at the point in the orbit closest to the Sun. When moving away from this point, $\hat{\boldsymbol{n}}$ slowly changes its direction so as to increase the pitch angle, until becoming perpendicular to the direction of sunlight and parallel to the radial direction, $\hat{\boldsymbol{r}}$, after one quarter of the orbital period. Thereafter, the sail is gradually reoriented to make $\hat{\boldsymbol{n}}$ be once again parallel to $\hat{\boldsymbol{s}}$ after another quarter of the orbital period. Finally, the entire process is repeated also in the second half of the orbit, thus making the pitch angle span across the 0-90 deg range twice per orbital period.

If eclipses last longer than the specified threshold duration, Δt_{Ecl}, the same eclipsing variant of the CSL presented in Section 3.1 for the calibration of the maximum SRP acceleration can be used. When this variant of the CSL is adopted, the pitch angle spans across the 0-90 deg range only once per orbital period. For the sake of visualization, this variant of the CSL is displayed in the left plot of Fig. 4.

3.2.2. *Planetary Radiation Pressure Acceleration*

When implementing the CSL for the PRP AE curve, the sailcraft gradually changes its attitude by translating its normal direction from $\hat{\boldsymbol{r}}$ to $\pm\hat{\boldsymbol{h}}$ (and vice versa) every quarter of the orbital period. In this way, the planetary cone angle (i.e., the angle between $\hat{\boldsymbol{n}}_{out}$ and $\hat{\boldsymbol{r}}$, see Figs. 3 and 4), $\alpha_{\oplus}$, spans across the entire 0-90 deg range twice per orbit. Implementing this steering law does not yield any aerodynamic drag, thus preventing the sailcraft from deorbiting. On the other hand, the SRP acceleration is present and acts as a perturbing acceleration. For the sake of visualization, this CSL is displayed in the center plot of Fig. 4.

3.2.3. *Aerodynamic Acceleration*

Similar to the CSL presented in the last subsection, the steering law to calibrate the aerodynamic AE curve considers a gradual variation of the sail normal direction between two reference directions: the velocity direction, $\hat{\boldsymbol{v}}$, and the orbital momentum direction, $\hat{\boldsymbol{h}} = (\hat{\boldsymbol{r}} \times \hat{\boldsymbol{v}}) / \|\hat{\boldsymbol{r}} \times \hat{\boldsymbol{v}}\|$. In particular, $\hat{\boldsymbol{n}}$ is continuously reoriented so as to point intermittently along $\hat{\boldsymbol{v}}$ and $\pm\hat{\boldsymbol{h}}$ every quarter of the orbital period. By doing so, the complementary angle to the angle of attack, ζ, spans across the entire 0-90 deg range twice per orbit. When employing this CSL, no PRP acceleration is experienced by the sailcraft, whereas the SRP acceleration acts as a perturbing acceleration. For the sake of visualization, this CSL is displayed in the right plot of Fig. 4.

3.3. *Calibration of the Residual Accelerations*

Solar sails experience no SRP, PRP, and aerodynamic accelerations when the sail normal direction, $\hat{\boldsymbol{n}}$, points perpendicular to the sunlight direction, $\hat{\boldsymbol{s}}$, radial direction, $\hat{\boldsymbol{r}}$, and velocity direction, $\hat{\boldsymbol{v}}$, respectively. The relative orientation of $\hat{\boldsymbol{s}}$, $\hat{\boldsymbol{r}}$, and $\hat{\boldsymbol{v}}$ then plays a central role in determining whether a zero-acceleration steering law can be designed. The only scenario in which all three accelerations can be simultaneously nullified is when $\hat{\boldsymbol{s}}$, $\hat{\boldsymbol{r}}$, and $\hat{\boldsymbol{v}}$ are coplanar. This only occurs for an orbit oriented parallel to the direction of sunlight. Then, the sail normal direction, $\hat{\boldsymbol{n}}$, can be directed perpendicular to the orbital plane, i.e., along $\pm\hat{\boldsymbol{h}}$. Because the SRP, PRP, and aerodynamic accelerations are equal to zero when this CSL is employed, only gravitational accelerations affect the dynamics. However, in the majority of orbital scenarios, these directions do not lie in the same plane and, therefore, a sail normal direction that is perpendicular to all of them is not possible to find. This implies that at least one non-zero acceleration is always obtained, independently of the sail attitude adopted.

4. Analyses

This section presents different analyses aimed at highlighting the benefits and implementation challenges of the CSLs introduced in the previous section. Indeed, while the CSLs can be used to successfully determine a sailcraft's achievable accelerations, their implementation also entails a number of operational difficulties to be taken into account. Among these, five are deemed of particular importance:

- Altitude decrease. Implementing the CSLs can yield considerable changes in the sailcraft's orbital parameters. Among these, the most significant is the decrease in orbital altitude, which is particularly evident for steering laws yielding a large aerodynamic drag.
- Solar-sail attitude rate of change. Some CSLs require rapid changes of attitude which can prove demanding for the attitude control system of the sailcraft.
- Exposure of the sail's back side to sunlight. Solar sails usually consist of a polymer film membrane covered with an aluminum coating on the front side in order to enhance reflectivity. Since the sail's back side is generally not illuminated, it is either left uncoated or has a chromium coating, so as to increase the sail's emissivity for thermal control [1, 20]. However, some CSLs allow the sail's back side to be

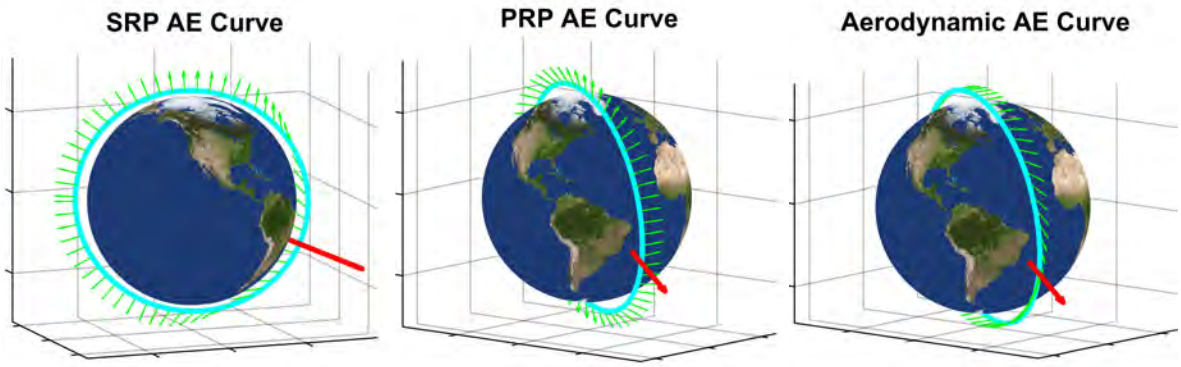

Fig. 4. Steering laws to calibrate the SRP, PRP, and aerodynamic AE curves for the ACS3 sailcraft orbit with local time of the ascending node at 12AM. The light blue curve, red arrow, and green arrows indicate the sailcraft orbit, Earth-to-Sun direction, and sail normal directions, respectively.

exposed to sunlight. When this occurs, ultraviolet radiation yields a rapid degradation of the sail material and its optical properties. It should be noted that since in this paper a double-coated, perfectly reflecting solar sail is considered, see Section 2.1, this degradation effects are not accounted for in the dynamics. Nevertheless, the analyses presented later in this section will provide insights on the frequency of exposure of the sail's back side to sunlight, so as to quantify its potential effect on real-life solar-sail missions to a first-order extent.

- Exposure of the sail's back side to the ram direction. In addition to sunlight, the sail's back side can experience rapid degradation also when exposed to the ram direction, i.e., the direction of motion. This is due to the effect of atomic oxygen, which deteriorates the sail's back side material upon impact, creating cracks in the polymer/chromium film. Although the dynamical model used in this paper does not account for these degradation effects, see Section 2, the analyses presented later in this section will provide insights on the frequency of exposure of the sail's back side to the ram direction, so as to quantify its potential effect on real-life sailcraft missions to a first-order extent.
- Power generation. In this paper, it is assumed that solar cells are mounted on the sailcraft in a plane parallel to the sail membrane, i.e., the solar cells generate power when the sail's front side is illuminated. Conversely, no power is produced when the sailcraft is oriented edgewise with respect to the direction of sunlight nor when its back side is exposed. Although these conditions can be endured for short periods of time, some CSLs require prolonged periods of times in which the sail attitude is such that the solar arrays are not exposed to sunlight, thus implying potential power issues.

The analyses presented in this section make use of NASA's ACS3 mission as baseline scenario, with a characteristic acceleration of $a_c = 0.045$ mm/s^2 and the following vector of initial orbital elements defined in frame $\mathcal{G}(x, y, z)$:

$$\left[a_0, e_0, i_0, \Omega_0, \omega_0, f_0\right]^T = \left[7093.1363 \text{ km}, 0, 98.249 \text{ deg}, \begin{Bmatrix} 157.328 \\ 202.328 \\ 247.328 \end{Bmatrix} \text{deg}, 0 \text{ deg}, 0 \text{ deg}\right]^T \quad (9)$$

where a_0, e_0, i_0, Ω_0, ω_0, and f_0 represent the initial orbit's semi-major axis, eccentricity, inclination, right ascension of the ascending node (RAAN), argument of pericenter, and true anomaly, respectively. The orbital elements in Eq. (9) identify a circular, Sun-synchronous orbit with an initial altitude of $h_0 = a_0 - R = 715$ km. In order to consider different orbit orientation with respect to sunlight, three values of the RAAN are considered, which correspond to local times of the ascending node (LTANs) at 6AM, 9AM, and 12AM. For each of these initial orbits and each CSL presented in Section 3, the dynamics given in Eq. (1) have been propagated using Matlab®'s *ode45* integrator, with absolute and relative tolerances set to 10^{-12}. The analyses consider a simulation start date of December 1st, 2023 (i.e., the expected deployment date of the sail) and a simulation duration of 10 days. Finally, to account for realistic solar-sail attitude-change capabilities, the CSLs have been implemented considering the ACS3 sailcraft's maximum attitude rate of change (RoC), equal to 0.5 deg/s.

Table 1 presents the results of the analyses for each combination of initial LTAN and CSL. In order to provide insights into the calibration of the target acceleration and perturbing effects of the other accelerations, the three columns on the left-hand side of the table specify the extent to which each AE curve is covered when employing a specific CSL. The acceleration to be calibrated (referred to as "calibration target") is displayed in bold, while the perturbing accelerations are given in brackets. Here, the terms "Max" and "Zero" indicate that a particular acceleration is constantly equal to its maximum achievable value or zero, respectively. Similarly, in the case a CSL covers a larger portion of the AE curve, the terms "Full", "Intermediate", and "Minor" are given, which indicate that the calibration target/perturbing AE curve is covered completely, partially, or only to a minor extent. The right-hand side of the table provides information on the operational difficulties introduced at the beginning of this section. Here, the altitude loss due to implementing the given CSL for 10 days, Δh, is shown, as well as the maximum attitude RoC. To quantify the effect the CSLs have on the degradation of the sail, two columns are added which provide the percentage of orbital period during which the sail's back side is exposed to sunlight and the ram direction. In a similar fashion, to measure the effect each steering law has on the sailcraft power-generation capabilities, the percentage of orbital period during which the sail's front side is exposed to sunlight with a pitch angle smaller than 80 deg is given. Finally, to enable a qualitative overview of the benefits and drawbacks of each CSLs, a color code has been applied to the data of Table 1, with green representing benefits and yellow, orange, and red indicating potential issues of increasing degree of severity.

As can be seen in the table, calibration of the maximum SRP acceleration and its AE curve can prove challenging due to multiple reasons. To begin with, the sailcraft experiences significant perturbations from the aerodynamic and PRP accelerations for increasing values of the initial LTAN, which lead to moderate decreases in altitude in the range 7.6-12.1 km. Furthermore,

Table 1. Calibration capabilities and implementation challenges of the calibration steering laws for different initial LTANs.

CSL	Initial LTAN	**Calibration Target** (Perturbation)			Δh [km]	Max. Attitude RoC [deg/s]	Sail's Back Side Exposure [% orbital period]		Solar Cells' Exposure to Sunlight ($\alpha \leq 80$ deg) [% orbital period]
		SRP Acc.	PRP Acc.	Aerodyn. Acc.			Sunlight	Ram direction	
Max. SRP Acc.	6 AM	**Max**	(Minor)	(Minor)	7.656	0	0	50	83.18
	9 AM	**Max**	(Intermediate)	(Intermediate)	9.736	0.5	0	36.08	68.21
	12 AM	**Max**	(Full)	(Full)	12.106	0.5	0	34.23	64.34
Max. PRP Acc.	6 AM	(Minor)	**Max**	(Zero)	0.013	0.061	50	0	21.87
	9 AM	(Intermediate)	**Max**	(Zero)	0.016	0.061	50	0	11.27
	12 AM	(Full)	**Max**	(Zero)	0.012	0.061	50	0	08.75
Max. Aerodyn. Acc.	6 AM	(Minor)	(Zero)	**Max**	36.985	0.061	41.63	0	36.00
	9 AM	(Intermediate)	(Zero)	**Max**	36.705	0.061	34.06	0	30.61
	12 AM	(Full)	(Zero)	**Max**	36.440	0.061	32.21	0	29.27
SRP AE Curve	6 AM	**Full**	(Full)	(Intermediate)	8.379	0.061	0	50	71.99
	9 AM	**Full**	(Full)	(Intermediate)	8.308	0.061	0	25	55.60
	12 AM	**Full**	(Full)	(Full)	9.282	0.061	0	25	53.24
PRP AE Curve	6 AM	(Full)	**Full**	(Zero)	0.006	0.086	50	0	28.93
	9 AM	(Intermediate)	**Full**	(Zero)	0.013	0.086	50	0	14.13
	12 AM	(Intermediate)	**Full**	(Zero)	0.007	0.086	48.36	0	08.41
Aerodyn. AE Curve	6 AM	(Full)	(Zero)	**Full**	17.961	0.096	41.63	0	39.53
	9 AM	(Intermediate)	(Zero)	**Full**	19.193	0.086	34.07	0	32.13
	12 AM	(Intermediate)	(Zero)	**Full**	19.594	0.086	32.05	0	21.70
Residual	12 AM	**Zero**	**Zero**	**Zero**	0.002	0	0	0	0

exposure of the sail's back side to the ram direction for long periods of time also occurs and, for the maximum SRP acceleration CSLs, a large attitude RoC may also be required. The CSLs for the maximum aerodynamic and PRP accelerations present common challenges due to the significant perturbation from SRP (especially for larger initial LTANs) and the prolonged exposure of the sail's backside to sunlight. Both these CSLs imply potential power issues, as the sail's front side is exposed to sunlight only for a limited time. This is particularly evident when calibrating the maximum PRP acceleration, as the sail has its front side constantly facing the Earth, therefore allowing little sunlight to illuminate it. The CSL for the maximum aerodynamic acceleration, on the other hand, presents another major disadvantage, that is, the deorbiting effect on the orbit. This happens because drag is maximized, therefore yielding a rapid loss in altitude in the order of 36 km. It should be noted that this large value of Δh is also due to the simulation start time considered. Indeed, because on December 1st, 2023 high solar activity is expected, the atmospheric density is high and, therefore, aerodynamic drag is significant. The steering laws to calibrate the PRP and aerodynamic AE curves present potential problems similar to the CSLs for the maximum PRP and aerodynamic accelerations. Large perturbations by the SRP are experienced and, once again, the sail's backside is exposed to sunlight frequently. The CSL for the PRP AE curve also yields short time windows in which the solar cells can generate power, whereas, on the other hand, the CSL for the aerodynamic AE curve yields large altitude loss, in the order of 19 km. The results in Table 1 also highlight an interesting property of the PRP and aerodynamic accelerations, that is, their orthogonality. Indeed, because the analyses in this section consider circular initial orbits, the radial and velocity directions are roughly perpendicular at all times during the propagations. This implies that it is always possible to design CSLs for which the PRP or aerodynamic acceleration is varied while the other is left unchanged. Because of this, in Table 1 the steering laws to calibrate the aerodynamic acceleration show that PRP never perturbs the dynamics. In a similar fashion, for the CSLs for the PRP acceleration, aerodynamic drag is always equal to zero. Finally, the CSL to quantify the residual accelerations only implies one major operational challenges, that is, the fact that sunlight never illuminates the sail's front side and no power can be generated. This is due to the particular attitude of the sail, which is constantly oriented edgewise with respect to sunlight. It is also worth noting that, to implement this CSL, the sail must be oriented edgewise also with respect to the velocity and the radial directions. These three conditions can be met only if an initial LTAN at 12AM is considered, which is the reason for which no simulation has been performed for this CSL with LTANs at 6AM and 9AM.

Although the operational constraints given in Table 1 may render the adoption of the CSLs more challenging, it should be noted that they do not necessarily constitute killer requirements for the implementation of these control strategies. For example, the CSLs requiring a large attitude RoC of 0.5 deg/s may be implemented allowing for a slower re-orientation of the sail when entering the eclipse region, so as to

decrease the attitude RoC and, therefore, the effort required by the sailcraft attitude control systems. Furthermore, even though exposure of the sail's back side to the ram direction and/or sunlight has a detrimental effect on the sail's material, it should be noted that these situations may be endured for a certain period of time, thus still allowing for the calibration of the solar-sail accelerations. In a similar fashion, CSLs that involve a large loss of altitude or inability to generate power may also be implemented for short periods of time. Nevertheless, because these constraints are deemed the most severe, implementing CSLs that entail loss of altitude and inability to generate power may only be possible for sailcraft with sufficiently large characteristic accelerations and energy storage capacities.

5. Conclusions

This paper provided a first-order investigation on strategies to calibrate the accelerations experienced by real-life solar sails in Earth-bound orbits, with particular focus on the solar radiation pressure (SRP), planetary radiation pressure (PRP), and aerodynamic accelerations. To quantify the maximum magnitude of these accelerations and their variation with the sail attitude, several calibration steering laws (CSLs) have been presented. Also, to assess the calibration capabilities of these steering laws, several analyses have been conducted using NASA's upcoming ACS3 mission as baseline scenario. The results show that the calibration of the SRP acceleration is more easily achieved for dawn-dusk sun-synchronous orbits than for other sun-synchronous orbits, as in the former case the PRP and aerodynamic accelerations affect the dynamics less severely. Indeed, for noon-midnight orbits, the PRP and aerodynamic accelerations produce larger perturbations which render the calibration process more challenging. Similarly, when the CSLs for the PRP and aerodynamic accelerations are employed, SRP represents a source of disturbance which hinders their calibration, regardless of the orbit's orientation. The analyses performed also highlighted practical implementation challenges of the CSLs. Indeed, it was found that the CSLs for the SRP acceleration can require rapid changes of attitude, which may prove challenging for the sailcraft's attitude control system. Furthermore, these CSLs also entail a prolonged exposure of the sail's back side to incoming atmospheric particles, which accelerates the sail's material degradation. Sail degradation also takes place when the CSLs for the PRP and aerodynamic accelerations are employed, as the sail's back side is often exposed to sunlight. Implementing these steering laws also entails potential issues for power generation, as the sailcraft's solar arrays are hardly exposed to sunlight along the orbit. Finally, it was found that the most challenging CSLs for orbital stability are the ones to calibrate the aerodynamic acceleration, as significant drag is generated during calibration and rapid altitude losses are achieved, even in the order of 3.6 km per day. Altitude loss and inability to generate power are considered the most crucial constraints that can hinder the implementation of the CSLs. As a consequence, the CSLs for the PRP and aerodynamic accelerations are deemed the most challenging to implement, whereas the CSL for the SRP acceleration proves to be more easily implementable.

References

[1] C. R. McInnes, Solar Sailing - Technology, Dynamics and Mission Applications, Springer, 2004.

[2] D. A. Spencer, L. Johnson and A. C. Long, "Solar sailing technology challenges," *Aerospace Science and Technology,* vol. 93, 2019. DOI: 10.1016/j.ast.2019.07.009.

[3] M. Macdonald and C. R. McInnes, "Solar Sail Science Mission Applications and Advancement," *Advances in Space Research,* pp. 1702-1716, 2011. DOI: 10.1016/j.asr.2011.03.018.

[4] W. K. Wilkie, J. M. Fernandez, O. R. Stohlman and et al., "An Overview of the NASA Advanced Composite Solar Sail (ACS3) Technology Demonstration Project," *AIAA Scitech 2021 Forum,* 2021.

[5] L. Carzana, P. Visser and J. Heiligers, "Locally optimal control laws for Earth-bound solar sailing with atmospheric drag," *Aerospace Science and Technology,* vol. 127, no. 107666, 2022. DOI: 10.1016/j.ast.2022.107666.

[6] L. Carzana, P. Visser and J. Heiligers, "A New Model for the Planetary Radiation Pressure Acceleration for Solar Sails," *under review at the Journal of Guidance, Control, and Dynamics,* 2023.

[7] B. Wie, "Solar Sail Attitude Control and Dynamics, Part 1," *Journal of Guidance, Control, and Dynamics,* vol. 27, no. 4, pp. 526-535, 2004.

[8] M. Macdonald, Advances in Solar Sailing, Springer, 2014, pp. 95-113.

[9] V. Stolbunov, M. Ceriotti, C. Colombo and C. R. McInnes, "Optimal Law for Inclination Change in an Atmosphere Through Solar Sailing," *Journal of Guidance, Control, and Dynamics,* vol. 36, no. 5, pp. 1310-1323, 2013. DOI: 10.2514/1.59931.

[10] G. Mengali and A. A. Quarta, "Near-Optimal Solar-Sail Orbit-Raising from Low Earth Orbit," *Journal of Spacecraft and Rockets,* vol. 42, no. 5, pp. 954-958, 2005. DOI: 10.2514/1.14184.

[11] A. Barles, M. Ceriotti, F. Ciampa and L. Felicetti, "An Optimal Steering Law for Sailing with Solar and Planetary Radiation Pressure," *Aerospace Science and Technology,* vol. 118, 2021. DOI: 10.1016/j.ast.2021.107051.

[12] A. De Iuliis, F. Ciampa, L. Felicetti and M. Ceriotti, "Sailing with Solar and Planetary Radiation Pressure," in *Proceedings of ISSS 2019: 5th International Symposium on Solar Sailing*, Aachen, Germany, 2019. DOI: 10.1016/j.asr.2019.11.036.

[13] J. R. Wertz and W. J. Larson, Space Mission Analysis and Design, El Segundo: Microcosm Press and Dordrecht: Kluwer Academic Publishers, 2005.

[14] E. Tiesinga, P. J. Mohr, D. B. Newell and B. N. Taylor, "CODATA recommended values of the fundamental physical constants: 2018," *Reviews of Modern Physics,* vol. 93, 2021. DOI: 10.1103/RevModPhys.93.025010.

[15] J. A. Storch, "Aerodynamic Disturbances on Spacecraft in Free-Molecular Flow," The Aerospace Corporation, 2002.

[16] P. C. Hughes, Spacecraft Attitude Dynamics, New York: Dover Publications Inc., 2004.

[17] L. Carzana, P. Visser and J. Heiligers, "A New Model for the Planetary Radiation Pressure Acceleration for Solar Sails," in *2022 AAS/AIAA Astrodynamics Specialist Conference [AAS 22-715]*, Charlotte, North Carolina, United States of America, 2022.

[18] K. F. Wakker, Fundamentals of Astrodynamics, Delft, The Netherlands: Delft University of Technology, Institutional Repository, 2015.

[19] R. S. Nerem et al., "Gravity Model Development for TOPEX/POSEIDON: Joint Gravity Models 1 and 2," *Journal of Geophysical Research,* vol. 99, no. C12, pp. 24,421-24,447, 1994. DOI: 10.1029/94JC01376.

[20] J. Ho Kang et al., "Durability characterization of mechanical interfaces in solar sail membrane structures," *Advances in Space Research,* vol. 67, no. 9, pp. 2643-2654, 2021.

A Solar Sail Shape Modeling Approach for Attitude Control Design and Analysis

Benjamin M. GAUVAIN[a,*], Daniel A. TYLER[a]

[a]*NASA Marshall Space Flight Center, Huntsville, Alabama, USA*

Abstract

Solar sails operating in the space environment experience deformations in sail shape that result in relatively large disturbance torques which dictate the required performance of the spacecraft attitude control and momentum management systems. These deformations are driven by thermal loads on the booms (due to uneven solar heating), manufacturing and assembly tolerances, and variations in membrane tension. The Solar Cruiser spacecraft utilizes a four-quadrant sail design with four 30-meter length booms and four triangular sail membranes, creating a square sail structure of >1600 m^2. Medium-fidelity mesh models were developed based on a characteristic deformed shape. A series of parametric studies were conducted using this shape paradigm to determine worst-case deformed sail shapes which produce bounding disturbance torques. A large database of shapes was produced, and the forces and moments induced by each individual shape were calculated using a Rios-Reyes reduced order generalized sail model [1]. Two were selected as reference worst-case shapes for the Solar Cruiser mission: one which produced the highest pitch/yaw root-sum-squared (RSS) torque, and one which produced the highest roll torque. The results showed that the worst-case shapes at high solar incidence angles induce significantly higher (2-10x) disturbance torques than an ideal, flat-plate sail. Even with considerable safety margins, assuming an ideal sail is unlikely to sufficiently bound the disturbances, which is critical when designing the attitude control system and sizing actuators. Accurate sail shape modeling methodologies should therefore be employed on future solar sail missions.

Keywords: Solar, Sail, Model, Attitude, Control

Nomenclature

AMT	Active Mass Translator
CM	Center of Mass
CP	Center of Pressure
FEEP	Field Emission Electric Propulsion
FEM	Finite Element Model
IFM	Indium FEEP Micro-thrusters
NEA	Near-Earth Asteroid
PDLC	Polymer-Dispersed Liquid Crystal
RCD	Reflectivity Control Device
RCS	Reaction Control System
RW	Reaction Wheel
SIA	Solar Incidence Angle
SRP	Solar Radiation Pressure
$\tilde{r}$	total reflectivity
s	specular reflectivity fraction
Bf	front side non-Lambertian coefficient
Bb	back side non-Lambertian coefficient
ef	front side emissivity
eb	back side emissivity

1. Introduction

SRP-induced disturbance torques are a major design driver for solar sails, impacting the architecture and design of the attitude control system, including control actuators and momentum management actuators. Traditionally, CM/CP offset of a flat sail has been the primary or sole metric for predicting disturbance torques and sizing systems accordingly [2]. However, it was discovered during development of the NEA Scout mission that deformed sail shape effects were a significant contributor to the overall SRP-induced disturbance torques [3]. A mesh model of the sail produced from a structural FEM was transformed into a reduced-order Rios-Reyes/Scheeres generalized sail tensor model [1] to efficiently calculate the forces and torques on the sail at varying sun-relative attitudes which resulted in a significant increase in the predicted magnitude of disturbance torques, especially about the roll axis, under worst-case conditions. The NEA Scout

* Corresponding author, benjamin.m.gauvain@nasa.gov

model was scaled and adapted for Solar Cruiser with the addition of further sail shape model manipulations to capture boom tip deflections and uncertainties specific to the Solar Cruiser sail.

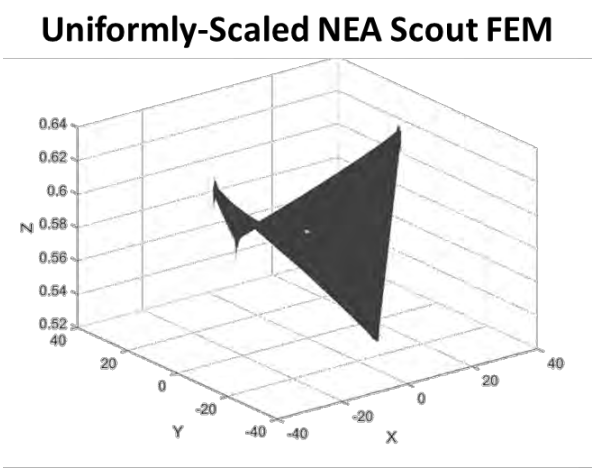

Figure 1. Scaled NEA Scout Deformed Sail Model

This process uncovered additional sensitivities of the disturbance torques to characteristics of the sail shape, namely the impact of boom tip deflection uncertainty on disturbance torques. It also showed that out-of-plane tip deflections were the biggest driver of disturbance torques, inducing magnitudes >5x for a flat sail of identical dimensions, and >2x for an identical sail with in-plane tip deflections only.

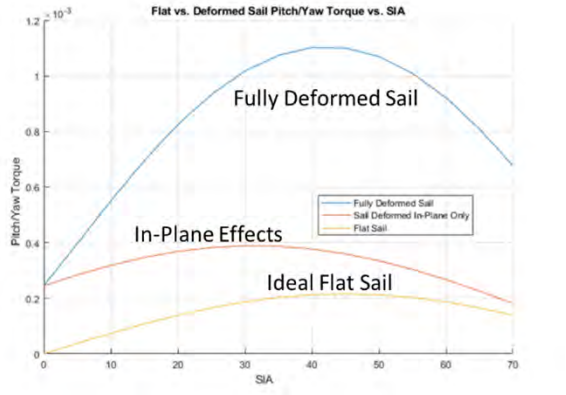

Figure 2. Dist. Torque Comparison, Scaled NEA Scout Model

However, this shape modeling approach was still fairly limited in flexibility and fidelity, given that it merely involved scaling the NEA Scout model, and left a lot of uncertainty in its ability to bound the problem. Thus, a more detailed approach was developed and implemented for Solar Cruiser that involves a wide parametric sweep over several key design parameters, predominantly related to sail shape, to improve the likelihood that the predicted disturbance torques are properly bounded during development.

2. Methodology

2.1. Process Overview

The strongest determinant of the sail shape is the deflection of each of the four booms. By far the largest known and predictable effect on boom deflections is the thermal gradient across the booms in the out-of-plane direction, from the sun-facing side (front) to the space-facing side (back). The resulting boom deflections, measured at the tip for simplicity, define the "nominal" sail shape which is used to create the initial deformed sail mesh before applying uncertainty/error terms. For Solar Cruiser, thermal analyses were conducted at various representative attitudes, including 0 to 17 degrees SIA (the range for its mission profile) with both "corner-on" and "edge-on" rotations, or clock angles of 0 and 45 degrees, respectively. The resulting thermal loads were applied to a structural FEM, and the resulting boom tip deflections were captured and tabulated. The case with the largest average boom tip deflections was chosen for conservatism.

With the nominal boom tip deflections defined, it was then necessary to identify other possible uncertainty/error terms. The uncertainties selected for this study include boom tip error, membrane deflections, and center of mass offsets, as described in Table 1.

Table 1. Deformation Uncertainty Parameter Descriptions

Parameter	Description
Membrane Deflections	Out-of-plane, billowing shape with peak/trough at the centroid of each quadrant. The magnitude was varied, and the direction varied in the sail out-of-plane axis.
Nominal Boom Tip Deflections	Out-of-plane, increasing parabolically from root to tip. The magnitude and direction (out of the sail plane and toward the sun) were held constant.
Boom Tip Deflection Errors	Random/uncertain out-of-plane boom tip deflections due to manufacturing and assembly tolerances, tension changes in the membrane, and thermal load uncertainties. The magnitude was varied, and the direction varied in the sail out-of-plane axis.
In-Plane Center of Mass (CM) Offsets	The difference in the center of mass in-plane position with the AMT homed relative to the designed geometric center, due to manufacturing and assembly tolerances.
Attitude	SIA varied from 0 to 17 degrees (target for Plane Change Demonstration) and clock angle varied from 0 to 360 degrees.

The parameter variations for these uncertainty terms are summarized in Table 2. Membrane deflections of up to 5 cm at the quadrant centroid were chosen as the maximum billowing amount, while tip error was varied

up to a 100% increase for conservatism. The maximum CM offset magnitude is based on sail manufacturability and was determined through discussion with the solar sail system prime contractor. All boom tip deflections were applied in the out-of-plane (z-axis/roll) direction only, to reduce model complexity; previous modeling efforts had shown (Fig. 2) that in-plane (x-axis/pitch, y-axis/yaw) deflections have a significantly smaller impact on disturbance torques compared to out-of-plane deflections. It is also expected that modeling membrane billowing will capture the reduced tension occurring across a quadrant from two booms deflecting closer relative to each other.

Table 2. Deformation Uncertainty Parameter Variations

Parameter	Tip Error Factor	Mem. Billow	CM Offset	Tip Direction Factor	Mem. Direction Factor
Variation	0	0 cm	0 cm	1x	-1x
	1x	1 cm	+/-1 cm X-axis	Tip A +/-1x	Membrane A +/-1x
	1.25x	2 cm	+/-2 cm X-axis	Tip B +/-1x	Membrane B +/-1x
	1.5x	3 cm	+/-1 cm Y-axis	Tip C +/-1x	Membrane C +/-1x
	1.75x	4 cm	+/-2 cm Y-axis	Tip D +/-1x	Membrane D +/-1x
	2.0x	5 cm	-	-	-

Deformed sail mesh models were created by modifying a flat sail mesh according to shape functions and geometric boundary conditions summarized in Table 1 and detailed in Section 2.2. A large parametric sweep was then conducted over uncertainty/error terms, with each combination producing a mesh model. This produced a large database of mesh models, all of which were transformed into a reduced-order Rios-Reyes generalized sail tensor model [1], as with NEA Scout. Finally, the SRP-induced forces and torques were calculated across the range of Solar Cruiser sun-relative mission attitudes, which included clock angle variations of 0 to 360 degrees and solar incidence angles of 0 to 17 degrees. The sail optical properties used for force and torque calculations were determined from prior NEA Scout optical testing conducted by NASA in 2015 which analyzed the effect of wrinkles on the specular fraction of reflection [3], shown below in Table 3.

Table 3. Reflectivity Coefficients

Coefficient	$\tilde{r}$	s	B_f	B_b	e_f	e_b
Value	0.91	0.89	0.79	0.67	0.025	0.27

Post-processing of the force and torque data was then done to identify two worst-case sail shapes: one which induced the largest pitch/yaw root-sum-squared torque, and one which induced the largest roll torque. Because in-plane disturbance torques are sensitive to different sail deformation parameters than out-of-plane disturbance torques, one deformed shape does not adequately bound both cases. Solar Cruiser utilized separate devices for momentum management in the pitch/yaw axes and roll axis. Sizing and design considerations for each axis are dependent on the maximum disturbance torque associated with the corresponding shape. Therefore, to adequately design the Solar Cruiser control and momentum management actuators, it was necessary to account for both possible shapes. Fig. 3 illustrates the functional process flow of the Solar Cruiser modeling methodology.

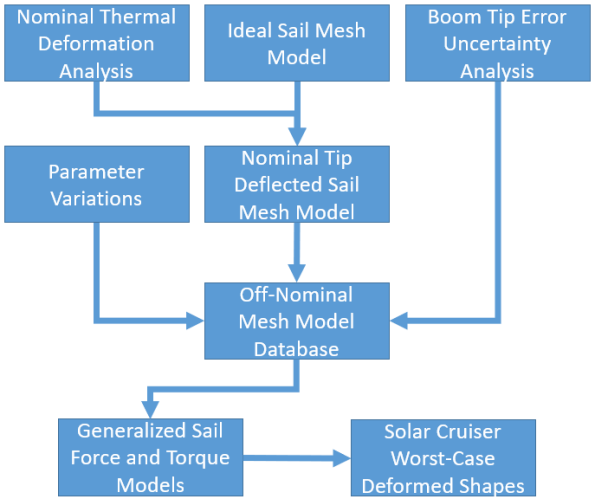

Figure 3. Model Methodology Process Flow

2.2. *Boundary Conditions and Assumptions*

In order to create the database of off-nominal, deformed sail shapes, a flat sail mesh model with Solar Cruiser dimensions was used as the starting point; deformed shapes were synthesized by applying changes to the z-axis location of each point in the mesh according to geometric shape functions with boundary conditions based on expected deformation patterns (e.g., parabolic booms and billowing membranes).

The out-of-plane deflection of a point p on a sail quadrant between booms *i* and *i+1* (where *i* ranges from 1 to 4) can be written as:

$$\Delta z_p = f\left(\mathrm{r}, \theta, \Delta Z_{tip\,i}, \Delta Z_{tip\,i+1}, \Delta Z_{billow,max}\right) \quad (1)$$

The boundary conditions at the edges of each membrane are defined such that they follow a parabolic curve from the centroid of the sailcraft to the tip of the adjoining boom, according to:

$$\Delta z_{edge\,i}(r) = \Delta Z_{tip\,i} \left(\frac{r}{L}\right)^2 \quad (2)$$

Where r is the radial distance from the sailcraft centroid of a point along the edge and L is the total length of the edge. The parabolic curve is chosen due to its conservatism indicated in an early sensitivity study comparing linear and quadratic deflections vs. radial distance.

The out-of-plane deflections for a point p on the membrane resulting from the boom boundary conditions, disregarding billowing effects, is derived by interpolating between the two edges along curves of constant radial distance from the centroid, as follows:

$$\Delta z_{p,base}(r,\theta) = \Delta Z_{tip\,i}\left(\frac{r}{L}\right)^2 + \frac{\theta-\theta_{edge\,i}}{\theta_{edge\,i+1}-\theta_{edge\,i}}\left(\Delta Z_{tip\,i+1} - \Delta Z_{tip\,i}\right)\left(\frac{r}{L}\right)^2 \quad (3)$$

$$\Rightarrow \Delta z_{p,base}\left(r,\theta_{edge\,i}\right) = \Delta z_{edge\,i}(r) \quad (4)$$

$$\Delta z_{p,base}\left(r,\theta_{edge\,i+1}\right) = \Delta z_{edge\,i+1}(r) \quad (5)$$

Finally, the effect of billowing is added using a boundary condition to constrain the out-of-plane billowing at the centroid of the triangular sail quadrant – located along the line from the vertex at the sailcraft centroid to the midspan of the distal edge, 2/3 of this length from the vertex – to be equal to the maximum billowing deflection magnitude for that membrane. The shape of the membrane out-of-plane deflection due to billowing smoothly connects this membrane centroid location to the previous defined membrane boundaries and is superimposed on the base deflection ($\Delta z_{p,base}$). This shape is modeled as a two-dimensional sinusoid as a function of radial location, r, and angular location, θ, in polar coordinates in the sail plane, according to Eq. (6) below, given the smooth transition between boundaries. Note, however, that this specific "shape function" is not necessarily reflective of physically realistic shapes.

$$\Delta z_{p,billow}(r,\theta) = \Delta Z_{billow,\max}\left|\sin\left(\frac{r}{\frac{2}{3}\left(\frac{L}{\sqrt{2}}\right)}\frac{\pi}{2}\right)\times \sin\left(\frac{\theta-\theta_{edge\,i}}{\theta_{edge\,i+1}-\theta_{edge\,i}}\pi\right)\right| \quad (6)$$

$$\Rightarrow \Delta z_{p,billow}\left(\frac{2}{3}\left(\frac{L}{\sqrt{2}}\right), \frac{\theta_{edge\,i}+\theta_{edge\,i+1}}{2}\right) = \Delta Z_{billow,\max} \quad (7)$$

Thus, the total out-of-plane deflection of any point on the membrane of the sail is calculated using the expression:

$$\Delta z_p(r,\theta) = \Delta z_{p,base}(r,\theta) + \Delta z_{p,billow}(r,\theta) \quad (8)$$

Other modeling assumptions in addition to the geometric boundary conditions:

- Non-sail membrane surfaces (including shadowing of the sail membranes by such), sail membrane wrinkles (which are not directly modeled, but captured via optical properties), and in-plane deformations or asymmetries of any kind are assumed to contribute a negligible amount to solar forces and torques relative to out-of-plane deflections of the sail membranes and are, therefore, excluded from the sail shape model.
- The sail membranes are modeled with a fixed-fixed interface to the booms at the roots and tips without any separation (e.g., free membrane inner diameter) or interference (e.g., catenary-boom rubbing).
- Boom tips and sail membranes can deflect out of plane in any arbitrary direction with respect to each other. The effect of out-of-plane deformations on the in-plane dimensions of sail elements (due to elongation, relaxation, or obliqueness) is neglected.
- The function used to calculate out-of-plane deformation at a node as a function of in-plane location, given some boom tip and sail membrane deformation magnitudes, is derived with the only constraint being that the boundary conditions dictated by the "fixed-fixed" assumption stated above and the sail membrane deformation magnitudes are met and without regards to any structural modeling.

3. Results and Discussion

3.1. Worst-Case Sail Shape Results

The disturbance torques induced by the Solar Cruiser worst-case shapes are shown in Fig. 4 and 5. Torques are plotted across the range of Solar Cruiser mission design attitudes (clock angles up to 360 degrees and SIA up to 17 degrees). Note that the relationship between torque, SIA, and clock angles inform mission operational considerations; clock angles can be commanded which minimize the induced disturbances while maintaining the required SIA for mission design. Additionally, at higher SIAs, the worst-case roll shape contains a zero crossing where torque can be completely eliminated. The torque curves obtained from this study are due to theoretical shapes; in practice, the efficacy of

clock angle control approaches depends on accurate sail characterization on-orbit after sail deployment.

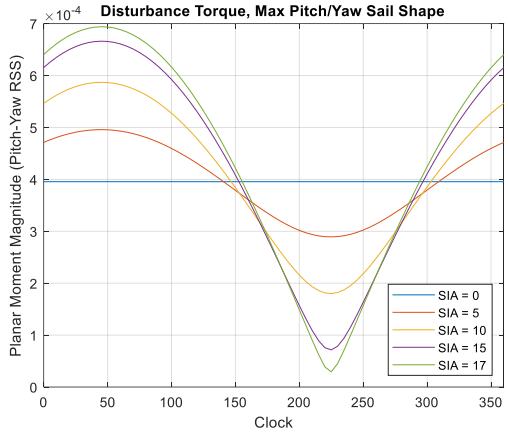

Figure 4. Max Pitch/Yaw Disturbance Torque

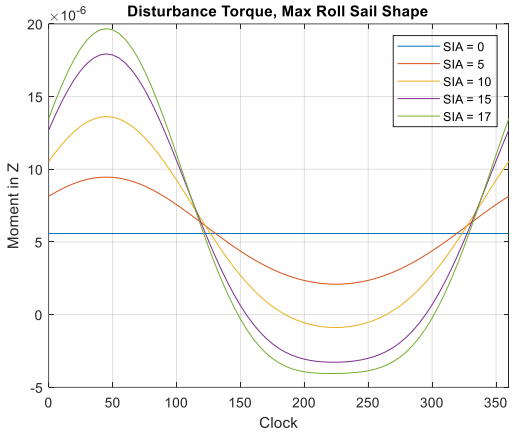

Figure 5. Max Roll Disturbance Torque

Plots of the worst-case sail mesh models are shown below in Fig. 6 and 7. The z-axis scale is amplified to illustrate how the deformations affect global sail shape.

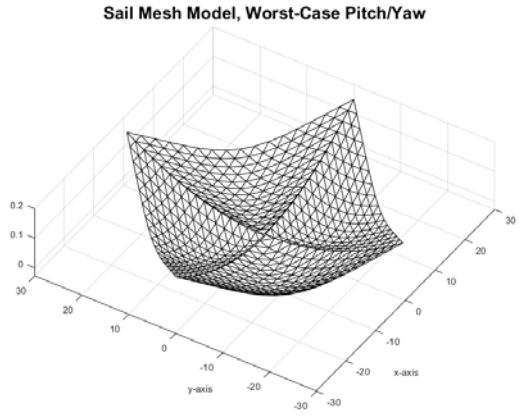

Figure 6. Solar Cruiser Worst-Case Pitch/Yaw Shape

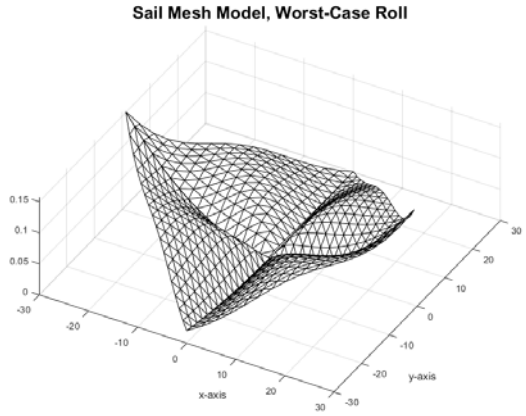

Figure 7. Solar Cruiser Worst-Case Roll Shape

The deformed sail shapes show significantly higher disturbance torques than an ideal flat sail, as shown in Fig. 8 and 9, for the updated medium-fidelity Solar Cruiser shapes. The worst-case maximum roll torque for the characteristic roll shape is a factor of 2.06 higher; this exceeds even the conservative amounts of margin typically carried in the early concept phases of missions. It is worth noting that increasing the model fidelity reduced the expected worst-case disturbance torques compared to the early mission low-fidelity scaled NEA Scout models; however, this was largely driven by increased model fidelity in the thermal analyses resulting in lower nominal boom tip deflections. This benefit was specific to the Solar Cruiser configuration and mission design.

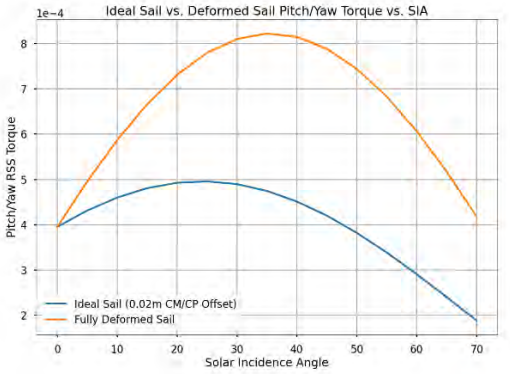

Figure 8. Ideal vs. Deformed Sail Comparison, Pitch/Yaw

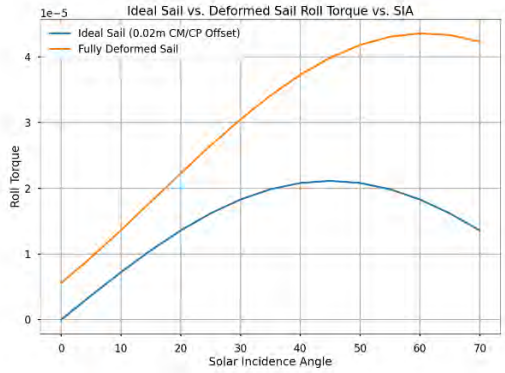

Figure 9. Ideal vs. Deformed Sail Comparison, Roll

3.2. Solar Cruiser Design Considerations

The development of the final worst-case sail models and subsequent torque predictions impacted the Solar Cruiser design and analysis cycle. These models were used to bound the expected SRP-induced disturbance torque. The disturbance torque values affected requirements derivation. Sail shape requirements were determined to ensure the as-manufactured flight sail deformations would remain within the modeled deformations. The predicted disturbance torques were used, in addition to other expected disturbances and slew rate capability requirements, to define the reaction wheel torque capability requirement.

The worst-case pitch/yaw torque predictions were used to define requirements for the momentum management systems. To desaturate momentum in the pitch/yaw (in-plane) axes, Solar Cruiser utilized an AMT, which separates the spacecraft bus from the sail using rails and drive motors, allowing changes in the center of mass with respect to the center of pressure applied to the sail from SRP [4], inducing a torque. The deformed sail disturbance predictions drive design considerations such as AMT range of motion, rail orientation, and bus mass allocation; a higher mass ratio between the bus and sail sides of separation yields better AMT performance.

For roll momentum management, Solar Cruiser utilized two actuator systems: RCDs and IFMs. RCDs contain electroactive PDLC materials which vary reflectivity when a voltage is applied; by orienting the RCDs at a tented angle relative to the sail plane and varying geometrically opposed RCD on/off states, torques about the roll axis can be imparted [4]. The IFMs fulfill the same role as that of a traditional RCS system, allowing RW desaturation in the event of RCD underperformance. Roll torque predictions drive requirements on RCD surface area, as well as IFM/RCS propellant mass needed.

To verify requirements and conduct design and analysis cycles, a sailcraft integrated model was developed which incorporates plant dynamics as well as a control system and flight software model. The worst-case torque predictions were integrated into this model using the Rios-Reyes generalized sail tensors, allowing computationally efficient force and torque calculation at simulated attitudes.

4. Conclusions and Forward Work

4.1. Conclusions

The deformed sail model results demonstrate considerably higher expected induced disturbance torques compared to the simplified assumption of a flat plate sail with a CM/CP offset. Accurate prediction of these disturbances is crucial when designing the spacecraft attitude control system. The reaction wheels (or other primary control actuator) must have sufficient torque capability to achieve a control authority >1, plus program-dependent margin. Similarly, the momentum management system must be sized accordingly. As disturbance torques grow with increasing SIA, more momentum management capacity is needed to prevent RW saturation. If the spacecraft uses an RCS for RW desaturation, this will result in additional propellant mass to meet mission objectives. As all required masses grow (control actuators, momentum management actuators, propellant mass, bus mass) the sailcraft characteristic acceleration decreases. Thus, sail deformations are a significant driver of the mission and sailcraft design. Because of the compounding effect of sail deformations on all aspects of the design, it is recommended to begin medium/high fidelity modeling as early as possible in the design cycle, even in the early mission concept phase.

4.2. Forward Work

The approach detailed in this paper yields a medium-fidelity model where inputs and assumptions on local conditions (e.g., nominal boom tip deflection, tip error uncertainty, and membrane deflection) drive the global sail shape. Forward work is currently ongoing to improve modeling fidelity using a globally-driven, top-down approach. An iterative process will be used where the interactions and interdependencies, especially the nonlinear ones, between the boom deformations and the membrane deformations are increasingly refined through interleaving “global” models driven by the booms and “local” models which represent membrane deformations given some boundary conditions (driven by the boom deformations). Assumed membrane shapes will be replaced with those derived from physics-based modeling with higher-fidelity models of the external and internal loads, material properties, and structural mechanics. This approach also aims to apply uncertainties and tolerances as inputs to the structural FEM so that their effects may be more accurately

captured, as opposed to using simplified models to predict the effects and applying them in post-processing (e.g., boom tip error terms). The end goal of this work is to ultimately obtain a more physically realistic, high-fidelity representation of the actual sail shape.

Acknowledgments

The authors would like to thank the Solar Cruiser Project for the opportunity to conduct this innovative work, as well as providing the funding through which it was completed and this paper was written. Additionally, thanks to Redwire Corporation and ATA Engineering for the solar sail design and modeling inputs used in the sail shape analysis. Thanks to NeXolve Holding Company, LLC, for providing technical data on the sail membrane. Finally, thanks to the NEA Scout project and Guidance and Control team for the knowledge they passed down including previous modeling, analysis, and testing that was used as the basis for the methods detailed in this paper.

References

[1] L. Rios-Reyes and D. J. Scheeres. Generalized Model for Solar Sails. Journal of Spacecraft and Rockets, 42(1):182–185, 2005. doi: 10.2514/1.9054.

[2] B. Wie. Solar Sail Attitude Control and Dynamics, Part 1. Journal of Guidance, Control, and Dynamics, 27(4):526-535, 2004. doi: 10.2514/1.11134.

[3] A. Heaton, N. Ahmad, and K. Miller. Near Earth Asteroid Scout Thrust and Torque Model. Kyoto, Japan, January 2017. International Symposium on Solar Sailing. Paper M17-5721.

[4] D. Tyler, B. Diedrich et al. Attitude Control Approach for Solar Cruiser, A Large, Deep Space Solar Sail. Breckenridge, Colorado, February 2023. AAS Guidance, Navigation and Control Conference. Paper AAS-23-117.

Cyclic Interplanetary Motion of a Cargo Solar Sail

Miroslav A. Rozhkov[a,*], Olga L. Starinova[a]

[a] *Flight Dynamics and Control Theory Department, Samara National Research University, Samara, Russia*

Abstract

Future of mankind lies in a Mars colonization and exploiting resources floating in our Solar system. Solar sails can become a key technology to provide that future with constant flow of materials to Earth and from it. We propose applying a solar sail to ensure cyclic heliocentric motion of a cargo spacecraft between Earth and inner planets. The work investigates following ballistic aspects of the suggested transport system: cyclic motion dynamics and numerical simulation that considers non-ideally reflecting surface of a solar sail and optical parameters degradation; heliocentric trajectory optimization by minimum time criterion. As a prototype spacecraft for the simulation, we use a design from work [1] that can carry 1905 kg of payload with 0.25 mm/s^2 acceleration. Applying Pontryagin's maximum principle we define Hamiltonian and solve the boundary value problem with consideration of non-ideal reflection and degradation. The simulation is carried out for 4 loops of cyclic motion Earth-Mars-Earth to demonstrate a possibility of the suggested transport system. Results show that the degradation causes an increase of flight time for 4 cycles up to 14 years. Despite that the system can be efficient with deployment of several cargo spacecrafts with solar sail to maintain a flow of material with shorter periods

Keywords: cargo solar sail, cyclic space motion, optical degradation, interplanetary flight, trajectory optimization

Nomenclature

a	Acceleration
A	Solar sail area
r	Heliocentric distance
u	Angular coordinate
V	Velocity
ω	Angular velocity
c	Speed of light
S_r	Solar irradiance at distance r
m	Spacecraft mass
θ	Solar radiation incidence angle (control)
ρ	Reflectivity
ς	Specular reflection factor
ε	Emissivity
B	non-Lambertian coefficient
p	Optical parameter
d	Degradation factor
λ	Degradation coefficient
Σ	Solar radiation dose
T	Time period
δ	Angular distance between planets
U	A set of possible control
H	Hamiltonian
ψ	Costate variable
$\mathbf{r}$	Position vector
$\mathbf{V}$	Velocity vector
$\mathbf{X}$	State vector
$\mathbf{D}$	Design parameters vector
$\boldsymbol{\psi}$	Costate vector

Superscripts

*	Optimal

Subscripts

$\perp$	Perpendicular to sail's surface
$\parallel$	In sail's surface plane
fr	Sail's front side
b	Sail's back side
yr	One year time
0	Initial
f	Final
r	Radial component
u	Transverse component
p	Target planet
∞	Optical parameter at maximum degradation
i	i^{th} interplanetary flight

1. Introduction

Interplanetary flights require significant energy costs, including a launch of a spacecraft from the Earth's surface to a departure trajectory, deceleration after

* Corresponding author, rozhkov.ma@ssau.ru

spacecraft enters a sphere of influence of a target planet, and landing. Thus, when designing a transport system that ensures the movement of cargo between two planets of the Solar System, traditional launch vehicles will have to spend their resources on delivering not only a payload, but also a fuel that will be consumed in an intermediate heliocentric and planetocentric flight stages. To increase a mass efficiency of transport interplanetary missions, it is proposed to use intermediate interplanetary transport spacecraft [2,3].

In Russia, nuclear electric rocket propulsion tugs have been suggested as prospective reusable transport vehicles [3], which possess high efficiency and autonomy. Another alternative is the use of an orbital station located away from the planet on which the spacecraft performs refueling. The fuel itself is planned to be extracted or produced directly in space. This concept is followed by NASA in its Deep Space Transport project [2], where the lunar orbital station (Lunar Gateway) [4], which is situated in the Earth-Moon halo orbit, serves as a port for refueling and cargo transfer.

This work discusses the possibility of an alternative variant of such a transportation system that applies solar sails capabilities of not consuming any fuel. A large-area reflective thin film is capable of providing a small but constant acceleration to the spacecraft through the pressure of solar electromagnetic radiation [5,6]. The feasibility of deploying large thin-film systems has been demonstrated by spacecraft such as Znamya-2 [7,8], *IKAROS* [9], *LightSail-2* [10], etc. Possibilities of using them for cargo delivery have been analyzed in [8,9].

Solar sails yield lower thrust compared to other propulsion systems, which increases the duration of mission. However, with a large number of interplanetary flights performed, their utilization becomes justified. Naturally, the trajectory along which the spacecraft moves must ensure minimal flight time requirement.

Such trajectories have been explored in the study [12], but the authors assumed a constant orientation of the sail relative to the Sun, considered phases of the spacecraft's passive orbiting at the Lagrange points, and applied direct optimization methods. In this dissertation, the Pontryagin's maximum principle is used for calculating nominal control programs, allowing for obtaining an optimal program of sail attitude control and the corresponding trajectory that satisfies the optimality criterion.

A schematic representation of the proposed transportation system's operation is presented in Fig. 1. One cycle of movement consists of two interplanetary flights.

Designing a transportation system that facilitates the transfer of cargo to a solar sail is an important part of the proposed method for interplanetary cargo delivery and requires separate investigation. Such a transportation system may involve a spacecraft with an electric propulsion engine [13]. However, a detailed analysis of it is beyond the scope of this work. The issues related to delivering the transport spacecraft with the solar sail from the surface of the Earth and deploying the sail are also not considered.

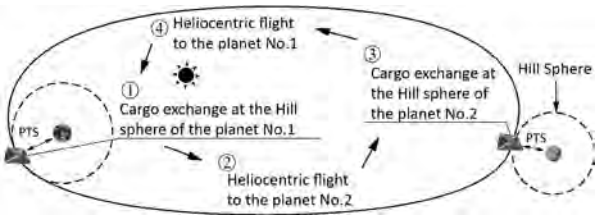

Fig. 1. Scheme of one cycle motion between two planets along heliocentric trajectory. The cargo delivery from solar sail at Hill Sphere to planet or orbital station is performed by planetary transport system (PTS).

For the ballistic scheme of a transport mission, the movement of the spacecraft with the solar sail is primarily influenced by the gravitational field of the Sun, with only minor perturbations from the planets at the beginning and end of the trajectory. Therefore, mathematical models and calculations for planetocentric segments are not included in this dissertation, which significantly simplifies the optimization process.

2. Mathematical Models

In order to evaluate a possibility of such motion we need to address a problem of optical parameters influence on the solar sail dynamics [14]. While searching for the optimal cyclic trajectory incorrect mathematical description of solar sail operation can lead to incorrect assumption of sail's abilities to execute the suggested cargo transportation system. In the paper we consider a non-ideally reflecting solar sail mathematical model and a degradation of front surface optical parameters.

2.1. Non-ideally reflecting solar sail

The acceleration of a spacecraft with a flat non-ideal reflective solar sail due to the pressure of electromagnetic radiation can be defined as the sum of two components directed normal ($a_{\perp}$) and parallel ($a_{||}$) to the sail surface in the plane passing through the radius vector:

$$a_{\perp} = 2\frac{S_r}{cm} A \cdot \cos\theta \cdot (a_1 \cos\theta + a_2), \quad (1)$$

$$a_{||} = -2\frac{S_r}{cm} A \cdot \cos\theta \cdot a_3 \sin\theta, \quad (2)$$

where

$$a_1 = \frac{1}{2}(1+\varsigma\rho), \quad a_3 = \frac{1}{2}(1-\varsigma\rho),$$

$$a_2 = \frac{1}{2}\left(B_f(1-\varsigma)\rho + (1-\rho)\frac{\varepsilon_f B_f - \varepsilon_b B_b}{\varepsilon_f + \varepsilon_b} \right).$$

Forward's optical model of the grey solar sail includes six different optical parameters, however only 3 of them, that are related to the sail's front surface, will be changing due to degradation.

When selecting $\rho = 1$ and $\varsigma = 1$ the Eq. (2) gives zero and Eq. (1) correspond to the model of ideally-reflecting solar sail where acceleration directs along the normal to sail's surface. We will use such conditions in order to get an initial guess for optimal trajectory. In addition, it allows to compare how non-ideal reflection and degradation influence dynamics of the solar sail cyclic motion.

The grey solar sail model also helps with the controlling through incident angle instead of cone angle. That simplifies the optimal control problem and gives some practical meaning since one can use sun sensors to realize calculated optimal control program. Hence it is useful for control system design.

There are many other things to consider that allows getting more accurate calculation of the generated acceleration: wrinkles, shape curvature and solar irradiance uncertainties, etc. All them that stacks together and may influence significantly in the real flight. However, in the scope of calculating nominal control program and optimal trajectory design it is rationally to consider only non-ideally reflecting and degradation.

2.2. Optical Parameters Degradation

The surface of the sail degrades during the flight due to the influence of various space factors. In particular, the reflectivity coefficient worsens, leading to an increased fraction of absorbed radiation. In the work [15], the authors propose a parametric model to describe the degradation process of the solar sail.

The model consists of a system of three equations that determine the ratio of the current value of one of the optical parameters *p(t)* to its initial value p_0:

$$\frac{p(t)}{p_0} = \begin{cases} \dfrac{1+de^{-\lambda\Sigma(t)}}{1+d} & \text{if } p \in \{\rho, \varsigma\}, \\ 1+d\left(1-e^{-\lambda\Sigma(t)}\right) & \text{if } p = \varepsilon_f, \\ 1 & \text{if } p \in \{\varepsilon_b, B_f, B_b\}. \end{cases} \tag{3}$$

The dimensionless radiation dose $\Sigma(t)$ is calculated as the ratio of the received radiation dose $\tilde{\Sigma}(t)$ accumulated by the sail during the flight to the total dose $\tilde{\Sigma}_0 = 15.768 \cdot 10^{12}$ TJ/m^2 received by a surface with an area of 1 m^2 at a distance of 1 AU over the course of one year.

$$\Sigma(t) = \frac{\tilde{\Sigma}(t)}{\tilde{\Sigma}_0} = \frac{1}{T_{yr}} \int_{t_0}^{t} \frac{\cos\theta(t)}{r^2} dt. \tag{4}$$

The degradation coefficient determines the intensity of degradation, and its mathematical description corresponds to half of the time of the sail's maximum degradation:

$$\lambda = \frac{\ln 2}{\hat{\Sigma}}. \tag{5}$$

Degradation factor d defines optical parameters values at which their change with time becomes infinitely low $\lim_{t\to\infty} p(t) = p_\infty$:

$$\rho_\infty = \frac{\rho_0}{1+d}, \quad \varsigma_\infty = \frac{\varsigma_0}{1+d}, \quad \varepsilon_{f\infty} = \varepsilon_{f0}(1+d). \tag{6}$$

2.3. Equation of Motion

The results of studies on the calculation of trajectories for spacecraft with solar sails have shown that even the most simplified model of the sail and its orbital motion provides sufficient results for the evaluation and prediction of interplanetary flight trajectories [6,16–18]. It can be used as an initial approximation for the optimization and modeling of more complex models of the spacecraft's motion with a solar sail. Therefore, a mathematical model of flat heliocentric motion of the spacecraft is used for assessing the dynamics of cyclic sail motion and optimizing control. In the paper, following assumptions are made:

- Planar motion is considered.
- Perturbations from celestial objects are not taken into account.
- The intensity of solar radiation varies inversely with the square of the distance and does not change over time (independent of solar activity).
- Planetary orbits are assumed to be circular and lying in the plane of the ecliptic.

To describe the motion of the spacecraft, a system of differential equations of motion in a planar polar coordinate system (Fig. 2) is used in dimensionless form.

$$\frac{d\mathbf{r}}{dt} = \mathbf{V}, \quad \frac{d\mathbf{r}}{dt} = \mathbf{a}(r, \theta, \Sigma) - \frac{\mathbf{r}}{\mathbf{r}^3}, \quad \frac{d\Sigma}{dt} = \frac{1}{T_{yr}} \frac{\cos\theta}{r^2}. \tag{7}$$

The coordinates, velocity components, and accelerations in Eq. (7) are dimensionless and scaled with respect to the radius of the Earth's orbit, its circular velocity, and the centripetal acceleration.

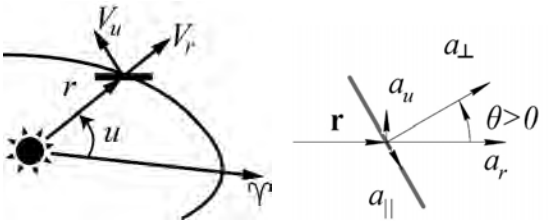

Fig. 2. Directions of vectors components in the plane polar coordinate system.

Scalar values of acceleration components in the planar polar coordinate system are calculated using the solar sail's installation angle θ, which serves as the control angle, through a rotation matrix in two-dimensional space.

$$\begin{aligned} a_r &= a_\perp \cos\theta - a_{||} \sin\theta, \\ a_u &= a_\perp \sin\theta + a_{||} \cos\theta. \end{aligned} \tag{8}$$

In the scales of interplanetary flights, the difference in distances from the Sun and orbital velocities between the planet and points on the boundary of the Hill sphere is less than 1%. In this case, phase coordinates of the departure and destination planets can be used as boundary conditions for interplanetary flights. The initial values of the spacecraft's phase coordinates are determined by the previous stages of the flight, while the final value of accumulated radiation dose Σ_f is not fixed:

$$\begin{aligned} &t = t_{i-1}, \quad \mathbf{X}_{0,i} = \left\{ r_{f,i-1}, u_{f,i-1}, V_{f,i-1}, V_{f,i-1}, \Sigma_{f,i-1} \right\}^{\mathrm{T}}, \\ &t = t_{i-1} + T_i, \quad \mathbf{X}_{f,i} = \left\{ r_{f,i}, u_{f,i}, V_{f,i}, V_{f,i}, \Sigma_{f,i} - unfix. \right\}^{\mathrm{T}}. \end{aligned} \tag{9}$$

The duration and angular distance of the flight should ensure that the angular motion of the destination planet and the spacecraft are equal.

$$\left\{ \frac{u}{2\pi} \right\} = \left\{ \frac{u_p + \omega_p T}{2\pi} \right\}. \tag{10}$$

where {.} denotes the operation of extracting the fractional part.

It is assumed that during cargo transfer, the sail is oriented edge-on to the Sun and does not generate thrust, while the spacecraft itself undergoes passive motion and awaits docking. In this study, the time required for cargo transfer was not considered in the calculations, as it does not affect the optimization algorithm of nominal control but only changes the angular distance between the planets at the start of the heliocentric transfer.

3. Optimization

3.1. Optimization Problem Statement

Let's consider the initial angular distance between the planets δ_0 as a ballistic parameter of the optimization problem. The criterion for the optimality of cyclic trajectories is the flight time for the given design parameters of the spacecraft with the sail (mass, optical parameters, and sail area). The control of the sail through the sail angle θ has a constraint: the electromagnetic radiation pressure cannot act in the direction opposite to the radiation source.

The problem of ballistic optimization of cyclic trajectories based on time efficiency is formulated as follows: determine the nominal control function (where U is the set of admissible controls) and the initial angular distance between the departure and destination planets δ_0 (corresponding to the departure date) that minimize the total travel time and satisfy the boundary conditions Eq. (9) and rendezvous conditions Eq. (10) when given the design parameter vector of the spacecraft $\mathbf{D} = \left\{ m, A, \rho_0, \varsigma_0, \varepsilon_{fr_0}, \varepsilon_b, B_{fr}, B_b \right\}^{\mathrm{T}}$:

$$\begin{aligned} t_f^* = \min_{\theta(t), \delta_0} t_f \big(\theta(t), \delta_0 \,\big|\, D = fixed, \theta(t) \in U, \\ \mathbf{X}_0 = \mathbf{X}(t_0), \mathbf{X}_f = \mathbf{X}(t_f) \big). \end{aligned} \tag{11}$$

For the considered in the paper transportation system, there are no waiting periods (passive motion of the spacecraft on the initial orbit), which determines the dependence of the initial phase coordinates of the current interplanetary flight $\mathbf{X}_{0,i}$ on the angular distance between the departure and destination planets at the end of the previous $\delta_{f,i-1}$. Based on this, it is assumed that the choice of δ_0 in the first cycle determines the subsequent optimal cyclic trajectory, which consists of individually optimized interplanetary flights based on minimum time criterion. For a given number of cycles *n*, it is possible to find a value δ_0^* that minimizes the total duration of the entire cyclic heliocentric trajectory by minimizing the duration of each individual interplanetary trajectory:

$$\begin{aligned} T_i^* = \min_{\theta(t)} T_i \big(\theta(t) \big| \mathbf{D} = \text{fixed}, \theta(t) \in U, \delta_{0,i} = \delta_{f,i-1}, \\ \mathbf{X}_{0,i} = \mathbf{X}(t_{i-1}), \mathbf{X}_{f,i} = \mathbf{X}(t_{i-1} + T_i) \big). \end{aligned} \tag{11}$$

3.2. Optimal Control Program

The solution to the optimization problem of the nominal control program for spacecraft motion with an ideally reflecting sail, based on the criterion of minimizing the flight duration, is well known and has been obtained using the Pontryagin's maximum principle by the authors of paper [19].

$$\tan\theta = \frac{\sqrt{9\psi_{Vr}^2 + 8\psi_{Vu}^2} - 3\psi_{Vr}}{4\psi_{Vu}}. \quad (12)$$

The Pontryagin's maximum principle provides a necessary condition for optimality: if a trajectory is optimal, then the value of the Hamiltonian reaches a maximum. To find the optimal control program, the first derivative of the Hamiltonian with respect to the sail installation angle θ is calculated and set equal to zero.

$$\frac{\partial H}{\partial \theta} = \frac{a_c}{r^2}\psi_{Vr}\left(a_3\sin^3\theta + 2\left(a_1 + a_2\right)\sin\theta\cos\theta - \right.$$

$$\left. -\left(3a_1 + 2a_3\right)\cos^2\theta\sin\theta\right) + \frac{a_c}{r^2}\psi_{Vu}\left(\cos^3\theta - \right.$$

$$\left. -2\sin^2\theta\left(a_2 + \cos\theta\right) + a_2\right) - \frac{\cos\theta}{T_{yr}r^2}\psi_{\Sigma} = 0. \quad (13)$$

Analytical solution to determine the optimal angle θ from the Eq. (13) is hardly obtainable. Moreover, it is necessary to determine the sign of the second derivative with respect to the angle θ to establish whether the found extremum is a maximum. Therefore, in the study, the maximum of the Hamiltonian with respect to the control variable is numerically searched for at each step of simulating the spacecraft's motion using the golden section method.

3.3. Boundary Value Problem

To formulate the boundary value problem conclusively, a system of differential equations for the costate variables is defined. This system consists of the following equations:

$$\frac{\partial \boldsymbol{\psi}_r}{\partial t} = -\frac{\partial H}{\partial \mathbf{r}}, \frac{\partial \boldsymbol{\psi}_V}{\partial t} = -\frac{\partial H}{\partial \mathbf{V}}, \frac{\partial \psi_{\Sigma}}{\partial t} = -\frac{\partial H}{\partial \Sigma}. \quad (14)$$

To normalize the problem, $\psi_r(t_0)$ is taken to be ± 1. From the results of similar works [20], it is known that a negative value corresponds to a decrease in the orbit radius, while a positive value corresponds to an increase. The subsequent calculation results in this study also confirmed this statement.

Thus, the variational problem reduces to a four-parameter boundary value problem, where it is necessary to find initial values of the costate variables $\boldsymbol{\psi}(t_0)$ that satisfy the boundary conditions.

For the numerical solution of the boundary value problem, a modified Newton's method with automatic convergence estimation and adjustment of step size for computing derivatives and constraints is used [20]. However, boundary value problems with a fixed angular distance converge poorly and require the application of additional methods to find an initial approximation. A sequential complexity increase method and descent along the parameter of the initial angular distance between the planets are employed.

Initially, the boundary value problem with an unfixed angular distance is solved i.e., the problem of spacecraft transfer from the initial to the target orbit. Such problems converge quickly, and their solution corresponds to satisfying the boundary condition of Eq. (10) (rendezvous mission) for the start date with the minimum transfer time and optimal planet positions.

The solution of the problem with the unfixed angular distance serves as a starting point for solutions along the parameter of the initial angular position of the planets. By solving boundary value problems with a fixed angular distance according to Eq. (10), a set of solutions can be obtained over the entire range of angular planet positions.

The obtained results are further used as a reliable close approximation for calculating the cyclic motion of the spacecraft with a non-ideally reflecting degrading sail. Thus, by forming two sets of solutions for the transfer from one planet to another and back, it is possible to determine trajectories for the spacecraft's motion along a cyclic trajectory.

Fig. 3 presents the results of Earth-to-Mars transfer calculations for a solar sail with a characteristic acceleration of 0.25 mm/s^2 and ideal reflection. The calculations were performed sequentially for the entire range of possible planet positions relative to each other, $\delta_0 = [0, 360]$ deg. Two types of control programs are shown: sail orientation edge-on to the Sun ($\theta = \pm 90$ deg.) at the end of the trajectory (for $\delta_0 = 145$ deg.) and at the beginning (for $\delta_0 = 340$ deg.).

The obtained results demonstrate a common pattern in the control programs. The solar sail tends to orient itself relative to the Sun at an angle of $\theta = \pm 35$ deg. for the fastest change in the transverse component of velocity V_u. If the departure date is different from the optimal (in this case $\delta_0 = 159$ deg.), a synchronization stage takes place, i.e., a change in the final value of the angular distance to reach the target planet. Synchronization can occur at the beginning or end of the trajectory. The trajectories have a multi-turn spiral shape, which is typical for low-thrust spacecraft.

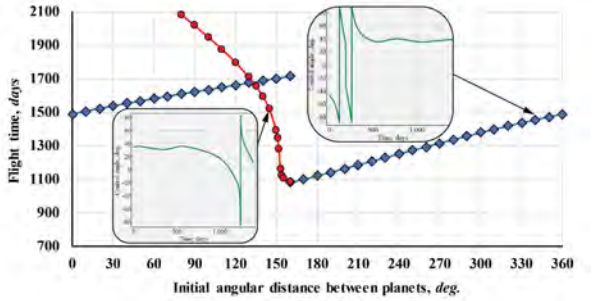

Fig. 3. The dependence of Earth-to-Mars transfer durations on the angular position of the planets. Two types of sail control programs are presented: ● – synchronization occurs at the beginning of the trajectory, ♦ – at the end.

The trajectories can exhibit non-monotonic changes in the heliocentric distance. This occurs during the synchronization stage, where the goal is to adjust the angular heliocentric velocity of the spacecraft and satisfy the boundary condition of Eq. (10) more quickly.

4. Earth-Mars-Earth Cyclic Motion Simulation

The design and optical parameters of the spacecraft with a solar sail are taken from references [1] and [21] and are showed in Table 1.

The threshold value for the reflectance coefficient, below which the film no longer degrades, is chosen as the value for low-carbon unpolished steel ($\rho_\infty = 0.32$) [22]. This allows obtaining parameters necessary for modeling degradation processes according to Eq. (6).

With these degradation parameters, the optical characteristics of the sail will deteriorate by 50% after 35 years of orbital motion around the Earth with perpendicular orientation to the Sun. Taking into account that modern technologies usually become obsolete morally after 20 years, the sail has a sufficient degradation lifespan to compete with existing propulsion systems in space and be economically viable for long-duration space missions. These results are consistent with the findings from MISSE 1 and MISSE 2 experiments [22].

As it was mentioned before in section 3.3 of this paper, it is necessary to generate a set of solutions for the entire range of possible planet positions relative to each other. The database for the Earth-Mars transfer was previously presented in Fig. 3. The solutions for the Mars-Earth transfer are shown in Fig. 4.

The calculation results are presented in Table 2. Fig. 5 shows the control programs for the 3rd and 4th cycles of the Earth-Mars transfer using both ideal and non-ideal reflecting solar sail. The Earth-Mars transfer trajectories for the 3rd cycle are shown in Fig. 6. The degradation of the optical parameters of the solar sail throughout all 4 cycles of the cyclic motion is depicted in Fig. 7.

Table 1. Design and optical parameters of the solar sail.

Parameter description and units		Value
Spacecraft mass, kg		2353
Cargo mass, kg		1905
Sail area, m2		75625
Characteristic acceleration, mm/s2		0.25
Reflectivity		0.91
Specular reflection factor		0.94
Emissivity	Front	0.05
	Back	0.55
non-Lambertian coefficients	Front	0.79
	Back	0.55
Degradation factor		1.75
Degradation coefficient		0.02

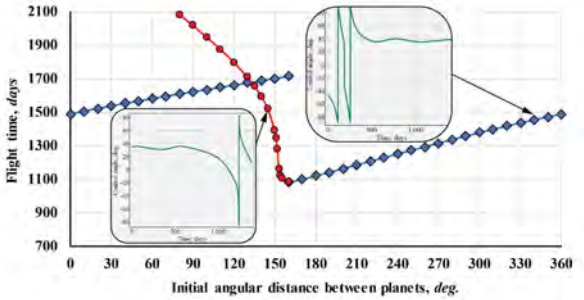

Fig. 4. The dependence of Mars-to-Earth transfer durations on the angular position of the planets.

Table 2. Flight time of interplanetary flights for 4 cycle of Earth-Mars-Earth cyclic motion.

Cycle	Flight time, years			
	Ideal sail		Non-ideal sail	
	to Mars	to Earth	to Mars	to Earth
I	2.96	3.16	3.58	5.00
II	3.23	3.18	4.11	4.62
III	3.23	3.18	6.29	4.52
IV	3.23	3.18	5.78	5.03

The optimal control program for an ideal reflecting sail, without degradation, is calculated in such way that the spacecraft performs cyclic motion with a constant cycle time. However, a non-ideal reflecting sail, due to degradation, is unable to maintain such stable motion. Nevertheless, the control program itself aims to minimize the possible variation in interplanetary transfer time.

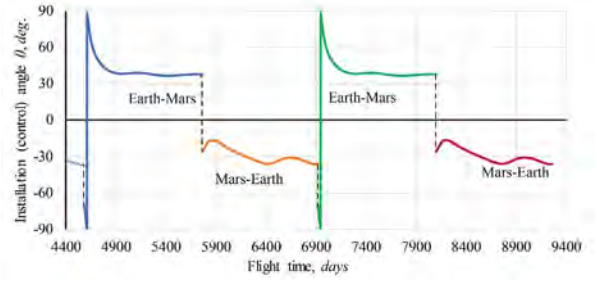

a)

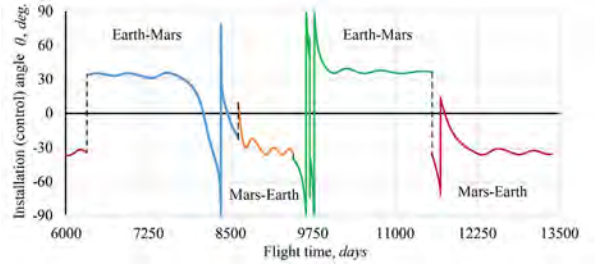

b)

Fig. 5. Nominal control program during 3rd and 4th cycles of motion for a) ideally reflecting and b) non-ideally reflecting solar sail that undergoes degradation.

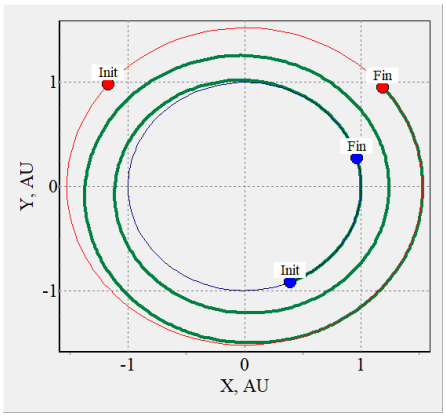

a)

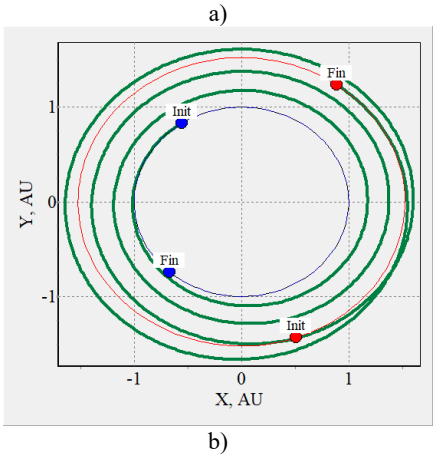

b)

Fig. 6. Earth-Mars heliocentric trajectory of the 3rd cycle for a) ideally reflecting and b) non-ideally reflecting solar sail.

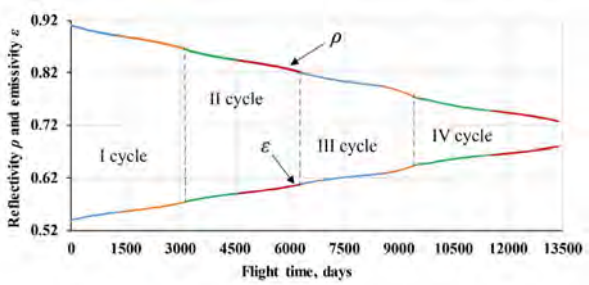

Fig. 7. Change of the solar sail's optical parameters with time throughout all 4 cycles of motion along Earth-Mars-Earth cyclic trajectory. Parameter ς is not shown since it has similar dependence as ρ with different initial value.

Another feature of the control program for a degrading, non-ideally reflecting sail is the selection of a trajectory for synchronizing the spacecraft's angular position with the target planet. The control is designed in such a way that synchronization occurs at the farthest distance from the Sun to reduce the received radiation dose. This holds true for all cycles except the fourth cycle, which is the final one. In this case, the control program may allow the spacecraft to descend closer to the Sun to quickly align its angular position since there is no need to preserve optical parameters for the last cycle.

5. Conclusion

The calculations of the heliocentric motion for the four cycles of Earth-Mars-Earth motion using a solar sail with a characteristic acceleration of 0.25 mm/s² were obtained. The travel time for an ideally reflecting solar sail along the cyclic Earth-Mars-Earth trajectories amounts to 6.4 years, and the total time for completing the four cycles is 25 years. However, in reality, due to the degradation of the sail's reflecting surface and considering the non-ideal reflection of electromagnetic radiation, the time for completing each cycle will inevitably vary. As a result, the minimum travel time for the four cycles amounts to 39 years.

The main challenge in accounting for solar sail degradation lies in determining the characteristics of the degradation process, namely, determining the degradation coefficient and factor. Ground-based facilities exist that can simulate material degradation processes in space [23], and there are even integrations with setups for measuring electromagnetic radiation pressure [24].

The economic feasibility of using a solar sail as a transportation system requires a comprehensive analysis of the expenses for design, assembly, launch, and operation. The considered interplanetary transportation system assumes that the solar sail leaves cargo and retrieves new cargo in the vicinity of a Lagrange point,

which means that the costs of a transportation system delivering cargo to the planet, orbital station, or natural satellite need to be taken into account as well.

References

[1] G.W. Hughes, M. Macdonald, C.R. McInnes, A. Atzei, P. Falkner. Sample Return from Mercury and Other Terrestrial Planets Using Solar Sail Propulsion, *Journal of Spacecraft and Rockets,* 43(2006): 828–835. https://doi.org/10.2514/1.15889.

[2] J.C. Crusan, R.M. Smith, D.A. Craig, J.M. Caram, J. Guidi, M. Gates, J.M. Krezel, N.B. Herrmann, Deep space gateway concept: Extending human presence into cislunar space. Big Sky, MT, USA, June 2018. IEEE Aerospace Conference Proceedings. doi.org/10.1109/AERO.2018.8396541.

[3] V. V Sinyavskii, Advanced technology for nuclear electric propulsion orbital transfer vehicle Hercules, *Kosm. Tekh. Tekhnol.* 3 (2013) 25–45.

[4] T.D. Haws, J.S. Zimmerman, M.E. Fuller, SLS, the Gateway, and a Lunar Outpost in the Early 2030s, in: IEEE Aerospace Conference Proceedings, IEEE Computer Society, 2019. https://doi.org/10.1109/AERO.2019.8741598.

[5] C.R. McInnes, *Solar sailing: technology, dynamics and mission applications*, Springer Berlin, Heidelberg, 2004.

[6] G. Vulpetti, L. Johnson, G.L. Matloff, *Solar sails: A novel approach to interplanetary travel*, 2nd ed., Springer New York, 2015. https://doi.org/10.1007/978-1-4939-0941-4.

[7] V.M. Melnikov, V.A. Koshelev, *Large Space Structures Formed by Centrifugal Forces*, CRC Press, 1998. https://doi.org/10.1201/9781003078203.

[8] V.M. Melnikov, K.M. Pichkhadze, Design of frameless SA deployed by centrifugal forces and its deployment mechanism as a basis of new technology of in-orbit power plant assembling, in: American Institute of Aeronautics and Astronautics (AIAA), 2005. https://doi.org/10.2514/6.iac-05-c2.p.01.

[9] O. Mori, H. Sawada, R. Funase, M. Morimoto, T. Endo, T. Yamamoto, Y. Tsuda, Y. Kawakatsu, J. Kawaguchi, Y. Miyazaki, Y. Shirasawa, I. Demonstration Team and Solar Sail Working Group, First Solar Power Sail Demonstration by IKAROS, *Transactions of The Japan Society for Aeronautical and Space Sciences*, Aerospace Technology Japan. 8 (2010) 25–31. https://doi.org/10.2322/tastj.8.To_4_25.

[10] D.A. Spencer, B. Betts, J.M. Bellardo, A. Diaz, B. Plante, J.R. Mansell, The LightSail 2 solar sailing technology demonstration, *Advances in Space Research*. 67 (2021) 2878–2889. https://doi.org/10.1016/j.asr.2020.06.029.

[11] R.H. Frisbee, Solar Sails for Mars Cargo Missions, AIP Conference Proceedings. 374 (2007) 374–380. https://doi.org/10.1063/1.1449747.

[12] M. Vergaaij, J. Heiligers, Time-optimal solar sail heteroclinic-like connections for an Earth-Mars cycler, *Acta Astronautica*. 152 (2018) 474–485. https://doi.org/10.1016/j.actaastro.2018.08.008.

[13] C. Du, O.L. Starinova, Y. Liu, Transfer between the planar Lyapunov orbits around the Earth–Moon L2 point using low-thrust engine, *Acta Astronautica*. 201 (2022) 513–525. https://doi.org/10.1016/j.actaastro.2022.09.056.

[14] M.A. Rozhkov, O.L. Starinova, I. V. Chernyakina, Influence of optical parameters on a solar sail motion, *Advances in Space Research*. 67 (2021) 2757–2766. https://doi.org/10.1016/j.asr.2020.06.017.

[15] B. Dachwald, G. Mengali, A.A. Quarta, M. Macdonald, Parametric model and optimal control of solar sails with optical degradation, *Journal of Guidance, Control, and Dynamics*. 29 (2006) 1170–1178. https://doi.org/10.2514/1.20313.

[16] M. MacDonald, *Advances in Solar Sailing*, Springer Science & Business Media, 2014. https://doi.org/10.1007/978-3-642-34907-2.

[17] R.Y. Kezerashvili, Space exploration with a solar sail coated by materials that undergo thermal desorption, *Acta Astronautica*. 117 (2015) 231–237. https://doi.org/10.1016/j.actaastro.2015.08.007.

[18] G. Vulpetti, Fast Solar Sailing, in: *Fast Solar Sailing*, Springer, Dordrecht, 2013: pp. E1–E2. https://doi.org/10.1007/978-94-007-4777-7_10.

[19] V.N. Lebedev, A.N. Zhukov, Variational problem of the transfer between heliocentric circular orbits by means of a solar sail, *translated from Kosmicheskie Issledovaniya (Cosmic Research)* (1964) 45-50.

[20] V. V. Salmin, O.L. Starinova, Optimization of interplanetary flights of spacecraft with low-thrust engines taking into account the ellipticity and noncoplanarity of planetary orbits, *Cosmic Research*. 39 (2001) 46–54. https://doi.org/10.1023/A:1002835811494.

[21] J.L. Wright, *Space sailing,* Gordon and Breach Science Publishers, 1992.

[22] J.A. Dever, S.K. Miller, E.A. Sechkar, T.N. Wittberg, Space Environment Exposure of Polymer Films on the Materials International Space Station Experiment: Results from MISSE 1 and MISSE 2, *High Performance Polymers*. 20 (2008) 371–387. https://doi.org/10.1177/0954008308089704.

[23] M. Sznajder, T. Renger, A. Witzke, U. Geppert, R. Thornagel, Design and performance of a vacuum-UV simulator for material testing under space conditions, *Advances in Space Research*. 52 (2013) 1993–2005. https://doi.org/10.1016/J.ASR.2013.08.010.

[24] N. Melnik, U. Geppert, B. Biering, F. Lura, Light Pressure Measurement at DLR Bremen, in: *Advances in Solar Sailing*. (2014) 399–406. https://doi.org/10.1007/978-3-642-34907-2_26.

Solar Sail Torque Model Characterization for the Near Earth Asteroid Scout Mission

Benjamin DIEDRICH[a,*]

[a]*NASA MSFC/EV42, ESSCA/Axient Corporation, Huntsville, AL, USA*

Abstract

Near Earth Asteroid Scout (NEA Scout) was a mission to test solar sail propulsion for orbital transfer from cislunar space to flyby and image an asteroid. Had it succeeded, one of the mission goals was to characterize the solar torque on the sail to ensure successful attitude control for the orbit transfer and imaging the asteroid. The simulation used to develop the flight attitude control software uses the generalized model for solar sails, a tensor equation of the forces and torques on sails of arbitrary shape. Rios-Reyes and Scheeres developed a general process to update the torque tensor coefficients using estimates of sail torque over a range of directions to the sun. Their process was adapted and implemented for the specific case of NEA Scout using spacecraft telemetry collected during sail characterization maneuvers in combination with simulation models and parameters. The NEA Scout maneuvers were limited to the operating range of the mission and constraints of the control hardware and allowed safe testing of each attitude before proceeding to the next. The NEA Scout reaction wheel speeds are used to measure accumulated momentum, while the Active Mass Translator (AMT) position is used to subtract out the torque from the center of mass crossed with the sail force and isolate the torque from only the sail shape. The process was tested by running attitude control simulations of the characterization maneuvers, generating simulated telemetry, estimating the solar torques, then using a least squares estimating the solar torque coefficients using least-squares and then performing a least-squares fit to the solar torque tensor coefficients. These estimated coefficients were tested by evaluating the solar torques under the same conditions as the simulated telemetry and comparing to the true simulated torques. Solar force model updates can be performed separately by observing the effect of the sail on the trajectory, and the torque model can be refined using those solar force updates. This process met the needs of the NEA Scout mission and can be adapted to characterize the solar torque for other missions with different sails.

Keywords: solar sail, NEA Scout, torque, characterization, modeling, controls

Nomenclature

$\bar{\boldsymbol{M}}_{shape}$	Torque vector due to sail shape
$\bar{\boldsymbol{M}}_{force}$	Torque vector due to force and center of mass
$\bar{\boldsymbol{M}}_{total}$	Total torque acting on sail
$\bar{\boldsymbol{f}}_{sail}$	Sail force vector
$\bar{\boldsymbol{r}}_{cm}$	Body frame vector of spacecraft center of mass
p	Solar pressure
$a_{1,2,3}$	Derived optical coefficients
$\mathbf{K}^2$, $\mathbf{L}$	3x3 sail torque tensors
$\mathbf{K}^3$	3x3x3 sail torque tensor
$\hat{\boldsymbol{r}}_s$	Unit sun vector in the sail body frame
$\boldsymbol{K}$	Vector of unique torque tensor coefficients
Subscripts	
est	From estimates of torque coefficients
plant	From plant model torque coefficients
Δ	Difference between plant and estimated torque model
err	Relative error between plant and estimated torque model

1. Introduction

Solar sail spacecraft perform trajectory maneuvers by changing the direction of thrust generated by sunlight reflecting on the sail. For current sail designs where the sail is fixed to the spacecraft body, this requires controlling the attitude of the sailcraft relative to the incident sunlight over time to generate the required force profile for the mission. To design a working attitude control system, the sail torques need to be understood over the range of attitudes required for the mission to size the actuators and design the control software. Sail torque is driven by the three-dimensional

* Corresponding author, benjamin.l.diedrich@nasa.gov

shape of the thin sail membrane, and even small deviations from flatness can generate sizeable torques that the attitude control system needs to manage with margin. By contrast, the force on a sail is insensitive to small deviations from flatness. One of the goals of the Near Earth Asteroid Scout (NEA Scout) mission was to measure the solar torque on the sail and characterize the solar torque model used for simulating attitude control, to better understand how to control this mission in particular, and to understand sail torque more generally so that attitude control systems can be designed with confidence for future sail missions. This paper describes the process developed for NEA Scout to use spacecraft telemetry, mission data, and models to update the torque model. It is a practical application of the approach originally published by Rios-Reyes and Scheeres [1], who also developed the Generalized Model for Solar Sails [2] that was used to model the torque of the three-dimensional shape of the NEA Scout sail film.

This paper discusses the sail characterization concept of operation, flight and model data used in the analysis, sail characterization procedure, theory, simulation results, and finally the conclusions and future work. The simulation results show some success in solving for torque coefficients that predict the truth torque due to sail shape, despite not matching the coefficients well. There is plenty of room for improvement for the process. The absolute torque errors from the estimated coefficients are small, but the relative torque errors can be large in many cases.

2. Sail Characterization Concept of Operations

Had the NEA Scout mission succeeded, the planned mission was to deploy the sail in cislunar space after a few weeks of trajectory correction maneuvers with the cold gas reaction control system (RCS), followed by cislunar sailing, then an interplanetary phase to flyby an accessible asteroid. To ensure control of the sail for performing those maneuvers and to collect data for refining the sail torque model, torque characterization maneuvers were planned for a period of several days after sail deployment.

Characterization would have started with one day pointed directly at the sun (with an additional day for margin). Once stable control was demonstrated with sun pointing, the incidence would be increased by 10 deg increments, to 49 deg (1 deg short of the 50 deg operational limit for attitude control margin). At each sun incidence angle, the sail would be rolled to +/- 30. The roll is incremented in 10 deg increments at 20 deg SIA and above, because the roll changes slowly with roll at 10 deg SIA. Every change in sail attitude was planned to happen during a communications pass, so that if problems arose the spacecraft can be commanded to return to the previous safe attitude. The schedule is shown in Table 1.

Table 1. Sail characterization attitudes

SIA (deg)	Roll (deg)
0	0
10	0
10	+30
10	-30
20	-30
20	-20
20	-10
20	0
20	10
20	20
20	30
…	…
49	30
49	20
49	10
49	0
49	-10
49	-20
49	-30

While this does not cover the entire range of possible sun angles, and therefore provides incomplete data for full sail characterization, it does test the entire range of motion required for this mission's trajectory maneuvers. NEA Scout has a critical piece of control hardware called the Active Mass Translator (AMT) that shifts the center of mass to control the pitch & yaw solar torque to manage the momentum of the reaction wheels in two axes. Because of the volume constraints imposed by the 6U cubesat bus, the AMT has a limited range of motion in one axis and reduced control authority at larger roll angles.

3. Telemetry, Data, and Models

The telemetry required to characterize the NEA Scout sail includes:

- Time: reference all other telemetry and data
- Reaction wheel speeds: measure total torque as derivative of momentum
- Control mode (Hold or Slew): identify when spacecraft is holding attitude or moving
- AMT momentum management status: identify when the AMT has stopped moving
- Attitude estimate: used to compute the sun vector in the sail body frame
- AMT position: used to compute the torque caused by the sail force crossed with the center of mass offset

Additional mission data required for sail characterization includes:

- Ephemeris: used to compute the sun vector and distance to the sun
- Solar flux [6]: used to compute solar pressure at the time of measurements

Model data used for sail characterization includes the following parameters. Any updates to this information, like sail force characterization, will improve the estimates of the torque model.

- Reaction wheel alignment: project wheel speeds into body frame
- Reaction wheel inertia: convert wheel speeds to momentum
- AMT axis polarity: correct AMT position sign
- Sail force model: compute torque of force crossed with center of mass
- Mass property model: compute center of mass as function of AMT position

4. Sail Characterization Procedure

The general approach to sail torque model characterization is to estimate the total torque from measurements of the reaction wheel speeds while holding the sail attitude inertially fixed and solve for the sail torque coefficients that produce the observed torque. The details of this process are described below.

Once the telemetry, mission data, and model data are available, the sail characterization process can proceed as follows:

- Load model data
- Load trajectory ephemeris and solar flux
- Load sailcraft telemetry (flight or emulated)
- Split the telemetry into segments where the control mode is HOLD and the AMT has stopped moving so that the dynamics of slewing and AMT movement don't increase the uncertainty on the torque estimates

For each data segment:

- Compute reaction wheel momentum by multiplying wheel speed by wheel inertias
- Compute reaction wheel body frame momentum by multiplying alignment matrix by the per-wheel momentum
- Compute mean AMT position per segment (should be constant since the AMT shouldn't be moving)
- Fit polynomial to body frame wheel momentum
- Find body frame torque polynomial by taking derivative of momentum polynomial
- Fit polynomial to attitude estimate quaternions

For each data segment, pick sample times (start, middle, final times) to perform calibration calculations to smooth the data and reduce the number of data points used in the least-squares problem. For each data segment & sample time:

- Lookup sailcraft position using ephemeris
- Compute solar pressure using sailcraft position and solar flux
- Evaluate inertial to body quaternion polynomial
- Calculate sun vector in the body frame using inertial position and attitude quaternion
- Calculate center of mass using the mass properties model and AMT position
- Calculate the solar force using the sail force model, solar pressure, and body sun vector
- Calculate the solar torque from solar force by taking the cross product of the force with the center of mass
- Calculate the sail shape torque by subtracting the torque due to force from the reaction wheel torque estimate
- Normalize the sail shape torque by dividing by the solar pressure
- Compute the linear system (A-matrix) that maps a vector of the sail torque coefficients into normalized sail shape torque measurements (detailed in Theory section)

Once these steps are completed for all the data segments and sample times:

- Build the total least-squares A-matrix by vertically stacking all the A-matrices for each segment and sample
- Build the total least-squares b-vector by stacking the normalized estimates of sail shape torque
- Solve the least-squares problem for the vector of sail torque coefficients
- Rearrange the estimated sail torque coefficients into tensor form
- Test the estimated torque coefficients using them to calculate the torque at each sample time using the corresponding sun vector and solar pressure; compare to the estimates and plant model values if available

5. Theory

The general least-squares problem is formulated as the solution $\boldsymbol{x}$ to the equation:

$$\boldsymbol{A}\,\boldsymbol{x} = \boldsymbol{b} \tag{1}$$

where $\boldsymbol{b}$ is a vector of observations, and $\boldsymbol{A}$ is a linearized model (i.e. matrix) that maps the parameters $\boldsymbol{x}$ to the observations of the system in question.

In the case of the sail torque characterization, this problem is formulated from the generalized sail torque model equation from [2]. For NEA Scout, no assumptions on symmetry were made, so a full set of 36 unique torque coefficients are solved for. With assumptions on symmetry, a smaller set of coefficients can be solved for. The tensor equation for the sail shape torque is:

$$\overline{\boldsymbol{M}}_{\text{shape}} = p(a_2\mathbf{K^2}\cdot\hat{\boldsymbol{r}}_s - a_1\hat{\boldsymbol{r}}_s\cdot\mathbf{K}^3\cdot\hat{\boldsymbol{r}}_s - a_3\hat{\boldsymbol{r}}_s\cdot\mathbf{L}\cdot\hat{\boldsymbol{r}}_s) \quad (2)$$

The sail characterization process estimates the coefficients of the rank-2 $\mathbf{K}^2$ and $\mathbf{L}$ tensors, and the rank-3 $\mathbf{K}^3$ tensor, for a total of 36 unique coefficients. The only symmetry is in the 2nd and 3rd indices of $\mathbf{K}^3$. The parameters a1, a2, and a3 are reformulations of the flat-plate optical coefficients *r*, *s*, B_b, B_f, e_b, and e_f:

$$\begin{aligned} a_1 &= 2rs \\ a_2 &= \frac{B_f(1-s)r+(1-r)\left(e_fB_f-e_bB_b\right)}{e_f+e_b} \\ a_3 &= 1-rs \end{aligned} \quad (3)$$

The tensor products were implemented in Matlab by reformulating them as matrix multiplications. $\mathbf{K}^2$ and $\mathbf{L}$ are represented as 3x3 matrices *K2* and *L*, and $\mathbf{K}^3$ as a 3x3x3 array *K3*. They were multiplied with the sun vector $\hat{\mathbf{r}}_s$ (represented as column vector *rsun*) using the following expressions:

$$\mathbf{K^2}\cdot\hat{\boldsymbol{r}}_s \equiv \text{K2} * \text{rsun} \quad (4)$$

$$\hat{\boldsymbol{r}}_s\cdot\mathbf{K}^3\cdot\hat{\boldsymbol{r}}_s \equiv \text{reshape}(\text{reshape}(\text{K3},9,3) * \text{rsun},3,3) * \text{rsun} \quad (5)$$

$$\hat{\boldsymbol{r}}_s\cdot\mathbf{L}\cdot\hat{\boldsymbol{r}}_s \equiv (\text{rsun'}*\text{L})*\text{skew(rsun)} \quad (6)$$

Where:

$$\text{skew(sun)} \equiv \begin{bmatrix} 0 & -\text{rsun}(3) & \text{rsun}(2) \\ \text{rsun}(3) & 0 & -\text{rsun}(1) \\ -\text{rsun}(2) & \text{rsun}(1) & 0 \end{bmatrix} \quad (7)$$

The Matlab implementation was used in the plant model of the simulation and in post-processing to test the estimated moment coefficients. It was also implemented in the computer algebra system Maxima to formulate the least-squares problem.

The sail torque equation was expressed as a symbolic function of the solar pressure, optical coefficients, sun vector components, and individual torque coefficients that returned a 3D torque vector.

The tensors K2a, K3a, and La were defined in Maxima as follows, so that they can be symbolically evaluated:

```
K2a : genmatrix(lambda([i,j],arraymake(K2,[i,j])),3,3);
K3a : [
genmatrix(lambda([i,j],
   arraymake(K3, cons(i,sort([j,1])))),3,3),
genmatrix(lambda([i,j],
   arraymake(K3,cons(i,sort([j,2])))),3,3),
genmatrix(lambda([i,j],
   arraymake(K3,cons(i,sort([j,3])))),3,3)];
La : genmatrix(lambda([i,j],arraymake(L,[i,j])),3,3);
```

The shape torque is defined as a Maxima function. The full expansion of all the coefficients is too long to express here, but it can be expanded using this function:

```
shape_torque(p,r,a,K2,K3,L) :=
   p * (a[2] * K2 . r
   - a[1] * addcol(K3[1] . r, K3[2] . r, K3[3] . r) . r
   - a[3] * transpose((transpose(rv) . L) . skew(r)));
```

The $\hat{\mathbf{r}}_s$ vector and *a* coefficients are defined symbolically in Maxima so the shape torque can be evaluated:

```
rv : genmatrix(lambda([i,j],arraymake(r,[i])), 3, 1);
ac : [a[1], a[2], a[3]];
```

With this, the sail shape torque can be symbolically evaluated with the following Maxima expression. The full expansion is too long to show here.

```
M_shape :
   expand(shape_torque(p, rv, av, K2a, K3a, La));
```

The moment equation is then reformulated into the linear form $\boldsymbol{A}\,\boldsymbol{x} = \boldsymbol{b}$ where the $\boldsymbol{x}$ being solved for is a vector of all 36 unique moment coefficients and $\boldsymbol{b}$ is the sail torque. The vector of torque coefficients is named $\boldsymbol{K}$ and is built from K2, K3, and L by listing their coefficients in order by index and removing redundant K3 coefficients (those with the same 2nd and 3rd indices). This results in the vector:

$$\boldsymbol{K} = \begin{matrix}[K^2_{1,1}\ K^2_{1,2}\ K^2_{1,3}\ K^2_{2,1}\ K^2_{2,2}\ K^2_{2,3}\ K^2_{3,1}\ K^2_{3,2}\ K^2_{3,3}\ \ldots \\ K^3_{1,1,1}\ K^3_{1,1,2}\ K^3_{1,1,3}\ K^3_{1,2,2}\ K^3_{1,2,3}\ K^3_{1,3,3}\ \ldots \\ K^3_{2,1,1}\ K^3_{2,1,2}\ K^3_{2,1,3}\ K^3_{2,2,2}\ K^3_{2,2,3}\ K^3_{2,3,3}\ \ldots \\ K^3_{3,1,1}\ K^3_{3,1,2}\ K^3_{3,1,3}\ K^3_{3,2,2}\ K^3_{3,2,3}\ K^3_{3,3,3}\ \ldots \\ L_{1,1}\ L_{1,2}\ L_{1,3}\ L_{2,1}\ L_{2,2}\ L_{2,3}\ L_{3,1}\ L_{3,2}\ L_{3,3}]^T \end{matrix} \quad (7)$$

This operation was done in Maxima by processing the arrays K2, K3, and L then processing it using the code:

```
K : transpose(matrix(
delete(0,append(unique(apply(append,args(K2a))),
unique(apply(append,apply(append,map(args,K3a)))),
unique(apply(append,args(La)))))));
```

Next, the A-matrix is solved for from the vector of coefficients $\boldsymbol{K}$ and vector of torques $\overline{\boldsymbol{M}}_{shape}$. Using Maxima, the following two functions are used. The first is a modified version of the 'isolate' function that factors out the K-vector coefficients from each term of the shape torque M_shape, without using intermediate expressions:

```
betterisolate1(expr,x) :=
 (iso : isolate(expr,x),
  if atom(iso) then 0 else
   (if subst(0,x,second(iso)) = 0
      then subst(1,x,second(iso))
      else subst(1,x,first(iso))));
```

This function is then used to create the entire A-matrix for the three dimensions of the shape torque and 36 K-vector coefficients:

```
make_A_matrix(M, K) :=
   genmatrix(lambda([i,j],
      betterisolate1(M[i,1], K[j,1])), 3, length(K));
Am : make_A_matrix(M_shape, K);
```

The A-matrix then satisfies the equation:

$$\overline{\boldsymbol{M}}_{shape} = \mathbf{A} \cdot \boldsymbol{K} \quad (8)$$

The transpose of the A-matrix with solar pressure divided out for a sail with no symmetry and all 36 torque coefficients is shown in Equation 9.

The torque due to the sail force and center of mass offset caused by the AMT is:

$$\overline{\boldsymbol{M}}_{force} = -\mathbf{r}_{\mathrm{cm}} \times \bar{\boldsymbol{f}}_{sail} \quad (10)$$

After the total torque on the sail is found from the derivative of the reaction wheel momentum, the estimate of the shape torque is found by subtracting the torque from the sail force.

$$\overline{\boldsymbol{M}}_{shape} = \overline{\boldsymbol{M}}_{total} - \overline{\boldsymbol{M}}_{force} \quad (11)$$

For each measurement, one shape torque is calculated, and all the individual shape torques are stacked vertically to form the complete least-squares $\boldsymbol{b}$ vector. An **A** matrix is also calculated for each observation, and these are stacked vertically into the complete **A** matrix. These are input to the least-squares solver to find the vector of torque coefficients, **K**. The **K** coefficients are reformulated into their corresponding tensors.

$$\frac{\mathbf{A}^{\mathrm{T}}}{p} = \begin{matrix} r_1a_2 & 0 & 0 \\ a_2r_2 & 0 & 0 \\ a_2r_3 & 0 & 0 \\ 0 & r_1a_2 & 0 \\ 0 & a_2r_2 & 0 \\ 0 & a_2r_3 & 0 \\ 0 & 0 & r_1a_2 \\ 0 & 0 & a_2r_2 \\ 0 & 0 & a_2r_3 \\ -a_1r_1 & 0 & 0 \\ -2a_1r_1r_2 & 0 & 0 \\ -2a_1r_1r_3 & 0 & 0 \\ -a_1r_2 & 0 & 0 \\ -2a_1r_2r_3 & 0 & 0 \\ -a_1r_3 & 0 & 0 \\ 0 & -a_1r_1 & 0 \\ 0 & -2a_1r_1r_2 & 0 \\ 0 & -2a_1r_1r_3 & 0 \\ 0 & -a_1r_2 & 0 \\ 0 & -2a_1r_2r_3 & 0 \\ 0 & -a_1r_3 & 0 \\ 0 & 0 & -a_1r_1 \\ 0 & 0 & -2a_1r_1r_2 \\ 0 & 0 & -2a_1r_1r_3 \\ 0 & 0 & -a_1r_2 \\ 0 & 0 & -2a_1r_2r_3 \\ 0 & 0 & -a_1r_3 \\ 0 & r_1a_3r_3 & -r_1r_2a_3 \\ -r_1a_3r_3 & 0 & r_1\ a_3 \\ r_1r_2a_3 & -r_1\ a_3 & 0 \\ 0 & r_2a_3r_3 & -r_2\ a_3 \\ -r_2a_3r_3 & 0 & r_1r_2a_3 \\ r_2\ a_3 & -r_1r_2a_3 & 0 \\ 0 & a_3r_3 & -r_2a_3r_3 \\ -a_3r_3 & 0 & r_1a_3r_3 \\ r_2a_3r_3 & -r_1a_3r_3 & 0 \end{matrix} \quad (9)$$

6. Results

The first set of results was generated for the planned NEA Scout sail characterization attitudes. A total of 33 simulations were run for each characterization attitude, as described in section 2. The first part of each simulation started with the AMT at position [0, 0], followed by a momentum management activation where the AMT converged on the non-zero equilibrium position for that attitude. Each simulation runs for 3 hours to generated simulated telemetry for processing.

The characterization process starts by fitting a 2nd order polynomial to the wheel momentum, normalized by solar pressure. A few examples of this data are shown in Fig. 1, collected at different SIA and roll angles. The gaps in the data are when the AMT activates to reduce the RW momentum and trim out the pitch/yaw torques. Data is only used when the AMT isn't moving and spacecraft is holding an inertial attitude to make the data smoother so a polynomial and its derivative can be easily calculated.

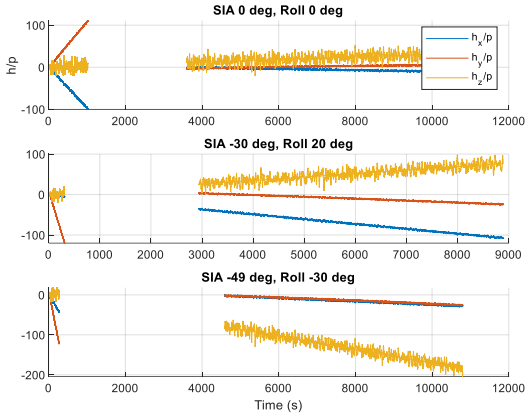

Fig. 1. Reaction wheel momentum / solar pressure

The total torque normalized by solar pressure is found by taking the polynomial derivative of the normalized momentum. These are 1st order polynomials to account for gradual changes in torque over the telemetry segment from effects like the movement of the sail relative to the sun direction. To use it in the characterization process without excessive data points, the torque polynomial is evaluated at the beginning, midpoint, and end of each continuous telemetry segment. Examples of these are shown in Fig. 2.

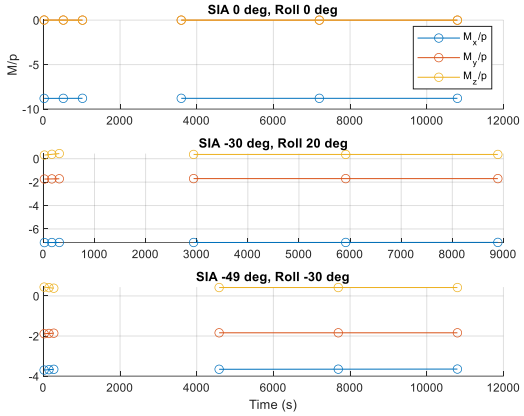

Fig. 2. Total solar torque / solar pressure

Once the total normalized torque is calculated, measurement of the sail shape torque is found by subtracting the torque from the solar force crossed with the CM. The CM is calculated from the mass model using the AMT position as an input. The sail force is calculated from a sail model, that can itself be updated by observing the sail's effect on the trajectory. This normalized torque, due only to sail shape is show in Fig. 3.

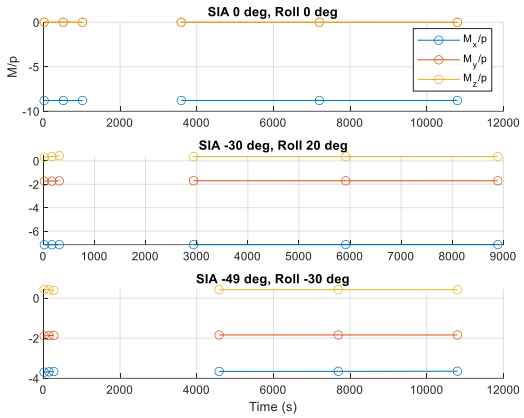

Fig. 3. Sail shape torque / solar pressure

This is the data needed for building the ***b*** vector in the least-squares problem. All these normalized shape torque vectors are stacked vertically into the total ***b*** vector. The sail body frame sun vector is calculated at times corresponding to the normalized shape torques from the inertial-to-body quaternions and position of the sun from the sail orbit and sun ephemeris. The unit sun vector components and optical coefficients are used to compute an ***A*** matrix according to Equation 9 for each normalized shape torque, and stacked vertically into the total ***A*** matrix.

Then, the least-squares problem is solved for the vector of shape coefficients (Equation 7). These are

reformulated back into the tensors in Equation 2. These tensors are then compared to those in the truth model. Unfortunately, with the NEA Scout simulation and attitude schedule, the torque coefficients do not clearly match the plant model. To demonstrate this, the **L** tensors are shown in Equations 12 and 13. The $\mathbf{K}^2$ and $\mathbf{K}^3$ tensors have similar differences.

$$\mathbf{L}_{est} = \begin{bmatrix} -0.0805 & -0.0122 & 0.0030 \\ 0.0035 & -0.0453 & 0.0043 \\ 0.0022 & 0.6433 & 0.1258 \end{bmatrix} \quad (12)$$

$$\mathbf{L}_{plant} = \begin{bmatrix} -0.2476 & -0.0009 & -0.0012 \\ -0.0025 & 0.2328 & -0.0050 \\ 0.0002 & 4.9006 & 18.2043 \end{bmatrix} \quad (13)$$

The reasons for the poor match are not clearly known, but some possibilities include the limited range of SIA and roll angle to accommodate NEA Scout operations, and the large number of coefficients being searched for (36) relative to the number of observations (33 attitudes with ~6 data points each).

Next, the estimated coefficients were used to compare the torques they calculate against the plant model torques. Using the same model inputs – sun vector, solar flux, solar distance – the torque from the sail shape was calculated using the estimated sail torque coefficients and compared to the same torque calculation using the plant model coefficients. Equation 14 is the difference between the torque calculations. It is plotted for all 219 samples (73 telemetry sets with 3 samples each) in Fig. 4. All the torques computed with the estimated coefficients come in below $10\text{x}10^{-8}$ Nm of the plant model.

$$\bar{\boldsymbol{M}}_{\text{shape},\Delta} = \bar{\boldsymbol{M}}_{shape,plant} - \bar{\boldsymbol{M}}_{shape,est} \quad (14)$$

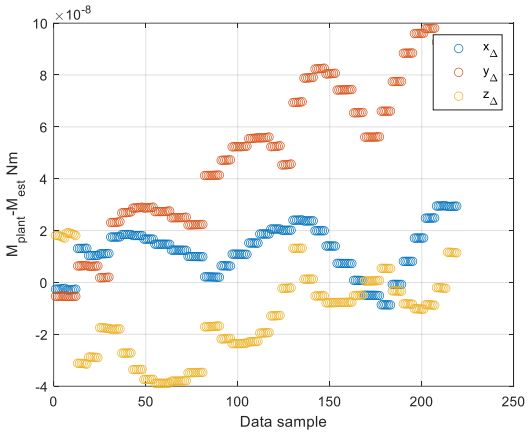

Fig. 4. Torque difference between plant model and estimated torque coefficients

Next, the error factor relative to the modeled plant moment was calculated according to Equation 15 and plotted in Fig. 5, both at full scale and zoomed in to within a factor of 0.1. The differences are much more significant, with a factor of ~150 for the worst data point. The relative error is much better for many of the data points. For the y-axis, many are within a factor of +/- 0.05. For the x-axis many are within +/- 0.1. The roll axis is less accurate, within a factor of +/- 1.0.

$$\bar{\boldsymbol{M}}_{shape,err} = \frac{\bar{\boldsymbol{M}}_{shape,plant} - \bar{\boldsymbol{M}}_{shape,est}}{\bar{\boldsymbol{M}}_{shape,plant}} \quad (15)$$

From the computation of the differences in sail torque, the absolute torque accuracy is bounded. In some cases, the relative error is quite large. The reasons for this are likely because the torque estimates are small and within the noise floor of the measurements. The AMT deliberately minimizes the total momentum and torque observable on the wheels, and the torque estimate is then driven by the model of the sail force crossed with the center of mass, rather than measurements. The torque differences plotted in Fig. 4 may represent a noise floor, below which the torque estimates will have large relative error. If both the torque measured by the wheels and modeled by the force and CM are within the that order of magnitude, they may be expected to have large errors.

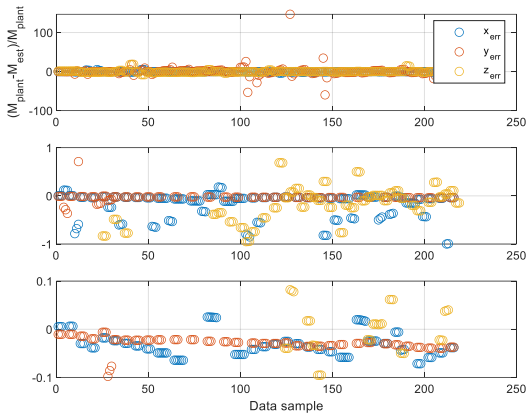

Fig. 5. Relative torque error from plant model and estimated torque coefficients

7. Conclusions and Future Work

The process described can solve for estimated torque coefficients of the sail that are able to replicate the plant model torques, although with large relative errors on the roll axis and with several large outlier torque errors. The results suggest that the process can be improved to reproduce the true torques of a sail more accurately.

Possible improvements to be examined include:

- Rejection of measurements that fall below the noise floor

- Enlarged range of angles to characterize the sail over for missions without the attitude constraints of the NEA Scout AMT, like the cloverleaf pattern studied by Rios-Reyes and Scheeres [1]
- Simplified set of moment coefficients that include symmetries to reduce the number of parameters being solved for
- Analyze noise sources of the different axes in more detail and how to mitigate them
- Tolerance of control system design to errors in torque model

This process is planned to be adapted to other solar sail missions with different attitude control hardware and mission scenarios, including Solar Cruiser [7] and the Advanced Composite Solar Sail System (ACS3) [8]. Solar Cruiser's mission to the sun-Earth L1 Lagrange region allows plenty of time to perform similar characterization operations as NEA Scout and has an AMT design that doesn't limit the range of roll angles. ACS3 will fly in Earth orbit where additional environmental torques (aerodynamic, gravity gradient, Earth radiation pressure) will need to be removed.

Acknowledgments

The author would like to acknowledge his fellow team members on the Near Earth Asteroid Scout and Solar Cruiser guidance & control teams. Their thorough job of developing the control software and models of those missions enabled this work to happen.

References

[1] L. Rios-Reyes and D. J. Scheeres, Solar-Sail Navigation: Estimation of Force, Moments, and Optical Parameters, Journal of Guidance, Control, and Dynamics Vol. 30 No. 3 (2007) 660-668.

[2] L. Rios-Reyes and D. J. Scheeres, Generalized Model for Solar Sails, Journal of Spacecraft and Rockets Vol. 42 No. 1 (2005) 182-185.

[3] Juan Orphee, Ben Diedrich, Brandon Stiltner, Chris Becker, and Andrew Heaton, Solar Sail Attitude Control System for the NASA Near Earth Asteroid Scout Mission, International Symposium on Solar Sailing 2017, Kyoto, Japan.

[4] Matlab, https://www.mathworks.com/products/matlab.html, Accessed: April 18 2023.

[5] Maxima: A Computer Algebra System, https://maxima.sourceforge.io/, Accessed: April 18 2023.

[6] TSIS-1: Total Solar Irradiance Data, https://lasp.colorado.edu/tsis/data/tsi-data/ Accessed: April 19 2023.

[7] L. Johnson and others. The NASA Solar Cruiser Mission – Solar Sail Propulsion Enabling Heliophysics Missions. Logan, Utah, USA, 2022. 36th Annual Small Satellite Conference. Paper SSC22-II-03.

[8] K. Wilkie. The NASA Advanced Composite Solar Sail System (ACS3) Flight Demonstration: A Technology Pathfinder for Practical Smallsat Solar Sailing. Logan, Utah, USA, 2021. 35th Annual Small Satellite Conference. Paper SSC21-II-10.

Solar Sail Attitude Control Using Shape Modulation: The Cable-Actuated Bio-inspired Lightweight Elastic Solar Sail Concept

Ryan J. Caverly,[a,*], Keegan R. Bunker[a], Nathan Raab[b], Vinh L. Nguyen[a], Garvin Saner[a], Zixin Chen[a], Tyler Douvier[a], Richard J. Lyman[a], Owen Sorby[a], Benjamin Sorge[a], Ebise Teshale[a], Benjamin Toriseva[a]

[a]*Department of Aerospace Engineering and Mechanics, University of Minnesota, Minneapolis, USA*
[b]*Minnesota Robotics Institute, University of Minnesota, Minneapolis, USA*

Abstract

This paper presents the Cable-Actuated Bio-inspired Lightweight Elastic Solar Sail (CABLESSail) concept that will enable robust, precise, and scalable attitude control of solar sails. This concept leverages lightweight cable-driven actuation to achieve large, controllable elastic bending and torsional deformations in the booms of a solar sail that mimic the motion of an elephant's trunk or a starfish's arms. These large cable-driven boom deformations modulate the shape of the entire sail to create an imbalance of SRP to induce control torques in all three solar sail axes. This actuation method scales well with an increase in solar sail size, as cables can transmit forces over kilometers in length from a lightweight and small stowed volume. This paper highlights early work on the CABLESSail concept, focusing on initial research efforts on its design, analysis, modeling, and prototyping.

Keywords: Attitude control, momentum management, flexible structures, cable-driven robots, solar sail design

1. Introduction

Through the use of solar radiation pressure (SRP)-based propulsion, solar sails offer unique mission capabilities, including orbits outside of the ecliptic plane [1–3], statites that "hover" in a fixed location [4], and interstellar travel [5–7]. Solar sail technology has advanced in recent years, and it is now possible to fabricate and deploy sails with areas of 10-100 m^2 (e.g., LightSail 2 [8] and NEA Scout [9]), with the likelihood that this will increase up to 7,000 m^2 or even larger in the coming years and decades (e.g., Solar Cruiser [3] and Solar Polar Imager [1, 2]). An unsolved challenge in the design of solar sails is ensuring its attitude and momentum can be controlled accurately and reliably using technology that scales up to the size of these large, next generation solar sails [10].

State-of-the-art solar sail attitude control methods can be sorted into three main categories: Conventional spacecraft attitude control methods (e.g., reaction wheels in the spacecraft hub [11, 12] and tip-mounted thrusters [13]), methods that control the offset between the solar sail's center of mass and center of pressure (e.g., sliding masses [13–19], shifted sails [20], billowed sails [21], variable reflectivity panels [22–25], and gimbaled ballast masses [26]), and those that use control vanes [27–31] or angled sails [32, 33].

Control methods in the first category are effective with smaller sails and relatively simple to operate, but are typically not scalable to larger solar sail designs. Methods in the second category are promising and have been incorporated into solar sail designs (e.g., Solar Cruiser uses Reflectivity Control Devices (RCDs) and an active mass translator (AMT) system [3]). However, some of them, such as sliding and gimbaled ballast masses, are difficult to scale up to larger sails, as they involve adding substantial mass to the design. Additionally, many methods within this category are incapable of generating control torques out of the plane of the sail (roll axis). Variable reflectivity panels, such as RCDs, can generate torques about the roll axis through a reflectivity gradient in the panel or a mounting offset from the normal axis of the sail, although this torque can be small in magnitude. Control methods in the third category, including control vanes, are typically capable of generating three-axis control torques, but also have limited torque capabilities due to their relatively small controllable area. For this reason, control vanes are often placed as far outwards on the sail as possible to in-

*Corresponding author, rcaverly@umn.edu

crease the torque they produce, which complicates the design of the system, specifically the storage and deployment of the sail, as well as the method of powering/controlling the vanes. Scaling up control vanes to larger solar sails is challenging, as larger control torques require vanes with larger mass and volume. A recently-proposed concept makes use of the entire solar sail as a control vane, where piezoelectric actuators are used to bend flexible booms and cause the sail to deflect, thus inducing a control torque through an imbalance in SRP [32, 33]. This technique has great potential in generating larger torques, as the entire sail is used an actuator; however, the use of piezoelectric actuation of the booms severely limits the deflections and yields small control torques.

The idea of using the entire solar sail as a control vane inspired the Cable-Actuated Bio-inspired Lightweight Elastic Solar Sail (CABLESSail) concept proposed in this paper. CABLESSail leverages lightweight cable-driven actuation to achieve large, controllable elastic bending and torsional deformations in the booms of a solar sail that mimic the motion of an elephant's trunk or a starfish's arms. These large cable-driven boom deformations, which are actuated using winches located near the solar sail's center of mass, will modulate the shape of the entire sail to act as a "control vane" and create an imbalance of SRP to induce control torques in all three solar sail axes. This actuation method scales well with an increase in solar sail size, as cables can transmit forces over kilometers in length from a lightweight and small stowed volume.

This paper highlights early work on the CABLESSail concept, focusing on 1) an initial conceptual design with preliminary analysis of the actuation requirements and magnitude of attitude control torques generated; 2) initial dynamic simulation development efforts to capture CABLESSail's structural dynamics and provide an environment in which to test the concept; 3) early prototyping results demonstrating the real-world feasibility of the proposed actuation mechanisms; and 4) plans for the control and estimation algorithms to be used to reliably actuate the cable-actuated mechanisms.

The remainder of this paper proceeds as follows. Section 2 provides a detailed overview of the CABLESSail concept and preliminary aspects of its design. Section 3 presents initial development of a CABLESSail dynamic simulation. Early prototyping results are highlighted in Section 4, followed by a discussion on CABLESSail's control and estimation challenges in Section 5. Concluding remarks are provided in Section 6.

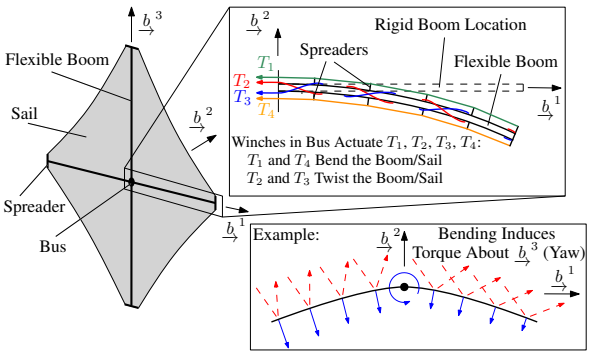

Figure 1: Schematic of the CABLESSail concept.

2. CABLESSail Concept Overview

This section presents an overview of the CABLESSail concept, followed by design options under consideration, and preliminary design evaluations using static simulations.

2.1. *Concept of Operations*

The CABLESSail concept is centered around the incorporation of cables/tendons routed throughout the booms of a solar sail, as shown in Figure 1. The cables are routed such that they pass through eyelets that are a distance from the boom's neutral axis, and thus, as the tension in the cable is increased and its length is reduced, bending or twisting of the boom is induced. Due to the unilateral force transmission of cables, a single cable provides bending or twisting actuation in a single direction (e.g., bending in the positive $\underrightarrow{b}^2$ direction shown in Figure 1, but not in the negative $\underrightarrow{b}^2$ direction). Bending is specifically achieved by routing the cable in a relatively straight line on one side of the boom, while twisting requires the cables to be routed helically about the boom. This type of cable-actuation mechanism is inspired by work in the area of bio-inspired cable-driven continuum robotics (also known as soft robotics) with applications ranging from surgical tasks [34] to ground-based locomotion [35, 36], and the manipulation of relatively small objects [36, 37].

The concept of operations in which CABLESSail induces attitude control through shape modulation is depicted in Figure 2. An idealized solar sail with four booms is shown in Figure 2(a), where photons are shown to bounce off the reflective sail surface with an incidence angle and transfer momentum to the sail in the form of solar radiation pressure. Figure 2(b) illustrates the effect of pulling on the appropriate cables to induce bending in the booms aligned in the $\underrightarrow{b}^1$ (pitch)

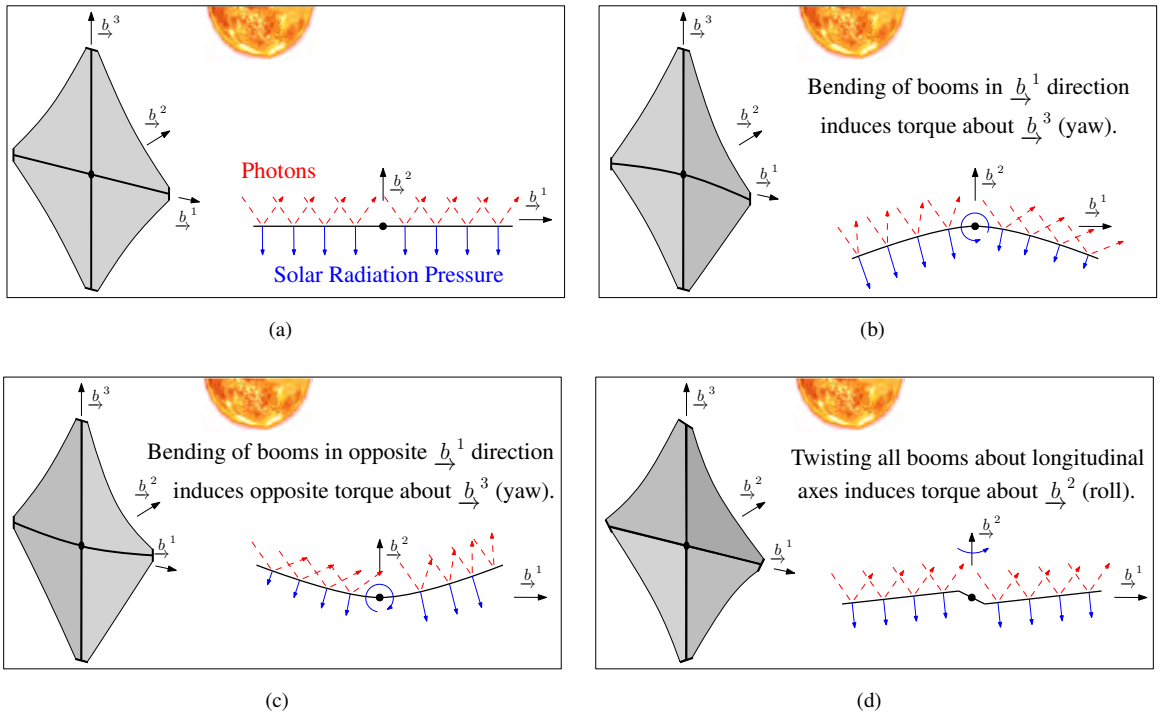

Figure 2: Schematic depicting CABLESSail's concept of operations, where the red dashed arrows denote the direction in which the photons bounce off the sail and the blue arrows denote the transfer of momentum imparted on the sail due to the photons. The undeformed sail is presented in (a). The schematic in (b) demonstrates the effect of bending the booms and sail about the yaw axis to create a smaller incidence angle on one half of the sail and a larger incidence angle on the other half of the sail, which leads to an imbalance in solar radiation pressure and a positive yaw torque. A similar effect is shown in (c), where the booms are bent in the opposite direction, resulting in a negative yaw torque. The booms are twisted in (d), which leads the sail to take on a "pinwheel" shape and induces a roll torque.

direction. This causes the shape of the sail to change such that the sun incidence angle on one side decreases, thus increasing the transfer of momentum from the photons, while the sun incidence angle of the other side of the sail increases, which decreases the transfer of momentum. This results in a net torque in the positive $\underrightarrow{b}^3$ (yaw) direction. Pulling on different cables that bend the booms in the opposite direction will induce a torque in the negative $\underrightarrow{b}^3$ direction, as shown in Figure 2(c). This approach can also be used to induce positive and negative torques in the $\underrightarrow{b}^1$ (pitch) direction by bending the booms aligned with the $\underrightarrow{b}^3$ (yaw) axis. Figure 2(d) illustrates the effect of pulling on the cables that induce a twist in all of the booms. This results in the sail taking on a pinwheel-like shape and a torque about the $\underrightarrow{b}^2$ (roll) axis is generated. Note that this pinwheel shape relies on the use of spreaders at the tips of the booms to induce a slope in the sail shape outside of the $\underrightarrow{b}^1$-$\underrightarrow{b}^3$ plane. This is a potential limitation of the CABLESSail design to generate roll torques, as not all solar sail designs are accommodating of tip-mounted spreaders.

2.2. *Design Considerations*

A central question in the design of CABLESSail is determining how to integrate the actuating cables within a deployable solar sail boom. Current work towards this is focused on assessing the possibility of integrating cables within the TRAC booms currently under development for Solar Cruiser [38], NASA Langley's ACS3 deployable booms [39], and coilable boom concepts previously developed by ATK Space Systems [40].

Another important CABLESSail design question is determining the ideal number of actuating cables. For full control over the bending and twisting of each boom in both the positive and negative directions, a total of six cables are required per boom: one cable to bend in the positive direction, one cable to bend in the negative direction, two helically-routed cables to twist in the positive direction and two helically-routed cables to twist in the negative direction. This results in a total of 24 cables actuated by motors to fully actuate all of CABLESSail's booms, which will require substantial mass and volume, while also introducing a large amount of system complexity. Fortunately, attitude control torques can be gen-

erated without requiring all booms to be fully actuated. For example, pitch and yaw torques can be generated by only bending one of the booms, rather than two, albeit with a smaller torque magnitude. This can reduce the need for two "boom-bending" cables in each boom down to one. The downside of this is a reduction in actuation redundancy, which will make the system susceptible to failures in any single actuating cable. A trade study is currently being conducted to quantify the trade-offs between actuator size, weight, and power (SWaP), attitude control torque magnitude, and actuation redundancy to provide guidelines on this design choice.

2.3. Preliminary Design and Static Simulation Tests

A preliminary CABLESSail design is developed for a Solar Cruiser-class sail focusing on the use of cable actuation to induce bending of the booms. For this initial design and analysis, tubular cross-section booms are considered that have a similar carbon fiber material and second moment of area to the proposed Solar Cruiser TRAC booms. Disks placed along the length of the booms are designed to route the cables 7.5 cm from the neutral axis of the booms. The booms are discretized into elements and their deformation as a function of the tension applied to the cables is computed using the tendon-driven continuum robot static modeling code developed by the University of Toronto [41]. The deformations of the discretized boom elements are then used to determine the boundary conditions of the surrounding sail quadrants. As part of this preliminary simulation, a two-dimensional representation of the sail as a flat plate between boundary conditions is used. The sail is discretized into a number of panels and the normal direction of each panel is determined to compute the local sun-incidence angle (SIA) of each panel. The idealized SRP model in [42] is used to compute the force on each sail panel, which is then used to determine the total force and moment acting on the solar sail by summing up the forces and moments acting across all sail panels.

The resulting torques generated by actuating a single cable/boom at 0 deg. SIA and 35 deg. SIA is shown in Figure 3 along with the minimum torque requirements provided by NASA to counteract the predicted disturbance torques [43]. As shown in Figure 3, the torques generated by actuating the cable exceed the Solar Cruiser disturbance torque requirements with less than a 7 mm change in length of the actuating cable. The maximum cable tension required for the largest boom deformation is 63 N. Figure 3(c) also includes a visualization of the boom deformation at the maximum cable tension, where the boom tip is displaced 0.71 m.

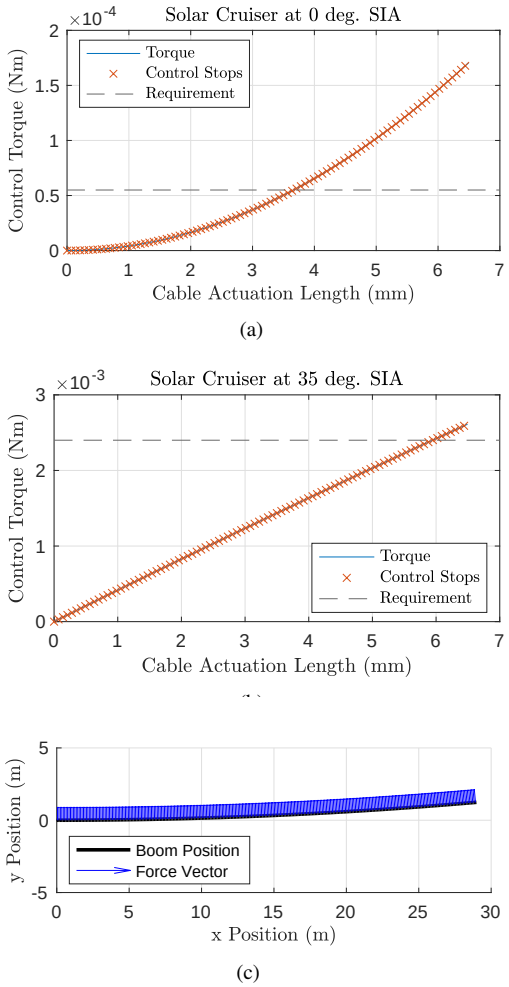

Figure 3: Results from a preliminary static simulation of the pitch and yaw control torques generated by the bending of one of CABLESSail's booms. The control torques generated as a function of cable actuation length at 0 deg. and 35 deg. sun-incidence angles (SIAs) are included in (a) and (b), respectively. The boom deformation at the maximum cable actuation length is shown in (c), where the SRP force vector at each sail node for 0 deg. SIA is included.

The preliminary design features eight stepper motors (Avior C62S-10N75-20) that are capable of providing more than the required 63 N of cable tension with a reasonably-sized winch drum. The motors are equipped with a mechanical brake capable of holding the winch at the desired angle when the boom is to be held in place, which reduces the power draw of the system. The total mass estimate of the CABLESSail actuation hardware is 3.1 kg, of which 1.6 kg is attributed to the motors, the actuating cables have a mass of 1 kg, and the supporting hardware (e.g., eyelets along the booms, nuts and bolts) and electronics make up the remaining 0.5 kg. In this first design iteration, the actuation mechanism is de-

signed to fit within 25 cm x 25 cm x 10 cm volume. This volume will likely be reduced in future iterations.

3. CABLESSail Dynamic Modeling

A dynamic model of the entire CABLESSail system is derived through the null-space method [44, 45], a modular dynamic modeling technique for multi-body systems with constraints. This method allows for an arbitrary number of actuating cables to be kinematically constrained to the flexible booms with arbitrary cable routings, as well as constrain the flexible booms to the bus and sail of the spacecraft. This modularity in the dynamic model and numerical simulation allows for a large design space to be tested without requiring the system's equations of motion to re-derived with each design change. An overview of the null-space method is first presented, followed by a description of how the null-space method is used to structure the CABLESSail dynamic simulation code, and initial simulation results.

3.1. Null-Space Method Overview

The equations of motion of the i^{th} component of the system (e.g., rigid spacecraft hub, flexible boom) are derived as

$$\mathbf{M}_i(\mathbf{q}_i)\ddot{\mathbf{q}}_i + \mathbf{D}_i(\mathbf{q}_i)\dot{\mathbf{q}}_i + \mathbf{K}_i(\mathbf{q}_i)\mathbf{q}_i = \mathbf{f}_i + \mathbf{f}_{\text{non}_i}(\dot{\mathbf{q}}_i, \mathbf{q}_i), \quad (1)$$

where $\mathbf{q}_i$ contains the generalized coordinates of the i^{th} component (e.g., position, attitude, elastic coordinates), $\mathbf{M}_i(\mathbf{q}_i)$ is the mass matrix, $\mathbf{D}_i(\mathbf{q}_i)$ is the damping matrix, $\mathbf{K}_i(\mathbf{q}_i)$ is the stiffness matrix, $\mathbf{f}_i$ contains the generalized forces and moments, and $\mathbf{f}_{\text{non}_i}(\dot{\mathbf{q}}_i, \mathbf{q}_i)$ contains nonlinear forces. The equations of motion in Eq. (1) can be derived using any methodology, such as a Langrange's equations, Kane's equations, or a Newton-Euler approach.

The kinematic constraints that must be maintained by the system's components are written out in Pfaffian form as $\mathbf{\Xi}(\mathbf{q})\dot{\mathbf{q}} = \mathbf{0}$, where $\mathbf{q} = \begin{bmatrix}\mathbf{q}_1^\mathsf{T} & \cdots & \mathbf{q}_n^\mathsf{T}\end{bmatrix}^\mathsf{T}$ and $\mathbf{\Xi}(\mathbf{q}) = \begin{bmatrix}\mathbf{\Xi}(\mathbf{q}_1) & \cdots & \mathbf{\Xi}(\mathbf{q}_n)\end{bmatrix}$. Examples of relevant kinematic constraints include the velocity of a point on one body matching the velocity of a point on another body, as well as the angular velocity of two bodies matching.

The constrained equations of motion are written as

$$\mathbf{M}\ddot{\mathbf{q}} + \mathbf{K}\mathbf{q} = \mathbf{f} + \mathbf{f}_{\text{non}} + \mathbf{\Xi}^\mathsf{T}\boldsymbol{\lambda}, \quad (2)$$

where $\boldsymbol{\lambda}$ is a Lagrange multiplier that maintains the constraints specified by $\mathbf{\Xi}(\mathbf{q})\dot{\mathbf{q}} = \mathbf{0}$, $\mathbf{M} = \text{diag}\{\mathbf{M}_1, \ldots, \mathbf{M}_n\}$, $\mathbf{D} = \text{diag}\{\mathbf{D}_1, \ldots, \mathbf{D}_n\}$, $\mathbf{K} = \text{diag}\{\mathbf{K}_1, \ldots, \mathbf{K}_n\}$, and the arguments of the terms in Eq. (2) are omitted for brevity.

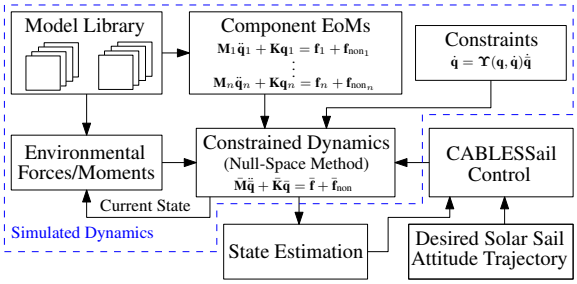

Figure 4: Block diagram of the proposed CABLESSail dynamic simulation code environment.

A set of independent coordinates $\bar{\mathbf{q}}$ is then chosen. For a system composed of rigid and flexible bodies, this is typically $\dot{\bar{\mathbf{q}}} = \begin{bmatrix}\dot{\mathbf{r}}^\mathsf{T} & \boldsymbol{\omega}^\mathsf{T} & \dot{\mathbf{q}}_e^\mathsf{T}\end{bmatrix}^\mathsf{T}$, where $\dot{\mathbf{r}}$ is the velocity of the rigid body, $\boldsymbol{\omega}$ is the angular velocity of the rigid body, and $\dot{\mathbf{q}}_e$ are elastic coordinate rates that describe the system's flexibility. A mapping from dependent to independent coordinates is then defined as $\dot{\mathbf{q}} = \mathbf{\Upsilon}\dot{\bar{\mathbf{q}}}$. Notice that $\mathbf{\Xi}\mathbf{\Upsilon} = \mathbf{0}$ (i.e., $\mathbf{\Xi}$ and $\mathbf{\Upsilon}$ are orthogonal complements) by substituting $\dot{\mathbf{q}} = \mathbf{\Upsilon}\dot{\bar{\mathbf{q}}}$ into the constraint $\mathbf{\Xi}(\mathbf{q})\dot{\mathbf{q}} = \mathbf{0}$. The independent coordinates are then substituting into the constrained equations of motion of Eq. (2) using $\dot{\mathbf{q}} = \mathbf{\Upsilon}\dot{\bar{\mathbf{q}}}$ and $\ddot{\mathbf{q}} = \mathbf{\Upsilon}\ddot{\bar{\mathbf{q}}} + \dot{\mathbf{\Upsilon}}\dot{\bar{\mathbf{q}}}$. The resulting equation is then premultiplied by $\mathbf{\Upsilon}^\mathsf{T}$ to yield

$$\underbrace{\mathbf{\Upsilon}^\mathsf{T}\mathbf{M}\mathbf{\Upsilon}}_{\bar{\mathbf{M}}}\ddot{\bar{\mathbf{q}}} + \underbrace{\mathbf{\Upsilon}^\mathsf{T}\mathbf{D}\mathbf{\Upsilon}}_{\bar{\mathbf{D}}}\dot{\bar{\mathbf{q}}} + \underbrace{\mathbf{\Upsilon}^\mathsf{T}\mathbf{K}\mathbf{q}}_{\bar{\mathbf{K}}\bar{\mathbf{q}}} = \underbrace{\mathbf{\Upsilon}^\mathsf{T}\mathbf{f}}_{\bar{\mathbf{f}}} + \underbrace{\mathbf{\Upsilon}^\mathsf{T}\left(\mathbf{f}_{\text{non}} - \mathbf{M}\dot{\mathbf{\Upsilon}}\dot{\bar{\mathbf{q}}}\right)}_{\bar{\mathbf{f}}_{\text{non}}} + \cancel{\mathbf{\Upsilon}^\mathsf{T}\mathbf{\Xi}^\mathsf{T}\boldsymbol{\lambda}}^{\mathbf{0}}. \quad (3)$$

After the removal of the Lagrange multipliers, Eq. (3) is rewritten as

$$\bar{\mathbf{M}}\ddot{\bar{\mathbf{q}}} + \bar{\mathbf{K}}\bar{\mathbf{q}} = \bar{\mathbf{f}} + \bar{\mathbf{f}}_{\text{non}},$$

which represents the system's constrained equations of motion without Lagrange multipliers.

3.2. CABLESSail Dynamic Simulation Code Structure

Within the context of the CABLESSail simulation code, the null-space method outlined in Section 3.1 serves as a way to create code that is modular and easily amenable to design changes and the evaluation of different modeling choices. A block diagram of the proposed CABLESSail dynamic simulation code is shown in Figure 4, where its modularity and use of the null-space method are displayed. The code is structured so that a library of component equations of motion is available, which may even include different fidelity models for the

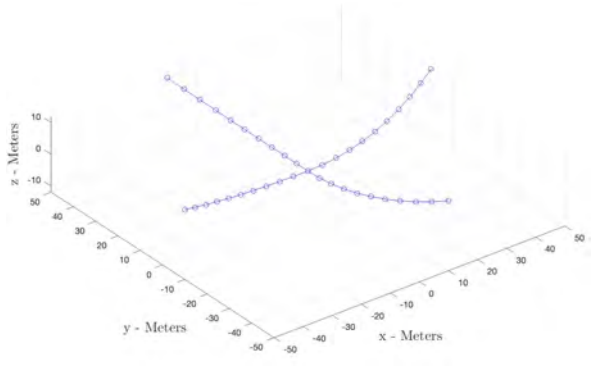

Figure 5: A screenshot of an animation from the preliminary CABLESSail dynamic simulation code.

same component. Another portion of the code is dedicated to selecting the relevant components that are to be incorporated into the simulation and also define the relevant kinematic mapping from dependent to independent coordinates $\dot{\mathbf{q}} = \Upsilon\dot{\tilde{\mathbf{q}}}$. The null-space method is then used to constrain the components together, resulting in nonlinear equations of motion that can be numerically simulated in feedback with the desired stated estimation and control strategies. The versatility and modularity of the null-space method allows for drastic changes in the system configuration to be implemented in the simulation by only changing the components that are selected and defining the new mapping $\dot{\mathbf{q}} = \Upsilon\dot{\tilde{\mathbf{q}}}$.

3.3. Preliminary CABLESSail Simulation Results

A preliminary version of the CABLESSail simulation code is in development, with an initial focus on modeling the elastic bending of the booms with cable-driven actuation. An animation image from this simulation is shown in Figure 5. The solar sail structure included in this simulation is representative of a CABLESSail geometry that is analogous to the dimensions of Solar Polar Imager with a free response to elastic deformations. This simulation allows for the dynamic behavior of CABLESSail's cable-actuated booms to be evaluated.

A complete three-dimensional CABLESSail simulation with a sail model inspired by [46] will be the focus of future development of this simulation code.

4. CABLESSail Prototyping

Small-scale prototyping will play an important role in the development and analysis of the CABLESSail concept. Specifically, aspects of the design that are difficult to model or simply cannot be modeled in the simulation will be tested through the evaluation of small-scale prototypes. This will include friction between components, deployment of the booms, as well as realistic noise and delays in sensing and actuation.

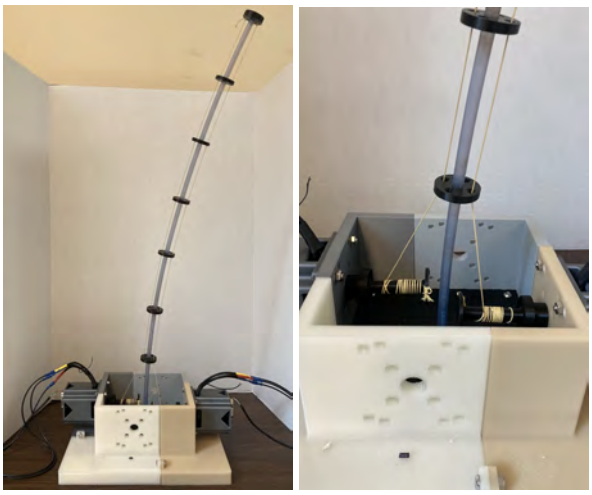

Figure 6: A preliminary CABLESSail prototype that tests the bending motion of a single small-scale cable-actuated boom. A test with constant tension applied to the cables is shown, along with a close-up view of the winch mechanism and the 3D-printed cable-routing disks that the cables pass through.

The remainder of this section presents work towards an initial prototype testbed, as well as plans for future prototype fabrication and testing.

4.1. Preliminary Prototype Development

A preliminary prototype of a single CABLESSail boom with two actuating cables used to induce bending in the boom is shown in Figure 6. This prototype uses a polycarbonate boom with 3D-printed cable-routing disks along the boom. The cables are actuated by ODrive BLDC motors operated in position mode.

This preliminary prototype demonstrates the ability to generate large boom deformations using cable actuation. It also provides a framework that can be used to fabricate more advanced CABLESSail prototypes with more realistic deployable solar sail boom geometries.

4.2. Planned Future Prototypes

Additional CABLESSail prototypes will be built to guide and assess important design choices. The first set of prototypes will focus on investigating the integration of the actuating cables within deployable solar sail boom designs. Similar to the preliminary prototype discussed in Section 4.1, this will involve a single boom and test different cable routing and integration options.

A four-boom small-scale prototype will also be fabricated to test the ability to perform controlled deformation of the booms with real sensors and actuators. A motion-capture system will be used with the prototypes to provide ground-truth data of the boom deflections and assist with model validation, as well as the assessment of our proposed control and estimation algorithms.

5. CABLESSail Control and State Estimation

Successful operation of CABLESSail will rely on carefully controlled deformation of its flexible booms using actuated cables. Ensuring robustness and reliability of this actuation in the presence of CABLESSail's complex, nonlinear elastic dynamics will require an onboard autonomous feedback control strategy. Moreover, cables only transmit forces in tension and significant hardware issues can occur if a cable goes slack unintentionally. CABLESSail's feedback control strategy will need to account for these challenges, which will likely take inspiration from robust control methods developed for cable-driven robotic systems [47, 48]. Accurate knowledge of the state of the solar sail booms (e.g., its deformed shape) is required to actively control the motion of the booms. This state estimation problem is challenging, due to the nonlinear elastic deformation of the booms and vibrations in the actuating cables. Different strategies may be employed to solve this problem, ranging from fusing cable length measurements with IMU measurements [49–51] to the use of fiber optic shape sensing [52]. Feedback control and state estimation will be a central focus of future research efforts, as they are essential to performing precise, controlled deformations of the CABLESSail booms.

6. Conclusions and Future Work

The work in this paper has set the stage for the development of the CABLESSail concept. Preliminary static simulations results showed that sufficiently large attitude control torques can be generated to cancel out the disturbance torques expected for large next-generation solar sails based on the parameters of Solar Cruiser. Initial progress towards developing a modular dynamic simulation and small-scale prototypes of CABLESSail were described, along with an outline of challenges to be addressed in the areas of control and state estimation.

Future work will focus on developing CABLESSail's dynamic simulation code and assessing design options through numerical simulations and prototypes. The dynamic simulation code developed as part of this effort will be publicly released to allows for others in the community to make use of this resource.

Acknowledgements

This work was supported by an Early Career Faculty grant from NASA's Space Technology Research Grants Program. V. L. Nguyen's contributions were supported by the National Science Foundation Graduate Research Fellowship under Grant No. 2237827.

References

[1] D. Thomas, M. Baysinger, S. Sutherlin, Q. Bean, K. Clements, K. Kobayashi, J. Garcia, L. Fabisinski, and P. Capizzo. Solar Polar Imager concept. In *ASCEND*, page 4060. 2020.

[2] K. Kobayashi, L. Johnson, H. Thomas, S. McIntosh, D. McKenzie, J. Newmark, A. Heaton, J. Carr, M. Baysingere, Q. Bean, et al. The high inclination solar mission. *arXiv preprint arXiv:2006.03111*, 2020.

[3] J. B. Pezent, R. Sood, A. Heaton, K. Miller, and L. Johnson. Preliminary trajectory design for NASA's Solar Cruiser: A technology demonstration mission. *Acta Astronautica*, 183:134–140, 2021.

[4] R. Linares, D. Landau, D. Miller, B. Weiss, and P. Lozano. Rendezvous mission for interstellar objects using a solar sail-based statite concept. *arXiv preprint arXiv:2012.12935*, 2020.

[5] X. Zeng, K. T. Alfriend, J. Li, and S. R. Vadali. Optimal solar sail trajectory analysis for interstellar missions. *The Journal of the Astronautical Sciences*, 59(3):502–516, 2012.

[6] S. Gong and M. Macdonald. Review on solar sail technology. *Astrodynamics*, 3(2):93–125, 2019.

[7] H.-T. Tung, H. Ling, and A. Davoyan. Fast transit interstellar probe mission with extreme solar sailing. In *AIAA SciTech Forum*, page 1220, 2023.

[8] D. A. Spencer, B. Betts, J. M. Bellardo, A. Diaz, B. Plante, and J. R. Mansell. The LightSail 2 solar sailing technology demonstration. *Advances in Space Research*, 67(9):2878–2889, 2021.

[9] T. R. Lockett, J. Castillo-Rogez, L. Johnson, J. Matus, J. Lightholder, A. Marinan, and A. Few. Near-Earth Asteroid Scout flight mission. *IEEE Aerospace and Electronic Systems Magazine*, 35(3):20–29, 2020.

[10] D. A. Spencer, L. Johnson, and A. C. Long. Solar sailing technology challenges. *Aerospace Science and Technology*, 93: 105276, 2019.

[11] M. Polites, J. Kalmanson, and D. Mangus. Solar sail attitude control using small reaction wheels and magnetic torquers. *Proceedings of the Institution of Mechanical Engineers, Part G: Journal of Aerospace Engineering*, 222(1):53–62, 2008.

[12] H. Gong, S. Gong, and D. Liu. Attitude dynamics and control of solar sail with multibody structure. *Advances in Space Research*, 69:609–619, 2021.

[13] B. Wie and D. Murphy. Solar-sail attitude control design for a flight validation mission. *Journal of Spacecraft and Rockets*, 44 (4):809–821, 2007.

[14] A. Bolle and C. Circi. Solar sail attitude control through in-plane moving masses. *Proceedings of the Institution of Mechanical Engineers, Part G: Journal of Aerospace Engineering*, 222(1): 81–94, 2008.

[15] V. Lappas, G. Mengali, A. A. Quarta, J. Gil-Fernandez, T. Schmidt, and B. Wie. Practical systems design for an Earth-magnetotail-monitoring solar sail mission. *Journal of Spacecraft and Rockets*, 46(2):381–393, 2009.

[16] D. Romagnoli and T. Oehlschlägel. High performance two degrees of freedom attitude control for solar sails. *Advances in Space Research*, 48(11):1869–1879, 2011.

[17] S. N. Adeli, V. J. Lappas, and B. Wie. A scalable bus-based attitude control system for solar sails. *Advances in Space Research*, 48(11):1836–1847, 2011.

[18] W. H. Steyn and V. Lappas. CubeSat solar sail 3-axis stabilization using panel translation and magnetic torquing. *Aerospace Science and Technology*, 15(6):476–485, 2011.

[19] H. Huang and J. Zhou. Solar sailing CubeSat attitude control method with satellite as moving mass. *Acta Astronautica*, 159: 331–341, 2019.

[20] B. Fu and F. O. Eke. Attitude control methodology for large solar sails. *Journal of Guidance, Control, and Dynamics*, 38(4): 662–670, 2015.

[21] B. Fu, E. Sperber, and F. Eke. Solar sail technology—a state of the art review. *Progress in Aerospace Sciences*, 86:1–19, 2016.

[22] R. Funase, Y. Mimasu, Y. Chishiki, Y. Shirasawa, Y. Tsuda, T. Saiki, and J. Kawaguchi. Modeling and on-orbit performance evaluation of propellant-free attitude control system for spinning solar sail via optical parameter switching. In *AAS/AIAA Astrodynamics Specialist Conference*, pages 1737–1754, 2012.

[23] A. Borggräfe, J. Heiligers, M. Ceriotti, and C. McInnes. Optical control of solar sails using distributed reflectivity. In *Spacecraft Structures Conference*, page 0833, 2014.

[24] D. C. Ullery, S. Soleymani, A. Heaton, J. Orphee, L. Johnson, R. Sood, P. Kung, and S. M. Kim. Strong solar radiation forces from anomalously reflecting metasurfaces for solar sail attitude control. *Scientific Reports*, 8(1):1–10, 2018.

[25] A. R. Davoyan, J. N. Munday, N. Tabiryan, G. A. Swartzlander, and L. Johnson. Photonic materials for interstellar solar sailing. *Optica*, 8(5):722–734, 2021.

[26] E. Sperber, B. Fu, and F. O. Eke. Large angle reorientation of a solar sail using gimballed mass control. *The Journal of the Astronautical Sciences*, 63(2):103–123, 2016.

[27] D. Lawrence and S. Piggott. Integrated trajectory and attitude control for a four-vane solar sail. In *AIAA Guidance, Navigation, and Control Conference and Exhibit*, page 6082, 2005.

[28] M. Mettler, A. Acikmese, and S. Ploen. Attitude dynamics and control of solar sails with articulated vanes. In *AIAA Guidance, Navigation, and Control Conference and Exhibit*, page 6081, 2005.

[29] M. Choi and C. J. Damaren. Structural dynamics and attitude control of a solar sail using tip vanes. *Journal of Spacecraft and Rockets*, 52(6):1665–1679, 2015.

[30] O. Eldad, E. G. Lightsey, and C. Claudel. Minimum-time attitude control of deformable solar sails with model uncertainty. *Journal of Spacecraft and Rockets*, 54(4):863–870, 2017.

[31] S. Hassanpour and C. J. Damaren. Collocated attitude and vibrations control for square solar sails with tip vanes. *Acta Astronautica*, 166:482–492, 2020.

[32] F. Zhang, G. Shengping, G. Haoran, and H. Baoyin. Solar sail attitude control using shape variation of booms. *Chinese Journal of Aeronautics*, 35(10):326–336, 2021.

[33] F. Zhang, S. Gong, and H. Baoyin. Three-axes attitude control of solar sail based on shape variation of booms. *Aerospace*, 8 (8):198, 2021.

[34] T. Kato, I. Okumura, S.-E. Song, A. J. Golby, and N. Hata. Tendon-driven continuum robot for endoscopic surgery: Preclinical development and validation of a tension propagation model. *IEEE/ASME Transactions on Mechatronics*, 20(5):2252–2263, 2014.

[35] V. Vikas, E. Cohen, R. Grassi, C. Sözer, and B. Trimmer. Design and locomotion control of a soft robot using friction manipulation and motor–tendon actuation. *IEEE Transactions on Robotics*, 32(4):949–959, 2016.

[36] D. Rus and M. T. Tolley. Design, fabrication and control of soft robots. *Nature*, 521(7553):467–475, 2015.

[37] K. Oliver-Butler, J. Till, and C. Rucker. Continuum robot stiffness under external loads and prescribed tendon displacements. *IEEE Transactions on Robotics*, 35(2):403–419, 2019.

[38] L. Nguyen, K. Medina, Z. McConnel, and M. S. Lake. Solar Cruiser TRAC boom development. In *AIAA SciTech Forum*, page 1507, 2023.

[39] W. K. Wilkie, J. M. Fernandez, O. R. Stohlman, N. R. Schneider, G. D. Dean, J. H. Kang, J. E. Warren, S. M. Cook, P. L. Brown, T. C. Denkins, S. D. Horner, E. D. Tapio, M. Straubel, M. Richter, and J. Heiligers. Overview of the NASA advanced composite solar sail system (ACS3) technology demonstration project. In *AIAA Scitech Forum*, page 1260, 2021.

[40] Florio Dalla Vedova and Pierre Morin. Survey of available boom technologies, the related TRL2 (and 3) and when will we reach our solar sails missions objectives. In *4th International Symposium on Solar Sailing (ISSS)*, pages 17–20, 2017.

[41] P. Rao, Q. Peyron, S. Lilge, and J. Burgner-Kahrs. How to model tendon-driven continuum robots and benchmark modelling performance. *Frontiers in Robotics and AI*, 7:630245, 2021.

[42] Bong Wie. Solar sail attitude control and dynamics, part 1. *Journal of Guidance, Control, and Dynamics*, 27(4):526–535, 2004.

[43] Space Technology Research Grants Program, Early Career Faculty Appendix B1, February 2022.

[44] O. A. Bauchau. *Flexible Multibody Dynamics*. Springer, Dordrecht, Netherlands, 2011.

[45] R. J. Caverly and J. R. Forbes. Dynamic modeling, trajectory optimization, and control of a flexible kiteplane. *IEEE Transactions on Control Systems Technology*, 25(4):1297–1306, 2016.

[46] L. Rios-Reyes. *Solar Sails: Modeling, Estimation, and Trajectory Conrol*. PhD thesis, University of Michigan, Ann Arbor, MI, 2006.

[47] R. J. Caverly and J. R. Forbes. Flexible cable-driven parallel manipulator control: Maintaining positive cable tensions. *IEEE Transactions on Control Systems Technology*, 26(5):1874–1883, 2018.

[48] H. A. Godbole, R. J. Caverly, and J. R. Forbes. Dynamic modeling and adaptive control of flexible cable-driven parallel robots. *Journal of Dynamic Systems, Measurement, and Control*, 141 (10):101002–18, 2019.

[49] V. L. Nguyen and R. J. Caverly. Cable-driven parallel robot pose estimation using extended Kalman filtering with inertial payload measurements. *IEEE Robotics and Automation Letters*, 6(2):3615–3622, 2021.

[50] S. Patel, V. L. Nguyen, and R. J. Caverly. Forward kinematics of a cable-driven parallel robot with pose estimation error covariance bounds. *Mechanism and Machine Theory*, 183:105231, 2023.

[51] N. Puri and R. J. Caverly. Coupled least-squares forward kinematics and extended Kalman filtering for the pose estimation of a cable-driven parallel robot. *International Journal of Mechanisms and Robotic Systems*, 5(3):270–289, 2023.

[52] E. M. Lally, M. Reaves, E. Horrell, S. Klute, and M. E. Froggatt. Fiber optic shape sensing for monitoring of flexible structures. In *Sensors and Smart Structures Technologies for Civil, Mechanical, and Aerospace Systems*, volume 8345, pages 831–839, 2012.

A New Model for the Planetary Radiation Pressure Acceleration for Optical Solar Sails

Livio Carzana[a,*], Pieter Visser[a], Jeannette Heiligers[a]

[a]*Faculty of Aerospace Engineering, Delft University of Technology, 2329 HS, Delft, The Netherlands*

Abstract

Solar sailing is a propellantless propulsion method that exploits solar radiation pressure to generate thrust. In recent years, several solar sails have been launched into Earth-bound orbit to demonstrate this technology's potential. Because planetary radiation pressure can reach magnitudes comparable to that of solar radiation pressure in proximity of the Earth, it cannot automatically be neglected in near-Earth solar-sail mission design studies. Nevertheless, its effect on the solar-sail dynamics has been investigated only to a very limited, first-order extent, and every study considered an "ideal" – i.e., perfectly reflecting – sail model. Although employing the ideal sail model proves useful for preliminary orbital analyses, its limited fidelity prevents more in-depth research into the near-Earth solar-sail dynamics and trajectory optimization. In light of this, this paper provides a new planetary radiation pressure acceleration model for optical solar sails. This model forms an extension of the "spherical" planetary radiation pressure acceleration model for ideal solar sails devised by Carzana et al. in Reference [1]. In the current paper, the underlying assumptions and full derivation of the newly devised optical model are presented. Subsequently, the accuracy of the optical model is analyzed through a comparison with the ideal model, using NASA's upcoming ACS3 mission as reference scenario.

Keywords: solar sail, dynamical model, Earth-bound, planetary radiation pressure, optical sail model, ACS3 mission

1. Introduction

Solar sailing is a propulsion method that uses solar radiation as main source of thrust [2]. Due to its propellantless nature and mission-enabling potential for a wide variety of applications [3, 4], solar sailing has drawn increasingly more attention in the scientific community over the last decades. As a result, a number of technology demonstration missions have been launched, both in the interplanetary and near-Earth environments. Among the most recent missions are, for example, NASA's NEA Scout and Gama's Gama Alpha missions. Even more missions are scheduled for the near future, such as NASA's Advanced Composite Solar Sail System (ACS3) and Gama's Beta missions [5]. Most of these sailcraft have flown (or are planned to fly) in low-Earth orbit [6], where several perturbations can affect the solar-sail dynamics, including gravitational perturbations, eclipses, atmospheric drag, and planetary radiation pressure (PRP). While a number of studies have been conducted on the dynamics and trajectory optimization of drag-perturbed solar sails [7, 8, 9], the effects of PRP on the sailcraft dynamics and control have been investigated only to a very limited, first-order extent. Studying the effects of PRP on the solar-sail dynamics is relevant because, for some orbital scenarios, PRP can achieve a non-trivial intensity, with magnitudes of up to 20% of the solar radiation pressure (SRP) [1]. However, determining the PRP acceleration accurately presents several difficulties, mainly related to the models used to represent the Earth's radiation and the optical properties of the solar sail. For this reason, early studies on this topic considered simplistic models. These studies characterized the PRP acceleration in proximity of the Earth [10] and investigated the optimization of PRP-perturbed sailcraft trajectories [11]. In these studies the sail is assumed to be ideal – that is, it is perfectly reflecting – while the Earth is approximated as a uniform bright disk, as per the finite-disk radiation model devised by McInnes [2]. As an extension of McInnes' finite-disk model, the so-called "spherical" radiation model has been developed in the work by Carzana [1], where a thorough investigation of the achievable blackbody and albedo radiation pressure accelerations experienced by sailcraft in close proximity of the Earth has been conducted. The analytical model derived in Ref. [1] considers the Earth as a spherical, uniform radiation source,

* Corresponding author, L.Carzana@tudelft.nl

whose brightness depends on the sailcraft altitude, latitude, and Sun-Earth-sailcraft angle. Although the spherical radiation model derived in Ref. [1] allows for more accurate results than the finite-disk model, it still assumes the sail to behave as an ideal, perfect reflector. Generally, the use of the ideal sail model leads to useful results for first-order analyses. For more in-depth analyses, the so-called optical sail model is often preferred [2]. This model accounts for the absorptivity, reflectivity, and emissivity properties of the sail and has been used extensively to model the SRP acceleration in several works, see the overview in Ref. [12]. A similar optical model for the PRP acceleration has not been found in available literature and, similar to the optical model for the SRP acceleration, would aid in increasing the fidelity of the solar-sail dynamics. In light of this, this paper aims to bridge this gap of knowledge by providing a new PRP acceleration model valid for optical solar sails and assuming a spherical Earth radiative model. As such, this model forms an extension of the spherical PRP acceleration model for ideal solar sails devised by Carzana in Ref. [1].

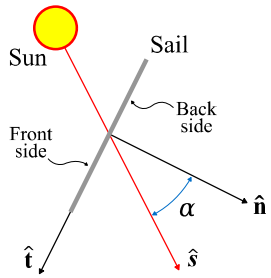

Fig. 1. Solar-sail pitch angle, α, normal direction, $\hat{\boldsymbol{n}}$, and SRP transversal direction, $\hat{\boldsymbol{t}}$.

2. Dynamical Model

The equations of motion of a solar sail in Earth-bound orbit are expressed in an inertial Earth-centered reference frame, $\mathcal{S}(x, y, z)$. In this frame, the x-axis points towards the vernal equinox, the z-axis is perpendicular to the equatorial plane and points towards the north pole, and the y-axis completes the right-handed frame. Within this frame, the equations of motion of a flat-shaped solar sail under the influence of Earth's central gravity, SRP and PRP can be expressed in vectorial form as:

$$\ddot{\boldsymbol{r}} + \frac{\mu}{r^3}\boldsymbol{r} = \boldsymbol{a}_{SRP} + \boldsymbol{a}_{PRP} \tag{1}$$

where $\mu = 398600.4415$ km^{3}s^{-2} is the Earth's gravitational parameter [13], $\boldsymbol{r} = [x, y, z]^{\mathrm{T}}$ is the sailcraft position vector, $r = \|\boldsymbol{r}\|$, $\boldsymbol{a}_{SRP}$ is the SRP acceleration, and $\boldsymbol{a}_{PRP}$ is the PRP acceleration. These accelerations will be described in more detail in the following sections.

2.1. Solar Radiation Pressure Acceleration

The SRP acceleration is defined using the optical sail model, which accounts for the absorption, reflection, and emission properties of the solar sail. When this model is employed, the SRP acceleration is given by [2]:

$$\boldsymbol{a}_{SRP} = \boldsymbol{a}_{SRP,n} + \boldsymbol{a}_{SRP,t} \tag{2}$$

where $\boldsymbol{a}_{SRP,n}$ and $\boldsymbol{a}_{SRP,t}$ are the normal and transversal components of the SRP acceleration, respectively. The former is directed along the sail normal direction with no component pointing towards the Sun, $\hat{\boldsymbol{n}}$, while the latter points in the SRP transversal direction, $\hat{\boldsymbol{t}}$, tangential to the sail plane, see Fig. 1. The SRP transversal direction can be defined from $\hat{\boldsymbol{n}}$ and the direction of sunlight, $\hat{\boldsymbol{s}}$, as follows:

$$\hat{\boldsymbol{t}} = \hat{\boldsymbol{n}} \times \frac{\left(\hat{\boldsymbol{s}} \times \hat{\boldsymbol{n}}\right)}{\left\|\hat{\boldsymbol{s}} \times \hat{\boldsymbol{n}}\right\|} \tag{3}$$

The acceleration components $\boldsymbol{a}_{SRP,n}$ and $\boldsymbol{a}_{SRP,t}$ are defined as [2]:

$$\begin{aligned}\boldsymbol{a}_{SRP,n} = \nu \frac{a_c}{2}\Big\{&\left(1+\tilde{r}_f s_f\right)\cos^2(\alpha) \\ &+\left(1-s_f\right)\tilde{r}_f B_f \cos(\alpha) \\ &+\left(1-\tilde{r}_f\right)\frac{\varepsilon_f B_f - \varepsilon_b B_b}{\varepsilon_f + \varepsilon_b}\cos(\alpha)\Big\}\,\hat{\boldsymbol{n}}\end{aligned} \tag{4}$$

$$\boldsymbol{a}_{SRP,t} = \nu \frac{a_c}{2}\left(1-\tilde{r}_f s_f\right)\cos(\alpha)\sin(\alpha)\,\hat{\boldsymbol{t}} \tag{5}$$

where $\alpha \in [0, \pi/2]$ represents the solar-sail pitch angle measured between $\hat{\boldsymbol{s}}$ and $\hat{\boldsymbol{n}}$, see again Fig. 1, and $\nu \in [0,1]$ is the shadow factor, which accounts for the effect of eclipses and ranges from 0 (no sunlight reaches the sail) to 1 (sail completely illuminated). In this paper, eclipses are modeled with a conical shadow model similar to the one presented in Ref. [14, 15], with the only difference that $\nu = 0$ both when in umbra and penumbra. The solar-sail characteristic acceleration, a_c, represents the maximum SRP acceleration (achieved for $\alpha = 0$) at a distance of 1 AU from the Sun and is defined as [2]:

$$a_c = \frac{2\mathbb{S}_\oplus}{c\sigma} \tag{6}$$

where $\mathbb{S}_\oplus = 1367$ W/m^2 is the solar flux at Earth [13], $c = 299792.458$ km/s is the speed of light in vacuum [16], and σ is the sailcraft mass-to-sail area ratio. Finally, the optical properties of the sail are specified

through the parameters $\tilde{r}$, s, B, and ε, which represent the reflectivity, specular reflection coefficient, non-Lambertian reflection coefficient, and emissivity of the sail, respectively, with the subscript *"f"* indicating that the optical coefficient refers to the sail front side and the subscript *"b"* is used to refer to the sail back side. It should be noted that Eqs. (4) and (5) are based on the assumption that only the sail front side is exposed to sunlight and, conversely, the sail back side is never illuminated. Because of this, the normal and transversal components of the SRP acceleration do not depend on the reflectivity and specular reflection coefficient of the sail back side, $\tilde{r}_b$ and s_b. As explained in the next section, this assumption does not hold for the PRP acceleration, as planetary radiation can illuminate both sides of the sail, thus requiring the knowledge of $\tilde{r}_b$ and s_b.

2.2. *Planetary Radiation Pressure Acceleration*

To determine the PRP acceleration exerted on a solar sail, knowledge of the amount of planetary radiation received by the sail, its corresponding flux and radiation pressure is required. The mathematical derivation to determine these quantities is provided in Ref. [1] and is reported here for the sake of completeness.

If an elementary piece of Earth's surface dA is considered, see Fig. 2a, the amount of power irradiated in a generic direction $\hat{\boldsymbol{l}}$ and enclosed within an infinitesimal solid angle $d\Omega$ is represented by the second differential d^2P as [17]:

$$d^2P = I\cos(\vartheta)d\Omega dA \tag{7}$$

where I represents the planetary radiation intensity (across the entire electromagnetic spectrum) along the normal direction to dA, $\hat{\boldsymbol{N}}$, and $\vartheta \in [0, \pi/2]$ is the angle between $\hat{\boldsymbol{N}}$ and $\hat{\boldsymbol{l}}$, see again Fig. 2a. Assuming the Earth's surface to be a Lambertian scatterer, the radiation intensity can be expressed as [18]:

$$I = \frac{S}{\pi} \tag{8}$$

where S is the planetary radiation power flux (i.e., the emitted radiation power per unit area) at the surface element, dA. When only the radiation received by the solar sail is considered, $d\Omega$ represents the solid angle subtended by an infinitesimal piece of illuminated sail surface, dA_{sail}. In this case, $d\Omega$ is defined as [19]:

$$d\Omega = \frac{dA_{sail}\cos(\theta)}{l^2} \tag{9}$$

where $\theta \in [0, \pi/2]$ is the angle between $\hat{\boldsymbol{l}}$ and the sail normal direction pointing away from dA, $\hat{\boldsymbol{n}}_{ill}$, and l is the magnitude of the vector $\boldsymbol{l}$ pointing from dA to dA_{sail}, see Figs. 2a and 2b. Making use of Eqs. (8) and (9), Eq. (7) can be rewritten as:

$$d^2P = \frac{S}{\pi}\frac{\cos(\vartheta)\cos(\theta)}{l^2}dA_{sail}\,dA \tag{10}$$

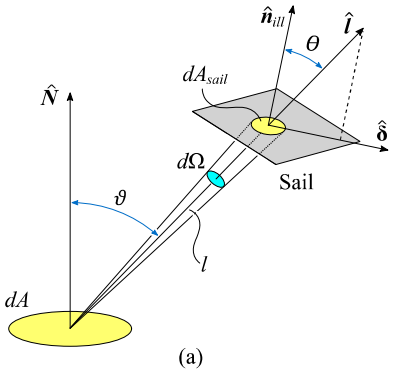

(a)

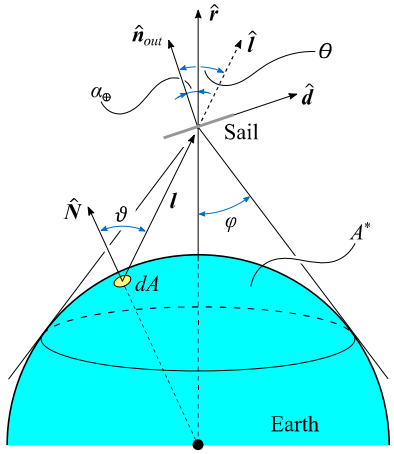

(b)

Fig. 2. Geometry of the problem to determine the PRP acceleration exerted on a solar sail.

Since this paper considers a flat-shaped solar sail whose dimensions are significantly smaller than l, θ and l can be assumed to be constant across the entire sail surface. This assumption allows to easily integrate Eq. (10) with respect to dA_{sail} over the entire sail surface, A_{sail}. Performing the integration yields the radiation power dP received by the entire sail due to the radiation emitted by dA:

$$dP = \frac{S}{\pi}\frac{\cos(\vartheta)\cos(\theta)}{s^2}A_{sail}\,dA \tag{11}$$

The power flux at the sail's location due to the radiation emitted by dA, dS_{sail}, is then found as:

$$dS_{sail} = \frac{dP}{A_{sail}\cos(\theta)} = \frac{S}{\pi}\frac{\cos(\vartheta)}{l^2}dA \tag{12}$$

so that the corresponding radiation pressure $d\mathbb{P}$ is given by [2]:

$$d\mathbb{P} = \frac{dS_{sail}}{c} = \frac{S}{\pi c}\frac{\cos(\vartheta)}{l^2}dA \tag{13}$$

Equation (13) allows to determine the acceleration exerted on the sail due to the radiation emitted by the surface element dA, $d\boldsymbol{a}_{PRP}$. Indeed, by taking into account the optical properties of the sail, $d\boldsymbol{a}_{PRP}$ can be defined in a similar fashion to the SRP acceleration as:

$$d\boldsymbol{a}_{PRP} = d\boldsymbol{a}_{PRP,n} + d\boldsymbol{a}_{PRP,\delta} \tag{14}$$

where the normal and transversal components of the infinitesimal PRP acceleration, $d\boldsymbol{a}_{PRP,n}$ and $d\boldsymbol{a}_{PRP,\delta}$, respectively, are given by:

$$\begin{aligned} d\boldsymbol{a}_{PRP,n} &= \frac{d\mathbb{P}}{\sigma}\Big\{\left(1+\tilde{r}_{ill}s_{ill}\right)\cos^2(\theta)\hat{\boldsymbol{n}}_{ill} \\ &\quad + \left(1-s_{ill}\right)\tilde{r}_{ill}B_{ill}\cos(\theta)\hat{\boldsymbol{n}}_{ill} \\ &\quad + \left(1-\tilde{r}_{ill}\right)\frac{\varepsilon_f B_f - \varepsilon_b B_b}{\varepsilon_f+\varepsilon_b}\cos(\theta)\hat{\boldsymbol{n}}\Big\} \\ &= \frac{S}{\pi c\sigma}\Big\{\left(1+\tilde{r}_{ill}s_{ill}\right)\frac{\cos(\vartheta)\cos^2(\theta)}{l^2}\hat{\boldsymbol{n}}_{ill} \\ &\quad + \left(1-s_{ill}\right)\tilde{r}_{ill}B_{ill}\frac{\cos(\vartheta)\cos(\theta)}{l^2}\hat{\boldsymbol{n}}_{ill} \\ &\quad + \left(1-\tilde{r}_{ill}\right)\frac{\varepsilon_f B_f - \varepsilon_b B_b}{\varepsilon_f+\varepsilon_b}\frac{\cos(\vartheta)\cos(\theta)}{l^2}\hat{\boldsymbol{n}}\Big\}dA \end{aligned} \tag{15}$$

$$\begin{aligned} d\boldsymbol{a}_{PRP,\delta} &= \frac{d\mathbb{P}}{\sigma}\left(1-\tilde{r}_{ill}s_{ill}\right)\cos(\theta)\sin(\theta)\,\hat{\boldsymbol{\delta}} \\ &= \frac{S}{\pi c\sigma}\left(1-\tilde{r}_{ill}s_{ill}\right)\frac{\cos(\vartheta)\cos(\theta)\sin(\theta)}{l^2}\,\hat{\boldsymbol{\delta}}\,dA \end{aligned} \tag{16}$$

In the above equations, the subscript *"ill"* is used to refer to the optical coefficients of the sail side illuminated by the radiation emitted by the surface element dA, while $\hat{\boldsymbol{\delta}}$ represents the PRP transversal direction relative to dA, which can be found from Eq. (3) by substituting $\hat{\boldsymbol{\delta}}$ for $\hat{\boldsymbol{t}}$ and $\hat{\boldsymbol{l}}$ for $\hat{\boldsymbol{s}}$, see Fig. 2a.

Although the decomposition of $d\boldsymbol{a}_{PRP}$ into its normal and transversal components is similar to that performed in Eq. (2) for the SRP acceleration, it should be noted that a major difference exists, which is due to the different definitions of the SRP transversal direction, $\hat{\boldsymbol{t}}$, and PRP transversal direction relative to dA, $\hat{\boldsymbol{\delta}}$. Indeed, while $\hat{\boldsymbol{t}}$ is uniquely defined for a given sail attitude, $\hat{\boldsymbol{\delta}}$ is not, as its direction depends on the specific surface element dA considered and it can point anywhere within the sail plane. When this dependency of $\hat{\boldsymbol{\delta}}$ on dA is taken into account, Eq. (14) can be integrated over the entire visible surface of the Earth as seen from the sailcraft, A^*, hence yielding the total PRP acceleration exerted on the solar sail, i.e.:

$$\boldsymbol{a}_{PRP} = \int_{A^*} d\boldsymbol{a}_{PRP} = \int_{A^*}\left(d\boldsymbol{a}_{PRP,n} + d\boldsymbol{a}_{PRP,\delta}\right) \tag{17}$$

The solution to the PRP acceleration integral in Eq. (17) depends on the Earth-sail geometrical configuration and, most importantly, on how the planetary flux, S, varies across the visible surface A^*. Because the planetary flux varies geographically following a complex pattern, no general closed-form analytical solution to the acceleration integral exists. To circumvent this problem, in the literature the PRP acceleration integral is usually solved numerically by discretizing the visible surface A^* and making use of maps providing the geographical distribution of the Earth's blackbody radiation flux and albedo coefficient. Such numerical methods enable a high accuracy which, however, comes at the cost of a large computational effort. Therefore, in this paper an analytical approach is pursued instead, which assumes a constant planetary flux S over the entire visible surface A^*. To compute this value of S, the previously mentioned maps are used to approximate the Earth's blackbody radiation flux and albedo coefficient as sinusoidal functions of latitude. Then, by performing a surface average, a constant, analytical value of S is found. For more information on the definition of the surface-averaged planetary radiation flux, the reader is referred to Ref. [1].

Considering a constant planetary flux allows to analytically solve the PRP acceleration integral in Eq. (17), yielding to:

$$\begin{aligned} \boldsymbol{a}_{PRP} = \frac{S}{c\sigma}\Big\{&\frac{2}{3}\Big[\left(1+\tilde{r}_{in}s_{in}\right)G_{FNS,in} - \left(1+\tilde{r}_{out}s_{out}\right)G_{FNS,out}\Big]\hat{\boldsymbol{n}}_{out} \\ &+ \Big[\left(1-s_{in}\right)\tilde{r}_{in}B_{in}G_{FND,in} - \left(1-s_{out}\right)\tilde{r}_{out}B_{out}G_{FND,out}\Big]\hat{\boldsymbol{n}}_{out} \\ &+ \frac{\varepsilon_f B_f - \varepsilon_b B_b}{\varepsilon_f+\varepsilon_b}\Big[\left(1-\tilde{r}_{in}\right)G_{FND,in} + \left(1-\tilde{r}_{out}\right)G_{FND,out}\Big]\hat{\boldsymbol{n}} \\ &+ \frac{2}{3\pi}\Big[\left(1-\tilde{r}_{in}s_{in}\right)G_{FT,in} + \left(1-\tilde{r}_{out}s_{out}\right)G_{FT,out}\Big]\hat{\boldsymbol{d}}\Big\} \end{aligned} \tag{18}$$

where $\hat{\boldsymbol{d}}$ is the PRP transversal direction relative to the Earth displayed in Fig. 2b, found from Eq. (3) by substituting $\hat{\boldsymbol{d}}$ for $\hat{\boldsymbol{t}}$ and the radial direction, $\hat{\boldsymbol{r}}$, for $\hat{\boldsymbol{s}}$. G_{FNS}, G_{FND}, and G_{FT} represent the normal specular, normal diffuse, and transversal geometrical factors, respectively, while the subscripts *"in"* and *"out"* indicate if the optical coefficients and geometrical factors refer to the inward or outward side of the sail with respect to the Earth. This differentiation is required because for

particular sail orientations planetary radiation can illuminate both the inward and outward sides of the sail, therefore contributing to $\boldsymbol{a}_{PRP}$. The geometrical factors are all defined in the range [0,1] and they correlate the Earth-sail geometrical configuration to the different components of the PRP acceleration. By indicating the regions of the surface A^* that are visible from the inward and outward sides of the sail by A^*_{in} and A^*_{out}, the geometrical factors can be defined as follows:

$$G_{FNS,\diamond} = \frac{3}{2\pi}\int_{A_\diamond}\frac{\cos(\vartheta)\cos^2(\theta)}{l^2}dA \tag{19}$$

$$G_{FND,\diamond} = \frac{1}{\pi}\int_{A_\diamond}\frac{\cos(\vartheta)\cos(\theta)}{l^2}dA \tag{20}$$

$$G_{FT,\diamond} = \frac{3}{2}\int_{A_\diamond}\frac{\cos(\vartheta)\cos(\theta)\sin(\theta)}{l^2}dA \tag{21}$$

where the symbol *"◇"* has been used as placeholder to indicate either the subscript *"in"* or *"out"*.

The solutions to the surface integrals on the right-hand side of Eq. (19)-(21) depend on the geometrical configuration of the sail with respect to the Earth, which is uniquely defined by the orbital radius, r, planetary cone angle (PCA), $\alpha_\oplus \in [0, \pi/2]$, and maximum view angle, $\varphi \in [0, \pi/2]$, see Fig. 2b. The PCA is defined as the angle between $\hat{\boldsymbol{n}}_{out}$ and $\hat{\boldsymbol{r}}$ while φ represents the angle between the direction pointing to the Earth's tangent as seen from the sailcraft and $-\hat{\boldsymbol{r}}$. The full analytical solution to the geometrical factor integrals is presented in the following subsections.

2.2.1. Normal Specular Geometrical Factor

Depending on the sail orientation with respect to the Earth, two possible configurations can be identified:

a) If $\alpha_\oplus + \varphi \leq \pi/2$, the incoming radiation from the visible surface A^* illuminates only the inward side of the sail. In this case, the outward geometrical factor is $G_{FNS,out} = 0$, while the inward geometrical factor, $G_{FNS,in}$, is given by Eq. (22), where $H = R/r$ is the adimensional inverse orbital radius, R = 6378.1363 km is the Earth radius [13], and:

$$A = \frac{\cos(\alpha_\oplus)}{\sin(\alpha_\oplus)}\sqrt{\frac{1}{H^2}-1} \quad ; \quad B = \sqrt{\frac{H^2}{\cos^2(\alpha_\oplus)}-1}$$

b) If $\alpha_\oplus + \varphi > \pi/2$, both sail sides are illuminated and the inward and outward geometrical factors are given by Eqs. (23) and (24).

2.2.2. Normal Diffuse Geometrical Factor

The normal diffuse geometrical factors correspond to the view factors of the sail sides with respect to the Earth. Their expressions were found by F.G. Cunningham in Ref. [19] and are reported hereinafter for completeness:

a) If $\alpha_\oplus + \varphi \leq \pi/2$, $G_{FND,in}$ is given by Eq. (25) and $G_{FND,out} = 0$.

b) If $\alpha_\oplus + \varphi > \pi/2$, $G_{FND,in}$ and $G_{FND,out}$ are given by Eqs. (26) and (27), respectively.

$$G_{FNS,in}(H,\alpha_\oplus) = 1-\sqrt{1-H^2}\left[1-H^2\left(1-\frac{3}{2}\sin^2(\alpha_\oplus)\right)\right] \tag{22}$$

$$G_{FNS,in}(H,\alpha_\oplus) = 1-\frac{1}{\pi}\left\{\frac{1}{2}\sqrt{1-H^2}\left[H^2\left(1-3\cos^2(\alpha_\oplus)\right)+2\right]\cos^{-1}(-A)+\tan^{-1}(B)-\frac{3}{2}B^3\cos^4(\alpha_\oplus)-\frac{1}{2}B\cos^2(\alpha_\oplus)\left(3\cos^2(\alpha_\oplus)-1\right)\right\} \tag{23}$$

$$G_{FNS,out}(H,\alpha_\oplus) = \frac{1}{\pi}\left\{-\frac{1}{2}\sqrt{1-H^2}\left[H^2\left(1-3\cos^2(\alpha_\oplus)\right)+2\right]\cos^{-1}(A)+\tan^{-1}(B)-\frac{3}{2}B^3\cos^4(\alpha_\oplus)-\frac{1}{2}B\cos^2(\alpha_\oplus)\left(3\cos^2(\alpha_\oplus)-1\right)\right\} \tag{24}$$

$$G_{FND,in}(H,\alpha_\oplus) = H^2\cos(\alpha_\oplus) \tag{25}$$

$$G_{FND,in}(H,\alpha_\oplus) = \frac{1}{2}-\frac{1}{\pi}\left\{\sin^{-1}\left(\frac{H}{\sin(\alpha_\oplus)}\sqrt{\frac{1}{H^2}-1}\right)+B\cos(\alpha_\oplus)\sqrt{1-H^2}-H^2\cos(\alpha_\oplus)\cos^{-1}(-A)\right\} \tag{26}$$

$$G_{FND,out}(H,\alpha_\oplus) = \frac{1}{2}-\frac{1}{\pi}\left\{\sin^{-1}\left(\frac{H}{\sin(\alpha_\oplus)}\sqrt{\frac{1}{H^2}-1}\right)+B\cos(\alpha_\oplus)\sqrt{1-H^2}+H^2\cos(\alpha_\oplus)\cos^{-1}(A)\right\} \tag{27}$$

$$G_{FT,in}(H,\alpha_\oplus) = \frac{3\pi}{4}H^2\sqrt{1-H^2}\sin(2\alpha_\oplus) \tag{28}$$

$$G_{FT,in}(H,\alpha_\oplus) = \frac{1}{2}\left\{B\left[2\sin(\alpha_\oplus)\cos^3(\alpha_\oplus)\left(B^2+2+\frac{\cos^2(\alpha_\oplus)}{\sin^2(\alpha_\oplus)}\right)-\left(1+H^2\right)\frac{\cos^3(\alpha_\oplus)}{\sin(\alpha_\oplus)}\right]+3H^2\sqrt{1-H^2}\sin(\alpha_\oplus)\cos(\alpha_\oplus)\cos^{-1}(-A)\right\} \tag{29}$$

$$G_{FT,out}(H,\alpha_\oplus) = \frac{1}{2}\left\{B\sin(\alpha_\oplus)\cos^3(\alpha_\oplus)\left[B^2\left(2-\frac{\cos^2(\alpha_\oplus)}{\sin^2(\alpha_\oplus)}\right)+3\right]-3H^2\sqrt{1-H^2}\sin(\alpha_\oplus)\cos(\alpha_\oplus)\cos^{-1}(A)\right\} \tag{30}$$

2.2.3. Transversal Geometrical Factor

Similar to the other geometrical factors, the definition of the transversal geometrical factor depends on whether both sides of the sail receive planetary radiation:

a) If $\alpha_{\oplus} + \varphi \leq \pi/2$, $G_{FT,in}$ is given by Eq. (28) and $G_{FT,out} = 0$.

b) If $\alpha_{\oplus} + \varphi > \pi/2$, $G_{FT,in}$ and $G_{FT,out}$ are given by Eqs. (29) and (30), respectively.

3. Accuracy Analysis

In this section, a parametric analysis is presented which aims to validate the optical PRP acceleration model presented in the previous section and quantify its accuracy compared to a high-fidelity numerical model. To achieve this, a wide variety of PRP perturbed, Earth-bound orbits have been propagated considering different models for the PRP acceleration, $\boldsymbol{a}_{PRP}$. These different models are:

a) NRTDM model. This numerical model computes the PRP acceleration by approximating the acceleration integral of Eq. (17) with a finite sum. This algorithm is implemented in NRTDM (Near Real-Time Density Model), a software tool developed at the Delft University of Technology under ESA contract [20, 21]. In order to model the planetary flux distribution across the Earth, this model makes use of two monthly averaged maps (one for the blackbody radiation flux and one for the albedo coefficient) obtained from the ANGARA software package developed by Hyperschall Technologie Göttingen GmbH [22]. Due to its numerical nature, this model allows to determine the PRP acceleration with a very high accuracy, although requiring a large computational effort. For more information on NRTDM, the reader is referred to [20].

b) Spherical PRP acceleration model for an optical solar sail, see Section 2.2. The sail optical coefficients employed have been taken from NASA's upcoming ACS3 solar-sail mission. The ACS3 sail membrane consists of a polymer film (polyethelene nepthalate) coated with an aluminum layer on the front side and a chromium layer on the back side [23]. The aluminum layer's optical coefficients are $\{\tilde{r}_f, s_f, B_f, \varepsilon_f\} = \{0.90,\ 0.74,\ 0.03,\ 0.79\}$, while the chromium layer's optical coefficients are $\{\tilde{r}_b, s_b, B_b, \varepsilon_b\} = \{0.43, 0.23, 0.60, 0.67\}$[2].

c) Spherical PRP acceleration model for an ideal solar sail. This model corresponds to the spherical PRP acceleration model devised by Carzana in Ref. [1] for ideal sails. It represents a special case of the optical PRP acceleration model presented in Section 2.2, found by considering the following "ideal" optical coefficients: $\{\tilde{r}_f, s_f, B_f, \varepsilon_f\} = \{1, 1, 2/3, 0\}$.

d) Model in which the PRP acceleration is neglected, i.e., $\boldsymbol{a}_{PRP} = \boldsymbol{0}$ at any time.

All analyses make use of the ACS3 mission orbit as baseline scenario, with a solar-sail characteristic acceleration of $a_c = 0.045$ mm/s^2 and the following vector of initial orbital elements defined in frame $\mathcal{G}$(x, y, z):

$$\left[a_0, e_0, i_0, \mathrm{LTAN}_0, \omega_0, f_0\right]^T = \left[7093.1363\ \mathrm{km},\ 0,\ 98.2490\ \mathrm{deg},\ \begin{Bmatrix} 00:00\,\mathrm{AM} \\ 00:30\,\mathrm{AM} \\ \vdots \\ 11:30\,\mathrm{AM} \end{Bmatrix},\ 0\ \mathrm{deg},\ 0\ \mathrm{deg}\right]^T \quad (31)$$

where a is the semi-major axis, e the eccentricity, i the inclination, ω the argument of perigee, f the true anomaly, LTAN stands for Local Time of the Ascending Node, and the subscript "0" denotes the initial value of these variables[3]. These orbital elements represent a circular, Sun-synchronous orbit with initial altitude $h_0 = a_0 - R = 715$ km. In Eq. (31), several values of the LTAN are considered, spaced by 0.5 hours along the entire 24-hour time span. This parameter defines the orbit orientation in frame $\mathcal{G}$(x, y, z) and is equivalent to the right-ascension of the ascending node, which, in a similar fashion, is spaced by 7.5 deg across the entire 360-degree angular span. The parametric analysis also considers 12 different simulation start times, corresponding to the 15th day of each month of 2023. For each initial orbit, the solar-sail dynamics given in Eq. (1) are propagated while implementing locally optimal orbit-raising and inclination-changing steering laws. These steering laws are computed based on an algorithm similar to the one devised by McInnes for ideal sails [2], though adapted to the optical sail model presented in Section 2.1. It should be noted that because these steering laws account only for SRP in the optimization process, in the analyses, the PRP acceleration is considered as an uncontrolled perturbing acceleration affecting the orbit. For each initial orbit, each simulation start time and each steering law, four different propagations have been performed in which the PRP acceleration is computed through the four models listed above. Then, the relative errors between the final altitude/inclination obtained by

[2] ACS3 solar-sail optical coefficients taken from personal communication with Andrew F. Heaton, NASA Marshall Space Flight Center, May 2023.

[3] ACS3 mission data taken from personal communication with W.K. Wilkie, Principal Investigator of the ACS3 mission, NASA Langley Research Center, May 2023.

the NRTDM model (taken as the ground truth) and each of the analytical models, ε_{rel}, are computed. The parameter ε_{rel} is used as metric of the accuracy of the analytical models and its definition is given by:

$$\varepsilon_{rel} = \frac{\left| \text{œ}_{NRTDM,f} - \text{œ}_{An,f} \right|}{\text{œ}_{NRTDM,f} - \text{œ}_{0}} \tag{32}$$

where œ_0 indicates the initial value of the steering law's target parameter (i.e., h or i) and $\text{œ}_{NRTDM,f}$ and $\text{œ}_{An,f}$ represent the final values of the target parameter found through the NRTDM and the analytical model under consideration, respectively. For each simulation, the dynamics have been propagated for 10 days, using Matlab®'s *ode45* integrator with absolute and relative tolerances of 10^{-12}.

The top plot of Fig. 3 shows the variation of the relative error with the LTAN for the orbit-raising steering law for all analytical models. For each model, a band is displayed which represents the range of relative errors obtained by considering simulation start times at different months. All the error bands follow a 12-hour periodic trend, approximately symmetric with respect to the LTAN at 12AM. This is due to the relative orientations of the Sun-synchronous orbits with respect to the direction of sunlight, which can be similar even for different LTANs and therefore yield similar errors, ε_{rel}. All models display small errors for an LTAN at 6AM/PM (corresponding to a dawn-dusk orbit), as in this case the PRP perturbs the orbit only to a very minor extent. On the other hand, when an LTAN at 12AM/PM is considered (corresponding to a noon-midnight orbit), the PRP acceleration is the largest and therefore the errors achieved, ε_{rel}, are maximal. As can be seen in the plot, neglecting the PRP acceleration in the dynamics yields large relative errors, even in the order of 12%. When employing the spherical ideal PRP model, these errors are strongly reduced, reaching values of 5% at most. Due to their higher fidelity with respect to the ideal PRP model, the optical PRP acceleration model achieves even smaller errors, in the range 0.2-1.1%. In addition to its increased accuracy, it is worth noting that the width of the optical PRP acceleration model's error band is smaller than the ideal model's error band, thus implying also a smaller error variation with the simulation start date.

The bottom plot of Fig. 3 displays the variation of ε_{rel} for the inclination-changing steering law, for different LTAN values and PRP acceleration models. In this case, a 12-hour periodicity in the errors is again obtained, although the error bands appear skewed and asymmetric, unlike the ones observed for the orbit-raising case (top plot of Fig. 3). This asymmetry is due to the complex, discontinuous nature of the inclination-

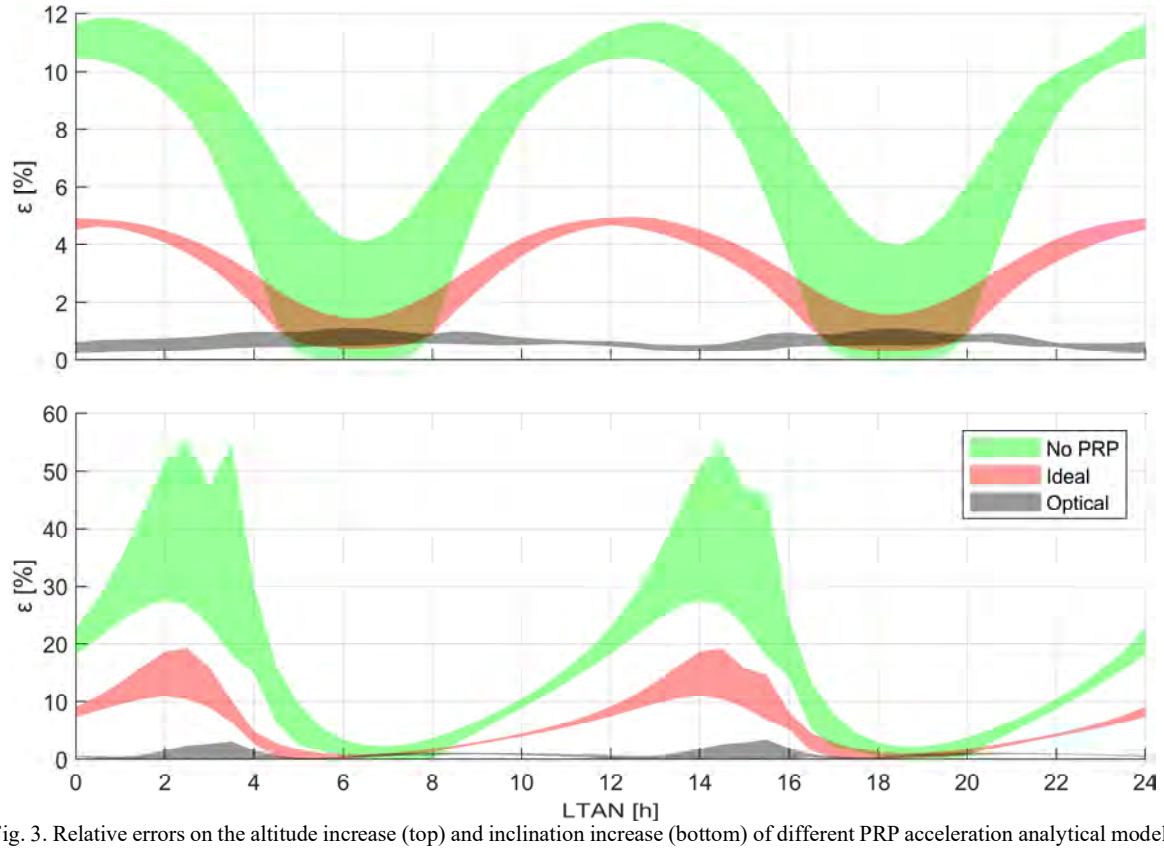

Fig. 3. Relative errors on the altitude increase (top) and inclination increase (bottom) of different PRP acceleration analytical models with respect to the NRTDM model.

changing steering law, for which orbits with similar orientations with respect to the sunlight direction still yield different increases in inclination. Similar to the orbit-raising case, all models achieve small errors for an LTAN around 6AM/PM, due to the small PRP acceleration achieved in this orbital scenario. Conversely, the largest errors are achieved for an LTAN approximately at 3AM/PM, as the PRP perturbation is maximal. The bottom plot of Fig. 3 shows that if the PRP acceleration is not accounted for in the dynamics, very large errors are produced, reaching magnitudes even in the order of 55%. When the PRP ideal acceleration model is employed, smaller errors are achieved, albeit still considerable: ε_{rel} reaches values up to 19.2%. On the other hand, significantly more limited errors are achieved when the PRP optical model is employed, as ε_{rel} reaches values of at most 3.4%. When comparing the error bands of the PRP ideal and optical acceleration models, it can again be noted that the former exhibits a wider spread than the latter, indicating that the optical model achieves a smaller error variation with the simulation start date.

4. Conclusions

This paper presented a new analytical model for planetary radiation pressure (PRP) acceleration, particular for optical solar sails. This model forms an extension of the "spherical" PRP acceleration model devised by Carzana for ideal (i.e., perfectly reflecting) solar sails [1]. A parametric analysis has been performed to quantify the model's accuracy compared to other PRP acceleration models. To this aim, the trajectory of NASA's upcoming ACS3 sailcraft has been propagated for a large set of initial orbital conditions, with the PRP acceleration either neglected or modeled through a high-fidelity numerical model, the newly devised optical model, or the pre-existent ideal model. The results show that employing the optical model yields a substantial increase in accuracy. Indeed, when an orbit-raising steering law is adopted, the maximum relative error in altitude increase of the optical model compared to the high-fidelity numerical model is in the order of 1.1%, whereas the relative error of the ideal model can reach values of 5%. Similarly, when an inclination-changing steering law is adopted, the optical PRP acceleration model attains a relative error of at most 3.4%, while the ideal model reaches a maximum value of 19.2%. Ultimately, the results also show that neglecting the PRP acceleration from the dynamics highly affects the results, as in that case the maximum relative errors on the altitude and inclination increases are 12% and 55%, respectively.

Acknowledgements

The authors thank W. Keats Wilkie from NASA Langley Research Center and Andrew Heaton from NASA Marshall Space Flight Center for sharing the ACS3 mission data. Also, special thanks go to Dr. Christian Siemes and Natalia Hladczuk from Delft University of Technology and Dr. Eelco Doornbos from KNMI for sharing the software tool NRTDM and their knowledge of the ANGARA Earth radiation maps.

References

[1] L. Carzana, P. Visser and J. Heiligers, "A New Model for the Planetary Radiation Pressure Acceleration for Solar Sails," *under review at the Journal of Guidance, Control, and Dynamics,* 2023.

[2] C. R. McInnes, Solar Sailing - Technology, Dynamics and Mission Applications, Springer, 2004.

[3] D. A. Spencer, L. Johnson and A. C. Long, "Solar sailing technology challenges," *Aerospace Science and Technology,* vol. 93, 2019. DOI: 10.1016/j.ast.2019.07.009.

[4] M. Macdonald and C. R. McInnes, "Solar Sail Science Mission Applications and Advancement," *Advances in Space Research,* pp. 1702-1716, 2011. DOI: 10.1016/j.asr.2011.03.018.

[5] W. K. Wilkie, J. M. Fernandez, O. R. Stohlman and et al., "An Overview of the NASA Advanced Composite Solar Sail (ACS3) Technology Demonstration Project," *AIAA Scitech 2021 Forum,* 2021.

[6] M. Macdonald, Advances in Solar Sailing, Springer, 2014, pp. 95-113.

[7] L. Carzana, P. Visser and J. Heiligers, "Locally optimal control laws for Earth-bound solar sailing with atmospheric drag," *Aerospace Science and Technology,* vol. 127, no. 107666, 2022. DOI: 10.1016/j.ast.2022.107666.

[8] G. Mengali and A. A. Quarta, "Near-Optimal Solar-Sail Orbit-Raising from Low Earth Orbit," *Journal of Spacecraft and Rockets,* vol. 42, no. 5, pp. 954-958, 2005. DOI: 10.2514/1.14184.

[9] V. Stolbunov, M. Ceriotti, C. Colombo and C. R. McInnes, "Optimal Law for Inclination Change in an Atmosphere Through Solar Sailing," *Journal of Guidance, Control, and Dynamics,* vol. 36, no. 5, pp. 1310-1323, 2013. DOI: 10.2514/1.59931.

[10] A. De Iuliis, F. Ciampa, L. Felicetti and M. Ceriotti, "Sailing with Solar and Planetary Radiation Pressure," in *Proceedings of ISSS 2019: 5th International Symposium on Solar Sailing*, Aachen, Germany, 2019. DOI: 10.1016/j.asr.2019.11.036.

[11] A. Barles, M. Ceriotti, F. Ciampa and L. Felicetti, "An Optimal Steering Law for Sailing with Solar and Planetary Radiation Pressure," *Aerospace Science and Technology,* vol. 118, 2021. DOI: 10.1016/j.ast.2021.107051.

[12] B. Fu, E. Sperber and F. Eke, "Solar sail technology — A state of the art review," *Progress in Aerospace Sciences,* vol. 86, pp. 1-19, 2016.

[13] J. R. Wertz and W. J. Larson, Space Mission Analysis and Design, El Segundo: Microcosm Press and Dordrecht: Kluwer Academic Publishers, 2005.

[14] C. R. Ortiz Longo and S. L. Rickman, "Method for the Calculation of Spacecraft Umbra and Penumbra Shadow Terminator Points," NASA Center for AeroSpace Information, Linthicum Heights, 1995.

[15] P. Kelly and R. Bevilacqua, "An Optimized Analytical Solution for Geostationary Debris Removal using Solar Sails," *Acta Astronautica,* vol. 162, pp. 72-86, 2019. DOI: 10.1016/j.actaastro.2019.05.055.

[16] E. Tiesinga, P. J. Mohr, D. B. Newell and B. N. Taylor, "CODATA recommended values of the fundamental physical constants: 2018," *Reviews of Modern Physics,* vol. 93, 2021. DOI: 10.1103/RevModPhys.93.025010.

[17] B. W. Carroll and D. A. Ostlie, An Introduction to Modern Astrophysics, Cambridge, UK: Cambridge University Press, 2017. DOI: 10.1017/9781108380980.

[18] J. Lissauer and I. de Pater, Fundamental Planetary Science: Physics, Chemistry and Habitability, Cambridge, UK: Cambridge University Press, 2013.

[19] F. G. Cunningham, "Power Input to a Small Flat Plate from a Diffusely Radiating Sphere, with Application to Earth Satellites," National Aeronautics and Space Administration, Washington DC, 1961.

[20] E. Doornbos et al., "Algorithm Theoretical Basis Document," in *GOCE+ theme 3: Air density and wind retrieval using GOCE data, ESA contract 4000102847/NL/EL*, 2014.

[21] E. Doornbos, Thermospheric density and wind determination from satellite dynamics, Delft, The Netherlands: Springer, Berlin, Heidelberg, 2012.

[22] B. Fritsche et al., "Radiation pressure forces on complex spacecraft, final report, ESOC contract 11908," 1998.

[23] J. Ho Kang et al., "Durability characterization of mechanical interfaces in solar sail membrane structures," *Advances in Space Research,* vol. 67, no. 9, pp. 2643-2654, 2021.

Factoring Thrust Uncertainty into Solar Sail Performance Validation

Bruce A. Campbell

[1] *B.C. Space (Consulting), NASA retired*
* Author email: B.C.Space@comcast.net

Abstract

Many solar sail mission development groups use the concept of "ideal" solar sails for initial mission concept proposal. This may be appropriate for very early feasibility sizing, however some concepts being considered for funded studies or potential flight opportunities may be presenting overly optimistic capabilities for solar sail missions. Use of a more "realistic" solar sail model, addressing both thrust performance and sailcraft trajectory control, would ensure that concept feasibility and required developments and potential mission success are better reflected.

1. Introduction

In the early 2000s, NASA's In-Space Propulsion (ISP) program at the Marshall Space Flight Center (MSFC) conducted significant development of solar sail technology, resulting in the fabrication and vacuum deployment testing of two different 20-meter size sail configurations. In addition to this system development, ISP supported two different efforts to develop solar sail simulation software packages to model sailcraft characteristics and performance to allow better solar sail mission planning.

This paper summarizes these "realistic" solar sail performance factors, and demonstrates how these should be incorporated into future solar sail mission planning. Recommendations on operations to characterize the actual performance of a solar sail propulsion system, either for a demonstration or operational mission, will also be described. In addition, recommendations for pursuing potentially more palatable initial solar sail missions are also provided.

2. Material and methods

This paper leverages sail characteristic information gathered during the ISP developments, and one of the simulation packages, and focuses on identifying and estimating factors that may detract from the expected performance of a "perfect" solar sail. Most of the information presented is from the author's PhD studies and dissertation [1].

3. Theory and calculation

A popular source describing solar sails, characteristics and forces, steering methods, and equations of motions for orbit propagation is given in [2].

3.1 "Perfect" sail

A "perfect" sail is represented by a flat surface that provides complete reflection of incident solar radiation, as depicted in Figure 1. In this case, the total incident (f_i) and reflected (f_r) photon forces imparted on the surface create a total force (f_{tot}) that is perpendicular to the flat sail surface (in the normal direction).

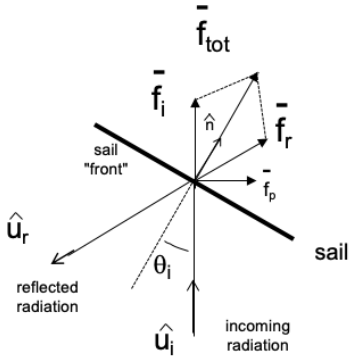

Fig. 1. "Perfect" solar radiation pressure force

This force can be calculated by Eq. 1, where θ_i is the incidence angle of the incoming solar radiation, P_I is the incident radiation pressure based on the solar luminosity energy flux (dependent on distance from the Sun), and A is the total area of the reflective surface.

$$\bar{f}_{tot} = 2P_I A\left(\cos\theta_i\right)^2 \hat{n} \quad (1)$$

Figure 2 shows the change in total force magnitude with changing incidence angle for a 100 x 100 meter square perfect surface at a 1 A.U. distance from the sun.

3.2 Non-ideal optical surface

Realistic surfaces have optical properties that affect the reflection of incident radiation. These properties include reflectivity (r_f), transmissivity (t_r), absorptivity (a_b), specularity (s), front and back emissivities (ε_f and ε_b), and front and back Lambertian reflection properties (B_f and B_b). Table 1 shows values for both and ideal surface and an example non-ideal sail surface (from ISP solar sail developments).

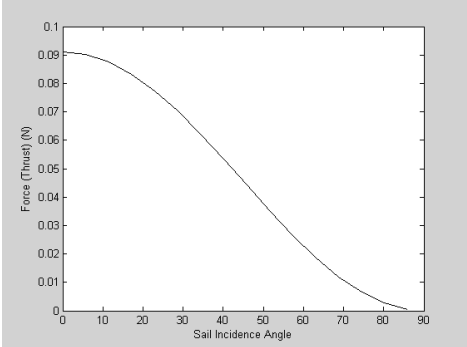

Fig. 2. "Perfect" solar radiation pressure force vs. sun-incidence angle (10,000 m^2 area @ 1 A.U.)

Table 1. Ideal and non-ideal optical properties

	t_r	a_b	r_f	s	ε_f	ε_b	B_f	B_b
Ideal sail	0	0	1	1	0	0	2/3	2/3
Non-ideal sail	0.02	0.1	0.88	0.94	0.05	0.55	0.79	0.55

Figure 3 shows the case of a solar sail with a flat surface, but with non-ideal optical characteristics.

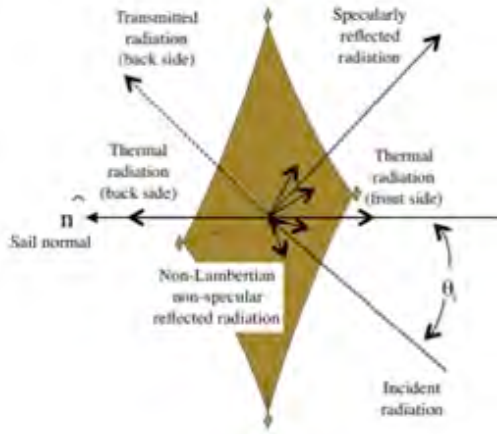

Fig. 3. Non-ideal optical solar sail

In this case, the incident radiation is not simply spectrally reflected, with some of the radiation transmitted, absorbed, and thermally and non-spectrally radiated from the surface. Incorporating these optical properties, the total force can be calculated using the following equations:

Normal force:

$$\bar{f}_n = P_I A\left[\left(1+r_f s\right)\cos^2(\theta_i) + B_f\left(1-s\right)r_f\cos\left(\theta_i\right) + \left(1-r_f\right)\frac{\varepsilon_f B_f - \varepsilon_b B_b}{\varepsilon_f + \varepsilon_b}\cos\left(\theta_i\right)\right]\hat{n} \quad (2)$$

Tangential force:

$$\bar{f}_t = P_I A\left(1-r_f s\right)\cos(\theta_i)\sin(\theta_i)\hat{t} \quad (3)$$

Total force:

$$f_{tot} = \left(f_n^2 + f_t^2\right)^{1/2} \quad (4)$$

Centerline angle:

$$\tan(\phi) = \frac{f_t}{f_n} \quad (5)$$

Figure 4 updates Figure 1 for this non-ideal case, and illustrates that the resulting total force is now offset from the normal direction by the centerline angle (ϕ). Note that for practical purposes the angle from the sun-line to the force direction is used for solar sail navigation, and is called the "cone" angle (α) as also shown. As we will show, this force angle from the sun-line has limitations.

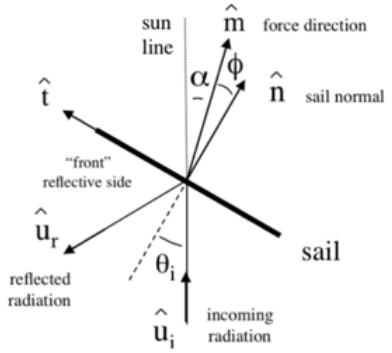

Fig. 4. Non-ideal optical solar radiation pressure force

Figure 5 compares the change in total force magnitude with changing incidence angle between this non-ideal sail and the same size ideal sail, showing a decrease in performance.

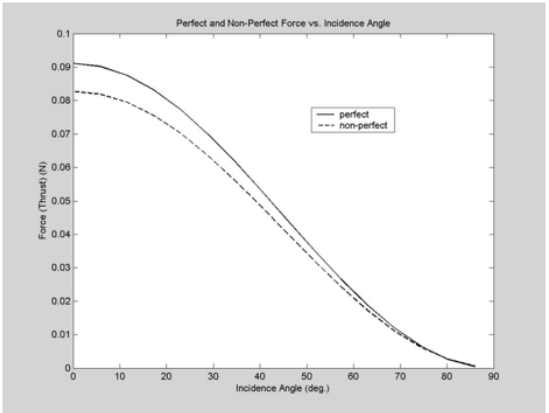

Fig. 5. Solar radiation pressure force vs. sun-incidence angle comparison (10,000 m^2 area @ 1 A.U.)

More importantly, Figure 6 plots the change in cone angle with increasing sun-incidence angle. As can be seen, due to the non-ideal optical properties there is a maximum angle that the force vector can be pointed away from the sun-line. This can have an impact on possible operation of the solar sail as a propulsion system.

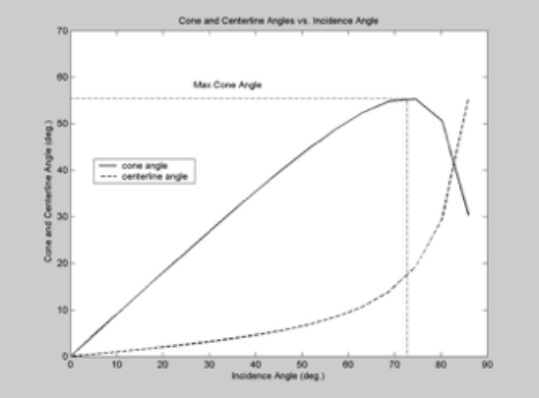

Fig. 6. Non-ideal sail cone angle vs. sun-incidence angle

Figures 7 and 8 plot impacts of changes in the surface optical properties, specifically for a 20% change from the example property values provided in Table 1. Figure 7 shows the impact on sail total force (thrust) magnitude, and Figure 8 the impact on thrust direction. As can be seen, surface reflectivity has the largest impact on both thrust magnitude and direction, however specularity also has a significant impact on force direction.

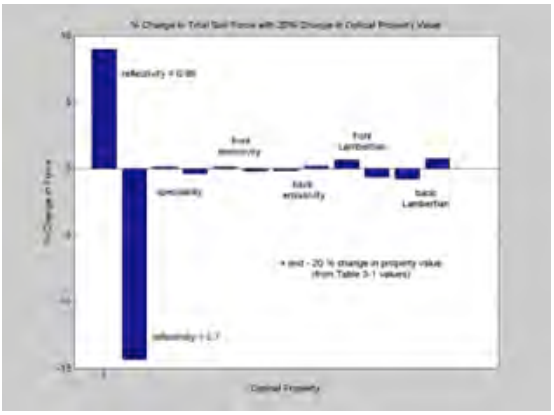

Fig. 7. Relative effects of optical properties on sail thrust magnitude

3.3 Sail shape

In addition to non-ideal optical properties, realistic solar sails will likely not have perfectly flat surfaces. Figures 9 and 10 show pictures of two different solar sail prototypes developed for the ISP program. Figure 9 shows a "tensioned" sail, pulled at its corners, and Figure 10 is a "draped" sail, more loosely supported by wires between the sail booms. (This latter approach intended to reduce the stiffness required by the booms, potentially reducing overall sail mass.)

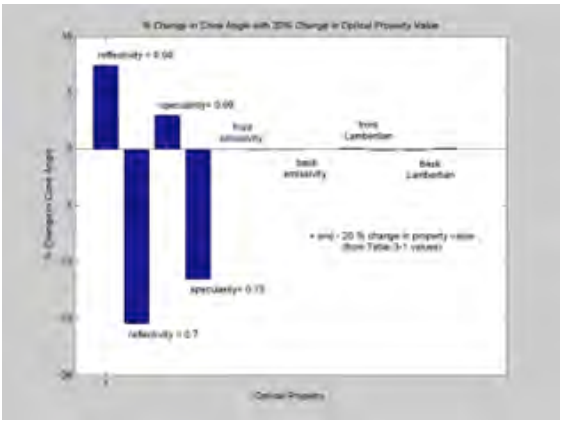

Fig. 8. Relative effects of optical properties on sail thrust direction

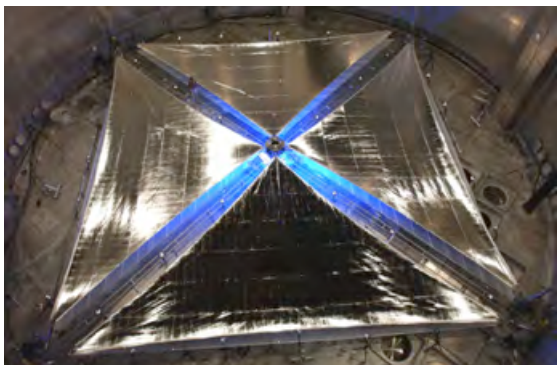

Fig. 9. Prototype "tensioned" sail

Fig. 10. Prototype "draped" sail

As can be seen, the tensioned sail has a flatter surface than the draped sail, which in addition to billow between the booms also shows "stripes" of material between the support wires between the booms that have their own billow. Both sails also have noticeable creases, wrinkles, and crinkles (Figures 11 and 12) mostly due to manufacturing (rip stops) and handling (folding, packaging and deploying). These shape properties also

affect the magnitude and direction of the resulting total radiation pressure force generated by the surface.

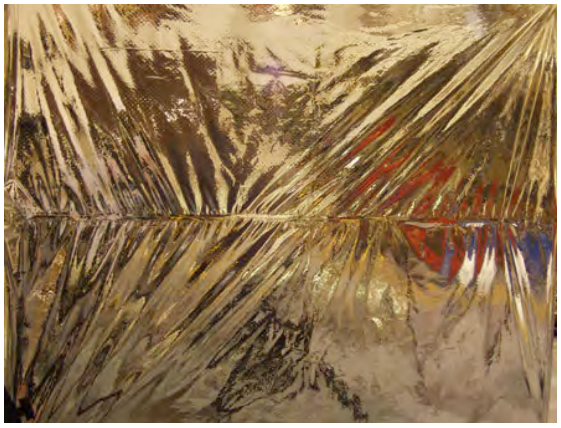

Fig. 11. Wrinkles and creases

Fig. 12. Crinkles

In order to analyse the comparative difference in performance for such non-ideal sails, models were created for four representative sail types, as shown in Figure 13. The first is an "ideal" sail with a flat, perfectly reflecting surface. The second is a flat sail with non-ideal optical properties. The third model is a reasonably flat sail surface with billow between the booms (similar to Figure 9), and the fourth model is of a draped sail similar to Figure 10.

The sail (and sailcraft) properties used for each model are shown in Table 2. Note that total (sailcraft) mass, and total sail (material) area are the same for each model. Optical and shape properties for each model were derived from information gathered during the ISP developments.

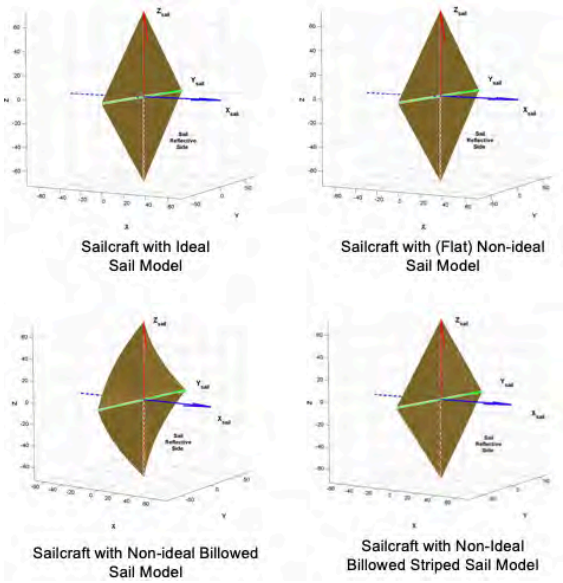

Fig. 13. Solar sail model types

Table 2. Solar sail model properties

	Ideal sail	Non-ideal (flat) sail	Realistic (billowed) sail	Realistic (striped) sail
m_{sc}	300 kg	300 kg	300 kg	300 kg
m_s	60 kg	60 kg	60 kg	60 kg
m_p	240 kg	240 kg	240 kg	240 kg
A_{sail}	10,000 m²	10,000 m²	10,000 m²	10,000 m²
Billow (θ_b)	0	0	10°	10°
Droop (θ_d)	0	0	5°	5°
t_r	0	0.02	0.002	0.02
a_b	0	0.1	0.08	0.12
r_f	1	0.88	0.918	0.86
s_{act}	1	0.94	0.978	0.55
ε_f	0	0.05	0.02	0.03
ε_b	0	0.55	0.269	0.4
B_f	2/3	0.79	0.79	0.89
B_b	2/3	0.55	0.55	0.65

These properties were input to a Solar Sail Module "toolbox" created by Princeton Satellite Systems (PSS) [3] developed for the ISP program. Each sail "quadrant" can be separately modelled and broken into a number of individual surface elements (Figure 14), for which each element radiation force can be calculated and summed together to determine overall sail force magnitude and direction. This can be done over a range of sun-incidence angles, and performance values displayed and plotted.

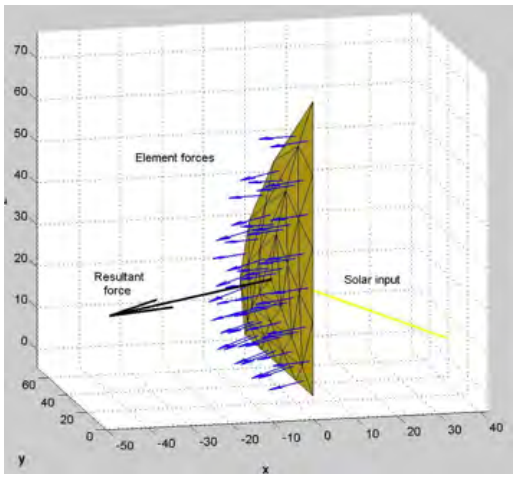

Fig. 14. Sail quadrant forces (PSS Solar Sail Module)

4. Results

Table(s) 3 show the total thrust levels (for 0^o and 35^o cone angles) and sailcraft characteristic acceleration (0^o cone angle at 1 A.U.) for each sail model. As can be seen, incorporating more of the non-ideal characteristics of the sail results in a decrease in overall performance (as might be expected). Note that this indicates between a 10 and 20 percent decrease in performance depending on the combination of sail optical and shape properties of the sailcraft.

Table 3. Solar sail model performance

Thrust Level Comparison

	Ideal sail	Non-ideal (flat) sail	Realistic (billowed) sail	Realistic (striped) sail
0^o (N)	0.091	0.082	0.074	0.067
35^o (N)	0.063	0.056	0.053	0.048

Characteristic Acceleration Comparison

	Ideal sail	Non-ideal (flat) sail	Realistic (billowed) sail	Realistic (striped) sail
a_C (mm/s^2)	0.304	0.273	0.267	0.243
		-10.2%	-12.2%	-20.1%

This decrease in performance is also illustrated in Figure 15 which plots each sail model total force over sun-incidence angle. Figure 16 plots the change in cone angle with incidence angle to the sun. While it is theoretically possible to point an ideal solar sail (the "front" shiny side used for propulsion) up to 90^o off the sun-line, it can be seen that there is a maximum angle off the sun-line that the force vector (direction) can be pointed, and which is significantly impacted by sail shape.

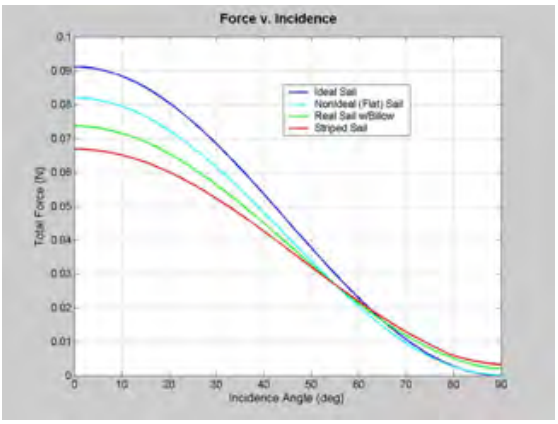

Fig. 15. Sail model force vs. sun-incidence angle

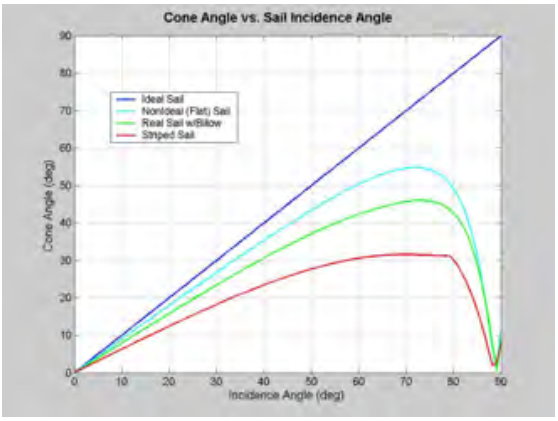

Fig. 16. Sail model cone angle vs. sun-incidence angle

5. Discussion

For a solar sail mission, attitude control is trajectory control is mission control – especially considering that under normal situations the sail will be continuously generating thrust. Mission trajectories, incorporating this persistent thrust and the cone angle limitations in direction of the thrust, must develop an associated sail attitude control (pointing) profile that will meet the objectives of the mission. This is challenging even for an ideal sail, and complicated even more for a non-ideal sail.

Two major points can be seen in the prior material. The first has to do with the inherent uncertainty in the magnitude and direction of the thrust force generated by the sail. Important sail properties, including optical and shape, are difficult to determine precisely during development and testing on the ground. An important component of this uncertainty is associated with the offset between the sailcraft center of mass (Cm) and center of pressure (Cp) generated by the sail forces. This can impact the stability and responsiveness of whatever attitude control system (ACS) approach that is implemented – many of which plan on using the same solar radiation pressure (SRP) forces and their own inherent uncertainties.

The second major point has to do with ensuring that these uncertainties are incorporated in the mission design. Development of mission trajectories must ensure that calculation of "optimal" flight paths and their associated sail pointing profiles include sufficient "margins" such that recovery from any underperformances do not require the sail to exceed its capabilities (thrust magnitude and/or direction). The resulting trajectory will provide information/requirements that can translate into sailcraft systems designs, such as ACS approach, on-board guidance and navigation (GN&C) design (position and attitude measurements) and the associated feedback (and frequency) to the control systems to meet the desired trajectory and mission objectives (attitude control is trajectory control is mission control).

Finally, it is urgent that a comprehensive solar sail demonstration mission be flown. Early missions such as Japan's IKAROS, NASA's NanoSail, and the Planetary Society's LightSail, demonstrated some important aspects of solar sailing, such as deployment and thrust generation, however none of these provided the kind of performance and operation necessary to validate the current models being used for solar sail mission (and sailcraft) design. A dedicated, fully capable and instrumented sailcraft could demonstrate not only thrust generation, but also positive control and trajectory performance as well as other important sailcraft operations information. This would provide actual sail performance that could be compared to the pre-flight models used for the mission design, and allow updates to allow better following mission design. Such a demonstration mission, the Advanced Composite Solar Sail System (ACS3) is currently being developed by NASA and scheduled for launch in the near future.

While these better models will allow better future, more complex solar sail mission (and sailcraft) design, there will still be inherent uncertainties associated with manufacturing and handling of the sail materials and components for each and every sailcraft developed. Because of this, even for identical "copies" of sailcraft, there is an obvious need for any solar sail mission to have a calibration campaign after deployment in space to compare to and adjust the models used for the mission planning. While not an integral part of the actual mission objectives, such a campaign will allow operational refinements of the mission to increase confidence of mission success.

6. Conclusions

Use of "ideal" sail models for solar sail mission concepts and proposals contain overly optimistic sail capabilities that do not sufficiently represent a configuration that would need to be developed to realize the mission. Use of more "realistic" solar sail models, addressing both thrust performance and sailcraft trajectory control, would ensure that concept feasibility and required developments and potential mission success are better reflected. Flying a dedicated and comprehensive solar sail demonstration mission would provide information needed to update current models and allow even better solar sail mission concept development and proposals for future missions.

References

[1] Campbell, Bruce A, An Analysis of Thrust of a Realistic Solar Sail with Focus on a Flight Validation Mission in a Geocentric Orbit, ProQuest Dissertations Publishing, 2010. (http://gateway.proquest.com/openurl?url_ver=Z39.88-2004&res_dat=xri:pqdiss&rft_val_fmt=info:ofi/fmt:kev:mtx:dissertation&rft_dat=xri:pqdiss:3407845)

[2] McInnes, Colin R., " Solar sailing: Technology, Dynamics and Mission Applications", Springer-Praxis 1999.

[3] Thomas, S., Paluszek, M., Wie, B., Murphy, D., "Design and Simulation of Sailcraft Attitude Control Systems Using the Solar Sail Control Toolbox", AIAA Guidance, Navigation, and Control Conference and Exhibit 16 - 19 August 2004, Providence, Rhode Island

Adaptive Terminal Sliding Mode Control for Asteroid Hovering by Solar Sailing: Application to 433 Eros

Zitong Lin[a,**], Matteo Ceriotti[a], Colin R. McInnes[a]

[a]*James Watt School of Engineering, University of Glasgow, Glasgow, United Kingdom*

Abstract

In this paper, we propose a second-order sliding mode control law of solar sail to hover on displaced orbits above an asteroid. To overcome the difficulties of solar sail control, firstly, dynamics in cylindrical coordinates are used and only the hovering radii and height are controlled, neglecting the polar angle; secondly, the angular velocity of two attitude angles is taken as the control input instead of the angles themselves; lastly, an adaptive estimation law is applied to increase the robustness to gravity uncertainty. The case of hovering on displaced orbits above 433 Eros is simulated. The effect of different hovering radius, height and sunlight incidence direction are studied. In addition, the robustness of the control law is tested against unknown gravity disturbances and imprecise sail force model. This work successfully demonstrates that it is feasible to achieve an asteroid-hovering mission using an underactuated solar sail with only two controllable attitude angles.

Keywords: Underactuated solar sail, asteroid hovering orbit, second-order sliding mode control, adaptive estimation

1. Introduction

Asteroids, a type of small bodies, are widely-distributed living fossils in the solar system. As the space exploration deepens, these inconspicuous space rocks have attracted more attention of researchers and space agencies around the world. Asteroid exploration not only helps to reveal the origin of solar system, but it also assists significantly with space resource exploitation and planetary defence. There have been many representative examples of asteroid missions. In 2001, NEAR-Shoemaker probe to 433 Eros had become the first one to orbit and land on an asteroid [1]. The Hayabusa mission to 25143 Itokawa had achieved sample return of an asteroid for the first time in 2010 [2]. The follow-up Hayabusa 2 mission to 162173 Ryugu made multiple surface interactions with MASCOT landers, as well as performing a sample return [2]. These missions have brought many successes, not only in better knowing of asteroid physical properties, but also in boosting technologies in deep space exploration.

Since transfers to asteroids usually require high delta-v budgets, solar sailing can be an ideal option as it is capable of providing a theoretically-unlimited delta-v. Extensive research has investigated the use of solar sails for asteroid rendezvous missions [3-5], while little effort has been made on the operations of a solar sail in close proximity of an asteroid. In order to maximise the scientific return of the mission, asteroid flying-by reconnaissance is not enough and close-proximity operations will be essential, including hovering.

Hovering is a practical option of mapping an asteroid: the spacecraft flies on the displaced orbit above a certain region of the asteroid or keep stationary at a certain location, which therefore takes advantage in high-resolution imaging [6], landing [7], lander deployment [8] and sampling [2]. However, hovering above an asteroid is energy-consuming as it seeks no benefit from natural motion in most cases, making it only suitable for asteroids of small dimension [9]. Regarding this issue, solar sailing may offer a possible solution to hovering above large asteroids because of the continuous propellant-free acceleration.

New concepts of spacecraft in asteroid missions bring new challenges in control. Firstly, differently from spacecraft with three-axis thrust, a conventional sail-craft only has two control variables, namely attitude angles, for orbit control, resulting in an acceleration vector that is constrained in both direction and magnitude. Thus, it is challenging or impossible to track any arbitrary orbit in three dimensions; this is indeed typical of an underactuated system. Secondly, the input sail attitude angles affect its dynamics via trigonometric

* Corresponding author email, z.lin.1@research.gla.ac.uk

terms; in other words, the control is not linear and non-affine. An additional complexity is that the gravity field of an asteroid is highly irregular and cannot be precisely known prior to a mission, adding uncertainty and disturbances to the control problem.

Yet some research provides insights in the control of solar sail in proximity of asteroids. Biggs and McInnes [10] proposed the Time-Delayed Feedback Control (TDFC) as a method of bounding the orbit of a spacecraft around a central body with large ellipticity. Rather than depending on some reference trajectory, this method uses the state known one period previous to the current state as the reference. Farrés et al. [11-13] have studied a series of work on the dynamics of solar sail near an asteroid. These works brilliantly inherited the complete theory of linear control and orbit dynamics in CR3BP, but the linearisation involved cannot guarantee global stability, which means stable controlled orbits can be designed only near the equilibrium points. Zeng [14] considered the solar sail with controllable reflectivity and globally searched the feasible hovering regions above an asteroid with sunlight incident direction taken into account. The reflectivity change is the third control that complements the attitude manoeuvres to solve the underactuated problem, but it will significantly increase the system complexity and cost. Moore and Ceriotti [15] proposed the Genetic Algorithm and Control Transition Matrix (GA & CTM) method and found its application in eliminating the non-spherical gravity perturbation of an asteroid on solar sail orbits. This method uses an optimisation approach to obtain the control so that non-affine and underactuated problems are avoided. However, due to the black-box nature of GA, the desired orbit can only be selected within unforeseeable candidates but cannot be predefined arbitrarily, especially in terms of non-Keplerian orbits above asteroids. In addition, the sliding mode control (SMC), a control strategy robust to disturbances, attracts as much attention for its wide application in spacecraft orbit control. There has been research about asteroid landing [7] and orbiting [16, 17] missions with SMC; in this paper, its application in the orbit control of solar sail will be investigated.

In this paper, an adaptive terminal sliding mode control is proposed for the hovering control close to asteroid Eros. A displaced (non-Keplerian) circular orbit is selected as reference, and by converting the dynamics from Cartesian to cylindrical coordinates, the desired displaced orbit radius and hovering height are tracked regardless of polar angle, which transforms the underactuated system into a fully-actuated one. By differentiating the dynamics, the first-order derivatives of the sail attitude angles appear in linear form and are therefore chosen as the control input so that the non-affine issue can be solved. Moreover, an estimation law is designed to update the upper bound of disturbances, making the control robust to the complex gravity field of an asteroid.

2. Dynamics

2.1. Frames of Reference

A sketch of the reference frames is shown in Fig. 1. The first frame is the principal axis frame fixed with the asteroid referred to as $Oxyz$ (denoted as frame a). It is centred at the barycentre of the asteroid and it rotates about z axis defined by the constant self-spin rate of the asteroid, $\boldsymbol{\omega} = \omega\hat{\boldsymbol{z}}$ (the hat above a vector is used throughout this paper to indicate its unit vector) where ω is the modulus of angular velocity. x axis lies in the equatorial plane normal to z axis and y axis completes the triad. The inertially-fixed frame $OXYZ$ (which is not shown in Fig. 1 and denoted as frame I) coincides with $Oxyz$ at the initial time. If only a short time of flight around the asteroid is considered, it is reasonable to take this frame as fixed with respect to the sun direction, because the asteroid spin period (in the order of hours) is negligible with respect to its orbital period (in the order of years). Another important frame is the light incidence frame $Oe_xe_ye_z$ (denoted as frame E). e_z is aligned with the solar incident direction, e_y coincides with Y axis and e_x completes the triad. The relative position between the Sun and the asteroid can be described by the solar incidence angle $\varphi \in [-\pi/2, \pi/2]$, defined as the angle between e_z axis and Z axis. The last frame is the hovering orbit frame $ox_hy_hz_h$ (denoted as frame h). The ox_hy_h plane lies in the hovering plane which is perpendicular to the z axis and x_h, y_h, z_h axes follow the directions of outward radial, forward tangential and upward respectively.

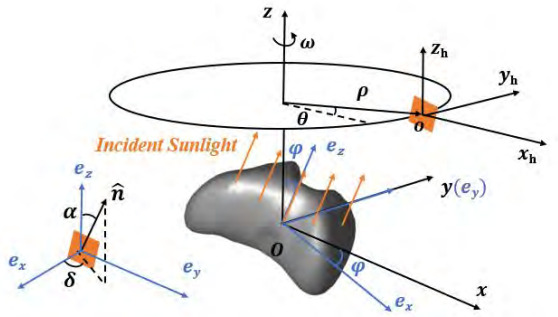

Fig. 1. Diagram of asteroid-fixed frame, light incidence frame, hovering orbit frame and solar sail attitude angles.

The coordinate transformations among the different frames are shown below:

$$E \xrightarrow{\mathbf{C}_y(\varphi)} I \xrightarrow{\mathbf{C}_z(\omega t)} a \xrightarrow{\mathbf{C}_z(\theta)} h \qquad (1)$$

where the rotation matrices are:

$$\mathbf{C}_E^I = \begin{bmatrix} \cos\varphi & 0 & -\sin\varphi \\ 0 & 1 & 0 \\ \sin\varphi & 0 & \cos\varphi \end{bmatrix} \quad (2)$$

$$\mathbf{C}_I^h = \begin{bmatrix} \cos(\theta+\omega t) & \sin(\theta+\omega t) & 0 \\ -\sin(\theta+\omega t) & \cos(\theta+\omega t) & 0 \\ 0 & 0 & 1 \end{bmatrix} \quad (3)$$

$$\mathbf{C}_a^h = \begin{bmatrix} \cos\theta & \sin\theta & 0 \\ -\sin\theta & \cos\theta & 0 \\ 0 & 0 & 1 \end{bmatrix} \quad (4)$$

2.2. Model of Asteroid Gravity

Polyhedron method is one of the methods to model the gravitational field of an asteroid while reflecting the perturbation induced by its irregular shape. The gravity potential in asteroid-fixed frame can be written as:

$$U = -G\rho \sum_{e\in edges} \mathbf{E}_e \boldsymbol{r}_e L_e + G\rho \sum_{f\in faces} \mathbf{F}_f \boldsymbol{r}_f \omega_f \quad (5)$$

where G is the gravitational constant and ρ is the constant density of the asteroid. As can be seen, this expression is made up of two different contributions: the first is associated with the edges of each face and the second with the faces of each tetrahedron which form the surface of the body. The term $\boldsymbol{r}_e$ represents a vector from a field point to any point on the edge e, while the term $\boldsymbol{r}_f$ represents a vector from a field point to any point on the face f. $\mathbf{E}_e$ and $\mathbf{F}_f$ are two tensors: the first takes into account the geometry of the edges and the second considers the geometry and the orientation of the faces. Finally, L_e and ω_f are two scalars: the first is the potential of a 1D straight wire and ω_f is the signed solid angle subtended by the face f. Further details about calculation can be referred to the work of Werner and Scheeres [18].

2.3. Model of Solar Sail

Consider an ideal solar sail, the solar radiation pressure (SRP) acceleration can be modelled as [19]:

$$\boldsymbol{a}_{SRP} = a_0 \cos^2\alpha\, \hat{\boldsymbol{n}} \quad (6)$$

where a_0 is the constant part in SRP acceleration determined by the lightness number β, the solar gravitational constant μ_s and heliocentric distance R.

$$a_0 = \frac{\beta\mu_s}{R^2} \quad (7)$$

$\hat{\boldsymbol{n}}$ is the unit vector of sail normal in light incidence frame, expressed as:

$$\hat{\boldsymbol{n}} = [\sin\alpha\cos\delta \quad \sin\alpha\sin\delta \quad \cos\alpha]^T \quad (8)$$

where $\alpha \in [0, \pi/2]$ is the cone angle, defined as the angle between $\hat{\boldsymbol{n}}$ and e_z axis, and δ is the clock angle, defined as the angle between e_x axis and the projection of $\hat{\boldsymbol{n}}$ on Oe_xe_y plane (see Fig. 1).

2.4. Dynamics in Cylindrical Coordinates

Similar to the work on SRP geocentric displaced orbit in Ref. [20, 21], dynamics in cylindrical coordinates is adopted in order to facilitate the design. The dynamics of a solar sail at position $\boldsymbol{r} = [x, y, z]^T$ in asteroid-fixed frame a is given by:

$$\ddot{\boldsymbol{r}} + 2\boldsymbol{\omega}\times\dot{\boldsymbol{r}} + \boldsymbol{\omega}\times(\boldsymbol{\omega}\times\boldsymbol{r}) = \nabla U + \boldsymbol{f}_{SRP} \quad (9)$$

where ∇U is the gradient of gravity potential and $\boldsymbol{f}_{SRP}$ is the SRP acceleration in asteroid-fixed frame.

By substituting $x = \rho\cos\theta$ and $y = \rho\sin\theta$, the dynamics in Cartesian coordinates can be converted into the cylindrical coordinates (ρ, θ, z) shown below:

$$\begin{cases} \ddot{\rho} = \rho\left(\omega+\dot{\theta}\right)^2 + g_\rho + f_\rho \\ \rho\ddot{\theta} = -2\dot{\rho}\left(\omega+\dot{\theta}\right) + g_\theta + f_\theta \\ \ddot{z} = g_z + f_z \end{cases} \quad (10)$$

where

$$\boldsymbol{g} = \left[g_\rho, g_\theta, g_z\right]^T = \mathbf{C}_a^h \nabla U \quad (11)$$

$$\boldsymbol{f} = \left[f_\rho, f_\theta, f_z\right]^T = \mathbf{C}_I^h \mathbf{C}_E^I \boldsymbol{a}_{SRP} \quad (12)$$

In the next chapter, $\boldsymbol{f}$, the SRP acceleration in hovering orbit frame h, is to be controlled so that the solar sail can hover on the displaced orbit with its plane normal to z axis.

3. Control

3.1. Sliding Mode Control

Because the manoeuvres required to achieve a hovering state are executed in a dynamical environment that is generally uncertain, an effective implementation of such requires employing control algorithms that are robust against unmodeled perturbations. To this regard, sliding mode control (SMC) is considered to be one of the most effective techniques for controlling dynamical systems with uncertainties [16]. The idea behind SMC is to design a controller capable of maintaining a properly chosen constraint, i.e. a sliding surface, by means of high-frequency control switching. Once the system dynamics is on the sliding surface, it is constrained to remain there, resulting in robust and adaptive control, although it often comes with actuator chattering due to the frequent switch of discontinuous control signal.

3.2. Design of Sliding Surface

Define vectors for state $\boldsymbol{\chi} = [\rho, \theta, z]^T$ and control $\boldsymbol{u} = [\alpha, \delta]^T$. Now the control objective is to force the reduced state $\boldsymbol{\chi}_r = [\rho, z]^T$ to asymptotically track the desired state $\boldsymbol{\chi}_d = [\rho_d, z_d]^T$, regardless of the polar angle θ, by only varying the attitude angles α and δ.

Define tracking error vector as $\boldsymbol{e} = \boldsymbol{\chi}_r - \boldsymbol{\chi}_d$, the sliding surface can be chosen as:

$$\boldsymbol{s} = \dot{\boldsymbol{e}} + \mathbf{k}\boldsymbol{e} \tag{13}$$

where $\mathbf{k}$ is a diagonal positive-definite matrix to be designed.

Then, inspired by the terminal sliding surface used in Ref. [22], a similar non-singular terminal sliding surface is designed as

$$\boldsymbol{\sigma} = \boldsymbol{s} + k_0 \dot{\boldsymbol{s}}^{\frac{p}{q}} \tag{14}$$

where k_0 is a positive constant, p and q are positive odd numbers, holding $1 < p/q < 2$. The application of this terminal sliding surface guarantees the convergence of tracking error within finite time.

3.3. Design of Controller

For the non-affine control system, it is more convenient to choose $\dot{\boldsymbol{u}}$ as the control input instead of $\boldsymbol{u}$. $\dot{\boldsymbol{u}}$ will appear in linear form if Eq. (10) is further differentiated to $\ddot{\boldsymbol{\chi}}$, shown as:

$$\ddot{\boldsymbol{\chi}} = \boldsymbol{h}(\chi_r, \dot{\chi}_r) + \dot{\mathbf{C}}_I^O \mathbf{C}_E^I \boldsymbol{a}_{SRP} + \mathbf{C}_I^O \mathbf{C}_E^I \mathbf{B}(\boldsymbol{u})\dot{\boldsymbol{u}} \tag{15}$$

There are two notable points: firstly, the result of $\mathbf{C}_I^O \mathbf{C}_E^I \mathbf{B}(\boldsymbol{u})\dot{\boldsymbol{u}}$ neglects the second row since θ is not concerned; Secondly, $\boldsymbol{h}$ can be further split as

$$\boldsymbol{h} = \boldsymbol{h_0} + \boldsymbol{d} \tag{16}$$

where $\boldsymbol{h_0}$ is the known part of the derivative of point-mass gravity $-\mu \boldsymbol{r}/r^3$, and $\boldsymbol{d}$ is the unknown part of non-spherical gravity disturbances. Such split takes account the normal case that the non-spherical perturbation of an asteroid is not precisely known until in-situ visit. Recall that in the module of dynamics, a polyhedron gravity field model is used for precise propagation. In addition, assumption is made that $\boldsymbol{d}$ is bounded, holding $\|\boldsymbol{d}\| \leq \boldsymbol{D}$.

After obtaining $\ddot{\boldsymbol{\chi}}$, Eq. (13) is differentiated twice so that, considering Eq. (15), the dynamics of $\boldsymbol{s}$ is obtained as:

$$\ddot{\boldsymbol{s}} = \boldsymbol{h} + \dot{\mathbf{C}}_I^O \mathbf{C}_E^I \boldsymbol{a}_{SRP} + \mathbf{C}_I^O \mathbf{C}_E^I \mathbf{B}(\boldsymbol{u})\dot{\boldsymbol{u}} - \dddot{\boldsymbol{\chi}}_{\boldsymbol{d}} + \mathbf{k}\ddot{\boldsymbol{e}} \tag{17}$$

Next, Eq. (14) is differentiated once so that $\ddot{\boldsymbol{s}}$ appears:

$$\dot{\boldsymbol{\sigma}} = k_0 \frac{p}{q} \mathrm{diag}\left(\dot{\boldsymbol{s}}^{\frac{p}{q}-1}\right)\left(\frac{q}{kp}\dot{\boldsymbol{s}}^{2-\frac{p}{q}} + \ddot{\boldsymbol{s}}\right) \tag{18}$$

If the reaching law to terminal sliding surface is chosen as:

$$\dot{\boldsymbol{\sigma}} = \mathrm{diag}\left(\dot{\boldsymbol{s}}^{\frac{p}{q}-1}\right)\left(-\varepsilon_1 \boldsymbol{\sigma} - \varepsilon_2 \mathrm{sign}(\boldsymbol{\sigma})\right) \tag{19}$$

once the dynamics flow to $\boldsymbol{\sigma} = \mathbf{0}$, $\boldsymbol{s}$ will converge to $\mathbf{0}$ rapidly as well as $\boldsymbol{e}$, where ε_1 and ε_2 are positive parameters to be designed.

Finally, substituting Eq. (17) into Eq. (18) and combining Eq. (18) and (19), the control law can be obtained as:

$$\dot{\boldsymbol{u}} = (\mathbf{C}_I^O \mathbf{C}_E^I \mathbf{B})^{-1} \begin{bmatrix} \dddot{\boldsymbol{\chi}}_d - \boldsymbol{h} - \dot{\mathbf{C}}_I^O \mathbf{C}_E^I \boldsymbol{a}_{SRP} \\ -\mathbf{k}\ddot{\boldsymbol{e}} - \frac{q}{kp}\dot{\boldsymbol{s}}^{2-\frac{p}{q}} - \varepsilon_1 \boldsymbol{\sigma} - \varepsilon_2 \mathrm{sign}(\boldsymbol{\sigma}) \end{bmatrix} \tag{20}$$

3.4. Design of Adaptive Estimation in Controller

The boundary of gravity disturbances $\boldsymbol{d}$ is separately updated by an adaptive estimation law, designed as:

$$\hat{\dot{\boldsymbol{D}}} = \gamma \frac{k_0 p}{q} \mathrm{diag}\left(\dot{\boldsymbol{s}}^{\frac{p}{q}-1}\right)|\boldsymbol{\sigma}| \tag{21}$$

where γ, the updating rate, is a positive number to be designed.

With the adaptive law, the control law of $\dot{\boldsymbol{u}}$ is finalised as:

$$\dot{\boldsymbol{u}} = (\mathbf{C}_I^O \mathbf{C}_E^I \mathbf{B})^{-1} \begin{bmatrix} \dddot{\boldsymbol{\chi}}_d - \boldsymbol{h}_0 - \hat{\boldsymbol{D}} - \dot{\mathbf{C}}_I^O \mathbf{C}_E^I \boldsymbol{a}_{SRP} \\ -\mathbf{k}\ddot{\boldsymbol{e}} - \frac{q}{kp}\dot{\boldsymbol{s}}^{2-\frac{p}{q}} - \varepsilon_1 \boldsymbol{\sigma} - \varepsilon_2 \mathrm{sign}(\boldsymbol{\sigma}) \end{bmatrix} \tag{22}$$

4. Results

4.1. Simulation of Hovering

In this section, the case of hovering on a displaced orbit above Eros is simulated. The physical parameters for simulation are listed in Table 1. The pre-defined parameters in the controller are listed in Table 2.

Choosing the desired hovering orbit as $[\rho_d, z_d]^T = [18{,}40]$ km and the initial conditions as $[\rho, \theta, z]^T = [18.1\ \mathrm{km}, -\pi/2, 39.9\ \mathrm{km}]$ (not on the reference orbit), $[\dot{\rho}, \dot{\theta}, \dot{z}]^T = [-1\ \mathrm{m/s}, -3.3117 \times 10^{-4}\ \mathrm{rad/s}, 1\ \mathrm{m/s}]$, the trajectory of solar sail is shown in Fig. 2 where the solar sail is driven to the desired trajectory clockwise. The control history is shown in Fig. 3. Detailed examination to the response curve shows that the cone angle α fluctuated above and below 53 deg with chattering, which is a net result of combating the non-spherical disturbances of the asteroid and inherent SMC characteristic. Fig. 4 is the response to tracking errors, showing that they converge to less than 1 m within 7.8 hours. Despite the polar angle is not controlled, the general pattern of its variation needs to be understood. Fig. 5 shows that time derivative of the polar angle $\dot{\theta}$

(presented in units of asteroid spin rate ω) behaves in near-sinusoidal way. Looking back into Eq. (10) may reveal the reason. At steady state, $\dot{\rho} = 0$ and g_θ is lower in magnitude than f_θ, therefore f_θ dominates the general variation of $\ddot{\theta}$. Furthermore, f_θ contains the trigonometric term of $\boldsymbol{u} = [\alpha, \delta]^T$ with near-constant α at steady state, and thus f_θ changes with δ sinusoidally, leading to a near-sinusoidal $\dot{\theta}$ as a result.

Table 1. Physical parameters for simulation

	Value
Eros Gravitational Constant μ	4.4602×10^4 km^3/s^2
Eros Spin Rate ω	3.3117×10^{-4} rad/s
Eros Heliocentric Distance R	1.6917×10^6 km
Solar Incidence Angle φ	0 deg
Sail Lightness Number β	0.2

Table 2. Parameters in controller

	Value
$\mathbf{k}$	diag(1,1) (s^{-1})
k_0	1×10^6 (km$^{1-p/q}$ / s$^{1-2p/q}$)
p	7
q	5
ε_1	1×10^{-9} (s^{-1})
ε_2	1×10^{-9} (s^{-1})
γ	1

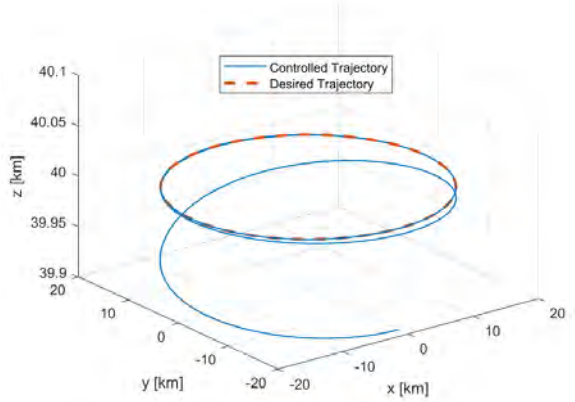

Fig. 2. Controlled trajectory of solar sail.

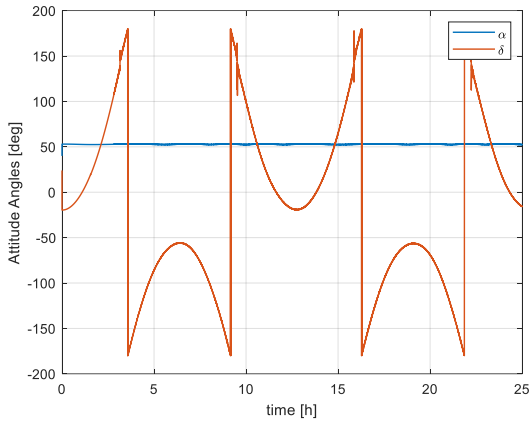

Fig. 3. Time history of control attitude angles.

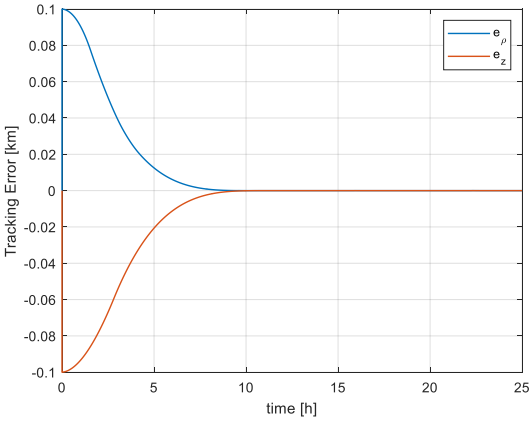

Fig. 4. Response to tracking errors.

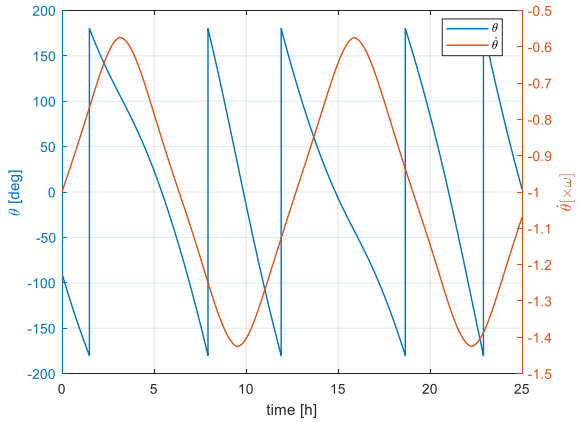

Fig. 5. Polar Angle θ and its time derivative $\dot{\theta}$.

4.2. *Robustness*

4.2.1. *Sail Degradation*

Optical degradation of a solar sail is a practical concern because it decreases both the magnitude of SRP

and sail control authority [23]. When degradation happens, the lightness number β decreases, which is equivalent to superpose an equi-magnitude but reverse disturbance onto the controlled SRP acceleration. A scenario is assumed that β is degraded from 0.2 to 0.15 exponentially with 99% attenuation at 15 hours (much faster than real degradation would be). It can be fitted as:

$$\beta(t) = 0.05e^{-t/13500} + 0.15 \qquad (23)$$

With the nominal value of β staying at 0.2, the simulation shows a successful controlled trajectory the same as that in Fig. 2, while the response of cone angle α is different. In Fig. 6, the control of cone angle α in ideal (Section 4.1) and optical degradation (Section 4.2) cases are compared. When optical degradation occurs, the cone angle automatically decreases to compensate the reduction of SRP magnitude and the orbit control is still maintained. This result demonstrates the robustness of the control law to internal disturbances of sail modelling error.

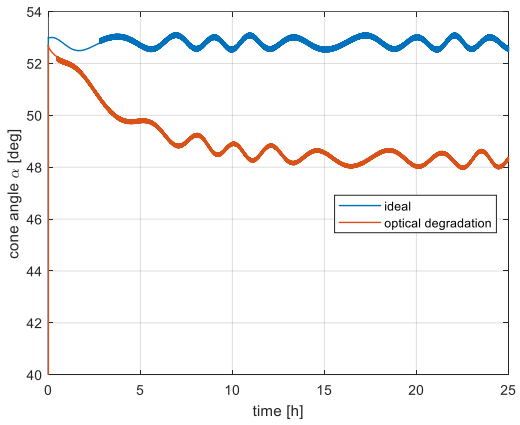

Fig. 6. Control of cone angle in ideal (blue) and optical degradation (red) cases.

4.2.2. *Gravity Field*

Recalling that the simple point-mass gravity is used in the controller design, the robustness to gravity disturbances can be further tested. Now it is assumed that, in the propagation of the dynamics, the real mass of Eros is two times of the nominal value used in the controller. Fig. 7 indicates that the scenario is identified by the control law and cone angle is adjusted down to about 41 deg while it remains around 53 deg with nominal Eros mass in dynamics. The fact that hovering control still works demonstrates that the control law is robust to the unknown external gravity disturbances. It is also worth noting that the control is still robust even without the adaptive estimation law of Eq. (21). Further enlarging the real mass of Eros shows that the robustness of control is increased by introducing the estimation on $\boldsymbol{D}$ (see Eq. (21)): the control without the adaptive estimation breaks down until the real mass increases to 3 times of the nominal value approximately, while with the adaptive estimation it fails with the real mass up to 3.4 times of the nominal value.

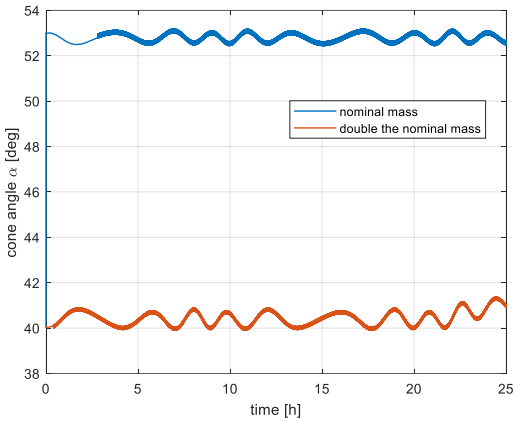

Fig. 7. Control of cone angle in real dynamics with nominal asteroid mass (blue) and double asteroid mass (red).

4.3. *Effect of hovering radius and height*

After the injection manoeuvre, the values of cone angle at steady state are relevant to the polar radius ρ_d and height z_d of the displaced hovering orbit. The cone angles with ρ_d = 18 km, z_d = 30, 40, 50 km are shown in Fig. 8, while those with z_d = 40 km, ρ_d = 10, 18, 24 km are shown in Fig. 9, which demonstrate that a solar sail can achieve hovering in different locations above the asteroid to implement tasks with different requirements without changing any optical properties or lightness number. It can be found that smaller hovering height and radii require smaller cone angles because larger SRP component is needed to counterbalance the gravity in z-axis direction as the solar sail gets closer to the barycentre of the asteroid, as well as to supply larger centripetal force in smaller circular orbits. Moreover, cone angles experience a more intense oscillation as a result of disturbance rejection in the cases of smaller hovering height and larger hovering radii. This is because the effect of perturbation of irregular shape becomes more obvious as the solar sail gets closer to the asteroid in z-axis direction. As the hovering radius becomes smaller, the solar sail undergoes less variation of gravity perturbation in Oxy plane. An extreme case will be the station-keeping above the north pole of the asteroid where planar gravity perturbation keeps constant.

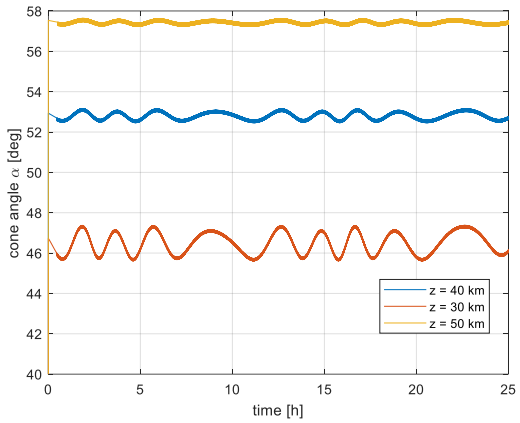

Fig. 8. Cone angle at steady state with ρ_d = 18 km.

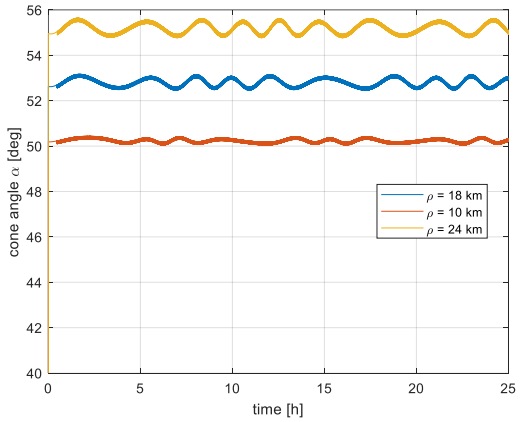

Fig. 9. Cone angle at steady state with z_d = 40 km.

4.4. Effect of Sunlight Incidence Direction

The sunlight incidence angle φ is affected by two elements: heliocentric orbital inclination and obliquity of the ecliptic. Within one orbital period of Eros, φ can vary in a large range. For example, when NEAR Shoemaker was orbiting Eros in 26 June 2000, its rotation axis was perpendicular to the Sun-Eros line ($\varphi = 90$ deg), and 7 months later, it became aligned with Sun-Eros line ($\varphi = 0$ deg) [24]. Simulations with φ = 0, 15, 30, 60, 90 deg are made to study the influence of sunlight incident direction on the hovering control. The results of trajectories and control are presented in Fig. 10. For the cases of φ = 0, 15 deg, the orbit keeping succeeds; when φ grows larger than 30 deg, the displaced orbit fails to be maintained; when φ = 90 deg, the control breaks down in manoeuvre stage. It is obvious that the control is only effective for a set of small values of φ. An explicit reason is that a solar sail can never produce sunward SRP force which is always required by the controller as long as φ is not zero. To this concern, an auxiliary SEP propulsion system may be installed on the sail to complement the missing component towards the Sun, or the solar sail should be driven into other anchor locations during infeasible sunlight incidence period, such as heliocentric solar synchronous orbit.

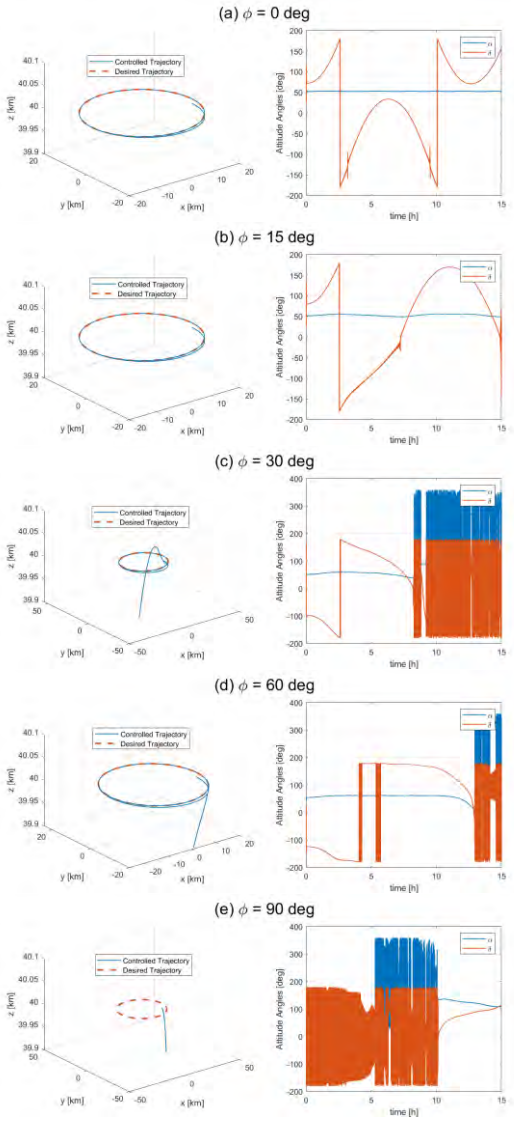

Fig. 10. Trajectories and control of hovering control with sunlight incidence angle (a) φ = 0 deg, (b) φ = 15 deg, (c) φ = 30 deg, (d) φ = 60 deg, (e) φ = 90 deg.

5. Conclusions

In this paper, a hovering orbit controller based on second-order sliding mode theory is designed for solar sail spacecraft on asteroid displaced orbit. Not only does it provide an insight into tackling the problems of underactuated and non-affine control, but also behaves robustly enough to the external unmodelled gravity disturbances and internal imprecise modelling of forces exerted on the sail. Simulation results indicate that smaller hovering radii and height lead to smaller cone

angle. In addition, smaller hovering height and larger radii induce more obvious oscillations in the cone angle. Furthermore, because of the natural shortcoming of solar sailing that it cannot generate sunward force, the controller only works for small sunlight incidence angles. However, a quantitative analysis is lacking in the result analysis. Future work can search feasible ranges of hovering height, radii and sunlight incident direction, as well as improving the quality of the control. The direct observer on gravity disturbance $\boldsymbol{d}$ will be designed instead of its boundary $\boldsymbol{D}$ as follow-up work.

References

[1] Prockter, L., et al., *The NEAR Shoemaker mission to asteroid 433 Eros.* Acta Astronautica, 2002. **51**(1-9): p. 491-500.

[2] Yoshikawa, M., et al., *Sample Return Missions*, in *Sample Return Missions*. 2021, Elsevier. p. 123-146.

[3] Zeng, X., S. Gong, and J. Li, *Fast solar sail rendezvous mission to near Earth asteroids.* Acta Astronautica, 2014. **105**(1): p. 40-56.

[4] Dachwald, B., W. Seboldt, and L. Richter, *Multiple rendezvous and sample return missions to near-Earth objects using solar sailcraft.* Acta Astronautica, 2006. **59**(8-11): p. 768-776.

[5] Peloni, A. and M. Ceriotti, *Solar-Sail Trajectory Design for a Multiple Near-Earth-Asteroid Rendezvous Mission.* Journal of Guidance, Control, and Dynamics 2016. **39(12)**.

[6] Guelman, M.M., *Closed-loop control for global coverage and equatorial hovering about an asteroid.* Acta Astronautica, 2017. **137**: p. 353-361.

[7] Yang, H., X. Bai, and H. Baoyin, *Finite-time control for asteroid hovering and landing via terminal sliding-mode guidance.* Acta Astronautica, 2017. **132**: p. 78-89.

[8] Moore, I., M. Ceriotti, and C.R. McInnes, *Station-keeping for a solar sail during lander/probe deployment using feedback control.* Acta Astronautica, 2022. **201**: p. 182-197.

[9] Scheeres, D.J., *Close proximity dynamics and control about asteroids*, in *American Control Conference*. 2014: Portland, Oregon, US. p. 1584-1598.

[10] Biggs, J.D. and C.R. McInnes, *Time-Delayed Feedback Control in Astrodynamics.* Journal of Guidance, Control, and Dynamics, 2009. **32**(6): p. 1804-1811.

[11] Farrés, A., S. Soldini, and Y. Tsuda, *JAXA's Trojan Asteroids Mission Trajectory Design of the Solar Power Sail and its Lander*, in *The 4th International Symposium on Solar Sailing*. 2017: Kyoto, Japan.

[12] Farrés, A., et al., *Periodic Motion for an Imperfect Solar Sail Near an Asteroid*, in *The 3rd International Symposium on Solar Sailing*. 2014: Glasgow, UK.

[13] Farrés, A., À. Jorba, and J. Mondelo, *Orbital Dynamics for a Non-perfectly Reflective Solar Sail Close to an Asteroid*, in *The 2nd IAA Conference on Dynamics and Control of Space Systems*. 2014: Rome, Italy.

[14] Zeng, X., et al., *Solar Sail Body-Fixed Hovering over Elongated Asteroids.* Journal of Guidance, Control, and Dynamics, 2016. **39**(6): p. 1223-1231.

[15] Moore, I. and M. Ceriotti, *Solar sails for perturbation relief: Application to asteroids.* Advances in Space Research, 2021. **67**(9): p. 3027-3044.

[16] Furfaro, R., *Hovering in Asteroid Dynamical Environments Using Higher-Order Sliding Control.* Journal of Guidance, Control, and Dynamics, 2015. **38**: p. 263-279.

[17] Batista Negri, R. and A.F.B.A. Prado, *Autonomous and Robust Orbit-Keeping for Small-Body Missions.* Journal of Guidance, Control, and Dynamics, 2022. **45**(3): p. 587-598.

[18] Werner, R.A. and D.J. Scheeres, *Exterior Gravitation of a Polyhedron Derived and Compared with Harmonic and Mascon Gravitation Representations of Asteroid 4769 Castalia.* Celestial Mechanics and Dynamical Astronomy, 1997. **65**: p. 313-344.

[19] McInnes, C., *Solar Sailing: Technology, Dynamics and Mission Applications*. 1999, Chichester, England, UK: Springer Praxis.

[20] McInnes, C. and J. Simmons, *Solar Sail Halo Orbits II: Geocentric Case.* Journal of Spacecraft and Rockets, 1992. **29**: p. 472-479.

[21] Bookless, J. and C.R. McInnes, *Dynamics and Control of Displaced Periodic Orbits Using Solar Sail Propulsion.* Journal of Guidance, Control, and Dynamics, 2006. **29**: p. 527-537.

[22] Chen, Y., et al. *Adaptive Second-order Sliding Mode Station-keeping Control for Solar Sail Spacecraft on Displaced Orbit*. in *The 38th Chinese Control Conference*. 2019. Guangzhou, China.

[23] Dachwald, B., W. Seboldt, and M.e.a. Macdonald, *Potential Solar Sail Degradation Effects on Trajectory and Attitude Control*, in *AIAA Guidance, Navigation and Control Conference and Exhibit*. 2005: San Francisco, California.

[24] Farquhar, R., J. Kawaguchi, and C.T.e.a. Russell, *Spacecraft Exploration of Asteroids: The 2001 Perspective*, in *Asteroids III*, W.F. Bottke Jr., et al., Editors. 2002, University of Arizona Press. p. 367-376.

Uncertainty quantification for solar sails in the near-Earth environment

Juan GARCIA-BONILLA[1,*], Livio CARZANA[1], Jeannette HEILIGERS[1]

[a] *Faculty of Aerospace Engineering, Delft University of Technology, Delft, the Netherlands*

Abstract

This paper addresses the significance of uncertainty quantification in solar-sail missions, focusing on the uncertainties associated with the sail's optical coefficients, structural deformation, and attitude profiles for missions in the Earth environment. Due to the relatively low technological maturity of solar-sailing systems, understanding and quantifying uncertainties is crucial for mission success and reliability. This paper employs the Gauss von Mises method for uncertainty propagation and stochastic integration of Ornstein-Uhlenbeck processes, which proved to be robust methodologies for quantifying and modelling uncertainties. The results show a significant impact of uncertainties in the optical coefficients on mission performance, exemplified by a 3-σ uncertainty of 7.5% on the increase in semi-major axis achieved during orbit raising maneuvers using the coefficient uncertainties of the NEA Scout mission. As another example, the analysis on attitude uncertainty demonstrates a 3% lower mean performance in terms of altitude gain compared to ideal control profiles. The research furthermore underscores the effectiveness of the Gauss von Mises method, offering great computational efficiency compared to Monte Carlo simulations. These findings highlight the necessity of considering uncertainty in solar-sail missions and provide valuable insights for improved mission planning, risk assessment, and decision-making.

Keywords: Solar sailing, near-Earth environment, Uncertainty quantification, Gauss von Mises, Stochastic Differential Equation

1. Introduction

Solar sailing has revolutionized space exploration by harnessing the pressure of sunlight to propel spacecraft, offering increased maneuverability and reduced fuel requirements compared to conventional propulsion systems [1]. However, the success and reliability of solar-sail missions depend on a comprehensive understanding and quantification of inherent uncertainties, considering the relatively low technological maturity of these systems.

Quantifying uncertainties is essential for risk mitigation, mission optimization, and informed decision-making. Moreover, it enables the development of robust control strategies capable of addressing unexpected variations and disturbances during operation.

Recent publications have highlighted the significance of uncertainty quantification in solar-sail missions. For instance, Yamaguchi et al. discussed the challenges of developing precise solar-sail force models on the ground and proposed estimation strategies based on orbital data [2]. Eldad et al. developed robust attitude control algorithms that account for uncertainties in sail deformation, moment of inertia, and effective reflectivity [3]. Similarly, Nicolai et al. employed a polynomial chaos procedure to investigate the impact of uncertain solar-sail optical coefficients and solar irradiance on heliocentric trajectories [4]. Oguri et al. explored robust trajectory design for the NEA Scout mission, considering uncertainties in solar pressure acceleration [5].

This paper, on the other hand, focuses on the uncertainties associated with the solar-sail optical coefficients, structural deformation, and non-ideal attitude profiles for missions in the Earth environment. Quantifying optical coefficients, which are influenced by complex phenomena like wrinkling, presents challenges; extensive testing campaigns for the NEA Scout solar-sail revealed significant uncertainties [6]. Modeling sail deformation, on the other hand, remains uncertain due to the lack of experimental data. Finally, mission data from, for example the LightSail-2 mission, has demonstrated the difficulty of adhering to predefined control profiles, resulting in notable attitude deviations [7].

As such, this paper provides the first insights into the effect of uncertainty in the solar-sail optical coefficients,

*Corresponding author, juan@garciabonilla.com

structural deformation, and attitude control in the Earth environment. Moreover, it does so by utilizing novel techniques in the field, such as the computationally-inexpensive Gauss von Mises uncertainty propagation method or the use of Ornstein-Uhlenbeck processes to model attitude uncertainty [8][9].

While the problem of uncertainty quantification is applicable to various scenarios and sources of uncertainty, we delve into a specific case study to shed light on the broader issue of uncertainty propagation for solar sails within the Earth environment. The selected case study draws inspiration from the ACS3 mission, utilizing its sail loading parameter and initial Dawn-Dusk Sun-Synchronous Orbit [10].

Following this brief introduction, the paper proceeds with two sections on the methodology employed, introducing the relevant dynamical models, studied uncertainties, and uncertainty propagation methods. Subsequently, the case study is further discussed and selected results of the uncertainty analysis are presented, followed by a concise conclusion.

2. Dynamical models

In this section, the solar-sail dynamical model and attitude control strategy employed in the remainder of the paper are presented.

2.1. Solar sail dynamics

The dynamics of the solar sail are expressed in the J2000 Earth-centered inertial reference frame through the following equation of motion:

$$\frac{d\mathbf{v}}{dt} = \mathbf{a}_{\text{total}} = \frac{\text{GM}_\text{E}}{r^3_{E\to s}}\vec{r}_{E\to s} + \mathbf{a}_{\text{J2}} + \mathbf{a}_{\text{SRP}} + \mathbf{a}_{\text{aero}} \quad (1)$$

where $\text{GM}_\text{E} = 398600.4415\text{km}^3/\text{s}^2$ is the Earth's gravitational parameter [11], $\vec{r}_{E\to s}$ is the position vector of the sail, $\mathbf{a}_{\text{J2}}$ is the acceleration due the J_2 coefficient perturbation, $\mathbf{a}_{\text{SRP}}$ is the Solar Radiation Pressure (SRP) acceleration, and $\mathbf{a}_{\text{aero}}$ is the acceleration due to aerodynamic forces. For this first investigation into uncertainty quantification in the solar-sail near-Earth orbital dynamics, smaller perturbations including planetary radiation pressure, third-body effects, and higher-order Earth gravity terms are ignored.

The J_2 acceleration, $\mathbf{a}_{\text{J2}}$, is modeled as per Eq. 20.6 in Ref. [11], taking values for the reference radius and J_2 as published in the GGM03 model [12].

The SRP acceleration, $\mathbf{a}_{\text{SRP}}$, is modelled through the Generalized Sail Model (GSM) developed by Rios-Reyes and Scheeres [13]. This method can compute the SRP force of non-ideal, non-flat solar sails at low computational costs under the following assumptions: the shape is fixed over time, the same side of the sail is always illuminated, and there is no self-shadowing.

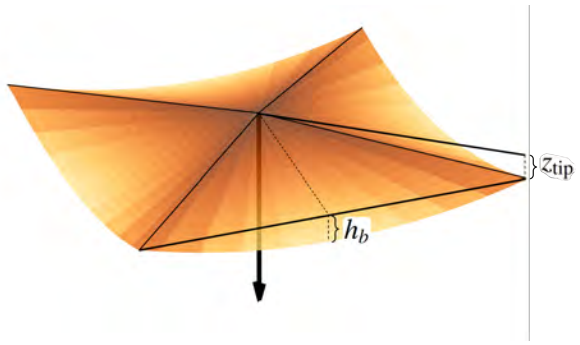

Figure 1: Four-quadrant, square solar-sail model with billowing and boom bending. Lighter colors are further apart from the nominal plane of the sail.

In this paper, the GSM is used to model a square-shaped solar sail subject to constant deformations. More specifically, the sail is modeled as a four-quadrant billowed surface with bent linear booms along the diagonals, as displayed in Fig. 1.

The sail billowing and bending are characterized by two parameters, the maximum billow height ($h_b > 0$) and the boom tip displacement ($z_{\text{tip}} > 0$), see Fig. 1. The maximum billow height represents the largest distance between the sail surface and the line connecting the boom tips. On the other hand, the boom tip displacement measures the distance between the sail nominal plane and the boom tips, assuming that the boom deflection is linear from root to tip.

Apart from the sail shape parameters, the SRP acceleration also depends on the sail's optical properties, which are described by the reflectivity ρ, specularity s, the Lambertian coefficients of the front and back sides of the sail, B_f and B_b, respectively, and emissivity of the front and back sides of the sail, ε_f and ε_b, respectively. For further insights into these optical coefficients, the reader is referred to Ref. [1].

The aerodynamic acceleration, $\mathbf{a}_{\text{aero}}$, is obtained by assuming a non-rotating flat sail in hyperthermal free-molecular flow. This model was considered because, given the low angular rate of the sail compared to its velocity, the non-rotating sail assumption is justified. Moreover, given that aerodynamic forces are an order of magnitude weaker than solar radiation pressure, the sail's deformation is considered negligible when computing the aerodynamic force.

Furthermore, the assumption of a hyperthermal free-molecular flow has been used often in the literature to

describe the dynamics of air particles relative to a sailcraft in Earth orbit [14][15]. It assumes the random thermal motion of the air molecules to be much slower than the velocity of the spacecraft and is valid for large Knudsen numbers, meaning that the fluid-continuum assumption of the air is no longer applicable [16].

Section 2.3.2 of Ref. [16] contains the relevant equations to compute the aerodynamic forces, using the following parameters as defined in this reference: $V_w/V = 0.05$, and $\sigma_t = \sigma_n = 0.8$. Moreover, this paper assumes an exponential atmosphere with reference radius $R_E = 6378.1363$ km, scale height $H = 7.02503$ km, and reference density $\rho_0 = 1.225$ kg/m^3.

2.2. Attitude control

Both the SRP acceleration and aerodynamic forces strongly depend on the attitude of the sail, and thus attitude control is the primary control strategy for solar-sailcraft. This paper considers ideal locally optimal steering laws for planet-centered solar-sailing, as described by Macdonald and McInnes [17][18].

3. Uncertainty

This section encompasses the modeling of uncertainties, their propagation, and their impact on a specific figure of merit.

3.1. Constant random value uncertainties

This study considers uncertainty due to unknown sail deformation parameters (h_b, z_{tip}) and optical coefficients (ρ, s, B_f, B_b, ε_f, ε_b). These values are assumed to be normally distributed random variables that remain constant during propagation.

The uncertainty in these input parameters is propagated into the uncertainty in some figure of merit through Monte Carlo (MC) simulations and the Gauss von Mises (GVM) method [8]. The GVM method is an uncertainty propagation method that requires only between 10 to 20 sample propagations to produce estimates of the figure of merit distribution, compared to the thousands of propagations that the MC method might require to do the same.

This paper presents results obtained using both the GVM and MC methods to demonstrate whether the GVM method is capable of accurately capturing output distributions at the benefit of being orders of magnitude faster than MC. As such, the MC method serves as the validation mechanism for the results shown in this paper.

3.2. Stochastic process uncertainties

In order to consider uncertainties in the attitude control of the sail over the mission profile, some simulations presented in this paper also consider an attitude offset with respect to the nominal attitude profile (i.e., the ideal locally optimal steering laws). This attitude offset is used to represent more realistic attitude profiles, as found in solar-sail missions with imperfect GNC systems [7].

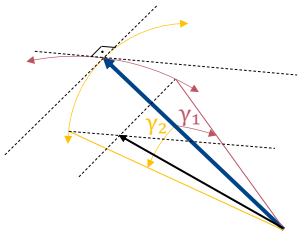

Figure 2: Sketch of the offset sail normal (shown as a black arrow) and the reference sail normal (blue arrow). The angular offsets γ_1 and γ_2 are shown in red and yellow respectively.

This attitude offset is defined by two parameters (γ_1 and γ_2) which represent angular displacements along two arbitrarily chosen perpendicular directions with respect to the sail normal, see Fig. 2.

The angular offsets γ_1 and γ_2 vary randomly in time and are modelled as independent and identical stochastic Ornstein-Uhlenbeck processes [9]. These can be regarded as variations of "random walks" (Wiener) processes, in which there is a tendency to drift towards the mean value $\gamma_1 = \gamma_2 = 0$. These processes are defined by the following Stochastic Differential Equation [9]:

$$d\gamma_i = -\theta\gamma_i dt + \sigma d\beta(t) \tag{2}$$

where θ and σ are the characteristic parameters of the Ornstein-Uhlenbeck process, and $\beta(t)$ is a one dimensional Brownian motion process. An important characteristic of these processes is that they have a bounded standard deviation, given by $\sigma_{\text{st}} = \sigma/\sqrt{2\theta}$.

Because the angular offsets γ_1 and γ_2 impact the direction of the sail normal and, therefore, the entire solar-sail dynamics, Eqs. 1 and 2 are coupled. Consequently, they ought to be propagated in parallel:

$$d\begin{bmatrix} \mathbf{v} \\ \gamma_1 \\ \gamma_2 \end{bmatrix} = \begin{bmatrix} \mathbf{a}_{\text{total}} \\ -\theta\gamma_1 \\ -\theta\gamma_2 \end{bmatrix} dt + \begin{bmatrix} \mathbf{0} \\ \sigma_{\text{st}}\sqrt{2\theta} \\ \sigma_{\text{st}}\sqrt{2\theta} \end{bmatrix} d\beta(t) \tag{3}$$

Moreover, due to the presence of Stochastic Differential Equations in the above system of equations, propagation must be performed using a stochastic integrator. In this paper, the weak third-order, additive-noise

stochastic integrator by Debrabant is used with a time step of 10 seconds [19].

Uncertainty due to stochastic processes cannot be modelled through the GVM method, as this method is only apt for modelling random but constant variables. Thus, only the MC method is used to generate results for the uncertainty due to an attitude offset.

4. Results

This section introduces the test case used to evaluate and validate the methodology presented in the previous sections, as well as to obtain insights into the wider problem of uncertainty in solar-sail missions in the Earth environment. Subsequently, the results of the uncertainty propagation analysis due to the constant random value uncertainties (deformation and optical parameters) and stochastic process uncertainties (attitude offset) are presented.

4.1. Test case

The following test case is inspired by the ACS3 mission, considering a similar initial Dawn-Dusk Sun-Synchronous orbit $[a, e, i, \Omega, \omega, f]_0 = [7071\ \text{km}, 0, 98.16\ \text{deg}, 0\ \text{deg}, 90\ \text{deg}, 0\ \text{deg}]$ [10]. A locally optimal steering law for the sail is employed that maximizes the rate of change of the semi-major axis (SMA) [17][18].

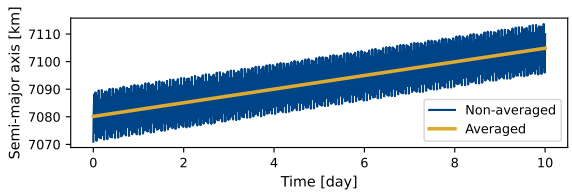

Figure 3: Evolution of the semi-major axis of the nominal test case (without uncertainties).

Figure 3 displays the increase in SMA for the nominal test case. The inclusion of J_2 perturbations introduces a strong oscillatory behaviour, as seen in the "Non-averaged" line. Because this hampers analysis, a locally averaged SMA is considered, which removes these oscillations and provides a more accurate depiction of the SMA increase due to the solar sail. Note that the averaged SMA increase is linear.

In this paper, the figure of merit for analysis is the SMA increase after some days of orbit raising maneuvers (Δa). This value is defined as the difference between the averaged SMA at some time t and the same quantity at time t_0. Finally, note that whenever reference values of the SMA increase Δa_{ref} are used, these values refer to the SMA gain obtained in the nominal case (as presented in Fig. 3).

Table 1: Nominal value and standard deviations of the input uncertainties considered in the studied test case. Note that $\sigma_2 = 2\sigma_1$.

	Nominal (Mean)	σ_1	σ_2
σ_{load} [kg/m^2]	0.20266	-	-
l [m]	7.0	-	-
ρ [-]	0.910	0.005	0.010
s [-]	0.890	0.045	0.090
B_f [-]	0.79	0.05	0.10
B_b [-]	0.67	0.05	0.10
ε_f [-]	0.025	0.005	0.010
ε_b [-]	0.270	0.005	0.010
h_b [m]	0.100	0.025	0.0430
z_{tip} [m]	0.3500	0.0875	0.175

Table 1 shows the the nominal parameters that define the solar sail considered in this paper, as well as the associated uncertainties that will be studied in Section 4.2.1. The sail's loading parameter, σ_{load}, which is the ratio between the sail's mass to its area, and its boom length, l, are obtained from data relevant to the Advanced Composite Solar Sail (ACS3)[1]. The optical coefficient data is obtained from the NEA Scout solar sail model [6]. Finally, deformation parameters have been chosen based on the limited data presented by Greschik and Mikulas, and their standard deviations were chosen conservatively large: a fourth and half of the nominal value for σ_1 and σ_2 respectively [20].

Propagation is done for either 1, 5, or 10 days, depending on the analysis. 10,000 samples are used for every Monte Carlo simulation presented in this paper. When no stochastic process have to be integrated, an 8th order Runge-Kutta integrator with 64 seconds time step is used.

4.2. Constant random value uncertainties

This section covers selected results from an analysis on the effect of constant random value uncertainties on the figure of merit uncertainty. First, different uncertainties are studied independently. Subsequently, a detailed analysis of the uncertainty due to specularity is presented. Finally, a coupled analysis of all uncertainties is discussed.

4.2.1. Uncertainty due to uncoupled uncertainties

This section presents the uncertainty in SMA increase after 1 day of maneuvers due the input uncertainties displayed in Table 1. Each source of uncertainty is studied

[1]Data taken from communication with the ACS3 team at NASA's Langley Research Center.

independently, and two standard deviations are considered for each input uncertainty (σ_1 and σ_2).

Table 2: Normalized semi-major axis gain standard deviation obtained after 1 day of maneuvers for different input uncertainties and according to the Monte Carlo and Gauss von Mises simulations. Columns labeled "Diff" show the difference between the Gauss von Mises and Monte Carlo results. Values for σ_1 and σ_2 are provided in Table 1.

	$\sigma_{\Delta a}/\Delta a_{\text{ref}}$ [%]					
	σ_1			σ_2		
	MC	GVM	Diff	MC	GVM	Diff
ρ	0.79	0.79	-0.001	1.56	1.57	0.010
s	2.55	2.57	0.019	4.25	4.44	0.190
B_f	0.41	0.41	-0.003	0.78	0.82	0.040
B_b	0.31	0.31	0.001	0.62	0.63	0.004
ε_f	0.16	0.16	0.001	0.31	0.31	0.007
ε_b	0.01	0.02	0.005	0.03	0.03	0.003
h_b	0.04	0.05	0.002	0.09	0.11	0.028
z_{tip}	0.20	0.21	0.002	0.46	0.46	0.004

Table 2 shows the ratio of the standard deviation and reference value of the SMA gain caused by each input uncertainty, as obtained from the Monte Carlo and Gauss von Mises methods. A value of 2.5% in this ratio, for example, means that for a nominal SMA gain of 10 km, the uncertain SMA increase would have a 750 m 3σ uncertainty.

It is apparent that the GVM method can provide accurate estimates of the true standard deviations (obtained from MC simulations) independently of the input uncertainty and its magnitude, at a computational cost that is orders of magnitude lower than Monte Carlo simulations. In most cases, the GVM method produces slightly larger (more conservative) standard deviations than MC.

Table 2 additionally provides a clear hierarchy of the most impactful input uncertainties. The uncertainty in specularity has the strongest effect, followed by the uncertainty in reflectivity. On the other hand, the uncertainty due to the emissivity coefficients and the deformation parameters is considerably smaller. As such, it is of interest to evaluate whether the effects of the latter uncertainties are negligible compared to the effects of the former in a coupled analysis, which is presented in Section 4.2.3.

4.2.2. Detailed analysis of uncertain specularity

The previous section provided a first order characterization of the impact of every input uncertainty on the figure of merit. This section, in turn, provides a deeper exploration of the figure of merit distribution due to a single uncertain input: the specularity.

Figure 4 shows the distribution of the normalized relative SMA gain with respect to the reference SMA gain after 10 days of maneuvers for three specularity standard deviations, σ_s.

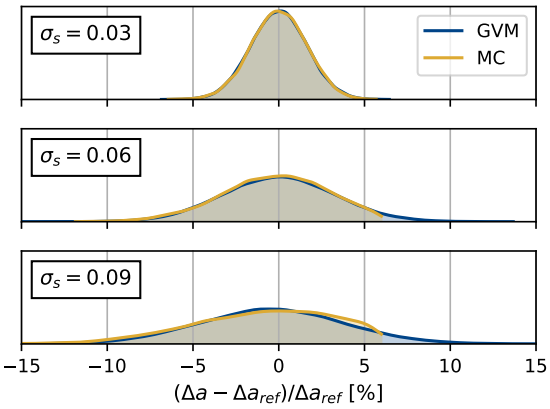

Figure 4: Distribution of the semi-major axis increase after 10 days of maneuvers according to Monte Carlo and Gauss von Mises simulations. Results are presented for three different specularity standard deviations, σ_s.

The normalized relative SMA gain measures how much the uncertain case underperforms or overperforms with respect to the nominal case. For instance, a -5% relative SMA gain when the nominal gain is 10 km means that the uncertain case obtained a SMA gain of only 9.5 km. Positive relative SMA gains, on the other hand, produce SMA gains above the nominal case, which can happen for specularities that are higher than the nominal specularity, and thus are closer to an ideal solar sail and are thus more performant.

Figure 4 also demonstrates that the SMA gain distribution closely follows a normal distribution. Moreover, the Gauss von Mises method is capable of accurately capturing the same behaviour as the more computationally expensive Monte Carlo simulations, independently of the standard deviation of the specularity.

Additionally, Figure 4 reveals that the results for the GVM method extend beyond those for the MC simulation for positive relative SMA gains. This means that the truncation behaviour that the MC method exhibits is not captured by the GVM method, which showcases how the latter method can miss certain details about the real distribution.

Figure 5 shows how the SMA distribution remains normal during propagation, with the results from the GVM method once again closely agreeing with the results from MC simulations. Interestingly, the spread of the distributions remains similar for the three times presented. This suggests that the standard deviation of the SMA gain $\sigma_{\Delta a}$ grows like the reference value Δa_{ref}: linearly.

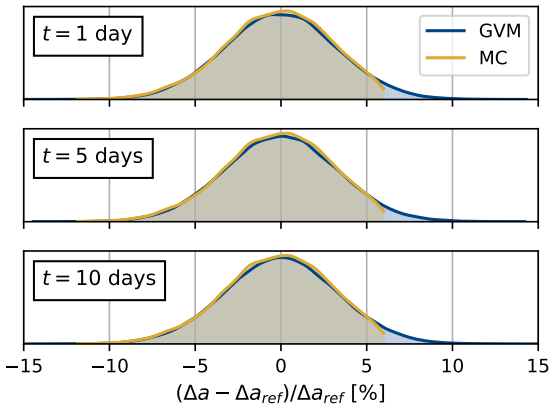

Figure 5: Distribution of the semi-major axis increase due to a specularity standard deviation of $\sigma_s = 0.06$ according to a Monte Carlo and Gauss von Mises simulation. Results are presented at three different propagation times (after 1 day, 5 days, and 10 days of maneuvers.)

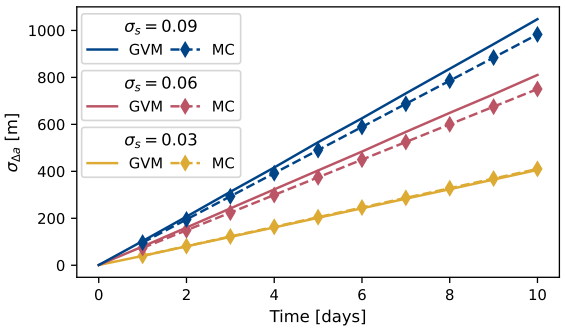

Figure 6: Evolution in time of the standard deviation of the increase in semi-major axis for three different specularity standard deviations, σ_s. Data was obtained through Monte Carlo and Gauss von Mises simulations.

Figure 6 confirms that growth of the standard deviation of the SMA gain is linear in time; if the standard deviation after 1 day of maneuvers is 100 m, for instance, then one could expect a standard deviation of 1 km after 10 days of maneuvers. As shown in the figure, the slope of these trends is driven by the standard deviation of the input uncertainty, the specularity. Higher input uncertainties lead to faster growing SMA uncertainties. This figure also shows how the GVM method tends to overestimate the output standard deviation, an effect that is more pronounced the greater the input standard deviation is.

4.2.3. Uncertainty due to coupled uncertainties

Sections 4.2.1 and 4.2.2 have dealt with the effects of individual input uncertainties on the uncertainty of the SMA increase. This section discusses the effects of multiple input uncertainties simultaneously on this same figure of merit. The results appear in Figure 7.

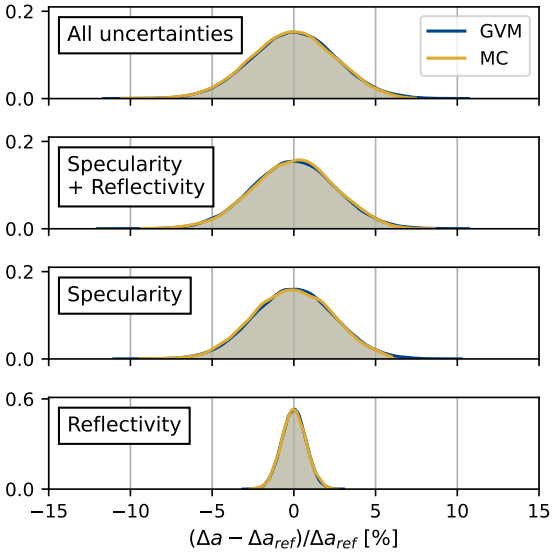

Figure 7: Distribution of the semi-major axis increase after 10 days of maneuvers according to Monte Carlo and Gauss von Mises simulations. Results are presented for different sets of input uncertainties.

Four sets of uncertainties are considered: all uncertainties shown in Table 1, only specularity and reflectivity, only specularity, and only reflectivity. All input uncertainties are normally distributed with standard deviations as shown in column σ_1 of Table 1. As seen in the figure, the distribution for "Specualarity + Reflectivity" largely resembles the distribution when considering all uncertainties. Moreover, once again, the results from the Gauss von Mises method seem to agree with those of the Monte Carlo simulations.

Table 3: Standard deviation of the distributions shown in Fig. 7.

	$\sigma_{\Delta a}/\Delta a_{\text{ref}}$ [%]	
	GVM	MC
All uncertainties	2.644	2.575
Specularity + Reflectivity	2.586	2.518
Specularity	2.471	2.408
Reflectivity	0.759	0.761

Table 3 provides further insight into the spread of the distributions for the four sets of input uncertainties. As expected, the standard deviation is larger the more uncertain parameters are considered. However, this table also shows that the specularity and reflectivity are very clearly dominant, with other uncertainties being essentially negligible. This demonstrates that analysis effort might be saved if the most dominant input uncertain-

ties (or, alternatively, the negligible ones) are identified early on.

It is important to highlight that these results indicate a 7.5% 3σ uncertainty in SMA gain due to the optical coefficient uncertainties in the NEA Scout solar-sail model. For instance, if the nominal SMA increase were 10 km, this would translate to a 3σ uncertainty of 750 m in the SMA increase. Such uncertainty could potentially have a significant and detrimental effect on mission performance.

4.3. Stochastic process uncertainties

Previous sections dealt with constant random value uncertainties, where certain input parameters, such as the reflectivity or the billow of the sail, were random but fixed during propagation. This section shows results for the uncertainty caused by considering a randomly evolving offset on the nominal attitude profile.

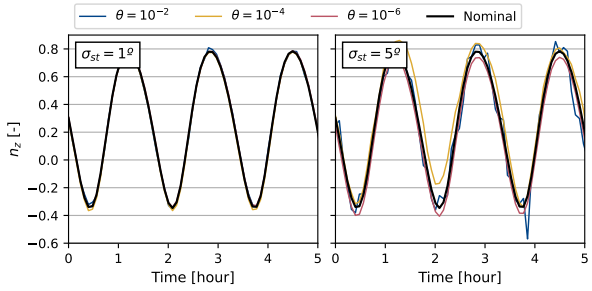

Figure 8: Evolution of the z component of the sail normal direction in the J2000 Earth-centered inertial reference frame for different values of σ_{st} and θ for the first hours of propagation of the test case. The "Nominal" line indicates the locally optimal direction (without random offset).

To gain insights into the impact of the Ornstein-Uhlenbeck parameters θ and σ_{st} (see Section 3.2) on the sail's attitude, refer to Figure 8. This figure illustrates the evolution of the z component of the sail normal direction for six different combinations of the Ornstein-Uhlenbeck parameters. By comparing these examples with the nominal evolution for this parameter, one can better understand the influence of θ and σ_{st} on the sail's behavior.

The effect of the stationary standard deviation σ_{st} is relatively easy to understand: higher values of this parameter mean that the offset direction will generally be further away from the reference direction. The θ parameter, on the other hand, influences how "fast" the offset changes. As seen for the lines corresponding to $\theta = 10^{-2}$, the behaviour is clearly "noisy", with the offset rapidly moving above and below the reference. Instead, for $\theta = 10^{-6}$, the offset evolves so slowly that it seems constant during the 10-hour window plotted in Fig. 8. The line for $\theta = 10^{-4}$ represents a middle point: it is not as "noisy", but one can see it move with respect to the reference.

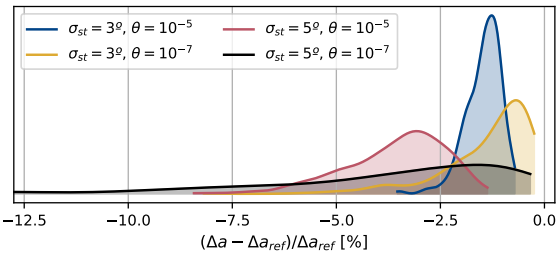

Figure 9: Distribution of the semi-major axis increase after 10 days of maneuvers for different Ornstein-Uhlenbeck parameters θ and σ_{st}.

Figure 9 shows how different values of the Ornstein-Uhlenbeck parameters θ and σ_{st} affect both the mean and standard deviation of the output distributions. This is in contrast to previous analysis showcased in this paper, where the mean of the distribution always remained equal to the nominal performance. As such, this section discusses the behaviour of both the mean $\mu_{\Delta a}$ and standard deviation $\sigma_{\Delta a}$ as a function of the Ornstein-Uhlenbeck parameters θ and σ_{st}.

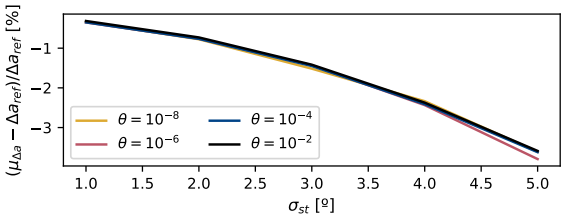

Figure 10: Mean semi-major axis increase after 10 days of maneuvers as a function of the Ornstein-Uhlenbeck parameter σ_{st} for different values of θ.

Figure 10 reveals the strong relationship between the stationary standard deviation σ_{st} and the mean gain in SMA $\mu_{\Delta a}$. In contrast, the parameter θ seems to have a negligible effect on this metric. As such, mean performance loss due to uncertain attitude is mainly driven by the stationary standard deviation of the attitude with respect to the optimal control profile. Note that for all cases studied, the mean performance was below the nominal performance $\mu_{\Delta a} < \Delta a_{\text{ref}}$. This indicates that neglecting to model attitude uncertainty will always lead to overestimated performance expectations.

On the other hand, Fig. 11 shows that both parameters θ and σ_{st} affect the spread of the SMA gain distribution. Perhaps unsurprisingly, higher values of the standard deviation of the attitude uncertainty σ_{st} lead to

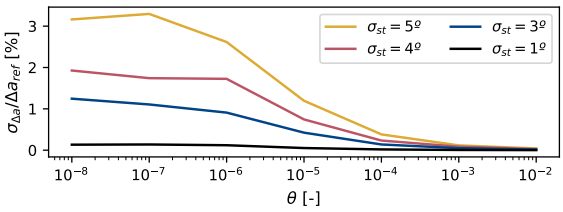

Figure 11: Standard deviation of the semi-major axis increase after 10 days of maneuvers as a function of the Ornstein-Uhlenbeck parameter θ for different values of σ_{st}.

higher values of the standard deviation of the figure of merit $\sigma_{\Delta a}$.

In contrast, when considering smaller values of θ, there is a notable increase in the standard deviation of the relative SMA gain. These smaller values of θ correspond to attitude offsets that evolve at a significantly slower pace, eventually reaching a point where they remain relatively constant for extremely small values of θ. Consequently, the attitude profiles across different propagations exhibit substantial dissimilarities, resulting in a higher standard deviation in the relative SMA gain. Conversely, higher values of θ yield rapidly changing attitude offsets. As a result, individual propagations exhibit comparable attitude profiles, leading to a reduced standard deviation in the relative increase of SMA.

5. Conclusion

In conclusion, this paper has shed light on the significance of uncertainty in solar-sail mission design. The findings underscore the substantial impact of uncertainty in optical coefficients on mission performance, as demonstrated by the NEA Scout's sail coefficients, which resulted in a notable 3-σ mission performance uncertainty of 7.5%. Notably, specularity uncertainty played a the largest role in this performance uncertainty.

Furthermore, the study on attitude uncertainty revealed not only its impact on mission performance uncertainty, but also highlighted that assuming an ideal control profile may lead to overestimated performance expectations. By incorporating the Ornstein-Uhlenbeck process with tunable parameters, different types of noise in attitude profiles were modeled, resulting in performance distributions with different means and spread.

The Gauss von Mises method proved to be an efficient and effective uncertainty propagation technique, demonstrating its capability at the benefit of a considerably lower computational cost compared to Monte Carlo simulations.

Future research will expand upon the analysis presented in this study by considering different test cases. This includes exploring other initial orbits, such as orbits with shadowing effects, as well as investigating alternative control strategies, such as inclination change maneuvers. Such endeavors will further enhance our understanding of uncertainty in solar-sail mission design and contribute to the development of more robust and reliable mission planning strategies.

References

[1] Colin McInnes. Solar Sailing Technology, Dynamics and Mission Applications. Technical report, 1999.

[2] Tomohiro YAMAGUCHI et al. Trajectory Analysis of Small Solar Sail Demonstration Spacecraft IKAROS Considering the Uncertainty of Solar Radiation Pressure. *TRANSACTIONS OF THE JAPAN SOCIETY FOR AERONAUTICAL AND SPACE SCIENCES, AEROSPACE TECHNOLOGY JAPAN*, 8, 2010. ISSN 1884-0485.

[3] Ofer Eldad, E. Glenn Lightsey, and Christian Claudel. Minimum-time attitude control of deformable solar sails with model uncertainty. *Journal of Spacecraft and Rockets*, 54(4):863–870, 6 2017. ISSN 15336794.

[4] Lorenzo Niccolai et al. Effects of optical parameter measurement uncertainties and solar irradiance fluctuations on solar sailing. *Advances in Space Research*, 67(9):2784–2794, 5 2021. ISSN 18791948.

[5] Kenshiro Oguri, Gregory Lantoine, and Theodore H Sweetser. Robust Solar Sail Trajectory Design under Uncertainty with Application to NEA Scout Mission. Technical report, 2021.

[6] Andrew Heaton, Naeem Ahmad, and Kyle Miller. Near Earth Asteroid Scout Thrust and Torque Model. In *The 4th International Symposium on Solar Sailing*, 2017.

[7] Justin R. Mansell et al. Orbit and attitude performance of the lightsail 2 solar sail spacecraft. *AIAA Scitech 2020 Forum*, 2020. doi: 10.2514/6.2020-2177.

[8] Joshua T. Horwood and Aubrey B. Poore. Gauss von Mises distribution for improved uncertainty realism in space situational awareness. *SIAM-ASA Journal on Uncertainty Quantification*, 2(1), 2014. ISSN 21662525.

[9] G. E. Uhlenbeck and L. S. Ornstein. On the Theory of the Brownian Motion. *Physical Review*, 36(5):823, 9 1930. ISSN 0031899X.

[10] W. Keats Wilkie et al. An Overview of the NASA Advanced Composite Solar Sail (ACS3) Technology Demonstration Project. 2021.

[11] Karel F Wakker. *FUNDAMENTALS OF ASTRODYNAMICS*. 2015. ISBN 9789461864192. URL `http://repository.tudelft.nl.`

[12] B. Tapley et al. The GGM03 Mean Earth Gravity Model from GRACE. *AGUFM*, 2007.

[13] L. Rios-Reyes and D. J. Scheeres. Trajectory control for general solar sails. In *AIAA Guidance, Navigation and Control Conference and Exhibit*. American Institute of Aeronautics and Astronautics Inc., 2008. ISBN 9781563479458. doi: 10.2514/6.2008-6830.

[14] Livio Carzana, Pieter Visser, and Jeannette Heiligers. A New Model for the Planetary Radiation Pressure Acceleration for Solar Sails. 2022.

[15] Giovanni Mengali and Alessandro A. Quarta. Near-optimal solar-sail orbit-raising from low earth orbit. *Journal of Spacecraft and Rockets*, 42(5):954–958, 2005. ISSN 15336794. doi: 10.2514/1.14184.

[16] Joel A. Storch. Aerodynamic Disturbances on Rapidly Rotating Spacecraft in Free-Molecular Flow. In *Engineering Construction and Operations in Challenging Environments Earth and Space 2004: Proceedings of the Ninth Biennial ASCE Aerospace Division International Conference*, pages 429–436. American Society of Civil Engineers (ASCE), 2004. ISBN 0784407223. doi: 10.1061/40722(153)60.

[17] Malcolm MacDonald and Colin R McInnes. Realistic Earth Escape Strategies for Solar Sailing. *JOURNAL OF GUIDANCE, CONTROL, AND DYNAMICS*, 28(2), 4 2005. doi: 10.2514/1.5165.

[18] Malcolm MacDonald and Colin R McInnes. Analytical Control Laws for Planet-Centered Solar Sailing. *JOURNAL OF GUIDANCE, CONTROL, AND DYNAMICS*, 28(5), 10 2005. doi: 10.2514/1.11400.

[19] Kristian Debrabant. Runge-Kutta methods for third order weak approximation of SDEs with multidimensional additive noise. 2010.

[20] G Greschik and M M Mikulas. Design Study of a Square Solar Sail Architecture. *JOURNAL OF SPACECRAFT AND ROCKETS*, 39(5), 2002. doi: 10.2514/2.3886.

Optimal deep-space heliocentric transfers with an electric sail and an electric thruster

Lorenzo NICCOLAI[a,*]

[a]*Department of Civil and Industrial Engineering, University of Pisa, Pisa, Italy*

Abstract

An electric solar wind sail is a propellantless propulsive system that generates thrust by exploiting the interaction of solar wind ions and one or more charged tethers. Assuming a realistic scenario in which the sail is composed by a limited number of tethers, the generated propulsive acceleration vector has a small magnitude, and it is constrained to lie in a cone centered on the outward radial direction with half-angle equal to about 20 degrees. In order to overcome this issue, a possible strategy consists in combining the sail with an electric thruster, which should provide a small thrust steerable around the circumferential direction. The effectiveness of such a combination is thoroughly analyzed in this work. Transfer trajectories are obtained as outputs of a multi-objective optimization, in which a suitable linear function of the flight time and the propellant consumption is minimized, considering different relative weights of the two competing requirements. Two exemplary case studies, consisting of Earth-Mars and Earth-Venus circle-to-circle transfers, are presented to show the effectiveness of the proposed strategy.

Keywords: electric solar wind sail, electric propulsion, hybrid propulsion, multi-objective trajectory optimization

1. Introduction

An electric solar wind sail (E-sail) consists of a number of charged tethers kept at a high positive voltage that interact with the solar wind ions to generate a propulsive acceleration [1]. In its originally-proposed configuration [2], an E-sail should be a large structure, with dimensions on the order of tens of kilometers and composed by hundreds to thousands tethers. However, due to the difficulty of deploying an controlling a huge tether structure in deep space, recent works suggest that near-term E-sail missions should involve small satellites with a limited number of spin-stabilized thrust-generating tethers [3]. Accordingly, the expected magnitude of the propulsive acceleration is small. Moreover, a recent E-sail thrust model suggests that the thrust vector is constrained within a cone with half-angle lesser than 20 degrees centered along the outwards radial direction [4], thus limiting the E-sail capability of generating a significant circumferential thrust component.

A possible strategy to overcome the aforementioned issues consists of combining with a small E-sail with one or more high specific impulse electric thrusters. This strategy resembles the hybrid sail concept, which can be traced back to 2002 [5], and consists of a combination of a solar sail and an electric thruster. Possible applications of hybrid sails have been deeply investigated since, considering different heliocentric [6, 7, 8] and geocentric [9, 10] scenarios and ultimately leading to the design of a solar power sail to propel JAXA's OKEANOS mission (eventually not financed) towards a Jupiter Trojan asteroid [11, 12].

Like the hybrid sail concept, the combination of an E-sail and an electric thruster could significantly increase their effectiveness. The compatibility of an E-sail tether grid and an electric thruster as a field emission electric propulsion (FEEP) has been previously assessed in literature for attitude control purposes [13]. In analogy with previous works, several very small FEEP thrusters could be located on the remote units placed at the tip of the spinning tethers. Alternatively, a larger thruster could be placed onboard the spacecraft body, where a limited interaction with the one or few spinning charged tethers is expected. Accordingly, in this analysis it is assumed that the interaction between the two propulsive systems does not cause any efficiency reduction.

This work focuses on deep-space heliocentric transfers performed by a small spacecraft equipped with

*Corresponding author, lorenzo.niccolai@unipi.it

an electric sail composed of a limited number of tethers and an electric thruster. The power available for the electric thruster is assumed to be provided by solar panels only, and, as such, to scale with the inverse square heliocentric distance. A recent and accurate model [4] is used to describe the E-sail thrust contribution as a function of the tether spin plane attitude and the Sun-spacecraft distance. Orbital transfers are analyzed within an optimal framework, in which a suitable performance index consisting in the combination of the flight time and the propellant consumption (with different relative weights) is minimized. It is assumed that the E-sail and the electric thruster can be steered independently. The solution of the optimal control problem makes use of an indirect multiple shooting method and is based on the Pontragyn's maximum principle [14]. Numerical simulations are performed in two circle-to-circle heliocentric transfer scenarios (Earth-Mars and Earth-Venus), and the transfer times are compared with those obtained with an E-sail alone, to quantify the advantage of the combination with an electric thruster.

2. Dynamical model

Consider a spacecraft equipped with a small E-sail and one (or more) electric thruster, powered by onboard solar panels. The spacecraft is performing a deep-space two-dimensional heliocentric transfer, so its dynamical equations can be conveniently written by using a heliocentric polar reference frame $\mathcal{T}(r,\theta)$, where r is the Sun-spacecraft distance and θ is a polar angle measured counterclockwise from a fixed direction. The latter is chosen so to coincide with the Sun-spacecraft direction at the initial time instant of the transfer $t_0 \triangleq 0$; see Fig. 1. The set of state variables of the system is completed by the radial velocity component u, the circumferential velocity component v, and the dimensionless spacecraft mass $m \triangleq M/M_0$, defined as the ratio of the instantaneous mass of the spacecraft M to the mass at the start of the transfer M_0. Accordingly, the dynamical equations of the spacecraft may be written as

$$\dot{r} = u \tag{1}$$

$$\dot{\theta} = \frac{v}{r} \tag{2}$$

$$\dot{u} = \frac{v^2}{r} - \frac{\mu_\odot}{r^2} + a_{ES_r} + a_{T_r} \tag{3}$$

$$\dot{v} = -\frac{uv}{r} + a_{ES_\theta} + a_{T_\theta} \tag{4}$$

$$\dot{m} = -\dot{m}_{\mathrm{ex}} \tag{5}$$

where $\mu_\odot$ is the Sun's gravitational parameter, and $\dot{m}_{\mathrm{ex}}$ is the dimensionless mass flow rate expelled by the electric

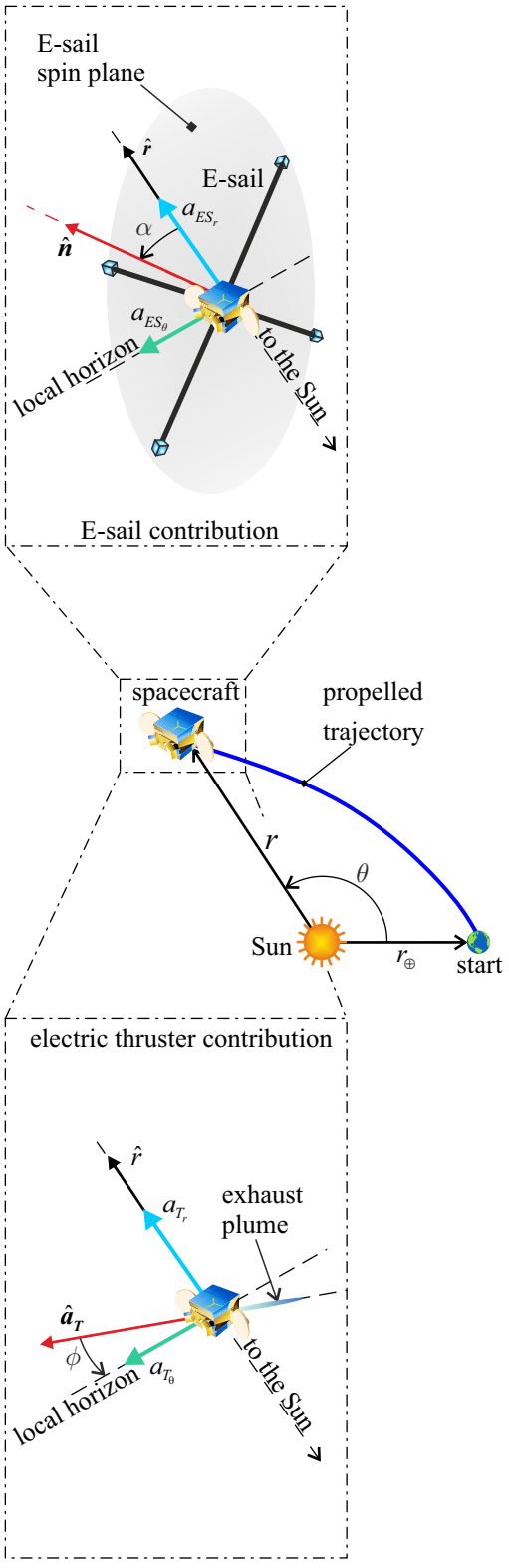

Figure 1: Sketch of the state variables and fundamental angles.

thruster. The a_{ES} and a_T terms in Eqs. (3) and (4) denote the propulsive acceleration provided by the E-sail and the electric thruster, respectively, and the subscripts r (or θ) identifies the radial (or circumferential) component. Therefore, a complete mathematical definition of the propulsive acceleration components provided by the E-sail and the electric thruster, as well as the expelled mass flow rate, is required to fully define the system dynamics.

2.1. E-sail propulsive acceleration model

The propulsive acceleration provided by the E-sail is generated by the electrostatic interaction between the ions immersed in the incoming solar wind and the charged tethers. Huo et al. [4] have analyzed the thrust generation assuming that the E-sail grid is axially-symmetric and kept stretched by the spacecraft spinning, and their results have been confirmed by more recent works [15]. The model presented in Ref. [4] is therefore consistent with a realistic near-term CubeSat spacecraft with a very limited number of spinning tethers. Accordingly, the propulsive acceleration generated by an E-sail is inversely proportional to the Sun-spacecraft distance and can be written as

$$\boldsymbol{a}_{ES} = \tau \frac{a_c}{2} \left(\frac{r_\oplus}{r} \right) [\hat{\boldsymbol{r}} + (\hat{\boldsymbol{r}} \cdot \hat{\boldsymbol{n}})\, \hat{\boldsymbol{n}}] \tag{6}$$

where the characteristic acceleration a_c is an E-sail performance parameter corresponding to the maximum propulsive acceleration that the E-sail is able to generate at a reference Sun-spacecraft distance of $r_\oplus \triangleq 1$ au. Based on the results discussed in Refs. [16, 17, 18], the value of a_c is calculated as a function of the solar wind properties, namely, the plasma density at Sun-Earth distance $n_\oplus \simeq 3.6\,\mathrm{cm}^{-3}$, the solar wind velocity $v_{sw} \simeq 400\,\mathrm{km/s}$ and potential $V_{sw} \simeq 1\,\mathrm{kV}$, and the mass of the dominating ion species (i.e., the proton mass $M_p = 1.672 \times 10^{-27}$ kg), viz.

$$a_c = \frac{NLK\,(V_{ES} - V_{sw})\,\sqrt{\epsilon M_p n_\oplus v_{sw}^2}}{M_0} \left(\frac{1}{m} \right) \tag{7}$$

where an E-sail composed of N tethers, each one with length L and maintained at a (constant) potential V_{ES} is assumed. The parameter K in Eq. (7) is an empirical constant that, according to Refs. [16, 17], is set equal to 0.18, and $\epsilon \triangleq 8.854 \times 10^{-12}$ F/m is the vacuum permittivity. The instantaneous value of the characteristic acceleration given by Eq. (7) is affected by the mass variation due to propellant consumption, so Eq. (7) is rewritten so to express the instantaneous value of a_c as a function of the value calculated at the start of the transfer, yielding

$$a_c = a_{c_0} \left(\frac{1}{m} \right) \tag{8}$$

where a_{c_0} is obtained from Eq. (7) with $m = m(t_0) = 1$. Furthermore, in Eq. (6), $\tau \in [0, 1]$ represents a switching parameter that models the possibility of adjusting the power supplied to the electron gun required to maintain the tether voltage, $\hat{\boldsymbol{r}}$ is the outwards radial unit vector, and $\hat{\boldsymbol{n}}$ is the unit vector normal to the E-sail spinning plane in the direction opposite to the Sun. Note that Eq. (6) implies that both the magnitude and the direction of the E-sail-generated propulsive acceleration is strictly related to the E-sail attitude (i.e., the spin plane spatial orientation expressed by the unit vector $\hat{\boldsymbol{n}}$), similarly to what happens for a solar sail.

Based on Eq. (6), the propulsive acceleration components are obtained as

$$a_{ES_r} = \tau \frac{a_{c_0}}{2m} \left(\frac{r_\oplus}{r} \right) \left(1 + \cos^2 \alpha \right) \tag{9}$$

$$a_{ES_\theta} = \tau \frac{a_{c_0}}{2m} \left(\frac{r_\oplus}{r} \right) \cos\alpha \sin\alpha \tag{10}$$

where $\alpha \in [-\pi/2, \pi/2]$ is the angle between $\hat{\boldsymbol{r}}$ and $\hat{\boldsymbol{n}}$, measured counterclockwise; see Fig. 1. The E-sail acceleration components given by Eqs. (9) and (10) may be substituted into Eqs. (3) and (4) to model the E-sail effect on the spacecraft dynamics.

2.2. Electric thruster propulsive acceleration model

In this analysis, the spacecraft is assumed to be equipped with an electric engine providing a low thrust, such as a field emission electric propulsion (FEEP) or an ion thruster. Since a small spacecraft is considered in this work, the power cannot be provided by a radioisotope thermal generator (RTG), so the thruster must be fed by onboard solar panels. The amount of power received from the solar panels scale as the inverse square heliocentric distance, and it is assumed that the generated thrust is directly proportional to the amount of power fed to the thruster. Accordingly, and in analogy with Ref. [7], the propulsive acceleration provided by the electric thruster is written as

$$\boldsymbol{a}_T = \kappa \frac{a_{T_0}}{m} \left(\frac{r_0}{r} \right)^2 \hat{\boldsymbol{a}}_T \tag{11}$$

where $\kappa \in [0, 1]$ is a parameter that defines the amount of available power that is supplied to the thruster, the unit vector $\hat{\boldsymbol{a}}_T$ identifies the thrust direction, and the subscript 0 denotes the initial condition. In particular, a_{T_0} is the propulsive acceleration magnitude at the beginning

of the transfer, and can be seen as a thruster performance parameter.

In analogy with previous works, the direction of the thrust contribution generated by the electric engine is identified by defining the thrust angle $\phi \in [\phi_{min}, \phi_{\max}]$ as the angle between $\hat{\boldsymbol{a}}_T$ and the local horizon, measured counterclockwise; see Fig. 1. The admissible values of the thrust angle take into account limitations in the steering capability of the thruster and possible constraints on the direction of the exhaust ions expelled that should not impinge on the E-sail tethers. Based on the thrust angle definition, the electric thruster contribution to the spacecraft propulsive acceleration may be decomposed into a radial and a circumferential component as

$$a_{T_r} = \kappa \frac{a_{T_0}}{m} \left(\frac{r_0}{r}\right)^2 \sin\phi \tag{12}$$

$$a_{T_\theta} = \kappa \frac{a_{T_0}}{m} \left(\frac{r_0}{r}\right)^2 \cos\phi \tag{13}$$

which may be substituted into Eqs. (3) and (4).

Finally, a complete definition of the system dynamics requires a mathematical expression of the dimensionless mass flow rate expelled by the electric thruster, to be inserted in Eq. (5). Specifically, the dimensionless mass consumption per time unit depends on the power that is supplied to the thruster, yielding [6]

$$\dot{m}_{\text{ex}} = \kappa \frac{a_{T_0}}{g I_{sp}} \left(\frac{r_0}{r}\right)^2 \tag{14}$$

where $g \triangleq 9.80665\,\text{m/s}^2$ is the standard gravity at Earth's sea level, and I_{sp} is the thruster specific impulse.

3. Optimal control problem formulation

Having fully characterized the system dynamics by obtaining a mathematical model for the terms involved in Eqs. (1)–(5), an orbital transfer with a spacecraft propelled by an E-sail and an electric thruster can be analyzed within an optimal framework. To this end, consider a circle-to-circle, two-dimensional, deep-space transfer from the Earth to a target celestial body whose heliocentric orbital eccentricity is neglected in this work.

First, it is assumed that the control variables that may independently selected at every time instant are the E-sail attitude angle α, its switching factor τ, the electric engine thrust angle ϕ and its power feeding factor κ. Then, the cost function J to be maximized is defined as a linear combination of the final (dimensionless) spacecraft mass and the negative flight time, viz.

$$J = \gamma m_f - (1-\gamma)\frac{t_f}{T} \tag{15}$$

where the subscript f denotes the end of the transfer, and $T \triangleq 2\pi\sqrt{r_0^3/\mu_\odot}$ is used as a reference time to obtain a dimensionless cost function. The expression of the cost function given by Eq. (15) highlights that the optimality of a transfer trajectory is defined by a trade-off between competing requirements, namely, performing the maneuver in a short flight time and using a small amount of propellant. In this regard, the weight $\gamma \in [0, 1]$ represents a trade-off parameter that defines the relative importance of the propellant-related objective with respect to the flight time objective. In particular, selecting $\gamma = 0$ amounts to searching for the minimum-time transfer trajectory regardless of the propellant consumption, while a value $\gamma = 1$ only minimizes the propellant consumption without taking into account the time required by the transfer.

The optimal control problem is then formulated by adding to the set of state variables of the system $\{r, \theta, u, v, m\}$ a set of costate (adjoint) variables $\{\lambda_r, \lambda_\theta, \lambda_u, \lambda_v, \lambda_m\}$, each one associated with a physical state variable. Accordingly, the system Hamiltonian function may be defined as [14]

$$\mathcal{H} \triangleq \lambda_r \dot{r} + \lambda_\theta \dot{\theta} + \lambda_u \dot{u} + \lambda_v \dot{v} + \lambda_m \dot{m} \tag{16}$$

where the time derivatives of the state variables are given by Eqs. (1)–(5). The time histories of the costate variables are obtained from the Euler-Lagrange equations as

$$\dot{\lambda_r} = -\frac{\partial H}{\partial r} \tag{17}$$

$$\dot{\lambda_\theta} = -\frac{\partial H}{\partial \theta} = 0 \tag{18}$$

$$\dot{\lambda_u} = -\frac{\partial H}{\partial u} = \frac{\lambda_v v}{r} - \lambda_r \tag{19}$$

$$\dot{\lambda_v} = -\frac{\partial H}{\partial v} = \frac{-\lambda_\theta - 2\lambda_u v + \lambda_v u}{r} \tag{20}$$

$$\dot{\lambda_m} = -\frac{\partial H}{\partial m} \tag{21}$$

where the explicit expressions of Eq. (17) and (21) are omitted for the sake of conciseness. Note that Eq. (18) highlights that λ_θ is a constant of motion.

3.1. Optimal control laws

According to Pontragyn's maximum principle, the optimal trajectory is obtained when the control variables $\{\tau, \alpha, \kappa, \phi\}$ are selected so to maximize the Hamiltonian given by Eq. (16). The portion of the Hamiltonian that explicitly depends on the control variables $\mathcal{H}'$ can be split into two separate contributions, viz.

$$\mathcal{H}' = \mathcal{H}'_{ES} + \mathcal{H}'_T \tag{22}$$

where the E-sail contribution $\mathcal{H}'_{ES}$ is given by

$$\mathcal{H}'_{ES} \triangleq \tau \frac{a_{c_0}}{2m}\left(\frac{r_\oplus}{r}\right)\left[\lambda_u\left(1+\cos^2\alpha\right)+\lambda_v\cos\alpha\sin\alpha\right] \tag{23}$$

while the electric thruster contribution $\mathcal{H}'_T$ can be expressed as

$$\mathcal{H}'_T \triangleq \kappa \frac{a_{T_0}}{m}\left(\frac{r_0}{r}\right)^2\left(\lambda_u\sin\phi+\lambda_v\cos\phi-\lambda_m\frac{m}{gI_{sp}}\right) \tag{24}$$

Assuming that the control variables can be freely selected at every time instant of the motion, the maximization of $\mathcal{H}'$ can be performed by independently maximizing the single contributions $\mathcal{H}'_{ES}$ and $\mathcal{H}'_T$. Paralleling the discussion provided in Ref. [4], the optimal values of the switching parameter $\tau^\star$ and the E-sail cone angle $\alpha^\star$ that maximize $\mathcal{H}'_{ES}$ are obtained as

$$\alpha^\star = \frac{1}{2}\arctan\left(\frac{\lambda_v}{\lambda_u}\right) \tag{25}$$

$$\tau^\star = \frac{1}{2}+\frac{1}{2}\text{sign}\left(1+\frac{3\lambda_u}{\sqrt{\lambda_u^2+\lambda_v^2}}\right) \tag{26}$$

Conversely, the maximum value of the portion of the Hamiltonian that depends on the electric thruster control variables $\mathcal{H}'_T$ is obtained by taking into account the admissible values of ϕ as

$$\phi^\star = \begin{cases} \phi_{\min} & \text{if} \quad \phi_{opt} < \phi_{\min} \\ \phi_{opt} & \text{if} \quad \phi_{\min} \le \phi_{opt} \le \phi_{\max} \\ \phi_{\max} & \text{if} \quad \phi_{opt} > \phi_{\max} \end{cases} \tag{27}$$

where the value of $\phi_{opt} \in [0, 2\pi)$ is calculated from the following conditions

$$\sin\phi_{opt} = \frac{\lambda_u}{\sqrt{\lambda_u^2+\lambda_v^2}} \qquad \cos\phi_{opt} = \frac{\lambda_v}{\sqrt{\lambda_u^2+\lambda_v^2}} \tag{28}$$

Finally, the optimal value of the power feeding parameter $\kappa^\star$ is obtained with a simple bang-bang control law

$$\kappa^\star = \frac{1}{2}+\frac{1}{2}\text{sign}\left(\lambda_u\sin\phi^\star+\lambda_v\cos\phi^\star-\lambda_m\frac{m}{gI_{sp}}\right) \tag{29}$$

which highlights that the electric thruster is either switched off ($\kappa^\star = 0$) or powered with the maximum available power ($\kappa^\star = 1$).

3.2. Boundary conditions

The dynamical equations (1)–(5) and the Euler-Lagrange equations (17)–(21) define a two-point boundary value problem, which is completed by a set of boundary conditions related to the system state at the start and the final time instant of the transfer. Assume that the spacecraft exits the Earth's sphere of influence with negligible hyperbolic excess velocity at time $t_0 \triangleq 0$, so that $r_0 = r_\oplus$, and let r_f be the heliocentric orbit radius of the target celestial body. Accordingly, the boundary conditions at the start of the transfer are given by

$$\begin{aligned} &r(0) = r_\oplus \qquad \theta(0) = 0 \qquad u(0) = 0 \\ &v(0) = \sqrt{\frac{\mu_\odot}{r_\oplus}} \qquad\qquad m(0) = 1 \end{aligned} \tag{30}$$

while the boundary conditions at the end of the transfer are

$$r(t_f) = r_f \qquad u(t_f) = 0 \qquad v(t_f) = \sqrt{\frac{\mu_\odot}{r_f}} \tag{31}$$

The problem needs to be completed by enforcing the transversality conditions [14], yielding

$$\lambda_\theta(t_f) = 0 \qquad \lambda_m(t_f) = \gamma \qquad \mathcal{H}(t_f) = \frac{1-\gamma}{T} \tag{32}$$

Note that the first of transversality conditions (32), combined with Eq. (18), shows that $\lambda_\theta \equiv 0$ for all $t \in [0, t_f]$. Accordingly, solving the optimal control problem amounts to finding the initial values of the costate variables $\{\lambda_r(0), \lambda_u(0), \lambda_v(0), \lambda_m(0)\}$ and the transfer time t_f, so that the boundary conditions (30), (31) and the transversality conditions (32) are met. It is evident that a different optimal solution will be obtained for each value of γ, which in turn expresses a different relative weight of the two competing requirements of short flight time and small propellant consumption.

4. Case study

The effectiveness of the previously discussed control law is tested in two exemplary mission scenarios, consisting of circle-to-circle, ephemeris-free, interplanetary transfers towards Mars or Venus. The spacecraft is assumed to be have a launch total mass $M_0 = 20\,\text{kg}$. A complete list of the E-sail data used in the numerical simulations is given in Tab. 1. The selected values are based on the preliminary mission design provided in Ref. [3], and are compatible with a near-term deep-space mission. The mass of the E-sail described in Tab. 1 has been estimated based on existing mass-budget breakdown models [13], considering a Heytether structure [19] and excluding components that are required only if a large grid is assumed, as auxiliary tethers. Under these assumptions, the E-sail system mass includes

a total tether mass of about 0.23 kg, a reel mass ranging from 0.24 kg (if $N = 1$ and $L = 20$ km) to 0.24 kg (if $N = 4$ and $L = 5$ km), and an E-sail-related power generation system mass of about 2.8 kg. Accordingly, the mass associated with the E-sail system is estimated to be about 3.5 kg, a value that is compatible with the total launch mass estimation.

Table 1: Characteristics of the E-sail used in the numerical simulations.

Quantity	Value	Measurement unit
NL	20	km
V_{ES}	20	kV
a_{c_0}	0.307	mm/s^2

The parameters of the electric thruster are taken from IFM Micro FEEP Thruster design, which is currently undergoing space-qualification tests [20] and should be fit into two CubeSat units, and are reported in Tab. 2. The total dry mass of the thruster is about 2.6 kg including the power processing unit. Note that the parameters of Tab. 2 are also compatible with a configuration in which a set of smaller FEEP thruster is placed inside the remote unit at the tip of each tether, assuming $N \geq 2$. The thrust direction is assumed to be steerable within a cone with half-angle 30 deg centered along the circumferential direction. The angle ϕ is assumed to be acute (or obtuse) for orbital transfers towards external (or internal) regions of the Solar System, so that the electric thruster propulsive acceleration has a positive (or negative) circumferential component a_{T_θ}.

Table 2: Characteristics of the electric thruster used in the numerical simulations.

Quantity	Value	Measurement unit
Nominal thrust	1.0	mN
I_{sp}	2 150	s
a_{T_0}	0.05	mm/s^2
Thrust cone half-angle	30	deg

The results for an Earth-Mars scenario (r_f = 1.524 au) are given in Fig. 2, where the Pareto front of the multi-objective optimization is plotted. In particular, different flight times and propellant consumptions are shown for different values of the trade-off constant γ. It

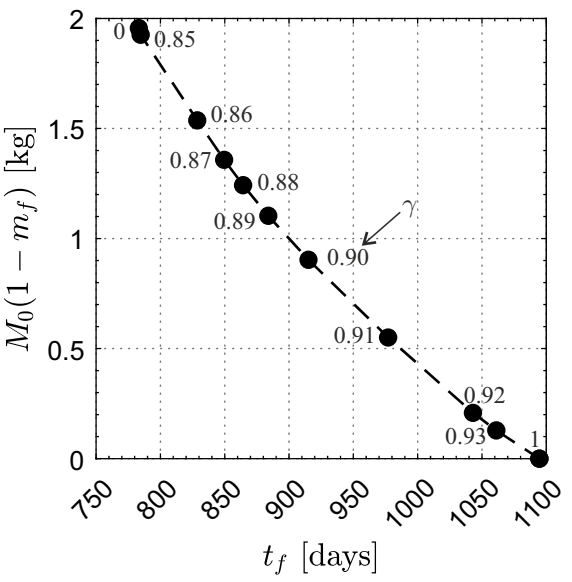

Figure 2: Pareto front of Earth-Mars transfer different values of γ.

is worth remarking that for $\gamma \in [0, 0.8]$, the optimal trajectories are almost identical, with the electric thruster firing for all of the flight time. Increasing the value of γ, the electric thruster is switched off for larger parts of the heliocentric transfer. When γ approaches 1, the solution of the optimal control problem tends to the limit case in which only the E-sail is used and the electric thruster is never switched on. The transfer time corresponding to the latter case is almost 3 years. Assuming a propellant consumption of about 1 kg [20] the flight time is reduced by 200 days, while the $\gamma = 0$ case (i.e., thruster always switched on and minimum-time trajectory) allows the flight time to be reduced by 320 days. The effectiveness of the combination of an E-sail and a high-specific impulse electric thruster is remarkable.

An example of optimal time histories of the control variables $\{\tau^\star(t), \alpha^\star(t), \kappa^\star(t), \phi^\star(t)\}$ calculated for an Earth-Mars transfer setting $\gamma = 0.86$ is given in Fig. 3. Note that the thruster is switched on for the majority of the flight time, consuming a total propellant mass of 1.54 kg but allowing Mars to be reached in 829 days. A different situation is shown in Fig. 4, where an optimal Earth-Mars transfer with $\gamma = 0.91$ is considered. In this scenario, the transfer is mostly E-sail-propelled, with the thruster switching on for short firing times. The transfer time is consequently larger with respect to the previous case, amounting to 977 days, but the propellant consumption is reduced to just 0.55 kg.

Considerations made for the Earth-Mars transfer can

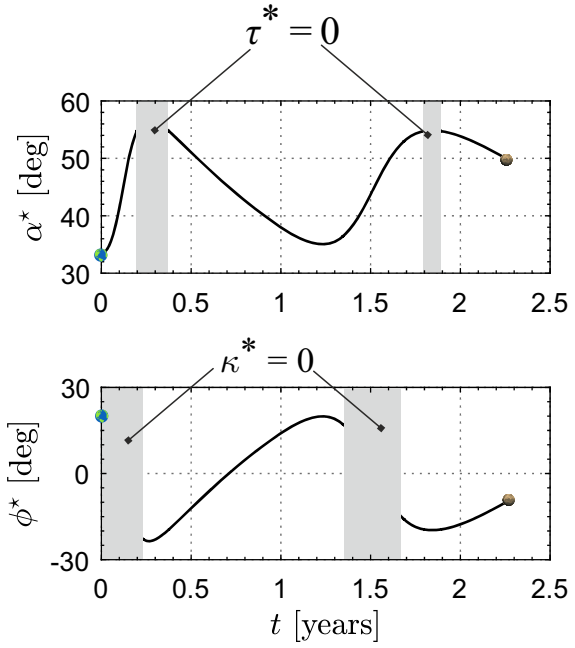

Figure 3: Time histories of the optimal control variables for an Earth-Mars transfer with $\gamma = 0.86$.

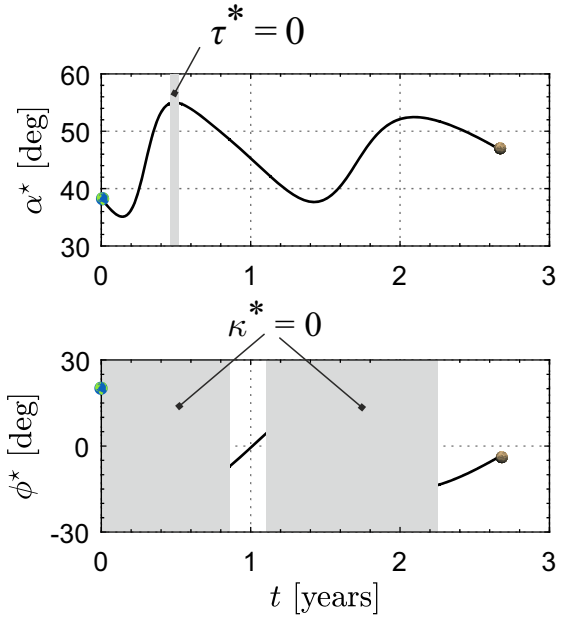

Figure 4: Time histories of the optimal control variables for an Earth-Mars transfer with $\gamma = 0.91$.

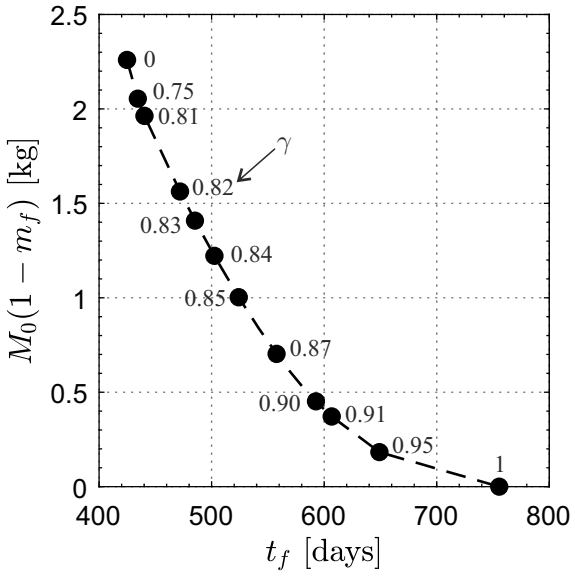

Figure 5: Pareto front of Earth-Venus transfer different values of γ.

be easily extended to an Earth-Venus transfer scenario. In this case, since $r_f = r_{\varphi} = 0.723$ au is lesser than $r(0) = r_{\oplus}$, the electric thruster is assumed to be placed onboard so to generate a negative circumferential thrust component a_{T_θ}, so $\phi \in [5\pi/6, 7\pi/6]$. The Pareto front generated by setting different values of γ is shown in Fig. 5. In this scenario, the global minimum of the transfer time amounts to 425 days (obtained with $\gamma = 0$) and the corresponding propellant consumption amounts to about 2.26 kg, while the transfer time if only the E-sail is used (i.e., $\gamma = 1$) is 756 days. A propellant consumption of 1 kg enables a significant flight time reduction, amounting to 232 days. These results suggest that the combination of an E-sail and an electric thruster proves its effectiveness even for orbital transfer towards inner regions of the solar system.

5. Conclusion

This work has discussed the possibility of combining an electric sail composed of a very small number of tethers with an electric thruster to perform deep-space heliocentric transfers. While the electric sail thrust scales as the inverse heliocentric distance, the power fed to the thruster has been assumed to scale as the power generated by onboard solar panels. The analysis has been performed within an optimal framework, in which a multi-objective cost function is minimized, consisting of the combination of the flight time and the propellant

consumption with different relative weights. Numerical simulations have shown the effectiveness of the combination of the sail and the thruster, with significant reduction of the transfer times obtained even with small propellant consumptions.

A natural extension of this work could assume that the electric sail is constantly kept in the Sun-facing configuration, thus significantly simplifying the attitude control. More refined developments could consist of the analysis of a scenario in which the sail attitude and the thruster exhaust direction cannot be freely selected but are coupled, and the extension to more realistic transfer trajectories (including planetary eccentricities and inclination with respect to the Ecliptic).

References

[1] M. Bassetto, L. Niccolai, A. A. Quarta, and G. Mengali. A comprehensive review of Electric Solar Wind Sail concept and its applications. *Progress In Aerospace Sciences*, 128(article no. 100768):1–27, 2022. doi: 10.1016/j.paerosci.2021.100768.

[2] P. Janhunen. Electric sail for spacecraft propulsion. *Journal of Propulsion and Power*, 20(4):763–764, 2004. doi: 10.2514/1.8580.

[3] A. Slavinskis, P. Janhunen, P. K. Toivanen, et al. Nanospacecraft fleet for multi-asteroid touring with electric solar wind sails. In *IEEE Aerospace Conference Proceedings*, volume 2018-March, pages 1–20, Big Sky (MT), USA, March 3–10 2018. doi: 10.1109/AERO.2018.8396670.

[4] M. Huo, G. Mengali, and A. A. Quarta. Electric sail thrust model from a geometrical perspective. *Journal of Guidance, Control, and Dynamics*, 41(3):734–740, 2018. doi: 10.2514/1.G003169.

[5] M. Leipold and M. Götz. Hybrid photonic/electric propulsion. techreport, Munich, Germany, 2002.

[6] G. Mengali and A. A. Quarta. Trajectory design with hybrid low-thrust propulsion system. *Journal of Guidance, Control, and Dynamics*, 30(2):419–426, 2007. doi: 10.2514/1.22433.

[7] G. Mengali and A. A. Quarta. Tradeoff performance of hybrid low-thrust propulsion system. *Journal of Spacecraft and Rockets*, 44(6):1263–1270, 2007. doi: 10.2514/1.30298.

[8] R. J. McKay, M. Macdonald, J. D. Biggs, and C. R. McInnes. Survey of highly-non-Keplerian orbits with low-thrust propulsion. *Journal of Guidance, Control, and Dynamics*, 34(3):645–666, May 2011. doi: 10.2514/1.52133.

[9] M. Ceriotti and C. R. McInnes. Generation of optimal trajectories for Earth hybrid pole sitters. *Journal of Guidance, Control, and Dynamics*, 34(3):847–859, May 2011. doi: 10.2514/1.50935.

[10] J. Heiligers, C. R. McInnes, J. D. Biggs, and M. Ceriotti. Displaced geostationary orbits using hybrid low-thrust propulsion. *Acta Astronautica*, 71:51–67, February 2012. doi: 10.1016/j.actaastro.2011.08.012.

[11] O. Mori, J. Matsumoto, T. Chujo, et al. Solar power sail mission of OKEANOS. *Astrodynamics*, 4(3):233–248, September 2020. doi: 10.1007/s42064-019-0067-8.

[12] M. Matsushita, T. Chujo, J. Matsumoto, et al. Solar power sail membrane prototype for OKEANOS mission. *Advances in Space Research*, 67(9):2899–2911, May 2021. doi: 10.1016/j.asr.2020.10.007.

[13] P. Janhunen, A. A. Quarta, and G. Mengali. Electric solar wind sail mass budget model. *Geoscientific Instrumentation, Methods, and Data Systems*, 2(1):85–95, February 2013. doi: 10.5194/gi-2-85-2013.

[14] A. E. Bryson and Y.-C. Ho. *Applied Optimal Control: Optimization, Estimation and Control*, chapter 2, pages 42–89. Hemisphere Publishing Corporation, New York (NY), USA, 1975.

[15] M. Bassetto, G. Mengali, and A. A. Quarta. Thrust and torque vector characteristics of axially-symmetric E-sail. *Acta Astronautica*, 146:134–143, May 2018. doi: 10.1016/j.actaastro.2018.02.035.

[16] P. Janhunen, P. K. Toivanen, J. Polkko, et al. Electric solar wind sail: toward test missions. *Review of Scientific Instruments*, 81 (11):1–111, November 2010. doi: 10.1063/1.3514548.

[17] P. K. Toivanen and P. Janhunen. Spin plane control and thrust vectoring of electric solar wind sail. *Journal of Propulsion and Power*, 29(1):178–185, January 2013. doi: 10.2514/1.B34330.

[18] P. K. Toivanen and P. Janhunen. Thrust vectoring of an electric solar wind sail with a realistic shape. *Acta Astronautica*, 131: 145–151, February 2017. doi: 10.1016/j.actaastro.2016.11.027.

[19] T. Rauhala, H. Seppänen, J. Ukkonen, et al. Automatic 4-wire Heytether production for the electric solar wind sail. In *The International Microelectronics Assembly and Packing Society Topical Workshop and Tabletop Exhibition on Wire Bonding*, San Jose (CA), USA, 2013.

[20] L. Grimaud, D. Krejci, and B. Seifert. The IFM Micro FEEP thruster: a modular design for smallsat propulsion. In *36th International Electric Propulsion Conference*, Vienna, Austria, September 2019.